Spatial Heterogeneity & Ecological Patterns: Their Role in Species Persistence

A thesis submitted in fulfilment of the requirements for the degree of Doctor of Philosophy by

Sounov Marick

Under the supervision of

Prof. Nandadulal Bairagi

Center for Mathematical Biology and Ecology
Department of Mathematics
Jadavpur University
Kolkata 700032, India

September 2025

যাদবপুর বিশ্ববিদ্যালয়

FACULTY OF SCIENCE
DEPARTMENT OF MATHEMATICS

JADAVPUR UNIVERSITY
Kolkata - 700 032, India
Telephone : 91 (33) 2457 2269

Ref. No. .....

Date 10/09/2025

CERTIFICATE FROM THE SUPERVISOR

This is to certify that the thesis entitled **"Spatial Heterogeneity & Ecological Patterns: Their Role in Species Persistence"** submitted by **Shri Sounov Marick**, who got his name registered **(Index No. 6/22/Maths./27)** on for the award of PhD (Science) degree of Jadavpur University, is based upon his work under the supervision of myself and that neither this thesis nor any part has been submitted for either any degree/diploma or any other academic award anywhere before.

Prof. Nandadulal Bairagi
(Supervisor)
Centre for Mathematical Biology and Ecology
Department of Mathematics
Jadavpur University

Nandadulal Bairagi (Ph. D.)
Professor, Dept. of Mathematics
Jadavpur University
Kolkata-700032

Declaration

This is to certify that the thesis titled **"Spatial Heterogeneity & Ecological Patterns: Their Role in Species Persistence"** has been authored by me. It presents the research conducted by me under the supervision of **Prof. Nandadulal Bairagi**.

To the best of my knowledge, it is an original work, both in terms of research content and narrative, and has not been submitted elsewhere, in part or in full, for a degree. Further, due credit has been attributed to the relevant state-of-the-art and collaborations with appropriate citations and acknowledgments, in line with established norms and practices.

Sounov Marick

Centre for Mathematical Biology and Ecology
Department of Mathematics
Jadavpur University

This thesis is dedicated to the memory of my father

Late Barun Kumar Marick

Acknowledgements

First and foremost, I would like to express my deepest gratitude to my supervisor, Prof. Nandadulal Bairagi, from the Department of Mathematics, Jadavpur University, Kolkata, India. From the very first day of my research journey, his unwavering dedication to mathematics, strong work ethic, and disciplined approach have been a constant source of inspiration. His invaluable guidance, insightful advice, and tireless support have played a crucial role in shaping this work. Beyond academics, his mentorship has left a profound impact on me, both professionally and personally. Without his encouragement and patience, completing this thesis on time would have been impossible.

I am also immensely grateful to the Center for Mathematical Biology and Ecology, the Biomathematical Society of India, and all my esteemed teachers at the Department of Mathematics, Jadavpur University, for their constant encouragement and support. Their insightful discussions and valuable feedback have greatly enriched my research.

I extend my sincere thanks to the Council of Scientific & Industrial Research (CSIR), Govt. of India, for their financial support through a Research Fellowship, which enabled me to pursue this work with focus and dedication.

A heartfelt appreciation goes to the seniors Dr. Santu Ghorai, Dr. Bhaskar Chakraborty, Dr. Chittaranjan Mondal, Dr. Abhijit Majumder, Dr. Santanu Bhattacharya, and Dr. Priyanka Saha for their invaluable help and guidance throughout this journey. Their encouragement and insights have played a vital role in shaping my research.

I am fortunate to have been surrounded by an incredible group of fellow researchers and friends: Mr. Chirodeep Mondal, Mr. Debjit Pal, Mr. Ayanava Basak, Mr. Aditya Bag, Mr. Sourav Ghorai, Mr. Sourav Maity, and Ms. Arnabi Saha. Their constant support have made this journey not just academically fulfilling but also personally rewarding.

Finally, words cannot express the depth of my gratitude to my mother, Smt. Mita Marick, and my wife, Smt. Amrita Pal. Their unwavering love, sacrifices, and steadfast belief in me have been my pillar of strength throughout this journey. Their support has given me the courage and motivation to overcome challenges and stay committed to my goals.

August 25, 2025 **Sounov Marick**

Contents

List of Publications

Publications from Thesis:

1. **Marick, S.**, Bhattacharya, S., & Bairagi, N. (2023). Dynamic properties of a reaction–diffusion predator–prey model with nonlinear harvesting: A linear and weakly nonlinear analysis. **Chaos, Solitons & Fractals**, 175, 113996. *https://doi.org/10.1016/ j.chaos. 2023.113996*.

2. **Marick, S.**, Takasu, F., & Bairagi, N. (2024). How do productivity gradient and diffusion shape patterns in a plant–herbivore grazing system? **Journal of Theoretical Biology**, 590, 111856. *https://doi.org/10.1016/j.jtbi.2024.111856*.

3. **Marick, S.**, Ghorai, S., & Bairagi, N. (2023). Dynamic characteristics of a hyperbolic reaction–diffusion predator–prey system with self-diffusion and non-identical inertia. **Mathematical Methods in the Applied Sciences**, 46(13), 14407-14421. *https://doi.org/ 10.1002/mma.9326*.

4. **Marick, S.**, & Bairagi, N. (2025). Spatiotemporal instabilities and climate-driven extinction in predator-prey systems. (*Communicated*)

5. **Marick, S.**, & Bairagi, N. (2025). Multiscale pattern complexity in vegetation: A modeling approach incorporating root plasticity and stratified soil water dynamics. (*Communicated*)

Additional publications during PhD tenure:

1. **Marick, S.**, & Bairagi, N. (2025). Effect of dispersal-induced death in predator-prey metapopulation system with bistable local dynamics. **Physica D: Nonlinear Phenomena**, 476, 134597. *https://doi.org/10.1016/j.physd.2025.134597*.

2. Chakraborty, B., **Marick, S.**, & Bairagi, N. (2024). Diffusion-driven instabilities in a tri-trophic food web model: From Turing to non-Turing patterns and

waves. **Chaos, Solitons & Fractals**, 189, 115634. *https://doi.org/10.1016/j.chaos.2024.115634*.

3. **Marick, S.**, Saha, S., Bairagi, N. (2025). Species extinction and revival in metapopulation under climate-induced tipping on the local scale. (*Communicated*)

4. Ghorai, S., **Marick, S.**, Bairagi, N., (2025). Bistable epidemic model on spatially discrete system: role of network topology, dispersal and initial infected nodes. (*Communicated*)

5. Ghorai, S., Basak, A., Dhar, R., **Marick, S.**, Bairagi, N. (2025). Impact of prospective and retrospective awareness programs on the average yearly dengue cases: A theoretical and computational study. (*Communicated*)

Chapter 1

Introduction

1.1 Spatial ecological systems

Understanding the dynamics of populations across space and time has long been a central concern in ecological research [1]. In natural settings, populations seldom exist in isolation or in homogeneous environments. Rather, they inhabit spatially structured and heterogeneous landscapes, where variation in habitat quality, patterns of dispersal or migration, and local-scale interactions critically influence ecological outcomes [2]. These spatial processes operating in tandem with local biological interactions such as competition, mutualism, and trophic relationships, shape fundamental population-level outcomes, including persistence, extinction risk, spatial synchrony, and the formation of steady-state heterogeneous distributions or spatial patterns [3, 4, 5]. As populations not only change over time but also move, spread, and interact across space, spatial structure emerges as a silent yet potent driver of ecological dynamics.

Classic empirical studies have illustrated these principles vividly. The cyclic oscillations of snowshoe hare and Canadian lynx populations, inferred from the Hudson's Bay pelt-trading records, exemplify the spatiotemporal dynamics of predator-prey systems [6]. Similarly, aerial imaging of patterned vegetation in arid ecosystems has revealed striking instances of spatial self-organization driven by plant-soil water feedbacks under environmental resource scarcity [7]. At the theoretical level, the concept of metapopulations has played a foundational role in formalizing spatial ecological thinking. Introduced by Levins [8] and later developed by Hanski [9], metapopulation models describe systems of spatially discrete yet connected populations, where

colonization and extinction dynamics across habitat patches determine regional persistence. These frameworks explain how populations can persist despite frequent local extinctions, as dispersal facilitates recolonization. Another central idea is spatial synchrony, the correlated fluctuations of populations across different locations [10]. While synchrony may arise due to correlated environmental fluctuations or dispersal-mediated coupling, it also poses risks by making systems more vulnerable to synchronized collapses [10, 11].

Traditional population models that neglected space, relying on mean-field or well-mixed assumptions, often failed to capture these nuanced dynamics. In contrast, spatially explicit models incorporating individual movement, patchiness, and environmental heterogeneity have become essential tools in contemporary ecology. To investigate such spatially extended dynamics, mathematical modeling has been instrumental. In particular, continuous-space models using partial differential equations (PDEs), such as reaction-diffusion systems, offer a powerful framework for analyzing ecological pattern formation and cyclic or oscillatory dynamics. These models capture how local interactions (defined by reaction terms) coupled with movement or dispersal (defined by diffusion terms) generate spatiotemporal phenomena, including travelling waves, spiral waves, and stationary Turing patterns. These models allow researchers to explore how fine-scale processes, such as neighborhood competition or edge effects, influence large-scale patterns and transitions. Importantly, such self-organized structures can emerge without external perturbations, highlighting the role of internal feedback and spatial heterogeneity in shaping ecological complexity. Moreover, spatially explicit studies are crucial for identifying thresholds or tipping points beyond which systems undergo undesirable shifts, such as regional extinction, community reassembly, or breakdown of synchrony.

In light of these developments, this thesis focuses on spatial population dynamics and emergent ecological patterns within the framework of reaction-diffusion models. The aim is to mathematically and qualitatively investigate how spatial interactions and movement influence ecological stability, pattern formation, and population persistence across scales. By bridging theoretical modeling with ecological insight, the work contributes to a deeper understanding of the role of space in governing population dynamics and the broader structure of ecosystems.

1.2 Real-world examples of spatial predator-prey interactions

Numerous real-world studies have demonstrated that predator-prey dynamics are deeply influenced by spatial and temporal complexities in natural environments. The classic and one of the pioneering examples is the cyclic interaction between the snowshoe hare (Lepus americanus) and the Canada lynx (Lynx canadensis) across the Boreal forest of North America. Historical data from the Hudson's Bay fur records revealed multi-year oscillations in their population densities, yet further ecological investigations showed that these cycles were not uniform across space, with regional variations in amplitude and timing due to habitat heterogeneity and dispersal barriers [12, 13]. In marine ecosystems, Paine's foundational experiments on intertidal communities demonstrated how the removal of the predator starfish Pisaster ochraceus led to dramatic shifts in prey populations, particularly mussels (Mytilus californianus), reshaping entire community structures depending on the spatial context of removal [14]. In agricultural landscapes, outbreaks of the spruce budworm (Choristoneura fumiferana) in North American conifer forests illustrate spatially synchronized population eruptions followed by collapses, a dynamic shaped by both predator abundance and environmental conditions [15]. Similarly, in the Serengeti ecosystem of East Africa, the predator-prey dynamics involving lions (Panthera leo) and migratory herbivores such as wildebeest (Connochaetes taurinus) are modulated by large-scale seasonal movements, landscape features, and spatial variation in resource availability [16]. In aquatic systems, the dynamic between northern pike (Esox lucius) and their prey fish in shallow lake environments has shown that spatial refuges such as vegetated areas significantly affect predator efficiency and prey survival, contributing to persistent but uneven population fluctuations across space [17]. In Åland Islands, Finland, Long-term landscape surveys show years of highly synchronous lows across local populations of Glanville fritillary butterfly (*Melitaea cinxia*) that coincide with elevated regional extinction rates and larger metapopulation crashes; increasing climate-driven synchrony has amplified that risk through time [18]. In the host–pathogen system of powdery mildew *Podosphaera plantaginis* on *Plantago lanceolata*, winters that synchronize dynamics across patches produce concurrent local crashes and higher patch-level extinctions, undermining regional persistence, illustrating the review's point that shared environmental forcing (Moran effects) can synchronize risk [19]. These diverse case studies demonstrate that predator-prey or consumer-resource relationships in nature are shaped by more than just species interactions; they are deeply conditioned by geography, landscape structure, movement patterns, and localised ecological contexts.

1.3 Vegetation patterns in arid ecosystems

Real-life observations of vegetation patterns across arid and semi-arid ecosystems worldwide provide compelling evidence of spatial self-organization in ecological systems. In the Sahel region of sub-Saharan Africa, remote sensing and aerial photography have revealed striking banded vegetation patterns, commonly referred to as "tiger bush", which appear as alternating stripes of dense and sparse vegetation oriented perpendicular to the slope [20, 21]. These bands are frequently formed by drought-tolerant shrubs such as Combretum micranthum, Guiera senegalensis, and Acacia senegal, which promote water infiltration and stabilize soil locally, thereby reinforcing their own growth while depleting surrounding areas. In the Australian outback, similar spotted and labyrinthine vegetation patterns are generated by species like Triodia basedowii (spinifex grass) and Eremophila spp., adapted to sandy soils and highly variable rainfall conditions [22]. In Israel's Negev Desert, perennial shrubs such as Hammada scoparia and Atriplex halimus form well-defined vegetation patches, driven by slope-driven runoff and feedbacks between water availability and plant biomass [23, 24]. In North America's Chihuahuan Desert, spatial clustering of grasses like Bouteloua eriopoda (black grama) and shrubs such as Larrea tridentata (creosote bush) occurs in response to microtopographic water capture and soil resource redistribution [25]. Additionally, in the Horn of Africa and India's Thar Desert, species such as Leptadenia pyrotechnica and Calligonum polygonoides have been observed to form patchy and stripe-like formations under arid conditions, highlighting the universal tendency of vegetation to self-organize in response to resource scarcity [26, 27]. These globally distributed patterns reveal a convergence of plant-soil-water feedback mechanisms, where localized facilitation and long-range competition interact nonlinearly to produce robust spatial structures. Moreover, changes in these patterns, such as fragmentation or reduced regularity, serve as early indicators of ecological degradation and increasing vulnerability to desertification [27, 28]. Thus, the study of vegetation pattern formation, especially through reaction-diffusion frameworks, is not only of theoretical interest but also vital for assessing and managing the resilience of dryland ecosystems worldwide.

1.4 Reaction-diffusion system

A reaction–diffusion system mathematically expresses how the density of one or more interacting species changes over space and time. As the name suggests, it combines two essential components: the reaction term, which represents local interactions such as birth, death, predation, and competition, in the context of ecological systems

and the diffusion term, which captures spatial movement due to random dispersal or motility.

Parabolic reaction-diffusion (PRD) equation

The most classical and straightforward model for describing spatial spread or dispersal is the diffusion equation, also known as Fick's second law. Adolf Fick's work in 1855 established the fundamental laws of diffusion, often referred to as Fick's first and second laws [29]. These laws describe how substances spread out from areas of high concentration to low concentration. This forms the basis of the diffusion term in the reaction-diffusion equation. In a two-dimensional spatial setting, it takes the form

$$\frac{\partial u}{\partial t} = D\left(\frac{\partial^2 u}{\partial x^2} + \frac{\partial^2 u}{\partial y^2}\right), \tag{1.1}$$

where D represents the diffusion coefficient. The framework is particularly well-suited for modeling continuum agents such as diffusing ink in a solvent like water, where the number of particles is virtually infinite. In an ecological setting, one can think of soil moisture or grassland vegetation, where the interacting quantities are effectively uncountable and vary smoothly over space and time. Even in ecological contexts involving a finite number of individuals (like in predator-prey systems), this approach offers a robust approximation by capturing the aggregate population-level dynamics. At the microscopic level, individual system agents following a simple random walk or Brownian motion exhibit diffusion-like behavior on a macroscopic scale. The applicability of the reaction-diffusion system in modeling population dynamics is validated in the last three decades [29, 30]. The diffusion equation preserves positivity. The fundamental solution from an initial point-source located at $x = 0$ and time $t = 0$, with $u(x, 0) = \delta(x)$ (where $\delta(.)$ is Dirac delta function), is given by

$$u(x, y, t) = \frac{1}{\sqrt{4\pi D t}} \exp\left(-\frac{x^2 + y^2}{4Dt}\right). \tag{1.2}$$

If the particles or individuals are also undergoing reactions or interactions governed by some rate function $f(u)$, it is natural to combine the diffusion equation with the rate equation $\dot{u} = f(u)$. This leads to the well-known reaction–diffusion equation:

$$\frac{\partial u}{\partial t} = D\left(\frac{\partial^2 u}{\partial x^2} + \frac{\partial^2 u}{\partial y^2}\right) + f(u), \tag{1.3}$$

which serves as a powerful framework for exploring the spatiotemporal dynamics of numerous systems in chemistry, biology, and ecology [30]. Apart from ad hoc additions

of the two effects, a well-studied phenomenological background of such formulation is present, starting from microscopic to macroscopic levels, which we partially discuss for the sake of brevity [29]. A general n-species reaction-diffusion system can be expressed in the following form:

$$\frac{\partial \mathbf{u}}{\partial t} = \mathbf{D}\left(\frac{\partial^2 \mathbf{u}}{\partial x^2} + \frac{\partial^2 \mathbf{u}}{\partial y^2}\right) + \mathbf{f}(\mathbf{u}), \tag{1.4}$$

where $\mathbf{u} = (u_1, u_2, ..., u_n) \in \mathbb{R}^n$ is the vector of abundance of n-species at a spatial position vector $\vec{\mathbf{x}} = (x, y)$ and time t. $\mathbf{D} = (D_{ij})_{n\times n}$ is the diffusion matrix, and $\mathbf{f} = (f_1, f_2, ..., f_n)$ is the vector function of local reaction terms, where $f_i : \mathbb{R}^n \to \mathbb{R}$ are the net birth or death (increment or decrement) of the species i by local interactions. The abundance of species i at a particular spatial location $(x, y) \in \Omega$ at time t is denoted by $u_i \equiv u_i(x, y, t)$. Along with the partial differential equations (1.4), non-negative initial condition and boundary conditions are also imposed as the following:

$$u_i(x, y, 0) = u_0(x, y) \geq 0, \quad \forall i = 1, 2, ..., n \quad \text{and} \quad (x, y) \in \Omega. \tag{1.5}$$

where $\Omega \in \mathbb{R}^2$ is the well defined two-dimensional spatial domain. For our analysis, we consider no-flux or Neumann boundary conditions across the boundary ($\partial\Omega$) of the domain which implies a confined domain with no in-flux or out-flux of species across the boundary. The mathematical expression is as follows:

$$\frac{\partial u_i}{\partial \mathbf{v}} = 0, \quad \forall i = 1, 2, ..., n \quad \text{and} \quad \forall (x, y) \in \partial\Omega, \tag{1.6}$$

where $\mathbf{v}$ is the outward normal vector and $\partial\Omega$ is the boundary of the domain. The reaction diffusion equation (1.4) is a parabolic reaction diffusion equation, where the diffusion process is parabolic type.

Hyperbolic reaction-diffusion (HRD) equation

From a mathematical viewpoint, the origin of the infinitely fast spreading of local disturbances in the diffusion equation can be traced to its parabolic character [31]. The fundamental solution of the parabolic diffusion equation (1.2) establishes the fact. Starting from localised density at the origin $(x, y) = (0, 0)$, the concentration spreads out even at an apparent infinite distance at a very small time increment. However, the spread occurs with heavy attenuation.

From macroscopic viewpoint, the parabolic diffusion equation follows from the continuity equation

$$\frac{\partial u}{\partial t} = -\nabla J + f(u) \tag{1.7}$$

and the use of Fick's first law. Fick's first law implies that the flux adjusts instantaneously to the gradient of the density, denoted by

$$J = -D\nabla u, \tag{1.8}$$

where D is the diffusion coefficient. Catteno and others [31, 32] have argued that the flux adjusts to the gradient with a small but non-zero relaxation time or delay time τ. Thus, Fick's first law should be replaced as the constitutive equation by the Cattaneo equation

$$\tau\frac{\partial u}{\partial t} + J = -D\nabla u. \tag{1.9}$$

Combining it with continuity equation gives the hyperbolic diffusion equation. From the parabolic diffusion equation (1.4), we obtain the telegraph equation, a damped wave equation

$$\tau\frac{\partial^2 u}{\partial t^2} + \frac{\partial u}{\partial t} = D\left(\frac{\partial^2 u}{\partial x^2} + \frac{\partial^2 u}{\partial y^2}\right). \tag{1.10}$$

The fundamental solution of equation (1.10) with a point source of concentration located at $x = 0$ and time $t = 0$, with $u(x, 0) = \delta(x)$ (where $\delta(.)$ is Dirac delta function) follows [29]:

$$u(x, y, t) = \begin{cases} \frac{1}{\mathcal{N}} exp\left(-\frac{t}{2\tau}\right) I_0\left(\frac{1}{\mathcal{N}}\sqrt{\xi}\right), & \text{for } \sqrt{x^2+y^2} < \sqrt{\frac{D}{\tau}}t, \\ 0, & \text{for otherwise,} \end{cases} \tag{1.11}$$

and converges to the solution (1.4) of the parabolic diffusion equation as $\tau \to 0$. Here I_0 is the modified Bessel's function, $\xi = \frac{Dt^2}{\tau} - (x^2 + y^2)$, and $\mathcal{N} = \sqrt{4D\tau}$. Equation (1.11) also shows explicitly that perturbations governed by the telegraph equation spread with a finite speed $\sqrt{\frac{D}{\tau}}$, as expected for a damped wave equation. See the comparison of solutions of PRD and HRD equations in Fig. 1.1, where starting from the initial location at $x = 0$, the fundamental solution of PRD spreads infinitely fast along the space at some finite times $t = t_1$ and t_2, although with heavy attenuation (see Fig. 1.1a). Whereas, at finite times, the solutions of HRD spreads only up to

finite intervals given by $-\sqrt{\frac{D}{\tau}}t < x < \sqrt{\frac{D}{\tau}}t$ in equation (1.11), marked by the dashed vertical lines in Fig. 1.1b.

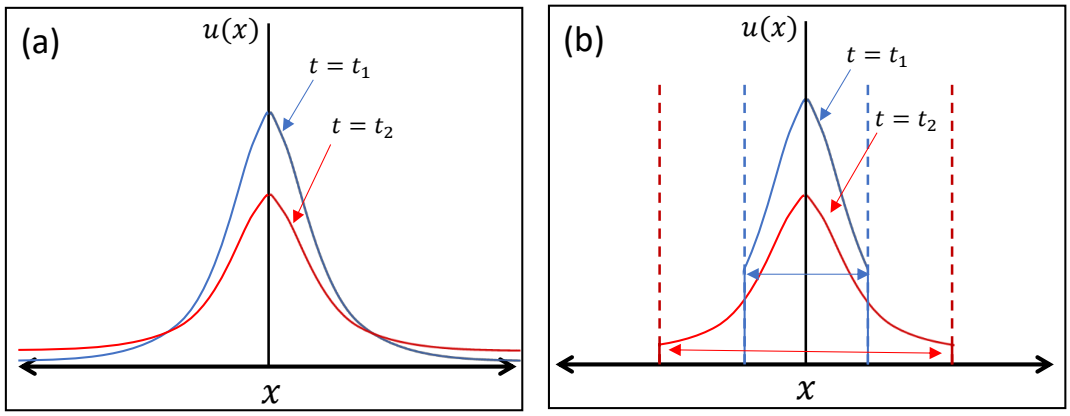

FIGURE 1.1: (a) Fundamental solution (1.2) of the parabolic diffusion equation. (b) Fundamental solution (1.11) of the hyperbolic diffusion equation at two different time points t_1 and t_2 ($t_2 > t_1$). Unlike the parabolic case, the diffusion of concentration $u(x)$ over the space is restricted within the interval $-\sqrt{\frac{D}{\tau}}t < x < \sqrt{\frac{D}{\tau}}t$ marked by blue (for $t = t_1$) and red dashed (for $t = t_2$) vertical lines.

Adding reaction terms with (1.10), we obtain hyperbolic reaction-diffusion equation (HRDE) as

$$\tau\frac{\partial^2 u}{\partial t^2} + \frac{\partial u}{\partial t} = D\left(\frac{\partial^2 u}{\partial x^2} + \frac{\partial^2 u}{\partial y^2}\right) + f(u). \tag{1.12}$$

This type of equation is encountered in other areas of science, such as nonlinear waves, nucleation theory, and phase field models of phase transitions, known as the damped nonlinear Klein-Gordon equation. The singular limit $\tau \to 0$ goes to the parabolic reaction-diffusion equation (1.3). Front propagation in HRDEs is studied analytically and numerically, where the disturbance spreads through space with finite velocity restricted into a circular domain of radius $\sqrt{\frac{D}{\tau}}t$ at time t. Similar to PRDEs, non-negative initial and boundary conditions are imposed on the system with additional interacting species.

1.5 Analysis of local dynamics

The local dynamics in all the spatially structured models discussed above serve a common purpose: they describe the temporal evolution of interacting species at a

specific spatial location or habitat patch. In the context of mathematical ecology, the rate equations are subject to biologically meaningful constraints. For instance, population abundances must remain non-negative, as negative values have no ecological interpretation. Similarly, real-world populations cannot grow without limit, so boundedness conditions are essential to ensure biological plausibility. Beyond these fundamental constraints, the nature of local interactions, such as birth-death processes, predation, or resource competition, can profoundly influence the behavior of the entire spatial system. Small changes in local parameters can trigger qualitative shifts in dynamics, or bifurcations, which may lead to transitions between stable coexistence, oscillatory behavior, or extinction. Thus, understanding the bifurcation structure of the local dynamics becomes critical for anticipating large-scale ecological outcomes. In the remainder of this section, we introduce key concepts and analytical tools from dynamical systems theory that will form the backbone of our investigation in the following chapters.

1.5.1 Feasibility of systems and their solution

Local dynamics describing evolution of population abundance of n-species can be written by simple rate equations

$$\frac{d\mathbf{u}}{dt} = \mathbf{f}(\mathbf{u}, \lambda), \quad \text{with} \quad \mathbf{u}(t=0) = \mathbf{u}_0 \geq 0, \tag{1.13}$$

where $\mathbf{u} \in \mathbb{R}^n_+$ and $\mathbf{f} = (f_1, f_2, ..., f_n)$ defined as $\mathbf{f} : \mathbb{R}^n \to \mathbb{R}^n$ and $\lambda \in \mathbb{R}$ is a control parameter of the system that affects the system. This is a initial value problem with non-negative initial components. It attains unique solution corresponding to given initial condition provided the following theorem holds.

Theorem 1.1. ***Picard–Lindelöf Theorem***
Let $\boldsymbol{f} : \mathbb{R}^n \to \mathbb{R}^n$ be a vector-valued function, and consider the initial value problem

$$\begin{cases} \dfrac{d\mathbf{u}}{dt} = \boldsymbol{f}(\mathbf{u}(t)), & t \in [0, T] \\ \mathbf{u}(0) = \mathbf{u}_0 \in \mathbb{R}^n. \end{cases}$$

Suppose that the function $\boldsymbol{f}$ is continuous in an open neighborhood $\mathcal{U} \subset \mathbb{R}^n$ containing $\mathbf{u}_0$, and the function $\boldsymbol{f}$ is locally Lipschitz continuous in $\mathcal{U}$; that is, there exists a constant $L > 0$ such that for all $\mathbf{u}, \mathbf{v} \in \mathcal{U}$,

$$\|\boldsymbol{f}(\mathbf{u}) - \boldsymbol{f}(\mathbf{v})\| \leq L\|\mathbf{u} - \mathbf{v}\|.$$

Then, there exists a unique local solution $\mathbf{u}(t)$ *to the initial value problem on some interval* $t \in [0, \varepsilon]$*, with* $\varepsilon > 0$*, such that* $\mathbf{u}(t) \in \mathcal{U}$ *for all* $t \in [0, \varepsilon]$*. If, in addition,* $\boldsymbol{f}$ *is globally Lipschitz continuous on* $\mathbb{R}^n$*, then the solution exists and is unique for all* $t \geq 0$ *[33].* □

Theorem 1.2. ***Positively invariant***
The evolution of all species population abundance in time $t \in \mathbb{R}_+$ *always remains non-negative, i.e.,* $u_i(t) \geq 0$ *for all* $i = 1, 2, ..., n$ *if*

$$f_i(u_1, u_2, ..., u_{i-1}, 0, u_{i+1}, ..., u_n) \geq 0, \quad \forall i = 1, 2, ..., n.$$

□

For the reaction-diffusion systems, the theorem is provided in the following form. Firstly, consider a system of n coupled reaction–diffusion equations of the form:

$$\begin{cases} \dfrac{\partial \mathbf{u}}{\partial t} = D\Delta\mathbf{u} + \mathbf{f}(\mathbf{u}), & \text{in } \Omega \times (0, T], \\ \mathbf{u}(\mathbf{x}, 0) = \mathbf{u}_0(\mathbf{x}), & \text{in } \Omega, \\ \mathcal{B}\mathbf{u} = 0, & \text{on } \partial\Omega \times (0, T], \end{cases} \tag{1.14}$$

where $\mathbf{u}(\mathbf{x}, t) = (u_1, u_2, \ldots, u_n)^T \in \mathbb{R}^n$ is the vector of individual population densities, $D = (D_{ij})_{n\times n}$ is positive definite diffusion coefficient matrix, Δ denotes the Laplacian with respect to the spatial variable $\mathbf{x} \in \Omega \subset \mathbb{R}^m$, $\mathbf{f} : \mathbb{R}^n \to \mathbb{R}^n$ is the vector-valued nonlinear reaction term, $\mathcal{B}$ is a suitable boundary operator (e.g., Neumann or Dirichlet conditions).

Theorem 1.3. ***(Existence and uniqueness of solutions of RDE)***
Let $\Omega \subset \mathbb{R}^m$ *be a bounded domain with boundary* $\partial\Omega$*. Suppose that:*

1. $\mathbf{f}(\mathbf{u})$ *is continuous and locally Lipschitz in* $\mathbf{u}$*,*
2. $\mathbf{u}_0(\mathbf{x}) \in C^0(\overline{\Omega}; \mathbb{R}^n)$*.*

Then, there exists a time $T > 0$ *such that the system admits a unique classical solution* $\mathbf{u}(\mathbf{x}, t) \in C^{2,1}(\Omega \times (0, T]; \mathbb{R}^n) \cap C^0(\overline{\Omega} \times [0, T]; \mathbb{R}^n)$*. If in addition* $\mathbf{f}(\mathbf{u})$ *satisfies suitable growth conditions (e.g., polynomial growth) and a priori estimates ensure boundedness of the solution, then the solution can be extended globally in time [34].* □

Thus, from the above theorem one can get, positivity of the reaction-diffusion system (1.14) can be extended from the positivity conditions of the local system (1.2).

1.5.2 Equilibrium states of the system

In the context of dynamical systems, an *equilibrium state* refers to a point in the system's phase space, where all temporal changes vanish, meaning the system remains constant over time if initialized at that state. Mathematically, it is defined as a solution $\mathbf{u}^*$ of

$$\mathbf{f}(\mathbf{u}^*) = 0,$$

where $\mathbf{f}$ represents the system of differential equations governing the dynamics of (1.13).

In ecological models, an equilibrium corresponds to a steady population level where birth and death processes and interactions between species are perfectly balanced. Understanding the nature of these equilibria, whether they are stable, unstable, or saddle points, is crucial, as it informs us about the system's long-term behavior. In spatially extended models, equilibria may be uniform (homogeneous across space) or spatially structured (heterogeneous over the space), and their stability can be affected by both local interactions and spatial coupling. Analyzing equilibrium states helps identify scenarios such as coexistence, extinction, or dominance of certain species, and offers insight into how ecosystems respond to external perturbations or parameter changes.

1.5.3 Linear stability analysis

Consider a nonlinear autonomous dynamical system described by

$$\frac{d\mathbf{u}}{dt} = \mathbf{f}(\mathbf{u}), \tag{1.15}$$

where $\mathbf{u} \in \mathbb{R}^n$ is the state vector and $\mathbf{f} : \mathbb{R}^n \to \mathbb{R}^n$ is a continuously differentiable vector field. Suppose $\mathbf{u}^* \in \mathbb{R}^n$ is an equilibrium point of the system, i.e., $\mathbf{f}(\mathbf{u}^*) = 0$.

To analyze the behavior of the system near the equilibrium $\mathbf{u}^*$, we consider a small perturbation $\mathbf{v}(t) = \mathbf{u}(t) - \mathbf{u}^*$. Substituting into the original equation and using a first-order Taylor expansion, we obtain the linearized system:

$$\frac{d\mathbf{v}}{dt} \approx D\mathbf{f}(\mathbf{u}^*)\mathbf{v} = A\mathbf{v}, \tag{1.16}$$

where $D\mathbf{f}(\mathbf{u}^*)$ is the Jacobian matrix of $\mathbf{f}$ evaluated at $\mathbf{u}^*$, given by

$$A = D\mathbf{f}(\mathbf{u}^*) = \left[\frac{\partial f_i}{\partial u_j}(\mathbf{u}^*)\right]_{i,j=1,2,\ldots,n}. \tag{1.17}$$

The linearized system describes how small perturbations evolve near the equilibrium. The eigenvalues of the Jacobian matrix determine the local stability of $\mathbf{u}^*$.

Consider a linearized time-invariant system governed by the ordinary differential equation

$$\frac{d\mathbf{v}}{dt} = A\mathbf{v}, \tag{1.18}$$

where $A \in \mathbb{R}^{n\times n}$ is a constant matrix. The stability of the equilibrium $\mathbf{u} = \mathbf{u}^*$ is determined by the eigenvalues of A, which are the roots of the characteristic polynomial

$$p(\lambda) = \det(\lambda I - A) = \lambda^n + a_1\lambda^{n-1} + a_2\lambda^{n-2} + \cdots + a_{n-1}\lambda + a_n. \tag{1.19}$$

If eigenvalues have a non-zero real part, the corresponding equilibrium is called a Hyperbolic equilibrium, and otherwise a non-hyperbolic equilibrium. In case of a hyperbolic equilibrium point, the linearized system perfectly describes the qualitative behavior of the nonlinear system close to the equilibrium, according to the Hartman-Grobman theorem. If all eigenvalues have negative real parts, the equilibrium is locally asymptotically stable; if any eigenvalue has a positive real part, the equilibrium is unstable.

Theorem 1.4. ***(Routh-Hurwitz theorem)***
All roots of the characteristic polynomial (1.19) have negative real parts (i.e., the system is asymptotically stable) if and only if all the principal minors of the associated Hurwitz matrix are positive.

The Hurwitz matrix H for a polynomial of degree n is defined as follows:

$$H = \begin{pmatrix} a_1 & a_3 & a_5 & \cdots & 0 \\ 1 & a_2 & a_4 & \cdots & 0 \\ 0 & a_1 & a_3 & \cdots & 0 \\ 0 & 1 & a_2 & \cdots & 0 \\ \vdots & \vdots & \vdots & \ddots & \vdots \end{pmatrix}_{n\times n}, \tag{1.20}$$

where missing coefficients (such as a_k for $k > n$) are treated as zero. Let Δ_k denote the $k \times k$ leading principal minor of the Hurwitz matrix. Then the necessary and

sufficient condition for asymptotic stability is

$$\Delta_k > 0, \quad a_n > 0 \quad \textit{for all } k = 1, 2, \ldots, n. \tag{1.21}$$

The stability of the equilibrium point changes if at least one of the above conditions is violated. The qualitative change in a dynamical system is analyzed using classical bifurcation theory. We provide some relevant analytical formulations of local bifurcations used in this thesis for future chapters. These classifications are foundational in both qualitative theory and bifurcation analysis. In analyzing dynamical systems, stationary bifurcations and Hopf bifurcations represent two distinct mechanisms of qualitative change in system behavior, both of which can be detected through the Routh-Hurwitz stability criteria. A stationary bifurcation, such as a saddle-node or transcritical bifurcation, occurs when a real eigenvalue of the Jacobian matrix crosses zero, leading to the appearance, disappearance, or exchange of stability between equilibria. A dynamical system with characteristic polynomial as (1.16) undergoes a stationary bifurcation if a_n changes its sign from positive to negative. Since $a_n = (-1)^n \det(A) = \Pi_{i=1}^{n} \lambda_i$, a change of sign of one eigenvalue causes the shift of sign. To obtain conditions for oscillatory or Hopf-Bifurcation, we exploit Orlando's formula [35]

$$\Delta_{n-1} = (-1)^{\frac{n(n-1)}{2}} \Pi_{1 \leq i < j \leq n} (\lambda_i + \lambda_j).$$

where λ_i are roots of the characteristic equation. If a pair of imaginary eigenvalues changes its sign from negative to positive, it implies a sign change of Δ_{n-1}. Thus, oscillatory bifurcation points are given by $\Delta_{n-1} = 0$

Consider a smooth one-parameter family of autonomous dynamical system defined by

$$\frac{d\mathbf{x}}{dt} = \mathbf{f}(\mathbf{x}, \lambda), \quad \mathbf{x} \in \mathbb{R}^n, \ \lambda \in \mathbb{R}, \tag{1.22}$$

where $\mathbf{f} \in C^k(\mathbb{R}^n \times \mathbb{R})$, $k \geq 2$.

Saddle-Node bifurcation

A saddle-node bifurcation occurs at the point $(\mathbf{x}_0, \lambda_0) \in \mathbb{R}^n \times \mathbb{R}$ in the system (1.22) if the following conditions are satisfied:

- Equilibrium Condition: $\mathbf{f}(\mathbf{x}_0, \lambda_0) = \mathbf{0}$.
- Simple Zero Eigenvalue: The Jacobian matrix $D_{\mathbf{x}}\mathbf{f}(\mathbf{x}_0, \lambda_0)$ has a simple zero eigenvalue $\mu_1 = 0$, and all other eigenvalues have nonzero real parts.

- Transversality Condition: The partial derivative of $\mathbf{f}$ with respect to λ evaluated at $(\mathbf{x}_0, \lambda_0)$, denoted $D_\lambda \mathbf{f}(\mathbf{x}_0, \lambda_0)$, satisfies

$$w^\top D_\lambda \mathbf{f}(\mathbf{x}_0, \lambda_0) \neq 0,$$

  where $w \in \mathbb{R}^n$ is the left eigenvector of $D_\mathbf{x}\mathbf{f}(\mathbf{x}_0, \lambda_0)$ corresponding to the zero eigenvalue, i.e., $w^\top D_\mathbf{x}\mathbf{f} = 0$.

- Non-degeneracy Condition: The second derivative of $\mathbf{f}$ with respect to $\mathbf{x}$ in the direction of the right eigenvector $v \in \mathbb{R}^n$ corresponding to the zero eigenvalue satisfies

$$w^\top D^2_{\mathbf{xx}}\mathbf{f}(\mathbf{x}_0, \lambda_0)(v, v) \neq 0.$$

Under these conditions, there exists a smooth curve of equilibria $\mathbf{x}(\lambda)$ near λ_0, such that: For $\lambda < \lambda_0$, there are no equilibria near $\mathbf{x}_0$. For $\lambda = \lambda_0$, a single non-hyperbolic equilibrium exists. For $\lambda > \lambda_0$, two equilibria exist: one stable (node) and one unstable (saddle). This bifurcation results in the creation or annihilation of a pair of equilibria as the parameter λ crosses the critical value λ_0.

Transcritical bifurcation

A transcritical bifurcation occurs at the point $(\mathbf{x}_0, \lambda_0) \in \mathbb{R}^n \times \mathbb{R}$ if the following conditions are satisfied:

- Equilibrium Condition: $\mathbf{f}(\mathbf{x}_0, \lambda) = \mathbf{0}$ for all λ near λ_0. That is, there is a *trivial* equilibrium branch passing through $\mathbf{x}_0$.

- Simple Zero Eigenvalue: The Jacobian $D_\mathbf{x}\mathbf{f}(\mathbf{x}_0, \lambda_0)$ has a simple eigenvalue at zero, and all other eigenvalues have nonzero real parts.

- Non-degeneracy Condition: Let v and w be the corresponding right and left eigenvectors of the Jacobian associated with the zero eigenvalue. Then,

$$w^\top D_\lambda \mathbf{f}(\mathbf{x}_0, \lambda_0) \neq 0, \quad \text{and} \quad w^\top D^2_{\mathbf{xx}}\mathbf{f}(\mathbf{x}_0, \lambda_0)(v, v) \neq 0.$$

- Bifurcating Branch Condition: There exists another smooth curve of equilibria $\mathbf{x}_1(\lambda)$ such that

$$\mathbf{x}_1(\lambda_0) = \mathbf{x}_0, \quad \text{and} \quad \mathbf{x}_1(\lambda) \neq \mathbf{x}_0 \text{ for } \lambda \neq \lambda_0.$$

Under these conditions, there is a local exchange of stability between the two equilibrium branches as the parameter λ passes through the critical value λ_0. Specifically, the trivial equilibrium $\mathbf{x}_0$ changes stability at $\lambda = \lambda_0$. The bifurcating equilibrium branch intersects the trivial branch at λ_0. The two branches exchange their stability through the bifurcation point. This bifurcation captures scenarios where an equilibrium exists for all parameter values but changes stability due to interaction with another branch.

Hopf bifurcation

Assume that $\mathbf{x}_0$ is an equilibrium point for all λ near λ_0, i.e., $\mathbf{f}(\mathbf{x}_0, \lambda) = \mathbf{0}$. A Hopf bifurcation occurs at $(\mathbf{x}_0, \lambda_0)$ under the following conditions:

- Equilibrium Condition: $\mathbf{x}_0$ is an equilibrium for all λ near λ_0.
- Pure Imaginary Eigenvalues: The Jacobian matrix $D_{\mathbf{x}}\mathbf{f}(\mathbf{x}_0, \lambda_0)$ has a pair of purely imaginary eigenvalues $\pm i\omega_0$, with $\omega_0 > 0$, and no other eigenvalue with zero real part.
- Transversality Condition: The real part of the eigenvalues crosses zero with nonzero speed as λ passes through λ_0, i.e.,

$$\frac{d}{d\lambda}\mathrm{Re}(\mu(\lambda))\bigg|_{\lambda=\lambda_0} \neq 0,$$

  where $\mu(\lambda)$ denotes the complex conjugate pair of eigenvalues depending on λ.
- Nondegeneracy Condition: A nondegeneracy condition on the normal form coefficients holds to ensure that a periodic orbit bifurcates from the equilibrium.

Under these conditions, a family of periodic solutions bifurcates from the equilibrium $\mathbf{x}_0$ as λ passes through λ_0. There are two types of Hopf bifurcations:

- Supercritical Hopf bifurcation: A stable limit cycle bifurcates from an unstable equilibrium point as λ increases through λ_0.
- Subcritical Hopf bifurcation: An unstable limit cycle bifurcates from a stable equilibrium point as λ decreases through λ_0.

Homoclinic bifurcation

A homoclinic bifurcation occurs when a stable and unstable manifold of a saddle point in a dynamical system intersect to form a homoclinic orbit. A trajectory that leaves the saddle along its unstable manifold and returns to it along the stable manifold. This type of bifurcation is particularly important because it often signals the onset of complex dynamics, including chaos, and leads to significant qualitative changes in the behavior of the system.

Suppose that for a parameter value $\lambda = \lambda_0$, the system (1.13) admits a saddle equilibrium $\mathbf{x}_s$, and there exists a homoclinic orbit Γ satisfying

$$\lim_{t \to \pm\infty} \mathbf{x}(t) = \mathbf{x}_s,$$

such that $\mathbf{x}(t) \in \Gamma$ for all $t \in \mathbb{R}$. The homoclinic orbit represents a global bifurcation since it involves the behavior of trajectories over long timescales and across the entire phase space. As the parameter λ is varied, the homoclinic orbit may break (i.e., the stable and unstable manifolds no longer intersect), leading to the disappearance of periodic orbits or the creation of complex dynamics. The homoclinic bifurcation is typically nonlocal and does not lend itself to analysis via linearization alone. Instead, global techniques such as Melnikov's method are often used to detect it. Depending on the system's structure, a homoclinic bifurcation can lead to the birth or destruction of limit cycles near the homoclinic orbit. Onset of chaos through a Shilnikov-type mechanism when the saddle point has one real positive eigenvalue and a pair of complex conjugate stable eigenvalues.

In ecological systems, homoclinic bifurcations may signal abrupt shifts between states, such as the sudden collapse of a population or ecosystem regime shift. A small change in environmental conditions or harvesting rates might destroy the homoclinic orbit, leading to either extinction or population outbreak, depending on the direction of bifurcation. Thus, identifying homoclinic bifurcations can be crucial in predicting tipping points and ensuring population persistence under environmental stress.

Heteroclinic bifurcation

Heteroclinic bifurcation is also a type of global bifurcation that occurs in dynamical systems when a trajectory connects two or more distinct saddle-type equilibria through their invariant manifolds. More precisely, a heteroclinic orbit is a trajectory that leaves one saddle point along its unstable manifold and approaches a different saddle point along its stable manifold. The bifurcation arises when the connection

between these saddles is created or destroyed as a system parameter is varied. Unlike local bifurcations, heteroclinic bifurcations involve the global structure of phase space and cannot be detected solely through linearization.

Suppose that for a critical parameter value $\lambda = \lambda_0$, the system admits two hyperbolic saddle equilibria $\mathbf{x}_1$ and $\mathbf{x}_2$, and there exists a trajectory $\mathbf{x}(t)$ such that

$$\lim_{t\to-\infty} \mathbf{x}(t) = \mathbf{x}_1, \quad \lim_{t\to+\infty} \mathbf{x}(t) = \mathbf{x}_2. \tag{1.23}$$

Then $\mathbf{x}(t)$ is a heteroclinic orbit, and the bifurcation that leads to its formation or disappearance as λ crosses λ_0 is termed a heteroclinic bifurcation.

Heteroclinic bifurcations are significant in systems exhibiting multistability or regime switching. The emergence of heteroclinic connections often implies slow switching behavior, long transients, or complex oscillatory patterns depending on the stability and geometry of the saddle points involved. In ecological contexts, heteroclinic bifurcations may describe transitions between alternative stable states, such as predator–prey coexistence and extinction scenarios or shifts between vegetated and barren states in spatial ecosystems. Small parameter changes like resource availability, dispersal rate, or mortality thresholds often trigger these transitions.

Lyapunov exponents and detection of chaos

In the study of dynamical systems, Lyapunov exponents quantify the exponential rates at which nearby trajectories diverge or converge in phase space. These exponents serve as a key diagnostic tool for identifying chaotic behavior.

Definition 1.5. Let $\mathbf{x}(t)$ be a trajectory of an autonomous dynamical system

$$\frac{d\mathbf{x}}{dt} = \mathbf{f}(\mathbf{x}), \quad \mathbf{x} \in \mathbb{R}^n,$$

and consider a small perturbation $\delta\mathbf{x}(t)$ to the trajectory. The Lyapunov exponents λ_i, $i = 1, 2, \ldots, n$, are defined as

$$\lambda_i = \lim_{t\to\infty} \lim_{\|\delta\mathbf{x}(0)\|\to 0} \frac{1}{t} \ln \frac{\|\delta\mathbf{x}_i(t)\|}{\|\delta\mathbf{x}_i(0)\|},$$

where $\delta\mathbf{x}_i(t)$ is the evolution of the i-th orthogonal perturbation vector under the linearized flow of the system.

Theorem 1.6 (Lyapunov Exponent Criterion for Chaos)**.** *Let $\{\lambda_1, \lambda_2, \ldots, \lambda_n\}$ be the Lyapunov spectrum of a smooth dynamical system in $\mathbb{R}^n$. If the system has at least*

one positive Lyapunov exponent, i.e.,

$$\max_i \lambda_i > 0,$$

then the system exhibits sensitive dependence on initial conditions, which is one of the hallmark features of chaos.

A positive Lyapunov exponent implies that infinitesimally close trajectories diverge exponentially fast, making long-term prediction impossible and indicating chaos. If all Lyapunov exponents are negative, the system converges to a stable fixed point or limit cycle. A zero exponent typically corresponds to perturbations along a neutrally stable direction, such as along a periodic orbit or due to time invariance. The sum of Lyapunov exponents also provides information on the volume contraction or expansion in phase space. In ecological models, a positive Lyapunov exponent may indicate population fluctuations highly sensitive to initial conditions or parameter values, such as overharvesting, climate-induced synchrony, or predator-prey oscillations. Recognizing chaotic regimes helps understand the unpredictability and potential fragility of ecosystems under environmental stress.

Maximum Poincaré map and detection of chaos

Among the many tools available to detect and characterize chaos, the *Poincaré map* is a powerful geometric technique. When adapted to ecological models where variables such as population densities exhibit regular peaks, the *Maximum Poincaré Map* provides an intuitive and computationally efficient method for identifying chaotic regimes. The idea behind the Maximum Poincaré Map is to record successive local maxima of a dynamical variable (e.g., prey or predator population abundance) over time. Let $u(t)$ be a continuous, smooth time series generated by a dynamical system. Define $\{u_n\}$ as the sequence of successive local maxima of $u(t)$, i.e.,

$$u_n = \max\{u(t) : t \in [t_n, t_{n+1}]\}, \quad \text{where } \left.\frac{du}{dt}\right|_{t_n} = 0 \text{ and } \left.\frac{d^2u}{dt^2}\right|_{t_n} < 0.$$

The Maximum Poincaré Map is then the discrete map:

$$u_{n+1} = P(u_n),$$

which plots x_n versus x_{n+1}. If the plot of x_n vs. x_{n+1} lies on a single point, the system has converged to a fixed point (steady state). The system exhibits a periodic

cycle if it lies on a finite set of points (e.g., two or three). If the points fill a closed curve or scatter without repeating, this indicates quasiperiodicity or chaos, respectively. Thus, the Maximum Poincaré Map translates the continuous time dynamics into a lower-dimensional discrete representation, where the presence of strange attractors, bifurcations, or sensitive dependence on initial conditions becomes visually and computationally tractable.

1.5.4 Multistability in dynamical systems

Multistability refers to the coexistence of multiple stable states in a dynamical system under the same environmental or intrinsic parametric conditions. These stable states may correspond to distinct ecological configurations such as high- and low-density populations [36], predator-prey coexistence versus extinction [37], or vegetated versus desertified landscapes [38]. Importantly, small perturbations or gradual parameter shifts can cause the system to transition from one stable state to another, often in a sudden and irreversible manner. Such transitions are commonly referred to as *tipping points* [39]. Ecologically, multistability implies that ecosystems can display radically different long-term behaviors depending on their initial conditions or transient shocks. For example, an overgrazed grassland may either recover to a lush state or collapse into a barren regime depending on initial vegetation density and the intensity of herbivory [36]. Understanding the structure and nature of these stable states is crucial for predicting regime shifts and designing intervention strategies to preserve ecosystem resilience.

The *basin of attraction* of a given attractor is defined as the set of all initial values in phase space that evolve in time and approaches asymptotically towards that attractor. Mathematically, for an autonomous system

$$\frac{d\mathbf{x}}{dt} = \mathbf{f}(\mathbf{x}),$$

and an attractor $\mathcal{A} \subset \mathbb{R}^n$, the basin of attraction $\mathcal{B}(\mathcal{A})$ is defined as

$$\mathcal{B}(\mathcal{A}) = \left\{ \mathbf{x}_0 \in \mathbb{R}^n : \lim_{t \to \infty} \mathbf{x}(t; \mathbf{x}_0) \in \mathcal{A} \right\}.$$

The boundary between different basins of attraction is called the *basin boundary*. These boundaries are often complex and may even possess fractal structures, making prediction and control challenging in multistable systems. A small perturbation near the basin boundary can send the system toward a qualitatively different long-term behavior.

Basins of attraction help ecologists understand the resilience of ecosystems. A large basin indicates that the ecosystem is robust to perturbations, while a narrow basin suggests vulnerability. Conservation efforts aim to maintain or expand the basin of desirable ecological states. Moreover, human-induced changes, such as habitat fragmentation or climate forcing, can shrink the basin of an ecologically favorable attractor or widen that of an undesirable one, thus pushing systems closer to collapse. In the context of spatially extended models, such as reaction-diffusion systems or metapopulations, multistability may emerge as different spatial patterns or population distributions across patches. Studying how initial spatial heterogeneity and dispersal influence basins of attraction provides insight into spatial resilience and the design of spatially targeted interventions.

1.6 Analysis of spatiotemporal system

Spatiotemporal instabilities lie at the heart of complex dynamics in extended ecological systems, where the interplay between local interactions and spatial movement leads to rich, often unexpected, patterns. Unlike purely temporal instabilities, which describe changes in the behavior of populations over time at a fixed location, spatiotemporal instabilities arise when spatial coupling, through diffusion or dispersal, destabilizes homogeneous steady states or periodic orbits. This section provides a mathematical analysis of spatiotemporal instabilities and bifurcations.

1.6.1 Linear stability analysis

We conduct the analysis in case of more general hyperbolic reaction diffusion equation and explain the analytical aspects and stability conditions and bifurcations. The governing equation takes the form:

$$\tau \frac{\partial^2 \mathbf{u}}{\partial t^2} + \frac{\partial \mathbf{u}}{\partial t} = D\nabla^2 \mathbf{u} + \mathbf{f}(\mathbf{u}),$$

where $\mathbf{u}(x,t) \in \mathbb{R}^n$ represents the state variables (e.g., species densities), $D = (D_{ij})_{n\times n}$ is the diffusion matrix, $\mathbf{f}(\mathbf{u})$ encapsulates the local reaction dynamics, and $\tau > 0$ is the relaxation time that controls the inertia or delay in diffusion. When $\tau = 0$, the equation reduces to the classical parabolic reaction–diffusion form.

We consider a spatially homogeneous equilibrium $\mathbf{u}^*$ satisfying $\mathbf{f}(\mathbf{u}^*) = \mathbf{0}$. Linearizing around this equilibrium with a perturbation $\mathbf{u}(x,t) = \mathbf{u}^* + \varepsilon\tilde{\mathbf{u}}(x,t)$, where $0 < \varepsilon \ll 1$,

we obtain:

$$\tau\frac{\partial^2\tilde{\mathbf{u}}}{\partial t^2}+\frac{\partial\tilde{\mathbf{u}}}{\partial t}=D\nabla^2\tilde{\mathbf{u}}+J\tilde{\mathbf{u}},$$

where $J=D\mathbf{f}(\mathbf{u}^*)$ is the Jacobian of the reaction term evaluated at equilibrium.

Assuming normal mode solutions of the form $\tilde{\mathbf{u}}(x,t)=\mathbf{v}e^{\lambda t+ikx}$, we substitute into the linearized system to obtain the eigenvalue equation:

$$\tau\lambda^2\mathbf{v}+\lambda\mathbf{v}=-Dk^2\mathbf{v}+J\mathbf{v},$$

which simplifies to the characteristic equation

$$|\tau\lambda^2 I+\lambda I+Dk^2 I-J|=0. \tag{1.24}$$

Stability requires that the real parts of all eigenvalues λ be negative for all spatial modes k. Therefore, spatiotemporal instabilities occur when there exists some wavenumber k such that $\lambda(k)>0$. Again, this eigenvalue problem can be solved using the Routh-Hurwitz theorem. Different stationary and oscillatory bifurcations or spatiotemporal instabilities can be derived from it. Expanding the determinant, one gets the characteristic polynomial as follows:

$$p(\lambda)=\tau^n\lambda^2 n+\tau^{n-1}a_1(k)\lambda^{2n-1}+\tau^{n-2}a_2(k)\lambda^{2n-2}+\cdots+a_{2n-1}(k)\lambda+a_{2n}(k). \tag{1.25}$$

The homogeneous stable state remains stable under small spatiotemporal perturbations if the above characteristic polynomial satisfies the Routh-Hurwitz stability criteria for all spatial wavenumbers k. Particular spatiotemporal instabilities appear if some specific conditions are violated.

Theorem 1.7. ***(Turing instability)*** *Turing instability appears when the local system remains stable in the absence of diffusion but becomes unstable in its presence, with a sign change of the real eigenvalue. Stability of the local system is satisfied following Routh-Hurwitz conditions at $k=0$ according to Theorem (1.4). The stationary Turing instability appears if*

$$a_{2n}(k)<0 \quad \textit{for some} \quad k\neq 0. \tag{1.26}$$

Theorem 1.8. ***(Hopf instability)*** *Hopf instability appears in the spatiotemporal system when the local system shows Hopf instability. The conditions of Hopf instability for general characteristic polynomial (1.25) is given by*

$$\Delta_{2n-1}(k)<0 \quad \textit{for} \quad k=0, \tag{1.27}$$

where Δ_{2n-1} is the $(2n-1)$-th order Hurwitz determinant.

Theorem 1.9. ***(Wave instability)*** *Wave instability appears when the local system remains stable in the absence of diffusion but becomes unstable in the presence of it with sign change of real part of a pair of imaginary eigenvalues. Stability of local system is satisfied following Routh-Hurwitz conditions at $k = 0$ according to Theorem (1.4). The oscillatory Turing instability appears if*

$$\Delta_{2n-1}(k) < 0 \quad \textit{for some} \quad k \neq 0, \tag{1.28}$$

where Δ_{2n-1} is the $(2n-1)$-th order Hurwitz determinant.

In spatially extended systems, different types of spatiotemporal instabilities give rise to a variety of dynamic behaviors. Turing instability results in stationary spatial patterns such as stripes, spots, or labyrinths, arising when diffusion destabilizes an otherwise stable equilibrium. These patterns emerge purely due to spatial interactions, even without time-dependent oscillations. On the other hand, Hopf instability leads to temporal oscillations, where populations at each spatial location begin to fluctuate periodically in time. Wave instabilities, also known as oscillatory Turing instabilities, give rise to travelling or standing waves across space, combining both spatial and temporal variation. These instabilities often mark the onset of complex dynamical regimes. They are key to understanding how localized interactions and spatial structure can produce diverse ecological patterns and rhythms, which we have discussed in a later chapter with model-specific analysis.

1.7 Numerical simulation

Analytical solutions of reaction–diffusion equations are generally difficult to obtain, particularly when the reaction involves a highly nonlinear term. Consequently, numerical simulations become essential for investigating and visualizing the spatiotemporal dynamics governed by such systems. In the subsequent study of parabolic reaction diffusion equations, we consider one- and two-dimensional rectangular spatial domains and employ a finite difference approach using the Forward Time Centered Space (FTCS) scheme to approximate the solutions. For Hyperbolic reaction–diffusion equations, a mix of forward time and centered time discretization is employed along with centered space.

The spatial domain is discretized uniformly with grid spacings $\Delta x = \Delta y$, and time is discretized using a constant time step Δt. For the one-dimensional case, the domain $L = [0, L_x]$ is divided into n equal intervals, giving spatial grid points $x_i = i\Delta x$, where $\Delta x = \frac{L_x}{n}$ and $i = 0, 1, \ldots, n$. Similarly, the temporal domain $T = [0, t]$ is divided

into time levels $t^n = n\Delta t$, where n is the time index. The discrete numerical solution at a particular grid is denoted by $u_i^n \equiv u(x_i, t^n)$. In the two-dimensional setting a rectangular spatial domain $L = [0, L_x] \times [0, L_y]$ is discretized into $n \times m$ equal square grids as $x_i = i\Delta x$, where $\Delta x = \frac{L_x}{n}$ for $i = 0, 1, 2, ..., n$ and $y_i = i\Delta y$, where $\Delta y = \frac{L_y}{m}$ for $i = 0, 1, 2, ..., m$. The discrete numerical solution at a spatial location (x_i, y_j) and time t^n is denoted by $u_{ij}^n \equiv u(x_i, y_j, t^n)$. For discretization schemes of one and two-dimensional space, the partial derivatives of different orders with respect to space variables $x,\ y$ and time variable t are discretized as follows:

- **1 dimensional space derivative:**

$$\nabla^2 u = \frac{\partial^2 u}{\partial x^2} \approx \frac{u_{i+1}^n - 2u_i^n + u_{i-1}^n}{\Delta x^2} + \mathcal{O}(\Delta x^3). \tag{1.29}$$

- **2 dimensional space derivative:**

$$\nabla^2 u = \frac{\partial^2 u}{\partial x^2} + \frac{\partial^2 u}{\partial y^2} \approx \frac{u_{i+1,j}^n - 2u_{i,j}^n + u_{i-1,j}^n}{\Delta x^2} + \frac{u_{i,j+1}^n - 2u_{i,j}^n + u_{i,j-1}^n}{\Delta y^2} + \mathcal{O}(\Delta x^3). \tag{1.30}$$

- **1^{st} order time derivative:**

$$\frac{\partial u}{\partial t} \approx \frac{u_{i,j}^{n+1} - u_{i,j}^n}{\Delta t} + \mathcal{O}(\Delta t^2). \tag{1.31}$$

- **2^{nd} order time derivative:**

$$\nabla^2 u = \frac{\partial^2 u}{\partial t^2} \approx \frac{u_{i,j}^{n+1} - 2u_{i,j}^n + u_{i,j}^{n-1}}{\Delta t^2} + \mathcal{O}(\Delta t^3). \tag{1.32}$$

The continuous partial derivatives are replaced by the discrete counterparts, omitting the higher-order terms, in the respective reaction-diffusion equations. The solutions at time point t^{n+1} are computed using the solutions at previous time points t^n. For a parabolic reaction-diffusion system, the computation of state variables at t^{n+1} requires the values of state variables only at the previous time point t^n and for hyperbolic reaction diffusion, state variables of two previous time points t^n and t^{n-1} are needed. Therefore, the scheme can be represented in the matrix form as

- Parabolic reaction-diffusion equation:

$$u^{n+1} = Lu^n + F^n. \tag{1.33}$$

- Hyperbolic reaction-diffusion equation:

$$u^{n+1} = L_1 u^n + L_2 u^{n-1} + F^n, \tag{1.34}$$

where L, L_i $(i = 1, 2)$ are the Laplacian matrices obtained by separating the coefficients of u^n and u^{n-1} in terms of diffusion coefficients and discritizaion step lengths (Δx, Δy, and Δt). $F^n = F(u^n)$ are the contributions of reaction terms at time t^n. To ensure the stability of the numerical scheme, we make sure that the Courant–Friedrichs–Lewy stability criterion [40] holds, i.e., $|\frac{D_i \Delta t}{\Delta x^2} + \frac{D_i \Delta t}{\Delta y^2}| \leq \frac{1}{2}$ for $i = 1, 2$.

1.8 Literature review and motivations

The implementation of spatiotemporal population models has a long history, originating in the study of physical and chemical systems. The seminal contribution of Alan Turing (1952) laid the foundation for understanding heterogeneous pattern formation in reaction–diffusion systems [41] in his seminal work "The Chemical Basis of Morphogenesis". Turing demonstrated the novel concept that while reaction or diffusion alone may lead to homogeneous distributions, their interplay can generate spatial heterogeneity [41]. These spatially heterogeneous structures, later termed Turing patterns, provided a unifying framework for understanding morphogenesis in chemical and biological systems. Building on this theoretical foundation, Segel and Jackson (1972) [42] were among the first to extend Turing's ideas to ecological contexts, demonstrating that differences in diffusion rates between interacting species could drive heterogeneous spatial distributions in population systems. More specifically, the inhibitor of the system must diffuse significantly faster than the activator of the system [30]. The spatial movement of species in bio-economic models under harvesting pressure has been increasingly explored in recent years [43, 44]. Various forms of harvesting mechanisms have been studied, including catch-per-unit-effort (CPUE) harvesting [45], Michaelis–Menten type harvesting with saturation [46, 47], and other nonlinear harvesting frameworks that better capture realistic exploitation dynamics. Despite these advances, the literature remains limited regarding selective harvesting measures that differentially target predator and prey populations, and their implications for spatiotemporal ecological dynamics remain underexplored. Furthermore, most studies have concentrated on the conditions leading to heterogeneous pattern formation, particularly in Turing and non-Turing dynamical regimes [48, 49]. Within these regimes, the qualitative characterization of spatial population distributions has received little attention. For instance, in Turing steady-state patterns, ecologically

relevant metrics such as the maxima, minima, and spatial mean of population densities can act as critical determinants of large-scale species persistence and ecosystem survival [36, 50]. Addressing these gaps is essential to bridge theoretical predictions with practical biodiversity conservation and sustainable harvesting considerations.

Cross-diffusion is a spatial mechanism in which the diffusion rate of a species depends not only on its own density gradient but also on the local density gradient of interacting species. This mechanism provides a theoretical basis for the well-documented chase–escape dynamics in predator–prey systems, where predators tend to move toward zones of high prey density while prey simultaneously disperse away from such zones to reduce predation risk [51, 52]. Similar avoidance-driven cross-diffusion dynamics have been observed in broader ecological contexts, where species escape adverse or disadvantageous spatial locations in search of favorable habitat patches [53]. Such spatial dynamics often interact with trophic control mechanisms at the community level. For instance, in top-down controlled regimes, upper trophic levels regulate the population densities of lower trophic species, while in bottom-up controlled systems, resource availability constrains higher trophic levels [54, 55]. A classic example of such dynamics is the temporal model of vegetation–herbivore grazing developed by van de Koppel et al. (1996) [56], which demonstrated how increasing vegetation productivity shifts system dynamics from a favorable top-down controlled regime, where vegetation and herbivores coexist, to an unfavorable bottom-up controlled regime, leading to herbivore extinction. However, the temporal framework does not adequately capture the gradual changes in productivity gradients across spatial scales. In reality, systems exhibiting localized bottom-up control may persist in such states over larger spatial extents, providing spatial refugia that can facilitate coexistence and enhance persistence of both vegetation and herbivores. Analysis of dynamical regimes across different spatial scales can yield contrasting perspectives on species persistence under adverse conditions.

Analysis of spatial systems on different scales helps identify pattern formation at various spatial scales. Mathematical models of vegetation patterns, often framed through monoscale (where a particular agent or species of the system diffuses at a fixed diffusion rates) reaction–diffusion or integro-differential systems, have long been used to explain how spatial heterogeneity such as spots and stripes can emerge from uniform conditions via Turing's diffusion-driven instability [26, 57, 58, 59]. Yet, growing evidence shows that many ecosystems exhibit multiscale organization, where nested or overlapping patterns occur at different spatial resolutions, as observed in Namibian drylands, where large barren gaps coexist with smaller vegetated patches, reflecting hierarchical self-organization [60, 61, 62]. Similar multiscale structures have been identified in non-ecological contexts such as layered chemical systems, where cross-diffusion produces superlattices and "white-eye" patterns [63, 64], and in plankton

communities of thermally stratified lakes, where gradient-dependent coupling maintains nested distributions of stripes and hexagons [65], underscoring the universality of such processes across natural systems. In ecological contexts, these complex patterns are closely tied to phenotypic plasticity, particularly in root systems that adapt morphology in response to environmental stress [66, 67, 68], with hydrotropism enabling plants to exploit moisture-rich soil layers [69]. Such plastic responses underpin Walter's two-layer hypothesis, which explains how vertical partitioning of soil moisture between shallow- and deep-rooted plants reduces competition and stabilizes coexistence in water-limited environments [70, 71], linking below-ground strategies with the emergence of multiscale vegetation patterns. Multiscale patterns in terrestrial vegetation have been identified by ecologists recently [72, 73].

Although the analytical and computational aspects of these instabilities have been extensively investigated, their actual ecological implications remain less well understood. Specifically, the role of spatiotemporal patterning in promoting species persistence, facilitating coexistence, and buffering ecosystems against perturbations is an active area of inquiry. Recent studies suggest pattern formation may enhance ecological resilience by providing spatial refugia, reducing the risk of synchronized extinctions, and acting as early-warning signals of critical transitions [74]. Types of non-Turing oscillations are also an interesting aspect that has not been appropriately explored in reaction-diffusion systems. Synchronous oscillations are viewed as a potential threat to species persistence. The spatiotemporal oscillations and chaos are not well explored in the spatial synchrony of population persistence. Moreover, empirical validations linking theoretical predictions of reaction–diffusion models to real-world conservation outcomes remain limited. Thus, a deeper exploration of how spatiotemporal ecological patterns shape persistence and stability under environmental stress is also crucial. The dominance of contrasting instability, like Turing and Hopf instability, in population persistence against adverse climatic conditions is not well studied.

This thesis seeks to contribute to that gap by systematically investigating the implications of spatiotemporal pattern formation for species survival, ecological resilience, and responses to perturbations across different ecological contexts. Integrating space into ecological models provides a more comprehensive understanding of population behavior, highlighting the spatial underpinnings of ecological resilience and transformation. This spatial perspective has catalyzed a growing body of work in spatial ecology, which seeks to answer key questions: How do localized interactions scale up to regional patterns? Which spatial configurations buffer ecological systems against environmental perturbations? How do dispersal mechanisms and local population dynamics synchronize or desynchronize populations across landscapes?

1.9 Thesis overview

This thesis delves into the fascinating interplay between space, species interactions, and environmental change, uncovering how populations survive, adapt, or collapse across complex landscapes. It investigates the central role of spatial pattern formation in driving ecological stability, persistence, and collapse. Through reaction–diffusion frameworks, it shows how local interactions, dispersal processes, and feedback mechanisms generate diverse spatiotemporal structures such as Turing patterns, regular and chaotic spatiotemporal oscillations, and multiscale vegetation mosaics. These emergent patterns are not only mathematical curiosities but also reflect ecological realities observed in predator–prey systems, grazing landscapes, and arid ecosystems, where spatial self-organization governs resilience and coexistence. The work further demonstrates how external pressures like harvesting, productivity gradients, and climate variability interact with intrinsic instabilities to alter or destabilize these patterns, sometimes leading to tipping points and extinction. By integrating analytical bifurcation theory with numerical simulations, the thesis advances a comprehensive understanding of how ecological patterns emerge, persist, and transform, offering predictive insights into the resilience and vulnerability of ecosystems under changing environments. A brief overview of the subsequent chapters are given below:

In **chapter 2**, we introduce nonlinear saturated harvesting in both predator and prey populations within a predator–prey model and examine its impact on spatial dynamics. The non-spatial system undergoes detailed bifurcation analysis, uncovering transcritical, Hopf, saddle-node, and homoclinic bifurcations as harvesting pressure and carrying capacity increase. Interestingly, the paradox of enrichment may be resolved under strong harvesting conditions. Spatial analysis identifies critical predator-to-prey diffusivity ratios for the emergence of Turing instability. Weakly nonlinear analysis yields amplitude equations to predict pattern structures. Simulations reveal that prey harvesting can induce spatiotemporal chaos, while predator diffusion plays a regulatory role. Moreover, intensive prey harvesting promotes spatial segregation, enriching total biomass, while predator harvesting reduces such segregation. The chapter highlights a striking observation: the occurrence or absence of spatiotemporal chaos within the Hopf–Turing interaction space, illuminating how human interventions shape ecological stability.

Chapter 3 turns attention to plant–herbivore dynamics in heterogeneous landscapes. Using a two-dimensional reaction–diffusion model, we examine how non-uniform species distributions arise due to the relative dispersal of herbivores. The non-spatial model reveals bottom-up control mechanisms and bistability between vegetation-only and coexisting vegetation-herbivore states. We derive analytical conditions for Turing instability by introducing space and relative dispersal into the system. When herbivores

move more actively from high to low vegetation zones, heterogeneity in population distributions emerges. Intriguingly, bistability leads to initial condition-dependent patterns, resulting in drastically different spatial configurations under identical parameter values. Pattern transitions, from mixed stripes and spots to sparse vegetated patches, occur as productivity increases. Additionally, we observe a shift from bottom-up to top-down control when herbivore dispersal is high, where herbivores actively regulate vegetation under high productivity, while low dispersal can lead to herbivore extinction. The chapter emphasizes how mobility and initial conditions interplay to determine long-term spatial structure and species persistence.

Chapter 4 explores the underappreciated role of individual-level adaptation in shaping community-level spatial patterns. Focusing on arid and semi-arid ecosystems, we develop a two-layer reaction–diffusion model incorporating root phenotypic plasticity and vertical soil stratification, inspired by Walter's two-layer hypothesis. Plants adaptively switch between shallow- and deep-rooted phenotypes, accessing variable water sources. Contrasting diffusion scales and infiltration gradients between soil layers drive complex multiscale pattern formation. Linear and weakly nonlinear analyses reveal that weak inter-layer coupling favors multiscale structures, while strong coupling promotes synchronized monoscale patterns. Simulations under realistic precipitation regimes reproduce transitions from gaps to stripes to spots, mirroring field observations. Deep-rooted plants reduce competition for surface water by exploiting subsoil moisture, allowing spatial niche partitioning. This chapter broadens our understanding of spatial patterning by integrating physiological plasticity and environmental constraints in water-limited ecosystems.

Building upon the established role of space and adaptation, **Chapter 5** introduces temporal environmental variability, specifically, climate-driven fluctuations, in a spatial predator–prey framework. We model prey intrinsic growth rate as a stochastic variable and explore its influence on system persistence under Hopf, Turing, and mixed-mode instabilities. Sudden climatic shifts can push prey densities below Allee thresholds, triggering localized extinctions and predator collapse. However, spatial diffusion facilitates recolonization via rescue waves from neighboring patches. Climate-favorable phases often synchronize population densities, which paradoxically increases vulnerability to synchronous collapses during environmental downturns. In contrast, Turing-type steady states arising during unfavorable conditions reduce synchrony and buffer against widespread extinctions. This chapter underscores the dual role of synchrony in resilience and collapse, emphasizing the importance of accounting for both deterministic patterning and environmental stochasticity in ecological modeling.

Chapter 6 explores a hyperbolic reaction–diffusion (HRD) system as an alternative to the classical parabolic reaction–diffusion (PRD) models for studying pattern formation in ecological interactions. Unlike PRD systems, HRD systems capture the finite-speed propagation of spatial disturbances. We consider a two-species HRD model governed by predator–prey dynamics with a type III functional response and a prey refuge. Analytical conditions are derived for the emergence of diffusion-driven instabilities, and numerical simulations validate the theoretical results. A key finding is that extending a PRD system to its hyperbolic counterpart can induce wave-driven instabilities, producing spatiotemporal patterns influenced by initial population densities. Importantly, the interplay between the prey refuge and inertial time scale reveals novel mechanisms for pattern selection, offering a new lens on predator–prey dynamics in space.

Chapter 7 presents the concluding discussion of the thesis. It highlights the major findings, provides an overall summary, and critically reflects on the limitations of the current study. In addition, it suggests possible improvements and outlines future research directions that can further strengthen and extend the scope of the work.

Chapter 2

Dynamic properties of a reaction-diffusion predator-prey model with nonlinear harvesting: A linear and weakly nonlinear analysis [1]

2.1 Introduction

Due to the ever-increasing demand for food and other natural resources, many biological renewable resources are overharvested, negatively impacting the environment, ecosystem functioning and services. It is a global challenge to prevent natural ecosystems from collapsing because of unplanned exploitation to protect our future generations [75, 76]. One challenge of resource harvesting is determining how much can be sustainably exploited from renewable resources, such as forests, fisheries, wildlife etc., without significantly affecting the harvested population and their habitat. Recently, many spatiotemporal population interaction models have been analyzed in the presence of harvesting [77, 78, 79, 80, 81]. Harvesting of species in these studies are implemented in different ways. It includes linear catch per unit harvesting, $H(x) = qEx$ [81], where q is the catchability coefficient, E is the harvesting effort, and x is the species biomass. The type II nonlinear harvesting has the form $H(x) = \frac{qEx}{d+x}$,

[1] Published article by Marick, S., Bhattacharya, S., & Bairagi, N. (2023). Dynamic properties of a reaction–diffusion predator–prey model with nonlinear harvesting: A linear and weakly nonlinear analysis. Chaos, Solitons & Fractals, 175, 113996. https://doi.org/10.1016/j.chaos.2023.113996

where the species harvesting rate becomes bounded by a saturation value of qE, and d is the half-saturation constant. This latter one is also called the Michaelis-Menten type functional form of catching rate, first introduced as a harvesting term by Clark [82]. These studies also include differences in outcomes in a single-species harvesting of prey or predator and harvesting of both species simultaneously [77]. But the study of predator-prey interaction with nonlinear harvesting of both species has received less attention, especially when the spatial effect is considered in two-dimensional spatial domains.

The rate equations of two species, sharing a common habitat with a typical predator-prey relationship, are defined as

$$\begin{aligned} \frac{dP}{dt} &= rP\left(1-\frac{P}{K}\right)-\frac{a_1PQ}{P+\alpha}, \\ \frac{dQ}{dt} &= \frac{a_2PQ}{P+\alpha}-sQ-gQ^2, \end{aligned}$$

where P and Q are the prey and predator biomasses at time t. It describes that prey grows with the biotic potential r and environmental carrying capacity K when no predator exists. In the presence of the predator, the interaction follows Rosenzweig–MacArthur type predator-prey relationship [83], where the predator's death follows Bazykin's quadratic mortality [84] with s and g as the coefficients of the death term. Quadratic species death becomes more evident when intraspecies competition becomes predominant rather than cooperation [85]. The effects of stress, diseases, overcrowding, and intraspecific competition may cause quadratic mortality rates of the predators even in the case of specialist predators [86] as considered here. The constants a_1, α, and a_2 involved in the response function are the maximum prey attack rate, half-saturation constant of predation and predator's food conversion rate. Parameters $r, K, a_1, a_2, \alpha, s, g$ are all non-negative. Readers may consult [87] for a detailed study of this model.

Assume that both the species are harvested following a saturated nonlinear harvesting rate $H_i(x) = \frac{q_i E_i x}{d_i+x}$ $(i = 1, 2)$. The harvesting efforts E_1 and E_2 are species-dependent, making the harvesting process selective. Moreover, due to limited effort and other constraints, the harvesting rate in real-world scenarios becomes bounded even when the resources are abundant [88, 82]. The parameters q_1 and d_1, respectively, denote the catchability coefficient and half-saturation constant of the harvesting rate for prey. The same for the predator is represented by q_2 and d_2. The spatiotemporal dynamics

of the above system then obey the following reaction-diffusion equations:

$$\begin{aligned}\frac{\partial P}{\partial t} &= rP\left(1-\frac{P}{K}\right)-\frac{a_1PQ}{P+\alpha}-\frac{q_1E_1P}{P+d_1}+D_1\nabla^2P,\\ \frac{\partial Q}{\partial t} &= \frac{a_2PQ}{P+\alpha}-sQ-gQ^2-\frac{q_2E_2Q}{Q+d_2}+D_2\nabla^2Q,\end{aligned} \tag{2.1}$$

where $\nabla^2=\frac{\partial^2}{\partial x^2}+\frac{\partial^2}{\partial y^2}$ is the two-dimensional Laplacian operator and D_1, D_2 are the diffusivity of prey and predator species, respectively. The spatial domain is bounded with a well-defined region $\Omega\in\mathbb{R}^2$ with Neumann boundary conditions, meaning $\frac{\partial P}{\partial \nu}=\frac{\partial Q}{\partial \nu}=0$ on $(x,y)\in\partial\Omega$, where ν is the normal outward vector on the boundary $\partial\Omega$. Therefore, the species remains confined within the domain, and no influx of species occurs across the boundary.

This chapter extends the knowledge of the dynamical complexities of two-species harvesting models. A similar temporal model with no harvesting was analyzed by Mcgehee et al [87]. They observed the coexistence of a steady state and a limit cycle of the local system and demonstrated the existence of different patterns, including the back-eye pattern. Lv et al. [89] studied an RM-type predator-prey model with linear death of predator and nonlinear harvesting of either prey or predator species. Their analysis revealed various bifurcations, including codimension two bifurcations like cusp and BT (Bogdanov–Takens) bifurcation. However, they did not consider species diffusion, so the spatial effect was ignored. Hossain et al. [77] considered a Crowley-Martin type response function with linear harvesting of both species. They found the parametric space for Turing structure and observed patterns like spots and stripes. Bistability in the local system and spatiotemporal chaos in the Hopf-Turing region were absent in their study. A reaction-diffusion predator-prey model with Crowley-Martin type local interaction with nonlinear harvesting of predator only was analyzed in [90]. They provide local and global analysis of the coexisting equilibrium point. The existence criteria of the non-constant positive equilibria are also determined. They demonstrated the effect of predator diffusion and predator harvesting on spatial pattern formation. Similar studies with a ratio-dependent predator-prey model with linear harvesting of predator [91], Beddington-DeAngelis type predator-prey interaction with linear harvesting of both species [92], and predator-dependent prey refuge with linear harvesting of prey [78] have enriched the literature of reaction-diffusion population models. Weakly nonlinear analysis and pattern selection were made in a Holling-Tanner model with type-I response function and nonlinear harvesting of predator [93]. This chapter contains the two-species predator-prey model with saturated harvesting of both species, which is not examined before, as per our knowledge. The analysis of the system (2.1) is accomplished in two stages. First, in Section 2.2, the local or nondiffusive system of (2.1) is studied, which shows very

rich temporal dynamics, like multiple coexistence attractors (stable limit-cycles, stable equilibrium points). The local system encounters several bifurcations, such as transcritical, Hopf, saddle-node and homoclinic bifurcations. The emphasis is given to the parameters carrying capacity K and harvesting efforts E_1, E_2. Bifurcations are analytically proven and verified by one-parameter bifurcations. A key observation found that harvesting prevents the population from encountering the paradox of enrichment at a higher value of carrying capacity. In the next stage, in Section 2.3, the spatiotemporal dynamics with pattern-forming instabilities are studied. We determine the critical ratio of species diffusivity to occur in self-organized Turing patterns. A weakly nonlinear analysis of the system (2.1) is performed to identify the patterns at the initiation of Turing instability. The numerical simulation contains two significant observations: (i) The existence and non-existence of spatiotemporal chaos in Hopf-Turing instability based on diffusion coefficient ratio. (ii) The transition of stationary patterns with variable harvesting efforts are simulated for the model. It is observed that self-organized patchy distribution elevates the total population level more than that of the homogeneous distribution. Finally, Section 2.4 summarizes the crucial observations of this study with ecological relevance and some of its limitations.

2.2 Analysis of local system

Study of the spatial model (2.1) requires the study and validation of the underlying non-diffusive system. The non-diffusive system can be recovered by nullifying the diffusion process by setting $D_1 = D_2 = 0$. In this case, the system (2.1) reads

$$\begin{aligned} \frac{dP}{dt} &= rP\left(1-\frac{P}{K}\right) - \frac{a_1 PQ}{P+\alpha} - \frac{q_1 E_1 P}{P+d_1} = P\mathcal{F}(P,Q) = F(P,Q), \\ \frac{dQ}{dt} &= \frac{a_2 PQ}{P+\alpha} - sQ - gQ^2 - \frac{q_2 E_2 Q}{Q+d_2} = Q\mathcal{G}(P,Q) = G(P,Q). \end{aligned} \tag{2.2}$$

For the predator-prey kinetic system (2.2), the environmental carrying capacity (K) and the harvesting effort are the most significant parameters and are responsible for various changes in the system dynamics [94, 95, 96, 97, 98]. Moreover, the harvesting process can be viewed as the external interference in the two species interaction. Therefore, carrying capacity and harvesting efforts can be considered control parameters of interest.

2.2.1 Positivity and boundedness

To confirm that the considered system (2.2) is ecologically and mathematically meaningful, it is necessary to show that the solution exists uniquely and solutions are positive and bounded. One can easily prove the following lemma for such results.

Lemma 2.1. *Each solution* $(P(t), Q(t))$ *of the system* (2.2) *having initial point* $(P_0, Q_0) \in \mathbb{R}^2_+$ *is positive and uniformly bounded in* L_l*, where*

$$L_l = \{(P, Q) : 0 < \mathcal{X}(P, Q) < \frac{p_2}{p_1} + \epsilon,\ \epsilon > 0\},$$

where $\mathcal{X}(P, Q) = \ln P + \ln Q$, $p_1 = \min\left\{\frac{r}{K}, g\right\}$ *and* $p_2 = r + a_2$. □

Proof. Presume a continuous function $f : [0, t] \to \mathbb{R}^{2,0}_+$, and consider $\mathcal{B}$ the set of all such Banach space of continuous functions. One can define the initial condition of the system (2.2) as

$$P_\theta = \mathcal{N}_1(\theta) > 0,\ Q_\theta = \mathcal{N}_2(\theta) > 0,\ \theta \in [0, t], \tag{2.3}$$

where $(\mathcal{N}_1(0), \mathcal{N}_2(0)) \in \mathcal{B}$, and the corresponding norm becomes

$$||\mathcal{N}|| = \sup_{0<\theta<t} (|\mathcal{N}_1(\theta)|, |\mathcal{N}_2(\theta)|),$$

where $\mathcal{N} = (\mathcal{N}_1, \mathcal{N}_2)$. Following the fundamental theorem of functional differential equations [99], one can conclude that the system (2.2) exhibits a unique solution having the initial condition (2.2).

Again from system (2.2), one can get

$$\begin{aligned} P(t) &= P_0 e^{\int_0^t \left[r\left(1-\frac{P(\sigma)}{K}\right) - \frac{a_1 Q(\sigma)}{P(\sigma)+\alpha} - \frac{q_1 E_1}{P(\sigma)+d_1}\right] d\sigma} > 0 \text{ if } P_0 > 0, \\ Q(t) &= Q_0 e^{\int_0^t \left[\frac{a_2 P(\sigma)}{P(\sigma)+\alpha} - s - gQ(\sigma) - \frac{q_2 E_2}{Q(\sigma)+d_2}\right] d\sigma} > 0 \text{ if } Q_0 > 0. \end{aligned}$$

Therefore, the solutions always remains positive or positively invariant whenever it starts with a positive initial point.

Following Eq. (2.2)a, one have

$$\frac{dP}{dt} \leq rP\left(1 - \frac{P}{K}\right).$$

Then the standard comparison theorem gives

$$\limsup_{t\to\infty} P(t) \leq \zeta, \tag{2.4}$$

where $\zeta = \max\{P_0, K\}$.

Now, define a function

$$\mathcal{X} = \ln P + \ln Q.$$

The time derivative of $\mathcal{X}$ along the solution of (2.2) provides

$$\begin{aligned}
\frac{d\mathcal{X}}{dt} &= \frac{1}{P}\frac{dP}{dt} + \frac{1}{Q}\frac{dQ}{dt} \\
&= r\left(1 - \frac{P}{K}\right) - \frac{a_1 Q}{P+\alpha} - \frac{q_1 E_1}{P+d_1} + \frac{a_2 P}{P+\alpha} - s - gQ - \frac{q_2 E_2}{Q+d_2} \\
&\leq (r+a_2) - \left(\frac{r}{K}P + gQ\right) \qquad (\text{since, } \frac{P}{P+\alpha} \leq 1 \ \forall P > 0) \\
&< (r+a_2) - \left(\frac{r}{K}\ln P + g\ln Q\right) \qquad (\text{since, } P > \ln P \ \ \forall P > 0) \\
&\leq p_2 - p_1\mathcal{X},
\end{aligned}$$

where $p_1 = \min\{\frac{r}{K}, g\}$ and $p_2 = (r + a_2)$, we have

$$\frac{d\mathcal{X}}{dt} + p_1\mathcal{X} < p_2.$$

Then applying differential inequality theorem [100], one can have

$$0 < \mathcal{X}(P,Q) < \frac{p_2}{p_1} + \frac{\mathcal{X}(P_0,Q_0)}{e^{p_1 t}}. \tag{2.5}$$

As $t \to \infty$, the inequality (2.5) gives $0 < \mathcal{X}(P,Q) < \frac{p_2}{p_1}$. Therefore, with positive starting points, the solutions of the system (2.2) are always bounded in

$$L_l = \{(P,Q) : 0 < \mathcal{X}(P,Q) < \frac{p_2}{p_1} + \epsilon, \text{ for any positive } \epsilon\}.$$

Hence, the lemma. □

2.2.2 Equilibrium points and their existence

The system (2.2) has three types of ecologically distinct equilibrium points: trivial, predator-free and interior or existence. The trivial equilibrium point $\Xi_0 = (0, 0)$ exists always. The predator-free equilibrium points may be expressed as $\Xi_P = (\hat{P}, 0)$, where $\hat{P}$ is given by

$$\hat{P} = \frac{1}{2r}[r\,(K - d_1) \pm \sqrt{\{r\,(K - d_1)\}^2 - 4r(E_1 q_1 - d_1 r)K}] \tag{2.6}$$

with $E_1 \leq \frac{r}{4q_1}(K + d_1)^2$. If $(K - d_1) > 0$, then there will exist two predator-free equilibrium points whenever $E_1 > \frac{d_1 r}{q_1}$, and one predator-free equilibrium point otherwise. On the contrary, if $(K - d_1) < 0$, then the system will have no predator-free equilibrium if $E_1 > \frac{d_1 r}{q_1}$, and one otherwise. The coexisting equilibrium point may be denoted by $\Xi^*(P^*, Q^*)$, where

$$Q^* = \frac{P^* + \alpha}{a_1}\left[r\left(1 - \frac{P^*}{K}\right) - \frac{q_1 E_1}{P^* + d_1}\right], \tag{2.7}$$

and P^* is the positive root of the equation

$$\mathcal{P}(P) = A_0 P^7 + A_1 P^6 + A_2 P^5 + A_3 P^4 + A_4 P^3 + A_5 P^2 + A_6 P + A_7 = 0. \tag{2.8}$$

Expressions of coefficients A_i are not given for the sake of brevity. As the explicit expression of the equilibrium points is difficult to obtain, we will numerically analyze the existence of different interior equilibrium points in the simulation subsection.

2.2.3 Local stability analysis

The variational matrix of the system (2.2) evaluated at an arbitrary equilibrium point $\tilde{\Xi} = (\tilde{P}, \tilde{Q})$ is

$$J(\tilde{P}, \tilde{Q}) = \begin{pmatrix} r\left(1 - \frac{2P}{K}\right) - \frac{Q\,a_1\alpha}{(P+\alpha)^2} - \frac{E_1\,q_1 d_1}{(P+d_1)^2} & -\frac{P\,a_1}{P+\alpha} \\ \frac{Q\,a_2\alpha}{(P+\alpha)^2} & \frac{P\,a_2}{P+\alpha} - 2gQ - s - \frac{E_2\,d_2\,q_2}{(Q+d_2)^2} \end{pmatrix}_{(\tilde{P},\tilde{Q})} \tag{2.9}$$

The stability of an equilibrium point is determined by the sign of the eigenvalues of this variational matrix evaluated at the equilibrium point. One can then have the following results.

Theorem 2.2. *(i) The equilibrium $\Xi_0 = (0, 0)$ is locally asymptotically stable (LAS) if $E_1 > \frac{d_1 r}{q_1}$, otherwise it is a saddle point.*

(ii) The equilibrium $\Xi_P = (\hat{P}, 0)$*, whenever it exists, is LAS if* $E_2 > \frac{d_2}{q_2}\left(\frac{\hat{P}\,a_2}{\hat{P}+\alpha} - s\right)$*, and a saddle point otherwise.*

(iii) The equilibrium point $\Xi^*(P^*, Q^*)$*, whenever it exists, is LAS if and only if* $\Lambda_1 < 0$ *and* $\Lambda_2 > 0$*, where* Λ_1*,* Λ_2 *are given in* (2.13)*.* □

Proof. (i) One can easily get two eigenvalues corresponding to the equilibrium point $\Xi_0(0,0)$ as $(r - \frac{E_1\,q_1}{d_1})$, and $(-s - \frac{E_2\,q_2}{d_2})$. The second eigenvalue is always negative. The first one may be negative (or positive) according to $E_1 > (<) \frac{d_1 r}{q_1}$. Therefore, $\Xi_0(0,0)$ is LAS if $E_1 > \frac{d_1 r}{q_1}$, and unstable (saddle) otherwise.

(ii) The variational matrix corresponding to the equilibrium point Ξ_P becomes

$$J(\hat{P}, 0) = \begin{pmatrix} b_{11} & b_{12} \\ 0 & b_{22} \end{pmatrix}, \tag{2.10}$$

where $b_{11} = -\frac{E_1\,d_1\,q_1}{\left(\hat{P}+d_1\right)^2} - r\left(\frac{2\hat{P}}{K} - 1\right)$, $b_{12} = -\frac{\hat{P}\,a_1}{\hat{P}+\alpha}$, $b_{22} = \frac{\hat{P}\,a_2}{\hat{P}+\alpha} - s - \frac{E_2\,q_2}{d_2}$. Thus, the eigenvalues are $-\frac{E_1\,d_1\,q_1}{\left(\hat{P}+d_1\right)^2} - \frac{\hat{P}\,r}{K} - r\left(\frac{\hat{P}}{K} - 1\right)$ and $\frac{\hat{P}\,a_2}{\hat{P}+\alpha} - s - \frac{E_2\,q_2}{d_2}$. The first one is always negative since $\hat{P} < K$. Therefore, the predator-free equilibrium $\Xi_P = (\hat{P}, 0)$ is LAS if the second eigenvalue is also negative, and this happens when $E_1 < \frac{d_1 r}{q_1}$ and $E_2 > \frac{d_2}{q_2}\left(\frac{\hat{P}\,a_2}{\hat{P}+\alpha} - s\right)$.

(iii) At the coexisting equilibrium point $\Xi^*(P^*, Q^*)$, the matrix (2.9) reads

$$J(P^*, Q^*) = \begin{pmatrix} f_{10} & f_{01} \\ g_{10} & g_{01} \end{pmatrix}, \tag{2.11}$$

where $f_{10} = \frac{P^*Q^*a_1}{(P^*+\alpha)^2} - \frac{P^*r}{K} + \frac{E_1P^*q_1}{(P^*+d_1)^2}$, $f_{01} = -\frac{P^*a_1}{P^*+\alpha}$, $g_{10} = \frac{Q^*a_2\alpha}{(P^*+\alpha)^2}$, $g_{01} = -gQ^* + \frac{E_2Q^*q_2}{(Q^*+d_2)^2}$. The corresponding characteristic equation has the form

$$\mathcal{F}(\lambda) = \lambda^2 - \Lambda_1\lambda + \Lambda_2 = 0, \tag{2.12}$$

where

$$\begin{aligned} \Lambda_1 &= (f_{10} + g_{01}) = \mathrm{Tr}(J(P^*, Q^*)), \\ \Lambda_2 &= f_{10}g_{01} - f_{01}g_{10} = \mathrm{Det}(J(P^*, Q^*)). \end{aligned} \tag{2.13}$$

For the local stability of $\Xi^*(P^*, Q^*)$, one needs $\Lambda_1 < 0$ and $\Lambda_2 > 0$.

□

2.2.4 Local bifurcation analysis

Several local bifurcations may be observed in the system (2.2) for the variation of the parameters K, E_1 and E_2. We show that the system may experience transcritical, Hopf and saddle-node bifurcations at some critical values of these parameters.

Theorem 2.3. *The system (2.2) exhibits a transcritical bifurcation at the predator-free equilibrium Ξ_P if*

(i) the harvesting effort E_2 attains the critical value $E_2^{TC} = \frac{d_2}{q_2}\left(\frac{\hat{P}a_2}{\hat{P}+\alpha} - s\right)$ with $E_2^{TC} \neq \frac{gd_2^2}{q_2}$,

(ii) the prey carrying capacity K attains the critical value $K^{TC} = \frac{2\hat{P}r(\hat{P}+d_1)}{r(\hat{P}+d_1)-E_1d_1q_1}$ with $\frac{\hat{P}\,a_2}{\hat{P}+\alpha} \neq s + \frac{E_2\,q_2}{d_2}$. □

Proof. (i) From (2.10), one can observe that the Jacobian matrix leaves a zero eigenvalue whenever the condition $E_2 = \frac{d_2}{q_2}\left(\frac{\hat{P}a_2}{\hat{P}+\alpha} - s\right) = E_2^{TC}$ holds. At E_2^{TC}, the eigenvector corresponding to the zero eigenvalue of $J(\hat{P},0)$ is $\zeta = \left(\frac{-b_{12}}{b_{11}}, 1\right)^T$, and that of $\left[J(\hat{P},0)\right]^T$ is $\eta = (0,1)^T$, where $\left[J(\hat{P},0)\right]^T$ is the transpose of $J(\hat{P},0)$. We now inspect the following three transversality conditions [33] so that there exists a degenerate transcritical bifurcation point at $E_2 = E_2^{TC}$:

$$\begin{aligned} \eta^T R_{E_2}\Big(\Xi_p(\hat{P},0); E_2 = E_2^{TC}\Big) &= 0, \\ \eta^T DR_{E_2}\Big(\Xi_p(\hat{P},0); E_2 = E_2^{TC}\Big)\zeta &= 0, \\ \eta^T D^2R\Big(\Xi_p(\hat{P},0); E_2 = E_2^{TC}\Big)(\zeta,\zeta) &\neq 0, \end{aligned} \tag{2.14}$$

where $R = \Big(F(P,Q), G(P,Q)\Big)^T$ and $DR_{E_2}\Big(J(\hat{P},0); E_2 = E_2^{TC}\Big)\zeta$ are the linear transformations (see [33] for the definitions). For the non-degenerate transcritical

bifurcation, the second condition of (2.14) must be non-zero. Now,

$$\eta^T R_{E_2}\left(\Xi_p(\hat{P},0); E_2 = E_2^{TC}\right) = 0,$$

$$\eta^T DR_{E_2}\left(\Xi_p(\hat{P},0); E_2 = E_2^{TC}\right)\zeta = 0,$$

$$\eta^T D^2R\left(\Xi_p(\hat{P},0); E_2 = E_2^{TC}\right)(\zeta,\zeta) = (0 \;\; 1)\begin{pmatrix} -\frac{2r}{K} - \frac{2q_1E_1d_1}{(\hat{P}+d_1)^3} & 0 \\ 0 & -2g + \frac{2E_2^{TC}q_2}{d_2^2} \end{pmatrix}\begin{pmatrix} \frac{-b_{12}}{b_{11}} \\ 1 \end{pmatrix}$$

$$= -2g + \frac{2E_2^{TC}q_2}{d_2^2}. \tag{2.15}$$

Thus, following Sotomayor's theorem [33], a degenerate transcritical bifurcation point arises at the critical value $E_2^{TC} = \frac{d_2}{q_2}\left(\frac{\hat{P}a_2}{\hat{P}+\alpha} - s\right)$ provided $E_2^{TC} \neq \frac{gd_2^2}{q_2}$.

(ii) Similarly, at $K = \frac{2\hat{P}r(\hat{P}+d_1)}{r(\hat{P}+d_1)-E_1d_1q_1} = K^{TC}$ (say), the variational matrix (2.10) again gives a zero eigenvalue. In this case, the eigenvector of $J(\hat{P},0)$ and $J(\hat{P},0)^T$, corresponding to the zero eigenvalue at K^{TC}, are $\zeta_1 = (1,0)^T$ and $\eta_1 = (\frac{-b_{22}}{b_{12}},1)^T$. Similar calculations show that there exists a degenerate transcritical bifurcation point at $K = K^{TC}$ whenever $\frac{\hat{P}\,a_2}{\hat{P}+\alpha} \neq s + \frac{E_2\,q_2}{d_2}$. □

Theorem 2.4. *The coexistence equilibrium $\Xi^*(P^*,Q^*)$ of the system (2.2) undergoes a supercritical Hopf bifurcation at $K = K^{Hf}$, whenever*

$$\mathrm{Det}(J(\Xi^*; K = K^{Hf})) > 0 \text{ and } \frac{d}{dK}\left(\mathrm{Tr}(J(\Xi^*; K = K^{Hf}))\right) \neq 0,$$

where $K^{Hf} = rP^*\left[\frac{a_1P^*Q^*}{(P^*+\alpha)^2} + \frac{q_1E_1P^*}{(P^*+d_1)^2} - gQ^* + \frac{q_2E_2Q^*}{(Q^*+d_2)^2}\right]$. The nature of Hopf bifurcation is determined by the sign of the first Lyapunov coefficient $\mathcal{L}$. □

Proof. In Theorem 2.2, one can observe that the sign of $\mathrm{Tr}(J(P^*,Q^*))$ indicates the nature of stabilities of the equilibrium point Ξ^*. The equilibrium point Ξ^* loses its stability as $\mathrm{Tr}(J(P^*,Q^*))$ changes its sign from negative to positive due to the smooth variation of the parameter K. Solving $\mathrm{Tr}(J(P^*,Q^*)) = 0$ for K, one obtains

$$K = rP^*\left[\frac{a_1P^*Q^*}{(P^*+\alpha)^2} + \frac{q_1E_1P^*}{(P^*+d_1)^2} - gQ^* + \frac{q_2E_2Q^*}{(Q^*+d_2)^2}\right] = K^{Hf}.$$

Thus, one pair eigenvalues will be purely imaginary at $K = K^{Hf}$, and a Hopf bifurcation will occur at this critical value of K if the transversality condition

$$\frac{d}{dK}\left(\mathrm{Tr}(J(\Xi^*; K = K^{Hf}))\right) \neq 0$$

holds [33].

The nature of Hopf bifurcation is determined by the sign of the Lyapunov coefficient ($\mathcal{L}$) [33]. Whenever $\mathcal{L} > 0$, the Hopf bifurcation is subcritical, and an unstable limit cycle will appear around the equilibrium point. The opposite case $\mathcal{L} < 0$ exhibits a supercritical Hopf bifurcation and results in a stable limit cycle. The case $\mathcal{L} = 0$ implies that the equilibrium point Ξ^* is a weak focus of multiplicity one. To find the nature of Hopf bifurcation, we first translate the coexisting equilibrium $\Xi^*(P^*, Q^*)$ to the origin with the translation $P = \tilde{P} + P^*$ and $Q = \tilde{Q} + Q^*$, where $\tilde{P}$ and $\tilde{Q}$ are the corresponding perturbed variables. The Taylor series expansion then gives

$$\begin{aligned}\frac{d\tilde{P}}{dt} &= f_{10}\tilde{P} + f_{01}\tilde{Q} + F_3(\tilde{P}, \tilde{Q}),\\ \frac{d\tilde{Q}}{dt} &= g_{10}\tilde{P} + g_{01}\tilde{Q} + F_4(\tilde{P}, \tilde{Q}),\end{aligned}$$

where

$$F_3(\tilde{P}, \tilde{Q}) = \sum_{i+j\geq 2} f_{ij}\tilde{P}^i\tilde{Q}^j \text{ and } F_4(\tilde{P}, \tilde{Q}) = \sum_{i+j\geq 2} g_{ij}\tilde{P}^i\tilde{Q}^j$$

with the coefficients

$$f_{ij} = \frac{1}{i!j!}\frac{\partial^{i+j}F}{\partial P^i \partial Q^j}\bigg|_{(P^*,Q^*)} \text{ and } g_{ij} = \frac{1}{i!j!}\frac{\partial^{i+j}G}{\partial P^i \partial Q^j}\bigg|_{(P^*,Q^*)} \quad (\text{for } i, j > 0).$$

Following [33], one can then get the first Lyapunov coefficient as

$\mathcal{L} = -\frac{3\pi}{2f_{01}\Lambda_2^{3/2}}\Big[f_{10}g_{10}(f_{11}^2 + f_{11}g_{02} + f_{02}g_{11}) + f_{10}f_{01}(g_{11}^2 + f_{20}g_{11} + f_{11}g_{02}) - 2f_{10}b_{10}(g_{02}^2 - f_{20}f_{02}) + g_{10}^2(f_{11}f_{02} + 2f_{02}g_{02}) - 2f_{10}f_{01}(f_{20}^2 - g_{20}g_{02}) + (f_{10}g_{10} - 2f_{10}^2)(g_{11}g_{02} - f_{11}f_{20}) - f_{10}^2(2f_{20}g_{20} + g_{11}g_{20}) - (f_{10}^2 + f_{01}g_{10})\{3(g_{10}g_{03} - f_{01}f_{30}) + 2f_{10}(f_{21} + g_{12}) + (g_{10}f_{12} - f_{01}g_{21})\}\Big]$. □

Theorem 2.5. *A saddle-node bifurcation of the coexistence equilibrium $\Xi^*(P^*, Q^*)$ of (2.2) may arise with respect to K whenever the Eq. (2.8) exhibits a double root.*

Proof. Presume $\Xi^*_{SN} = (P^*_{SN}, Q^*_{SN})$ is a double root of Eq. (2.8) that corresponds to $K = K^{SN}$, giving

$$\mathcal{P}(P^*_{SN}; K^{SN}) = \mathcal{P}'(P^*_{SN}; K^{SN}) = 0,$$

where $\mathcal{P}'$ is the derivative of $\mathcal{P}$ with respect to P. At the saddle-node bifurcation point of the coexistence equilibrium (K^{SN}, Ξ^*_{SN}), the non-trivial nullclines

$$\mathcal{F}(P,Q) = r\left(1 - \frac{P}{K}\right) - \frac{a_1 Q}{P+\alpha} - \frac{q_1 E_1}{P+d_1} = 0 \quad \text{and}$$

$$\mathcal{G}(P,Q) = \frac{a_2 P}{P+\alpha} - s - gQ - \frac{q_2 E_2}{Q+d_2} = 0$$

become tangent to each other, implying that the slope of the two nullclines at the bifurcation point becomes identical, i.e.,

$$\frac{\partial Q^{(\mathcal{G})}}{\partial P} = \frac{\partial Q^{(\mathcal{F})}}{\partial P}, \tag{2.16}$$

where $\frac{\partial Q^{(\mathcal{F})}}{\partial P}$ and $\frac{\partial Q^{(\mathcal{G})}}{\partial P}$ are the slopes of the tangent lines corresponding to the curve $\mathcal{F}(P,Q) = 0$ and $\mathcal{G}(P,Q) = 0$. One can then write the Jacobian matrix (2.11) at Ξ^*_{SN} and its determinant, respectively, as

$$J(\Xi^*_{SN}) = \begin{pmatrix} P\frac{\partial \mathcal{F}}{\partial P} & P\frac{\partial \mathcal{F}}{\partial Q} \\ Q\frac{\partial \mathcal{G}}{\partial P} & Q\frac{\partial \mathcal{G}}{\partial Q} \end{pmatrix}_{(P^*_{SN}, Q^*_{SN})} = \begin{pmatrix} -P\frac{\partial \mathcal{F}}{\partial Q}\frac{\partial Q^{(\mathcal{F})}}{\partial P} & P\frac{\partial \mathcal{F}}{\partial Q} \\ -Q\frac{\partial \mathcal{G}}{\partial Q}\frac{\partial Q^{(\mathcal{G})}}{\partial P} & Q\frac{\partial \mathcal{G}}{\partial Q} \end{pmatrix}_{(P^*_{SN}, Q^*_{SN})}, \tag{2.17}$$

and

$$\mathrm{Det}(J(\Xi^*_{SN})) = \left\{ PQ\frac{\partial \mathcal{F}}{\partial P}\frac{\partial \mathcal{G}}{\partial Q}\left(\frac{\partial Q^{(\mathcal{G})}}{\partial P} - \frac{\partial Q^{(\mathcal{F})}}{\partial P}\right)\right\}_{(P^*_{SN}, Q^*_{SN})}.$$

Following (2.16), one must have $\mathrm{Det}(J(\Xi^*_{SN})) = 0$, giving a zero eigenvalue of the Jacobian matrix (5.5). Then $\eta = [1, p]^T$ and $\zeta = [q, 1]^T$ are the eigenvectors of $J(\Xi^*_{SN})$ and $J(\Xi^*_{SN})^T$ corresponding to the zero eigenvalue, where

$$p = \frac{\alpha a_2 (Q^*_{SN} + d_2)^2}{(g(Q^*_{SN} + d_2)^2 - q_2 E_2)(P^*_{SN} + \alpha)^2}, \quad q = \frac{(q_2 E_2 - g(Q^*_{SN} + d_2)^2)(P^*_{SN} + \alpha)}{a_1 (Q^*_{SN} + d_2)^2}.$$

The transversality conditions of the saddle-node bifurcation [33] are

$$\begin{aligned} \eta^T R_K(\Xi^*_{SN}; K = K^{SN}) &= \frac{r P^{*2}_{SN}}{K^{SN^2}} \neq 0, \\ \eta^T D^2 R(\Xi^*_{SN}; K = K^{SN})(\zeta, \zeta) &= [\, \frac{\partial^2 F}{\partial P^2} p^2 + 2\frac{\partial^2 F}{\partial P \partial Q} p + \frac{\partial^2 F}{\partial Q^2} + \\ &\quad q\left(\frac{\partial^2 G}{\partial P^2} p^2 + 2\frac{\partial^2 G}{\partial P \partial Q} p + \frac{\partial^2 G}{\partial Q^2}\right)]_{(P^*_{SN}, Q^*_{SN})} \\ &\neq 0. \end{aligned} \tag{2.18}$$

Remark 2.6. One can perform similar bifurcation analysis with respect to the parameters E_1 and E_2. Instead of tackling analytically these, numerical bifurcation analysis is presented in the next section.

□

2.2.5 Simulation results of the local system

First we determine the number of feasible coexistence equilibrium points of the system (2.2) by a graphical nullcline analysis. The Fig. 2.1 gives us a prototypical understanding of the equilibrium points. Fig. 2.1 indicates that there may exist one, two or three coexistence equilibrium points of the system depending on the values of K, E_1 and E_2. It also shows that there may be one or two predator-free equilibrium points.

One-parameter bifurcation analysis

The system (2.2) shows different dynamics due to a smooth variation in the carrying capacity, K. The one-parameter bifurcation diagram (Fig. 2.2) reveals that there exists five different dynamical regimes R_1 to R_5 separated by the bifurcation points K^{TC}, K^{Hf}, K^{SN} and K^{Hom}. The predator-free equilibrium is stable in the region R_1. The stable behaviour of the system is further illustrated by plotting the phase trajectories of the system (see Fig. 2.3a). A transcritical bifurcation occurs in the system at $K = K^{TC} = 4.89$ with the appearance of a interior equilibrium point, as K exceeds K^{TC}. Thus, a unique interior equilibrium appears and becomes stable in the region R_2 (also see Fig. 2.3b). The stable coexisting equilibrium $\Xi^* = (4.1688, 1.6994)$ undergoes a Hopf bifurcation at $K = K^{Hf} = 32.66$, satisfying the transversality condition $\frac{d}{dK}\left(\mathrm{Tr}(J(\Xi^*; K = K^{Hf}))\right) = 0.0031 \neq 0$. Further, the first Lyapunov coefficient is

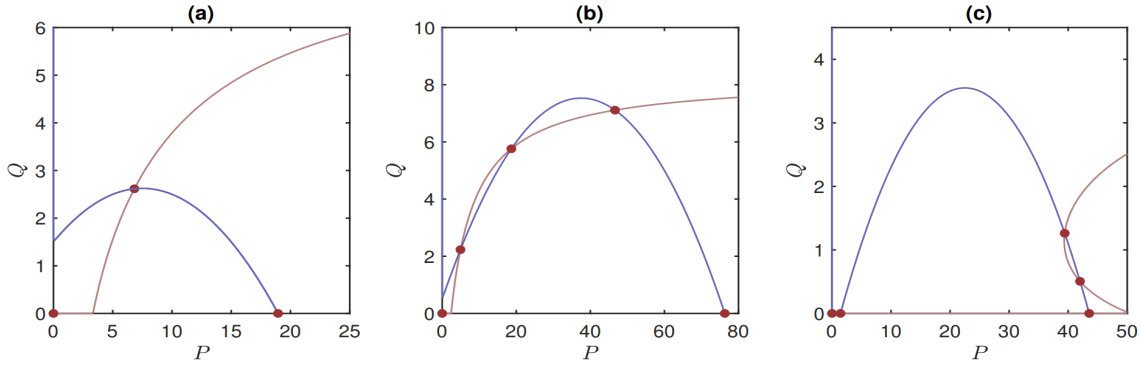

FIGURE 2.1: **Nullcine analysis:** Existence of equilibrium points (red dots) of the system (2.2) for different values of K, E_1 and E_2. Here blue curve represents the prey nullcline $F(P,Q) = 0$, and the red curve is the predator nullcline $G(P,Q) = 0$. The intersection of these two curves is the equilibrium point. **(a)** A unique coexistence equilibrium and a single predator-free equilibrium exist for $K = 20, E_1 = 1, E_2 = 1$. **(b)** Three coexistence equilibria and a single predator-free equilibrium occur for $K = 80, E_1 = 4, E_2 = 1$. **(c)** Two coexistence equilibria and two predator-free equilibria occur when $K = 50, E_1 = 4, E_2 = 4.4$. A $(0,0)$ equilibrium exists in every case. Other parameters are $r = 0.4, a_1 = 1, a_2 = 0.8, q_1 = 0.5, q_2 = 0.6, s = 0.2, g = 0.07, \alpha = d_1 = d_2 = 5$.

$\mathcal{L} = -2.0448\pi$, indicating that the Hopf bifurcation is supercritical, and the system populations switch from a stable state to an unstable state surrounded by a stable limit cycle as K crosses $K^{Hf} = 32.66$ from lower to higher value.

Thus, a stable limit cycle emerges around the unstable spiral interior equilibrium in the region R_3. The phase portrait of the system (see Fig. 2.3c) shows the existence of a limit cycle for a particular value of K, taken from R_3. A saddle-node bifurcation occurs at $K = K^{SN} = 70.62$ through the appearance of two new interior equilibrium points. The polynomial $\mathcal{P}$ (see Eq. (2.8)) possesses a double root at $(P^*, Q^*) = (28.0304, 6.4657)$ for $K^{SN} = 70.62$. At this point, $\eta^T D^2 R(\Xi^*_{SN}; K = K^{SN})(\zeta, \zeta) = 0.0705$, satisfying the transversality condition (5.7). Therefore, the system shows a saddle-node bifurcation at $K^{SN} = 70.62$. Thus, three interior equilibrium points exist in the region R_4. The unstable coexistence equilibrium continuing from the region R_3 remains unstable in R_4 surrounded by the stable limit cycle. One of the other two coexistence equilibrium points is a stable node, and the other is a saddle. Thus, R_4 is a bistable regime containing two attractors: a stable node and a stable limit cycle. Their basin of attractions is separated by the stable manifold of the saddle point (see Fig. 2.3d). The system finally undergoes a homoclinic bifurcation at $K = K^{Hom} = 97$, where the stable limit cycle is destroyed by the collision with the saddle point, making them disappear. Therefore, one stable (node) interior equilibrium exists in the region R_5, where $K > 97.0$. The other two interior equilibria exist but are unstable. The

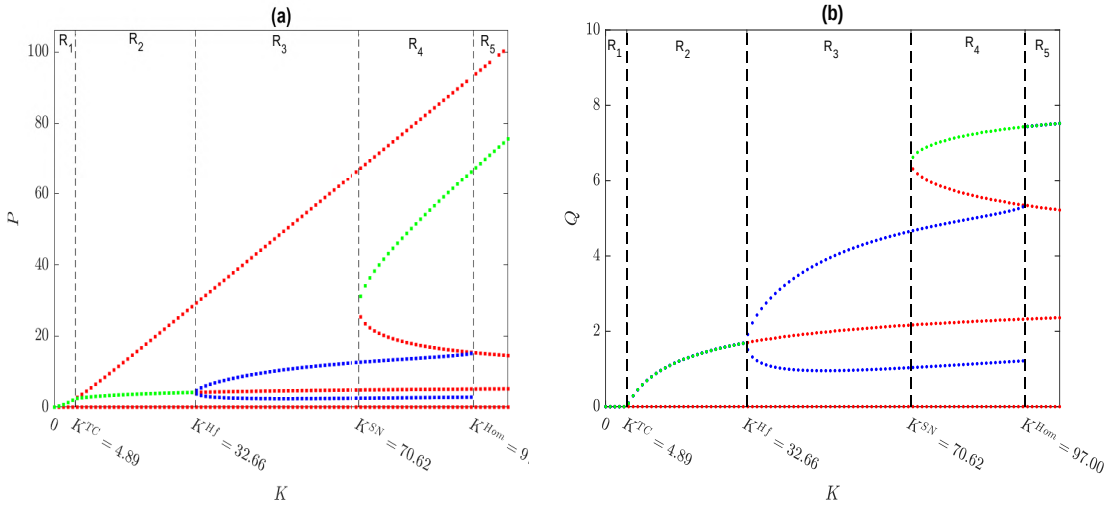

FIGURE 2.2: **One-parameter bifurcation diagram with respect to K:** Variation in the prey (Fig. a) and predator (Fig. b) densities for a change in the carrying capacity, K. Black dashed vertical lines are the bifurcation points K^{TC}, K^{Hf}, K^{SN} and K^{Hom}, representing transcritical, Hopf, saddle-node and homoclinic bifurcations, respectively. Red and green dotted curves are the unstable and stable equilibrium points of the system (2.2). Blue dotted curves are the amplitude of the stable limit cycle. Parameter values are as in Fig. 2.1 with $E_1 = 3, E_2 = 0.5$.

corresponding phase portrait (Fig. 2.3e) deciphers the system behaviour for $K = 100$, taken from R_5. We further discuss the stability switching of the system with the prey harvesting rate E_1 (see Fig. 2.4). There is a single stable interior equilibrium point in the region A_1, where both the species coexist in a stable state for low harvesting effort. A saddle-node bifurcation occurs with an increase in E_1, and the system possesses three interior equilibria, of which two are stable (one stable node and one stable focus), and the other is a saddle. Thus, there is bistability in the region A_2. While entering from region A_2 to A_3 for increasing E_1, a Hopf bifurcation occurs at the equilibrium with lower prey biomass, surrounded by a stable limit cycle. The limit cycle vanishes in the region A_4, following a homoclinic bifurcation. The system still has three equilibrium points in A_4, but only the higher biomass equilibrium is stable, and the other two are unstable. A stable limit cycle reappears as E_1 is further increased. Thus, there is a unique equilibrium point in the region A_5, as the other two coexistence equilibrium vanishes at the border of the A_4 and A_5 via a saddle-node bifurcation. In A_6, a stable limit cycle of very high amplitude and a stable trivial equilibrium (where both populations are zero) coexist depending on the initial point, giving a bistable regime. Further increase in E_1 causes extinction of entire population (region A_7).

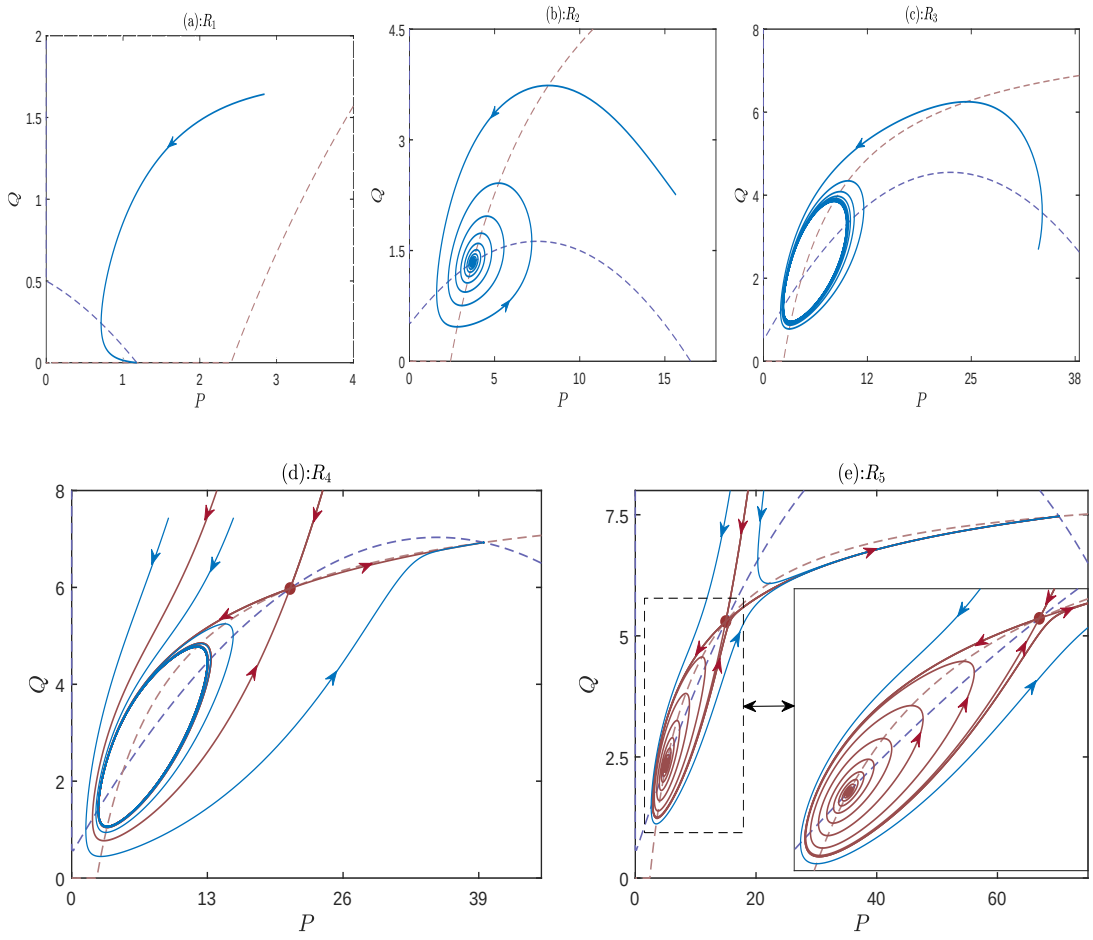

FIGURE 2.3: Phase portraits corresponding to the five distinct dynamical regions of Fig. 2.2. Purple and brown dashed lines are the prey and predator nullclines. Blue solid lines are the trajectories starting from a chosen point. Brown solid lines are the trajectories passing through the equilibrium points. (a) Existence of a unique stable predator-free equilibrium point for $K = 4$, taken from the region R_1. (b) Existence of a unique stable coexistence equilibrium point for $K = 20$, taken from the region R_2. (c) Existence of a unique unstable interior equilibrium surround by a stable limit cycle for $K = 50$, taken from R_3. (d) Existence of a three coexistence equilibrium points for $K = 80$, taken from R_4. A stable limit cycle exists at the lower equilibrium point. The intermediate equilibrium is unstable (saddle) and the higher equilibrium is a stable node. The domain of the two attractors is separated by the stable manifold of the saddle point. (e) Existence of three coexistence equilibrium points for $K = 100$, taken from R_5. The limit cycle disappears due to homoclinic bifurcation. See inset figure for an enlarged view. Other parameters are as in Fig. 2.1 with $E_1 = 3$ and $E_2 = 0.5$.

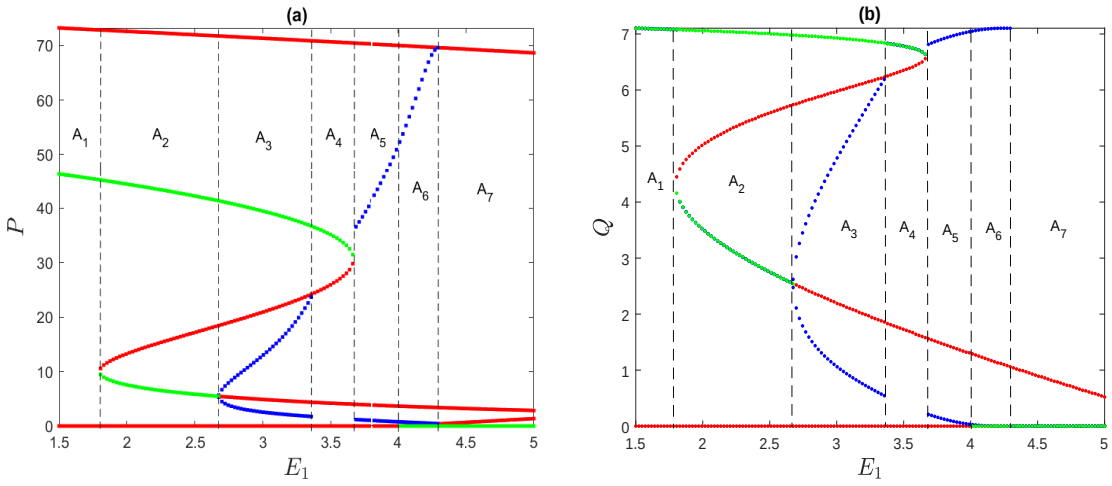

FIGURE 2.4: **One-parameter bifurcation diagram with respect to E_1:** Variation in the prey (Fig. a) and predator (Fig. b) populations for a change in the prey harvesting effort, E_1. Red and green dotted curves are the unstable and stable equilibrium points of the system (2.2). Blue dotted curves are the amplitude of the stable limit cycle. Parameter values are as in Fig. 2.1 with $K = 75, E_2 = 0.5$.

2.3 Analysis of the spatiotemporal system

In this section, we study the spatiotemporal system (2.1) and reveal the diffusion-driven instabilities. For such analysis, we consider that the kinetic parameters are in the regions R_2 and R_3 of Fig. 2.2, where a unique coexistence equilibrium point of the non-diffusive system exists. For bistable region R_4 and monostable region R_5, one interior equilibrium is stable (node) but does not satisfy the activator-inhibitor kinetics [101]. So, it has no additional contribution to the pattern-forming dynamics of the system.

2.3.1 Turing instability

Turing instability occurs when the corresponding non-diffusive system is stable, and destabilization occurs by some unstable mode of spatial perturbations caused by species diffusion. Turing instability studied here is about the unique coexistence equilibrium point $\Xi^*(P^*, Q^*)$, stability of which in the absence of diffusion is discussed in Theorem 2.2(iii). Linearization of the spatial system about Ξ^* with small spatiotemporal perturbations of the form $\delta P = \sum_{\vec{k}} C_p e^{\lambda t + i\vec{k}.\vec{x}}$ and $\delta Q = \sum_{\vec{k}} C_q e^{\lambda t + i\vec{k}.\vec{x}}$, where $\vec{x} = (x, y)$ is space vector, and $\vec{k} = (k_x, k_y)$ are the wavenumber vector of the spatial

perturbation, gives the dispersion equation

$$\lambda^2 + B_1(k^2)\lambda + B_2(k^2) = 0, \tag{2.19}$$

where $k = |\vec{k}|$ and

$$\begin{aligned} B_1(k^2) &= \Lambda_1 - k^2(D_1 + D_2), \\ B_2(k^2) &= D_1 D_2 k^4 - (D_1 g_{01} + D_2 f_{10})k^2 + \Lambda_2. \end{aligned} \tag{2.20}$$

The eigenvalue λ depends on the spatial wavenumbers. If for some non-zero wavenumber k, λ attains positive real value, then the Turing instability occurs. Recall that the Turing instability occurs under a stable local system, implying $\Lambda_1 = Tr(J(\Xi^*)) < 0$. Since the diffusion coefficients are positive, $B_1(k^2) < 0 \ \ \forall k$. Therefore, Turing instability can occur only when $B_2(k^2) < 0$ for some non-zero wavenumber k. Further, note that $D_1 D_2 > 0$ and $\Lambda_2 = Det(J(\Xi)) > 0$ (corresponding to the stability of the local system). Therefore, $B_2(k^2) < 0$ holds only when

$$D_1 g_{01} + D_2 f_{10} > 0, \tag{2.21}$$

where g_{01} and f_{10} are given in (2.11). The condition $B_2(k^2) < 0$ provides an interval of unstable wavenumbers responsible for the Turing instability, given by $k^2_{T_1} < k^2 < k^2_{T_2}$, where $k^2_{T_1}$, $k^2_{T_2}$ are the roots of $B_2(k^2) = 0$ with

$$k^2_{T_1,T_2} = \frac{(D_1 g_{01} + D_2 f_{10}) \mp \sqrt{(D_1 g_{01} + D_2 f_{10})^2 - 4 D_1 D_2 \Lambda_2}}{2 D_1 D_2}. \tag{2.22}$$

Positivity of these roots are ensured when

$$(D_1 g_{01} + D_2 f_{10})^2 > 4 D_1 D_2 \Lambda_2. \tag{2.23}$$

The parameters, satisfying the stability of the coexistence equilibrium Ξ^* and the conditions (2.21), (2.23) together, give the Turing parameter space. At the critical point of Turing instability, $min_{k^2>0} B_2(k^2)$ must be equal to zero, leading to (cf. Eq. (2.20)b)

$$min_{k^2>0} B_2(k^2) = B_2(k^2_{min}), \quad \text{where} \quad k^2_{min} = \frac{D_1 g_{01} + D_2 f_{10}}{2 D_1 D_2}. \tag{2.24}$$

Some further reductions [102], the critical wavenumber for Turing instability (k_c^T) reads

$$k_c^T = \sqrt[4]{\frac{\Lambda_2}{D_1 D_2}}. \tag{2.25}$$

2.3.2 Critical diffusion ratio for Turing instability

Here, we provide a relationship between the diffusion ratio of predator to prey and the occurrence of Turing instability.

Theorem 2.7. *Suppose that the coexistence equilibrium Ξ^* is LAS following Theorem 2.2(iii). If $d = \frac{D_2}{D_1}$ be the diffusion ratio of predator to prey, then the spatiotemporal model (2.1) undergoes a Turing instability for $d > d_c$, where*

$$d_c = d_+ = \frac{1}{f_{10}^2}[-(2f_{01}g_{10} - f_{10}g_{01}) + \sqrt{(2f_{01}g_{10} - f_{10}g_{01})^2 - f_{10}^2 g_{01}^2}].$$

Proof. Define the expressions of Turing instability criteria (2.21) and (2.23) as

$$\begin{aligned} \mathcal{C}_1(D_1, D_2) &= (D_1 g_{01} + D_2 f_{10})^2 - 4D_1 D_2 \Lambda_2 \\ &= D_2^2 f_{10}^2 + 2D_1 D_2 (2f_{01}g_{10} - f_{10}g_{01}) + D_1^2 g_{01}^2, \\ \mathcal{C}_2(D_1, D_2) &= D_1 g_{01} + D_2 f_{10}. \end{aligned} \tag{2.26}$$

Noting $d = D_2/D_1$,

$$\begin{aligned} & \mathcal{C}_1(D_1, D_2) = 0 \iff d^2 f_{10}^2 + 2d(2f_{01}g_{10} - f_{10}g_{01}) + g_{01}^2 = 0, \\ \text{and} \quad & \mathcal{C}_2(D_1, D_2) = 0 \iff d = -\frac{g_{01}}{f_{10}} := d^*. \end{aligned} \tag{2.27}$$

The two solutions of (5.14) are

$$d_\pm = \frac{-(2f_{01}g_{10} - f_{10}g_{01}) \pm \sqrt{(f_{01}g_{10} - f_{10}g_{01})^2 - f_{10}^2 g_{01}^2}}{f_{10}^2}. \tag{2.28}$$

LAS of Ξ^* gives $\Lambda_2 = (f_{10}g_{01} - f_{01}g_{10}) > 0$, along with $f_{01} < 0$, $g_{10} > 0$ (see Theorem 2.2(iii)). Therefore, $(2f_{01}g_{10} - f_{10}g_{01})^2 - f_{11}^2 g_{01}^2 = 4f_{01}g_{10}(f_{01}g_{10} - f_{10}g_{01}) > 0$, implying that both roots $d_\pm$ are real. Since $2(f_{01}g_{10} - f_{10}g_{01}) = f_{01}g_{10} - (f_{10}g_{01} - f_{01}g_{10}) < 0$, so $d_\pm$ are also positive. Therefore,

$$0 < d_- < d^* < d_+.$$

Conditions of Turing instability are satisfied if $\mathcal{C}_1(D_1, D_2) > 0$ and $\mathcal{C}_2(D_1, D_2) > 0$ hold simultaneously for the choices of D_1, D_2, or, equivalently, for the choice of the ratio, $d = \frac{D_2}{D_1}$. This is achievable if $d \notin (d_-, d_+)$ and $d > d_+$. Therefore, the critical diffusion ratio for the onset of Turing instability is $d_c = d_+$. □

2.3.3 Weakly nonlinear analysis and derivation of amplitude equation

The method of weakly nonlinear analysis (WNA) is one type of multiscale analysis based on the assumption that, near the instability threshold, the homogeneous steady state is forced to Turing instability only regarding the modes of perturbation close to the critical Turing wavenumber k_c^T [103]. Very close to the onset of instability, the eigenvalues (λ_k) close to the critical mode are nearly zero, and the corresponding modes vary slowly. The off-critical modes, also called the slave modes [104], on the other hand, relax quickly. Therefore, the whole dynamics reduces to dynamics of these slow varying modes, overshadowing the dynamics of the fast varying modes [105]. The selection of different patterns close to the onset of instability can be made using *amplitude equation* that governs the dynamics of these active unstable modes.

The Turing structures constitute the superposition of three pairs of modes $(\vec{k_j}, -\vec{k_j})$ for $j = 1, 2, 3$, making angles of $\frac{2\pi}{3}$, such that $\vec{k_1} + \vec{k_2} + \vec{k_3} = \vec{0}$. The system of these three active resonant pairs of wavenumbers describes the Turing pattern very well [104, 106]. Using the results of WNA analysis, the specific expression of the coefficients of the amplitude equation of the system can be obtained, which specifies the transitions of the Turing patterns. The formation of the amplitude equation is succinctly derived below.

Consider e as the control parameter and e_T as the critical value of the control parameter at the onset of Turing instability. We linearize the spatiotemporal system (2.1) about the homogeneous steady state $\Xi^*(P^*, Q^*)$ with perturbation terms $(p, q) = (P - P^*, Q - Q^*)$, leaving with

$$\frac{\partial}{\partial t}\begin{pmatrix} p \\ q \end{pmatrix} = L\begin{pmatrix} p \\ q \end{pmatrix} + N. \tag{2.29}$$

Here L, the coefficients of the linear terms, is expressed as

$$L = \begin{pmatrix} f_{10} + D_1\nabla^2 & f_{01} \\ g_{10} & g_{01} + D_2\nabla^2 \end{pmatrix}, \tag{2.30}$$

and N represents the nonlinear terms defined by

$$N = \begin{pmatrix} f_{20}p^2 + f_{11}pq + f_{02}q^2 \\ g_{20}p^2 + g_{11}pq + g_{02}q^2 \end{pmatrix} + \begin{pmatrix} f_{30}p^3 + f_{21}p^2q + f_{12}pq^2 + f_{03}q^3 \\ g_{30}u^3 + g_{21}u^2v + g_{12}pq^2 + g_{03}q^3 \end{pmatrix} + \mathcal{O}(p, q) \tag{2.31}$$

with $f_{ij} = \frac{1}{i!j!}\left(\frac{\partial^{i+j}F}{\partial P^i \partial Q^j}\right)_{\Xi^*}$ and $g_{ij} = \frac{1}{i!j!}\left(\frac{\partial^{i+j}G}{\partial P^i \partial Q^j}\right)_{\Xi^*}$. Note that Ξ^* contains the control parameter e. So, the expressions (2.29) - (2.31) are all functions of e. These equations

will be further expanded by Taylor's series about $e = e_T$. Very close to the Turing threshold, e can be expressed as

$$e_T - e = \epsilon e_1 + \epsilon^2 e_2 + \epsilon^3 e_3 + o(\epsilon^3). \tag{2.32}$$

Here, $0 < \epsilon << 1$ and e_1, e_2, e_3 are the coefficients of different orders. Similar expansion of the perturbation gives

$$\begin{pmatrix} p \\ q \end{pmatrix} = \epsilon \begin{pmatrix} p_1 \\ q_1 \end{pmatrix} + \epsilon^2 \begin{pmatrix} p_2 \\ q_2 \end{pmatrix} + \epsilon^3 \begin{pmatrix} p_3 \\ q_3 \end{pmatrix} + o(\epsilon^3). \tag{2.33}$$

Expanding the terms f_{ij} and g_{ij} about $e = e_T$, one gets

$$\begin{aligned} f_{ij} &= f_{ij}^T - (e_T - e) f_{ij}^{'T} + o(\epsilon^3), \\ g_{ij} &= g_{ij}^T - (e_T - e) g_{ij}^{'T} + o(\epsilon^3), \end{aligned} \tag{2.34}$$

where $f_{ij}^{'} = \frac{\partial f_{ij}}{\partial e}$, $g_{ij}^{'} = \frac{\partial g_{ij}}{\partial e}$, and T stands for the value of the corresponding terms at the Turing threshold $e = e_T$. For the sake of brevity, we drop T for further proceedings.

Substituting (2.32) and (2.34) in (2.30), we expand L about $e = e_T$ as

$$L = L_T + (e_T - e)M := \begin{pmatrix} f_{10} + D_1\nabla^2 & f_{01} \\ g_{10} & g_{01} + D_2\nabla^2 \end{pmatrix} - (e_T - e) \begin{pmatrix} f_{10}^{'} & f_{01}^{'} \\ g_{10}^{'} & g_{01}^{'} \end{pmatrix}. \tag{2.35}$$

Similarly, substituting (2.32), (2.33) and (2.34) in (2.31), one gets

$$N = \epsilon^2 N_2 + \epsilon^3 N_3 + \circ(\epsilon^3), \tag{2.36}$$

where

$$N_2 = \begin{pmatrix} f_{20}p_1^2 + f_{11}p_1q_1 + f_{02}q_1^2 \\ g_{20}p_1^2 + g_{11}p_1q_1 + g_{02}q_1^2 \end{pmatrix},$$

$$N_3 = \begin{pmatrix} 2f_{20}p_1p_2 + f_{11}(p_1q_2 + p_2q_1) + 2f_{02}q_1q_2 \\ 2g_{20}p_1p_2 + g_{11}(p_1q_2 + p_2q_1) + 2g_{02}q_1q_2 \end{pmatrix} + \begin{pmatrix} f_{30}p_1^3 + f_{21}p_1^2q_1 + f_{12}p_1q_1^2 + f_{03}q_1^3 \\ g_{30}p_1^3 + g_{21}p_1^2q_1 + g_{12}p_1q_1^2 + g_{03}q_1^3 \end{pmatrix}.$$

Furthermore, we introduce multiple time scales of different orders of ϵ as

$$\frac{\partial}{\partial T} = \epsilon \frac{\partial}{\partial T_1} + \epsilon^2 \frac{\partial}{\partial T_2} + \epsilon^3 \frac{\partial}{\partial T_3} + o(\epsilon^3). \tag{2.37}$$

Substituting (2.35)-(2.37) in (2.29), and comparing the coefficients of like terms in $\epsilon^j (j = 1, 2, 3)$, we have

$$\circ(\epsilon) : L_T \begin{pmatrix} p_1 \\ q_1 \end{pmatrix} = 0, \tag{2.38}$$

$$\circ(\epsilon^2) : L_T \begin{pmatrix} p_2 \\ q_2 \end{pmatrix} = \frac{\partial}{\partial T_1} \begin{pmatrix} p_1 \\ q_1 \end{pmatrix} - e_1 M \begin{pmatrix} p_1 \\ q_1 \end{pmatrix} - N_2, \tag{2.39}$$

$$\circ(\epsilon^3) : L_T \begin{pmatrix} p_3 \\ q_3 \end{pmatrix} = \frac{\partial}{\partial T_1} \begin{pmatrix} p_2 \\ q_2 \end{pmatrix} + \frac{\partial}{\partial T_2} \begin{pmatrix} p_1 \\ q_1 \end{pmatrix} - e_1 M \begin{pmatrix} p_2 \\ q_2 \end{pmatrix} - e_2 M \begin{pmatrix} p_1 \\ q_1 \end{pmatrix} - N_3. \tag{2.40}$$

The solution of the equation (2.38) yields the first level perturbation coefficients close to the Turing threshold. Such a solution is expressed as [104]

$$\begin{pmatrix} p_1 \\ q_1 \end{pmatrix} = \begin{pmatrix} \phi \\ 1 \end{pmatrix} \left(\sum_{j=1}^{3} W_j e^{i\vec{k}_j . \vec{r}} + \ c.c. \right), \tag{2.41}$$

where $\phi = -\frac{f_{01}}{f_{10} - D_1 k_c^{T\,2}}$, $|\vec{k}_j| = k_c^T$, W_j's are the amplitudes corresponding to the modes $e^{i\vec{k}_j \vec{r}}$ $(j = 1, 2, 3)$ and *c.c.* are the conjugate coefficients.

The nontrivial second-level perturbation terms may be obtained from Eq. (2.39). According to the Fredholm solubility condition [104], the vector function on the right-hand side of (2.39) must be orthogonal to the zero eigenvectors of the operator L_T^+ (the adjoint operator of L_T). The zero eigenvectors of L_T^+ are given by

$$\begin{pmatrix} 1 \\ \psi \end{pmatrix} W_j e^{-i\vec{k}_j . \vec{r}} + \ c.c. \ \ (j = 1, 2, 3),$$

where $\psi = -\frac{f_{01}}{g_{01} - D_2 k_c^{T\,2}}$. Satisfying the Fredholm solvability condition [104], we get the first order amplitude equations as

$$\begin{aligned} (\phi + \psi)\frac{\partial W_1}{\partial T_1} &= p_1 \mathcal{Q} W_1 + (I_1 + \psi I_2) 2 \bar{W}_2 \bar{W}_3, \\ (\phi + \psi)\frac{\partial W_2}{\partial T_1} &= p_1 \mathcal{Q} W_2 + (I_1 + \psi I_2) 2 \bar{W}_3 \bar{W}_1, \\ (\phi + \psi)\frac{\partial W_1}{\partial T_1} &= p_1 \mathcal{Q} W_3 + (I_1 + \psi I_2) 2 \bar{W}_1 \bar{W}_2, \end{aligned} \tag{2.42}$$

where

$$I_1 = f_{20}\phi^2 + f_{11}\phi + f_{02}, \quad I_2 = g_{20}\phi^2 + g_{11}\phi + g_{02}, \quad \mathcal{Q} = (\phi f_{10}^{'} + f_{01}^{'}) + \psi(\phi g_{10}^{'} + g_{01}^{'}).$$

Consider the second level perturbation terms as [104]

$$\begin{pmatrix} p_2 \\ q_2 \end{pmatrix} = \begin{pmatrix} P_0 \\ Q_0 \end{pmatrix} + \sum_{j=1}^{3} \begin{pmatrix} P_j \\ Q_j \end{pmatrix} e^{i\vec{k}_j\vec{r}} + \sum_{j=1}^{3} \begin{pmatrix} P_{jj} \\ Q_{jj} \end{pmatrix} e^{2i\vec{k}_j\vec{r}} + \sum_{j,l=1;j\neq l}^{3} \begin{pmatrix} P_{jl} \\ Q_{jl} \end{pmatrix} e^{i(\vec{k}_j-\vec{k}_l)\vec{r}} + c.c. \tag{2.43}$$

Substituting (2.41) and (2.43) in Eq. (2.39) and comparing the coefficients of like terms from the identity, we have

$$\begin{aligned} \begin{pmatrix} P_0 \\ Q_0 \end{pmatrix} &= \begin{pmatrix} \mu_{00} \\ \nu_{00} \end{pmatrix} (\textstyle\sum_{j=1}^{3} |W_j|), \quad P_j = \phi Q_j, \\ \begin{pmatrix} P_{jj} \\ Q_{jj} \end{pmatrix} &= \begin{pmatrix} \mu_{11} \\ \nu_{11} \end{pmatrix} W_j^2, \quad \begin{pmatrix} P_{jl} \\ Q_{jl} \end{pmatrix} = \begin{pmatrix} \mu_{22} \\ \nu_{22} \end{pmatrix} W_j \bar{W}_l, \end{aligned} \tag{2.44}$$

where

$$\begin{aligned} \begin{pmatrix} \mu_{00} \\ \nu_{00} \end{pmatrix} &= -2L_T^{-1} \begin{pmatrix} I_1 \\ I_2 \end{pmatrix}, \\ \begin{pmatrix} \mu_{11} \\ \nu_{11} \end{pmatrix} = -(L_T - 4k_c^{T^2} D)^{-1} \begin{pmatrix} I_1 \\ I_2 \end{pmatrix}, &\quad \begin{pmatrix} \mu_{22} \\ \nu_{22} \end{pmatrix} = -2(L_T - 3k_c^{T^2} D)^{-1} \begin{pmatrix} I_1 \\ I_2 \end{pmatrix}. \end{aligned} \tag{2.45}$$

Again, for the existence of nontrivial third-level perturbation terms given by Eq. (2.40), the vector function of the right-hand side of (2.40) must be orthogonal with the zero eigenvectors of the operator L_T^+. Utilizing those conditions, we get the second-order amplitude equations as

$$\begin{aligned} (\phi+\psi)\left(\frac{\partial V_1}{\partial T_1} + \frac{\partial W_1}{\partial T_2}\right) &= \mathcal{Q}(e_1V_1 + e_2W_1) + 2(I_1+\psi I_2)(\bar{W}_2\bar{V}_3 + \bar{W}_3\bar{V}_2) \\ &\quad - \left[G_1|W_1|^2 + G_2(|W_2|^2 + |W_3|^2)\right] W_1, \\ (\phi+\psi)\left(\frac{\partial V_2}{\partial T_1} + \frac{\partial W_2}{\partial T_2}\right) &= \mathcal{Q}(e_1V_2 + e_2W_2) + 2(I_1+\psi I_2)(\bar{W}_1\bar{V}_3 + \bar{W}_3\bar{V}_1) \\ &\quad - \left[G_2|W_2|^2 + G_2(|W_1|^2 + |W_3|^2)\right] W_2, \\ (\phi+\psi)\left(\frac{\partial V_3}{\partial T_1} + \frac{\partial W_3}{\partial T_2}\right) &= \mathcal{Q}(e_1V_3 + e_2W_3) + 2(I_1+\psi I_2)(\bar{W}_2\bar{V}_1 + \bar{W}_1\bar{V}_2) \\ &\quad - \left[G_1|W_3|^2 + G_2(|W_1|^2 + |W_2|^2)\right] W_3, \end{aligned} \tag{2.46}$$

where $G_1 = (\mu_{00}+\mu_{11})(H_1+\psi H_2) + (\nu_{00}+\nu_{11})(H_3+\psi H_4) + 3(R_1+\psi R_2)$, $G_2 = (\mu_{00}+\mu_{22})(H_1+\psi H_2) + (\nu_{00}+\nu_{22})(H_3+\psi H_4) + 6(R_1+\psi R_2)$, $H_1 = 2f_{20}\phi + f_{11}$, $H_2 = 2g_{20}\phi + g_{11}$, $H_3 = 2f_{02}\phi + f_{11}$, $H_4 = 2g_{02}\phi + g_{11}$.

Finally, we expand the amplitude of perturbations as the combination of different orders of amplitude as

$$A_j = \epsilon W_j + \epsilon^2 V_j + o(\epsilon^3). \tag{2.47}$$

The evolution of amplitude of the perturbation at multiple timescales is as

$$\frac{\partial A_j}{\partial t} = \epsilon^2 \frac{\partial W_j}{\partial T_1} + \epsilon^3 \left(\frac{\partial W_j}{\partial T_2} + \frac{\partial V_j}{\partial T_1} \right) \quad (j = 1, 2, 3). \tag{2.48}$$

Substituting the first and second level amplitude equations (2.42) and (2.46) in Eq. (2.48) and reducing it in terms of A_j $(j = 1, 2, 3)$, we get the desired amplitude equations

$$\begin{aligned}
\tau_0 \frac{\partial A_1}{\partial t} &= \eta A_1 + h \bar{A}_2 \bar{A}_3 - \left[g_1 |A_1|^2 + g_2 (|A_2|^2 + |A_3|^2) \right] A_1, \\
\tau_0 \frac{\partial A_2}{\partial t} &= \eta A_2 + h \bar{A}_3 \bar{A}_1 - \left[g_1 |A_2|^2 + g_2 (|A_3|^2 + |A_1|^2) \right] A_2, \\
\tau_0 \frac{\partial A_3}{\partial t} &= \eta A_3 + h \bar{A}_1 \bar{A}_2 - \left[g_1 |A_3|^2 + g_2 (|A_1|^2 + |A_2|^2) \right] A_3,
\end{aligned} \tag{2.49}$$

where

$$\tau_0 = \frac{\phi + \psi}{e_T \mathcal{Q}}, \ \eta = \frac{e - e_T}{e_T}, \ h = \frac{2(I_1 + \phi I_2)}{e_T \mathcal{Q}}, \quad g_1 = -\frac{G_1}{e^T \mathcal{Q}}, \quad g_2 = -\frac{G_2}{e^T \mathcal{Q}}. \tag{2.50}$$

Each amplitude A_i $(i = 1, 2, 3)$ is decomposed into $A_i = \rho_i e^{i\xi_i}$, where $\rho_i = |A_i|$ are the modes and ξ_i are the corresponding phase angles. Substituting these in Eq. (2.49) and then separating the real and imaginary parts, we obtain the system of ODEs as

$$\begin{aligned}
\tau_0 \frac{d\xi}{dt} &= -h \frac{\rho_1^2 \rho_2^2 + \rho_2^2 \rho_3^2 + \rho_3^2 \rho_1^2}{\rho_1 \rho_2 \rho_3} sin(\xi), \\
\tau_0 \frac{d\rho_1}{dt} &= \eta \rho_1 + h \rho_2 \rho_3 cos(\xi) - g_1 \rho_1^3 - g_2 (\rho_2^2 + \rho_3^2) \rho_1, \\
\tau_0 \frac{d\rho_2}{dt} &= \eta \rho_2 + h \rho_3 \rho_1 cos(\xi) - g_1 \rho_2^3 - g_2 (\rho_3^2 + \rho_1^2) \rho_2, \\
\tau_0 \frac{d\rho_3}{dt} &= \eta \rho_3 + h \rho_1 \rho_2 cos(\xi) - g_1 \rho_3^3 - g_2 (\rho_1^2 + \rho_2^2) \rho_3,
\end{aligned} \tag{2.51}$$

where $\xi = \xi_1 + \xi_2 + \xi_3$. Eq. (2.51) provides us the conditions of existence of the steady state patterns with different modes and their stability conditions [104] as follows:

1. The homogeneous stationary state: Modes are $\rho_1 = \rho_2 = \rho_3 = 0$ with the stability condition $\eta < \eta_2$, where $\eta_2 = 0$.

2. Striped pattern (S): Modes are $\rho_1 = \sqrt{\frac{\eta}{g_1}} \neq 0, \quad \rho_2 = \rho_3 = 0$ with the existence condition $\eta > \eta_2$ and stability condition $\eta > \eta_3$, where $\eta_2 = 0$ and $\eta_3 = \frac{h^2 g_1}{(g_2 - g_1)^2}$.

3. Hexagonal pattern (H_π) and (H_0): Modes for H_π and H_0 are $\rho_1 = \rho_2 = \rho_3 = \rho_\pm = \frac{|h| \pm \sqrt{h^2 + 4(g_1+2g_2)\eta}}{2(g_1+2g_2)}$ with the existence condition $\eta > \eta_1$. ρ_+ is stable if $\eta < \eta_4$ but ρ_- is always unstable, where $\eta_1 = -\frac{h^2}{4(g_1+2g_2)}$ and $\eta_4 = -\frac{h^2(2g_1+g_2)}{(g_1-g_2)^2}$.

4. Mixed pattern: Modes are $\rho_1 = \frac{|h|}{g_2 - g_1}$, $\rho_2 = \rho_3 = \sqrt{\frac{\eta - g_1\rho_1^2}{g_1+g_2}}$ with the existence conditions $g_2 > g_1$, $\eta_1 > g_1\rho_1^2$, and it is always unstable.

2.3.4 Numerical simulations of spatiotemporal system

For the simulations of spatiotemporal model (2.1), we have used the five-point discretized Laplacian operator $\mathbb{L}$, using the central difference rule on a two-dimensional space. The discretized Laplacian contains the Neumann boundary conditions in itself. The spatial grid length is $\delta_h = \delta_x = \delta_y = 1$, and temporal evolution follows the standard Euler scheme of step size $\delta_t = 0.01$. Uniformly distributed random perturbation about the coexistence equilibrium point $\Xi^*(P^*, Q^*)$ is considered as the initial values of the population biomass. Here, all parameters remain fixed as in Fig. 2.1 with $K = 20$, and only the harvesting efforts and the species diffusion rates are varied.

Turing and Hopf-Turing patterns

Fig. 2.5a shows different pattern-forming instability regions on $E_1 - D_2$ parametric space. It shows that there are four dynamic regimes: stable (green colour), Hopf instability (orange colour), Turing instability (blue colour) and Hopf-Turing instability (purple colour). In the lower range of predator diffusivity, the system enters from the stable to the Hopf region with increasing prey harvesting effort. However, in the higher range of predator diffusivity, the system enters from the Turing region to the Hopf-Turing region with increasing prey harvesting effort. On the other hand, for lower values of prey harvesting effort, the system losses its stability due to increasing predator diffusivity, causing Turing instability. The system experiences a Hopf-Turing instability when both the prey harvesting effort and predator diffusivity are high. In Fig. 2.5b, four dispersion curves are presented for four sample points, one from each region. Spatiotemporal instabilities occur if the real part of at least one eigenvalue becomes positive for some nonzero wavenumber. The dispersion curves (1) and (2) show the existence of pure Hopf and Hopf-Turing instabilities corresponding to the

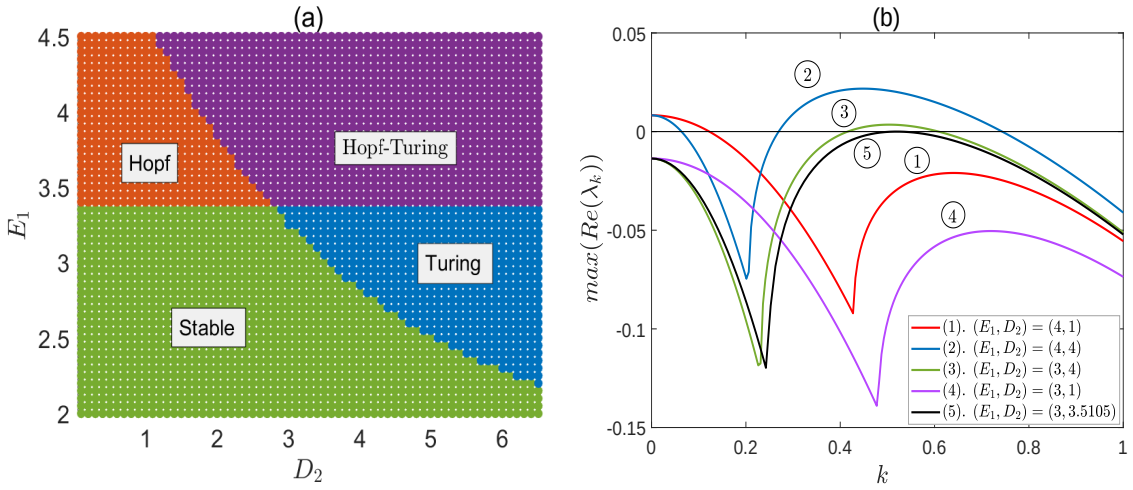

FIGURE 2.5: **(a)** Stability and instability regions of the system (2.1) on $D_2 - E_1$ plane: green dots represent the stable region, orange dots represent the Hopf region, blue dots represent the Turing region, and purple dots represent the Hopf-Turing region. **(b)** Plot of the dispersion curves for four sample points, one from each of the four regions. Parameter values are as in Fig. 2.1 with $K = 20$, $E_2 = 0.85$, $D_1 = 0.1$.

points $(E_1, D_2) = (4, 1)$ and $(E_1, D_2) = (4, 4)$. On the other hand, Turing instability is represented by the curve (3) corresponding to the point $(E_1, D_2) = (3, 4)$ and the curve (4) indicates that there is no change in the stability when $(E_1, D_2) = (3, 1)$. Dispersion curve (5) corresponds to critical diffusion ratio $d = d_+ = 35.105$ for the chosen parameter values obtained from the expression in Theorem 5.4. For $d > d_+$, one gets the Turing instability (See Fig. 2.5, curve (3)) and for $d < d_+$ we get homogeneous steady state (See Fig. 2.5, curve (4)). We compare the spatiotemporal dynamics of the system in the Hopf-Turing region (see Fig. 2.6) for different values of D_2 but the fixed value of $E_1 = 4.5$. Any dispersion curve in the Hopf-Turing region typically gives two peaks of the positive real part of λ_k: one at $k = 0$ (due to Hopf instability of the non-diffusive system) and another one for some $k \neq 0$ (due to the Turing instability caused by diffusion). It is observed that the solutions of the system and corresponding patterns depend on which instability dominates. The dominant character of these two instabilities relies on the height of the two peaks. If the peak height for $k \neq 0$, giving the Turing instability, is significantly lower than the peak height of the Hopf instability at $k = 0$, then Hopf instability dominates over the Turing instability, and the solutions show spatiotemporal chaos in the Hopf-Turing region. On the flip side, if the peak height for $k \neq 0$ is sufficiently greater, then Turing instability dominates over the Hopf. If both peak heights are almost the same, the solution oscillates irregularly but is not chaotic. Fig. 2.6a shows three dispersion relations for $D_2 = 1.5,\ 2.5, \text{and } 4.5$, while E_1 is fixed at 4.5. The corresponding time

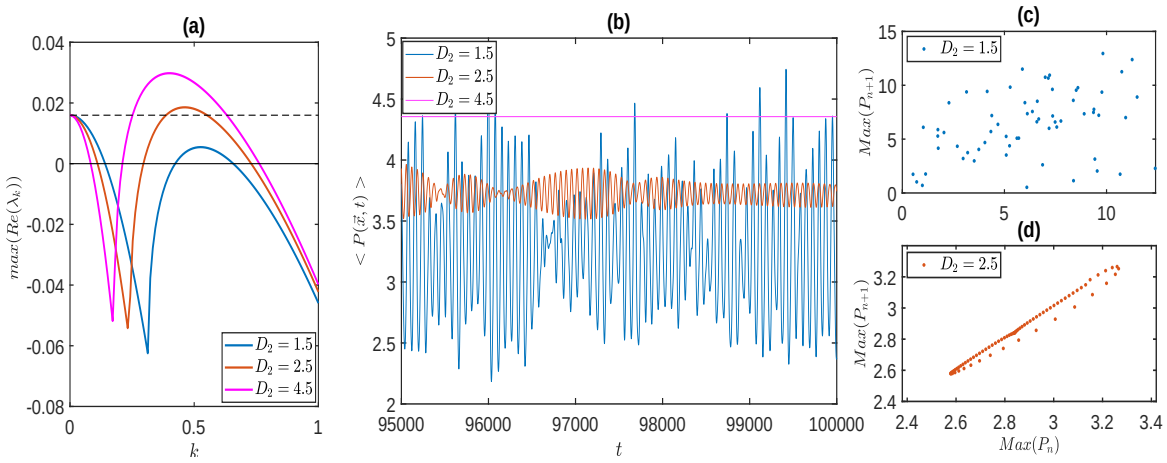

FIGURE 2.6: Spatiotemporal dynamics in the Hopf-Turing region for different values of D_2 while E_1 remains fixed. **(a)** Plot of dispersion relations for $D_2 = 1.5,\ 2.5,\ 4.5$. **(b)** Time series of spatial average of prey population ($\langle P(\vec{x},t)\rangle$) for the corresponding values of D_2. **(c-d)** Poincaré return map of prey biomass at the spatial grid $(x, y) = (100, 100)$ for $D_2 = 1.5$ (blue points Fig. (c)) and 2.5 (red points Fig. (d)) in the time span $t = 95000$ to 100000. Parameter values are as in Fig. 2.1 with $K = 20$, $E_1 = 4.5$, $E_2 = 0.85$, $D_1 = 0.1$.

series solutions of the spatial mean prey biomass over the space are plotted in Fig. 2.6b. Notice that the peak height for non-zero k is significantly lower than that of $k = 0$ for $D_2 = 1.5$, showing the chaotic oscillations. However, the peak height for $k \neq 0$ is significantly high compared to $k = 0$, showing the Turing-like steady state heterogeneous species distribution. The system shows quasiperiodic oscillations for $D_2 = 2.5$, where the two peak heights are almost similar. The irregularity of the time series for $D_2 = 1.5, 2.5$ is further verified using Poincaré return map at the spatial grid $(x, y) = (100, 100)$ within the time range of $t = 95000$ to 100000 in Figs. 2.6c, d. Clearly, for $D_2 = 1.5$, a scattered return map is observed (see Fig. 2.6c), which justifies chaos. Whereas for $D_2 = 2.5$, a closed-loop distribution of the return map is observed (see Fig. 2.6d), which implies quasiperiodic behaviour. The corresponding spatiotemporal patterns at different times are presented in Fig. 2.8. The simulations are performed for a very long time (up to $t = 100000$) to justify that the chaotic nature of the time series and patterns are not merely a prolonged transient dynamics. The snapshots of patterns at different times for $D_2 = 1.5$ do not repeat and show high irregularity, justifying the spatiotemporal chaos (Figs. 2.8(a)-(c)). Whereas, for $D_2 = 2.5$, a Turing-like pattern is visible, but the biomass oscillates (Figs 2.8(d)-(f)) as is clear from the colour bar. Similar behaviour of the system is observed for different values of E_1, E_2 and D_2. Thus higher predator diffusion controls the spatiotemporal chaos. This observation is further validated by plotting the maximum Lyapunov exponent (MLE) of the average prey density ($\langle P(\vec{x},t)\rangle$) over the space with

respect to D_2 in Fig. 2.7, where the MLE becomes negative for $D_2 \geq 2.5$, justifying chaos control.

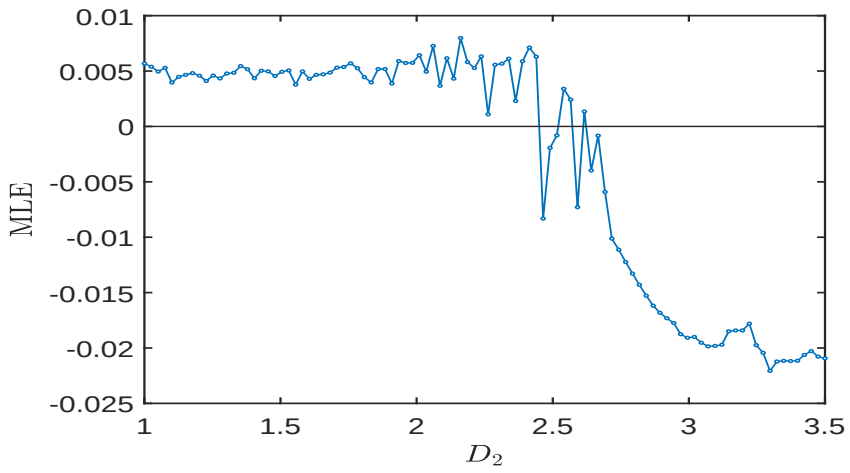

FIGURE 2.7: Maximum Lyapunov exponent (MLE) of the average prey population ($\langle P(\vec{x}, t)\rangle$) with respect to D_2. Other parameters are the same as in Fig. 2.6.

Spatial pattern formation with varying harvesting efforts E_1, E_2

One characteristic result present in all our simulations is that the dynamics of the non-diffusive system is of a pure activator-inhibitor type (as the Jacobian of the non-diffusive system at Ξ^* has $f_{10} > 0$, $f_{01} < 0$, $g_{10} > 0$, $g_{01} < 0$) [101]. This results in an in-phase distribution of the two species over the space [102], i.e., the distribution of the high and low-density regions of prey and predator populations over the space will have a positive correlation. Our aim here is to describe the effect of harvesting in terms of harvesting effort on the pattern formation of species over the spatial domain for given diffusivity. The significantly higher diffusion rate of predators will support the steady state heterogeneity even for Hopf-Turing instability, as described in the previous subsection (see Fig. 2.6b). The pattern observed in the total population distribution (i.e., $P(\vec{x}, t) + Q(\vec{x}, t)$) over a spatial domain of size 400×400 due to the variations in E_1, E_2 over the range $0 < E_1 < 4.5$ and $0 < E_2 < 1.5$ is presented in Fig. 2.9, Left. Since both species are considered for harvesting, the sum of distributions of both species is considered instead of considering a single one. The colour bar denotes the sum of the densities of the two species at a particular spatial grid. This figure shows that species gather differently depending on different harvesting efforts. The population creates various patterns, including cold spots, stripes, hot spots, and a mixture of spots and stripes in the intermediate zone.

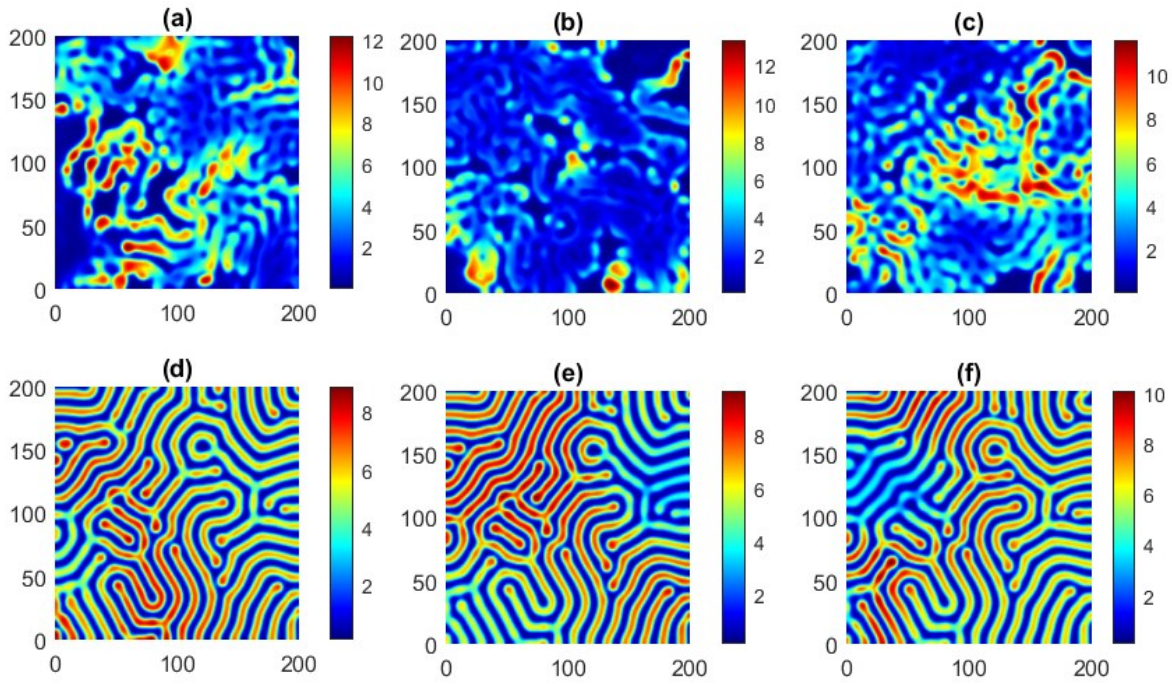

FIGURE 2.8: Snapshots of prey biomass distribution. (a-c) Snapshots of Hopf-dominated chaotic patterns in the Hopf-Turing region at time $t = 99000, 99500, 100000$ for $D_2 = 1.5$. (d - f) Snapshots of Turing-dominated patterns in the Hopf-Turing area at time $t = 99000, 99500, 100000$ for $D_2 = 2.5$. Parameters are the same as in Fig. 2.6.

Patterns generated here are stationary, implying that Turing instability occurs in the intermediate zone (see Fig. 2.9, Right). Total population density is homogeneously distributed with a high concentration at the lower-right region, where the harvesting effort for the predator population is greater than that of the prey population. It is worth mentioning that the contribution of prey to the total population is significantly higher than the predator population. However, the biomass is segregated into smaller patches of high biomass among predominately low prey biomass with the increasing effort of prey harvesting. As the prey is harvested with a greater effort, its density decreases, and a complementary decrease also occurs in the predator population due to the scarcity of the former. Thus, the total population decreases when E_1 is high. Further note, when prey is harvested intensively compared to predator, then the latter forces the former to accumulate into smaller patches. Thus, a transition of patterns from cold spots→stripes→hot spots can be observed with the increase of E_1. However, if the prey is intensively harvested, a relaxation in the force of accumulation occurs as the predator harvesting effort is gradually increased. In this case, a pattern transition in the species biomass occurs from hot spots→stripes→cold spots. We further compare the average species density (prey and predator) in the presence and

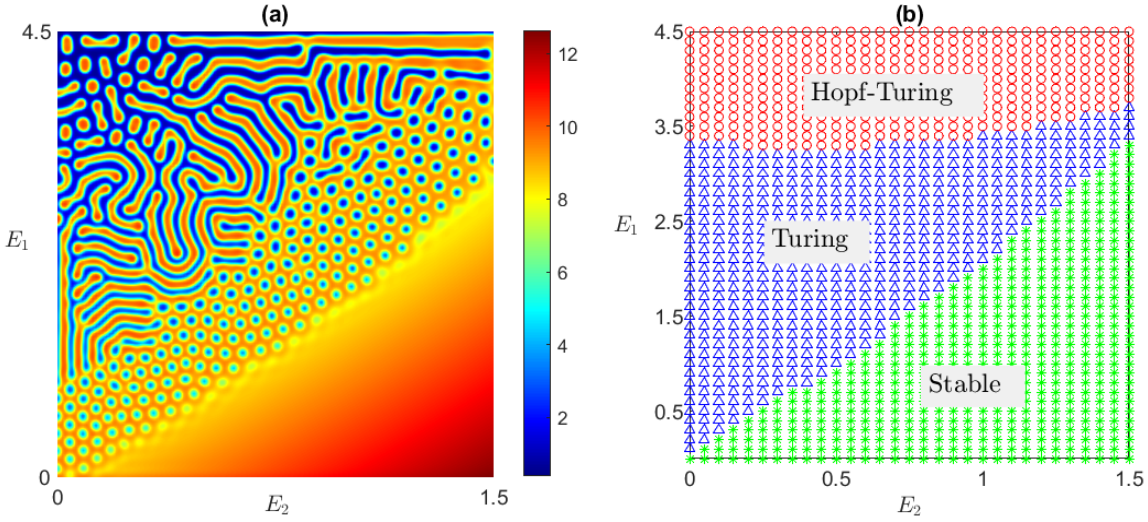

FIGURE 2.9: **Left:** The snapshot describes the pattern of the sum of distribution of the two populations (i.e., $P(\vec{x},t)+Q(\vec{x},t)$) in a heterogeneous space at time $t = 10000$, where harvesting efforts E_1 and E_2 are varied over space. **Right:** Corresponding nature of instabilities for the same values of E_1 and E_2. Green asterisks represent a homogeneous steady state, blue triangles represent the Turing instability, and the red circles represent the Hopf-Turing instability. Parameter values are as in Fig. 2.1 with $K = 20$, $D_1 = 0.1$, $D_2 = 10$.

absence of diffusion (see Table 2.1). For the diffusive system, we consider different sample points from the two instability regions, Turing and Hopf-Turing of Fig. 2.9b, and compute the average species density at a particular time where steady-state heterogeneity is achieved. The results are produced from simulations on a 200×200 spatial domain. It is worth mentioning that species biomass (P^*, Q^*) remains the same at each spatial grid of the domain in the non-diffusive system for a given pair of (E_1, E_2). The results show that the average species biomass is always higher in the spatial system in presence of heterogeneous state than its non-spatial counterpart, indicating the positive role of diffusion in species persistence.

Validation of Turing patterns through WNA results

We validate the pattern selection and pattern transition results from the analysis derived from the amplitude equation for our model. Here, E_1 is the control parameter to capture the pattern transition. Other parameter values are the same as in Fig. 2.1 except $E_2 = 0.1$, $D_1 = 0.09$ and $D_2 = 4$. For this set of values, the critical value of E_1 for the onset of Turing instability is $E_1^T = 1.4836$. Values of h, g_1 and g_2 in (2.51), as derived from Eq. (2.50), are $h = 3.1174$, $g_1 = 49.1098$ and $g_2 = 96.8783$. The

TABLE 2.1: Nature of instability and measure of total population (prey plus predator) for different sample points taken from the Turing and Hopf-Turing regions of Fig. 2.9b.

Observation	(E_1, E_2)	Region	Pattern	Average (with diffusion)	Average (without diffusion)
I.	$(4.3, 0.05)$	Hopf-Turing	Hot-spot	3.6517	2.4238
II.	$(4.3, 0.75)$	Hopf-Turing	Stripe	5.1047	4.0562
III.	$(4.3, 1.45)$	Hopf-Turing	Mixed	6.7313	6.1085
IV.	$(2.3, 0.05)$	Turing	Stripe	5.7911	4.9225
V.	$(2.3, 0.75)$	Turing	Cold-spot	7.1608	6.6957
VI.	$(0.5, 0.05)$	Turing	Cold-spot	7.8887	7.6300

transition points of patterns η_1, η_2, η_3, η_4 are $-0.0100,\ 0,\ 0.2092,\ 0.8309$, respectively. Turing instability and the corresponding steady-state heterogeneous patterns appear for $\eta \in (\eta_2, \infty)$. H_π-pattern is stable in the range (η_2, η_4), and stripe pattern is stable in (η_3, ∞). A bistable state is observed in the intermediate range (η_3, η_4). Fig. 2.10 provides the amplitude plots of different steady-state patterns. We consider the observation points $\eta = 0.05,\ 0.19,\ 0.35,\ 0.85$ to show the pattern transitions. Cold spots are observed for $\eta = 0.05 \in (\eta_2, \eta_3)$ (see Fig. 2.11a). For $\eta = 0.19$, sufficiently close to the transition point η_3, stripe patterns start to appear along with the cold spots (see Fig. 2.11b). For $\eta = 0.35$, which belongs to (η_3, ∞), we observe stripe patterns all over the spatial domain (see Fig. 2.11c). At $\eta = 0.85$, cold spots start to appear along with stripes (see Fig. 2.11d).

2.4 Discussion

This work focuses on the temporal and spatiotemporal dynamics of a two-species predator-prey interaction under the influence of nonlinear harvesting of both species. We have analytically studied the kinetic system and shown the existence of different bifurcations, like transcritical, Hopf, and saddle-node. The presence of such bifurcations is numerically demonstrated by the variation of the system's carrying capacity (Fig. 2.2) and harvesting effort (Fig. 2.4). A substantially low carrying capacity causes species extinction; an intermediate value provides stable coexistence. Species coexist in the stable oscillatory state caused by a supercritical Hopf bifurcation as K increases. The amplitude of oscillations grows with K, indicating the occurrence of the well-known ecological phenomenon, the paradox of enrichment [107]. If the system is further enriched, the system shows bistability. Here, species coexistence occurs in a stable or oscillatory state, depending on the initial value. A homoclinic bifurcation occurs for further increment in K, destroying the limit cycle and the saddle point.

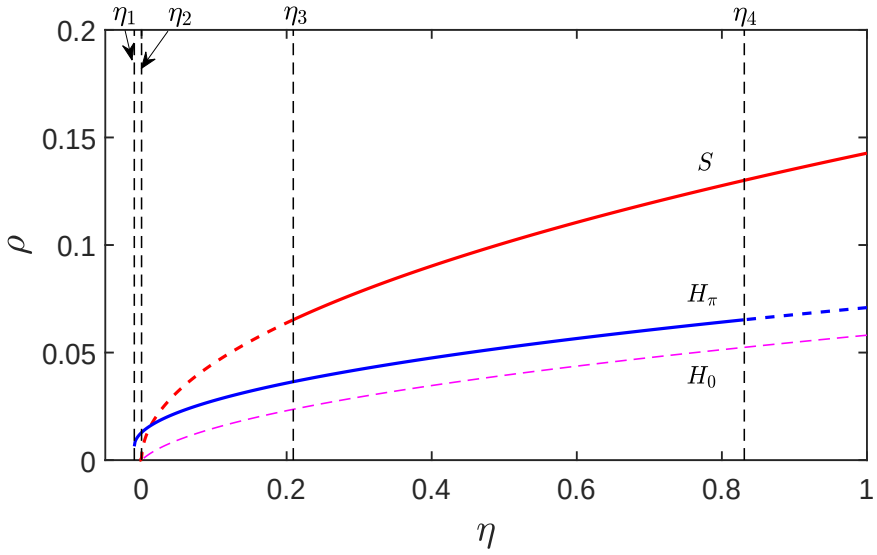

FIGURE 2.10: Amplitude plot of different steady-state (Turing) patterns. The solid line stands for stable range, dashed lines for unstable range. Red curve: stripe pattern (S). Blue curve: (H_π) cold-spot pattern. Magenta curve: (H_0) hot-spot pattern. Parameter values are as in Fig. 2.1 with $K = 20$, $E_2 = 0.1$, $D_1 = 0.09$, $D_2 = 4$.

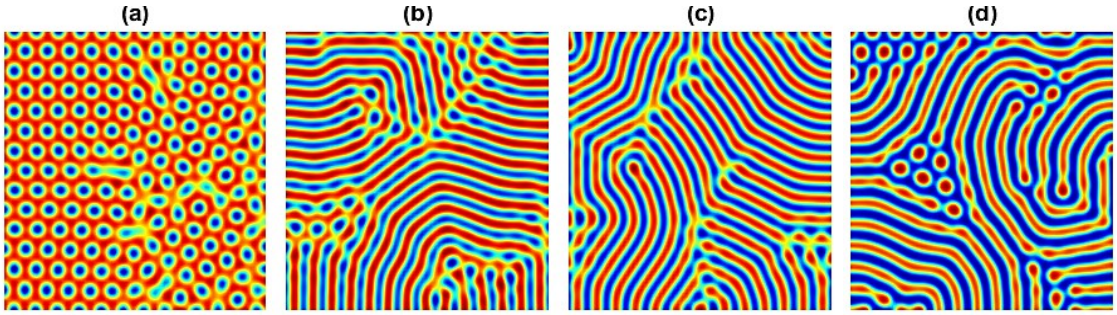

FIGURE 2.11: Patterns for different η values. (a) $\eta = 0.05$, $E_1 = 1.5578$, (b) $\eta = 0.19$, $E_1 = 1.7655$, (c) $\eta = 0.35$, $E_1 = 2.0039$, (d) $\eta = 0.85$, $E_1 = 2.7447$. The rest of the parameters are as in Fig. 2.10.

In this case, the system again becomes monostable for higher values of $K > K^{Hom}$, contrary to the paradox of enrichment. This study thus reveals that a system may or may not show the paradox of enrichment, supporting the observation of previous field results [94] and theoretical works [95, 96]. Similar rich dynamics are observed for the harvesting efforts as well. In particular, the dynamics are more complicated in prey harvesting than predator harvesting. The prey species can be considered the

resource on which the predator survives. Thus overharvesting of prey species generates oscillations in the population levels, indicating increasing system vulnerability. However, the predator acts as the inhibitor of the system. Thus, increased predator harvesting stabilizes the system from an oscillatory state. However, a significantly high harvesting rate may cause predator population extinction.

For a specialist predator, who feeds on a particular food, the increased number of predators may give rise to competition among themselves, which may cause additional deaths in the predator population. This competition may further increase for solitary predators. In this scenario, predators will forage more in search of food and disperse widely to avoid competition. Consequently, the diffusion rate of predators is expected to be much larger than that of prey [87], which facilitates the occurrence of diffusion-driven (Turing) instabilities [87, 102]. In this study, we have proved the occurrence of Turing instability through two mechanisms, viz. the wave number (k) of the spatial perturbations and the diffusion ratio d ($= \frac{D_2}{D_1}$) of predator to prey. In the first case, it is shown that Turing instability may occur when the wave number lies in between two critical values, $k_{T_1}^2 < k^2 < k_{T_2}^2$, along with some other parametric conditions. In the second case, we have proved that Turing instability may also occur if the diffusion ratio d exceeds a critical value d_c, involving parameters of the local system.

Different spatiotemporal patterns are observed with variations in harvesting efforts and species diffusivity. It is demonstrated that prey harvesting facilitates spatiotemporal chaos, and predator diffusion controls chaotic dynamics. A unique observation of this study is the occurrence and nonoccurrence of spatiotemporal chaos in the Hopf-Turing zone in $E_1 - D_2$ parametric plane (see Fig. 2.6). It is observed that the solutions and patterns depend on which instability dominates more. The dominant character of these two instabilities relies on the height of the two peaks. If the peak height (i.e., the maximum real part of the eigenvalue) for $k = 0$ is significantly larger than that of $k \neq 0$, then the Hopf instability dominates the Turing, giving rise to spatiotemporal chaos in the Hopf-Turing region. In the opposite case, the Turing instability dominates the Hopf, and a heterogeneous steady state prevails in the Hopf-Turing area. Simulation results further decipher that greater prey harvesting forces spatial segregation. In contrast, predator harvesting relaxes spatial segregation, resulting in more areas of high biomass zones when the predator is intensively harvested (see Fig. 2.9, Left). A comparative study shows that the spatial system's average population density is always higher than its non-spatial counterpart. Thus, spatial segregation enriches the overall species density.

Turing pattern formation and stability are also derived from weakly nonlinear analysis. One crucial observation obtained from the amplitude equation for our model is that whenever the system undergoes Turing instability, the cold-spot pattern (or H_π hexagonal pattern) appears. Cold and hot are characterized according to higher

and lower biomass. A limitation of the weakly nonlinear analysis is that the patterns become inconclusive for higher values of η [105]. It does not match the results of the amplitude equation as we drift far away from the critical Turing threshold, and the primary slave modes become active modes.

This chapter provides detailed analytical and numerical results of a two-species predator-prey model; however, it has some limitations that need to be addressed. The model studied here is based on the mean-field concept, which does not consider uncertainty. So, the first modification should be the stochastic extension [108] of the considered model and study how instability and patterns appear in the presence of noise. Secondly, other biological traits may be introduced to make the kinetic system more realistic. For example, species frequently show the Allee effects [109] when population size is small. Allee effects may be significant in the presence of harvesting, which causes population reduction. Therefore, a reaction-diffusion predator-prey model in the presence of Allee effects and harvesting will be more worthy of studying the pattern-forming instabilities. The current study establishes a fundamental understanding of how harvesting, irrespective of spatial considerations, impacts predator-prey dynamics. However, the study would be more realistic and worthy if one considers location-dependent harvesting. This would enable us to explore the intricate interplay between resource exploitation and spatial heterogeneity of species, thereby contributing to a comprehensive view of the predator-prey system's behaviour. Despite these shortcomings, this study will significantly improve our understanding of a two-species population model with nonlinear harvesting and diffusion.

Chapter 3

How do productivity gradient and diffusion shape patterns in a plant-herbivore grazing system? [2]

3.1 Introduction

The most fundamental components of each ecosystem are the autotrophs, also referred to as the natural vegetation, which includes plants in terrestrial ecosystems and phytoplankton or algae in wetland and marine ecosystems. Through photosynthesis, autotrophs generate their food and pass on the energy to herbivores, positioned right above the autotrophs in the ecological food chain [110, 111]. The classical exploitation theory postulates a positive correlation between increasing primary productivity of the system and increasing herbivore growth through intense grazing [112], resulting in a top-down control mechanism. Top-down control can be seen in a variety of ecological interactions along the gradient of primary productivity, where the species' growth in the upper trophic level controls the species' growth at the lower trophic level [112, 113]. For example, in a predator-prey interaction, the predator population influences and suppresses the prey's growth even in a highly productive environment for the prey species. Under these circumstances, the prey's steady-state density is determined by the predation parameters [114]. Koppel et al. [56] proposed a model of alternative control mechanism regarding plant-herbivore interaction, where a bottom-up control mechanism is assumed. In this case, the lower trophic level species, the

[2]Published article by Marick, S., Takasu, F., & Bairagi, N. (2024). How do productivity gradient and diffusion shape patterns in a plant–herbivore grazing system?. Journal of Theoretical Biology, 590, 111856. https://doi.org/10.1016/j.jtbi.2024.111856

plants control the population of their consumers, the herbivores. This control mechanism is different from population suppression due to the scarcity of resources at lower trophic levels. The bottom-up control was supported by empirical data [56] of three herbivore species: geese, rabbits, and hares, in a variety of vegetation phases, such as short, sparse *Puccinellia-Carex* swards and tall, dense *Calamagrostis* swards. It is revealed that an intermediate vegetation density is favourable to host the maximum herbivore density. On the other hand, low herbivore density is correlated with either high or low vegetation density. In a microcosm experiment of plant and invertebrate herbivore interactions under nutrient enrichment, Schädler et al. [115] reported a bottom-up control of vegetation by nutrient availability and a weak top-down control by herbivores. In contrast, the experimental findings of Jia et al. [116] demonstrated the top-down regulation of terrestrial plant-herbivore interactions. Therefore, understanding the growth of vegetation and its consumers as well as the interaction mechanism between them is essential [117, 118].

Large-scale spatial vegetation patterns have been documented in a significant number of studies [119, 21, 120] using satellite images and aerial photography. Different patterns, like spots with little to no vegetation or open ground inside a grass matrix [121, 122], fairy rings [123, 124], fairy circles [125, 126] and spiral patterns [127, 128] of vegetation have been observed in natural systems. The patchy distribution of natural vegetation can be caused by several factors, such as the type of consumer grazing pressure [128], weather patterns [59], and geographical terrain [120]. Under arid and semi-arid climate conditions, the vegetation shows heterogeneous patchy distributions, including cold spots, labyrinth patterns, and hot spots [121, 57, 59, 20].

Herbivore foraging has long been recognized as a critical factor affecting the structure and functioning of vegetation from individual plant species to entire landscapes [111, 129]. However, empirical investigations have shown that herbivores' foraging behaviour depends on several factors, which include the spatial distribution of vegetation, the efficiency of the grazers, and the behaviour of the grazers, along with others [130]. Even, within various plant species, the presence of herbivore populations can lead to alterations in the chemical, physical, or other attributes of foliage, thereby triggering the "inducible defences" [131, 132]. Many theoretical and empirical investigations have unequivocally demonstrated that these inducible defences significantly impact the stability and long-term survival of herbivore populations [133, 134] and patterns [122, 127].

There are two types of diffusion: self-diffusion and cross-diffusion. In the former, the population moves according to its own concentration gradient. The species in the latter scenario moves depending on the other species' concentration gradient [135]. According to thermodynamic theory, cross-diffusion coefficients can be either positive or negative, while self-diffusion coefficients are always assumed to be positive [136].

A positive cross-diffusion coefficient, $D_{ij} > 0$, implies that the i-species travels from high concentration to low concentration zones of the j-species. The negative cross-diffusion coefficient, $D_{ij} < 0$, implies that the i-species travels from low concentration to high concentration zones of the j-species [135]. The self-diffusion can be used to model the natural tendencies of species to avoid intraspecific competition and infection, for mate searching, etc. [30]. Cross-diffusion can mimic the spatial behaviour of a species in response to the concentration of other species, e.g., avoidance of interspecific competition, predators' movement to higher prey concentration zones, predators' avoidance of group defence made by the prey, etc.

Jackson and Segel [42] first used the reaction-diffusion predator-prey model in an ecological scenario. Subsequently, different researchers used reaction-diffusion population models in a range of ecological systems [137, 138], eco-epidemiological systems [139, 140], harvesting models [141, 142], and epidemic models [143, 144]. It was later utilized in terms of how patterns arise in vegetation and how vegetation interacts with soil water by Klausmeier [26]. Following the work of Lambers et al. [121], different vegetation patterns in arid and semi-arid environments have been studied. The herbivore outbreak and spatiotemporal oscillations of the herbivore population have been analyzed in [134, 145]. Additionally, spatiotemporal models of plant-herbivore interactions from the perspective of predator-prey interactions have been studied by many researchers [146, 147, 148]. Some integro-differential equation-based models have assumed the factor of grazing but do not consider the herbivore species explicitly [127, 128].

This chapter discusses a spatiotemporal model of plant-herbivore interaction based on the reaction-diffusion equation. The underlying non-spatial system includes a bottom-up regulation mechanism on species growth with increasing productivity, derived from the model of Koppel et al. [56]. We then use the diffusion phenomena [41] to undertake a spatiotemporal extension of the model, where herbivores' avoidance of the densely vegetated state is expressed in terms of cross-diffusion. The bottom-up control mechanism generates an alternative stable state of plant-dominated equilibrium point and creates bistability. In various real-world scenarios, bistability is observed theoretically [149, 150] and empirically [151]. However, only a few works address the effect of bistability in spatiotemporal models. Rodrigues et al. [152] studied a spatiotemporal predator-prey model with bistability in the underlying non-spatial system. They have observed the pattern formations in the bistable regime using numerical simulations dependent on initial conditions. The following issues, which were not previously addressed to the best of our knowledge, are our primary goals: (1) to incorporate the bottom-up control phenomenon in terms of cross-diffusion of herbivores, which elucidates herbivores' avoidance of highly vegetated regions, and to investigate whether it can be beneficial for the herbivore's persistence, (2) to investigate how the patterns may depend on the initial population distribution and

TABLE 3.1: Description of system parameters of (3.1) and their range of values [153]. We have considered generic units for biomass, length and time as $[M]$, $[L]$ & $[T]$, respectively.

Notation	Parameter definitions	Values	Units
r	Plant intrinsic growth rate	0 - 2.5	$[T^{-1}]$
K	Primary productivity level of the environment	0 - 50	$[M]$
c_{max}	Maximum food intake rate by herbivores	1	$[T^{-1}]$
a	Half-saturation constant of functional response	10	$[ML^{-2}]$
e_{max}	Conversion-efficiency of herbivores	0.45	-
b	Exponent of the reduced food conversion rate	0 - 0.04	$[M^{-1}]$
d	Linear death rate of Herbivores	0 - 0.2	$[T^{-1}]$

species diffusion for the bistable regime, (3) to investigate whether top-down control may arise in the plant-herbivore interaction with productivity gradient instead of bottom-up control.

3.2 Temporal model

There are two components in a reaction-diffusion model. The non-spatial dynamics resulting from birth and death processes and interactions between species at a particular site are covered in the reaction part. The diffusion component deals with the species' spatial mobility within a defined landscape. We explain the non-spatial system suggested by Koppel et al. [56] before exploring the full spatiotemporal dynamics. The non-spatial dynamics will be used to study the dynamics of the spatiotemporal system. The model used for the non-spatial system is a modification of the well-known Rosenzweig-MacAurther (RM) model and is represented by the following coupled nonlinear differential equations:

$$\frac{dP}{dt} = rP\left(1-\frac{P}{K}\right) - c_{max}\left(\frac{P}{a+P}\right)H, \tag{3.1a}$$

$$\frac{dH}{dt} = e_{max}\left(\frac{P}{a+P}\right)e^{-bP}H - dH. \tag{3.1b}$$

Here, P and H represent the plant and herbivore densities at time t. The plant has an intrinsic growth rate of r and grows logistically. The parameter K measures the system's productivity. At increased plant biomass, the interaction between herbivores and plants exhibits a saturation effect, represented by a Holling type-II response function. The maximum rate at which herbivores can consume plant biomass is denoted by c_{max}, and a is the plant biomass level where the consumption rate becomes

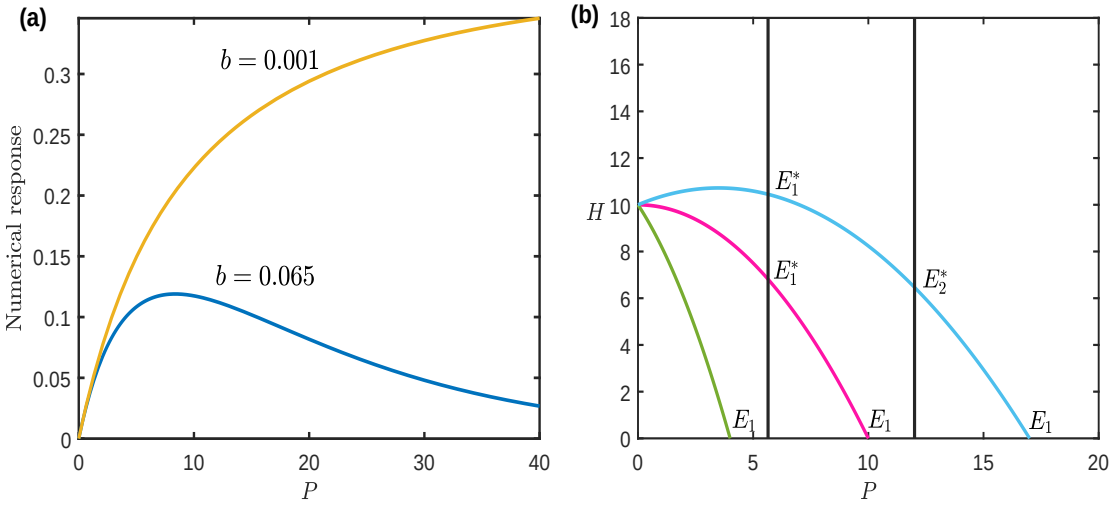

FIGURE 3.1: **(a)** Prototypical numerical response function ($e_{max}\frac{P}{a+P}e^{-bP}$) with respect to plant density (P) for different values of b. For the low value of $b(= 0.001)$, the response function is monotonic in the considered range of P and resembles the Holling type-II function. However, for a higher value of $b(= 0.065)$, the response function is nonmonotonic and attains its maximum at an intermediate plant density. **(b)** The nullcline analysis of the system (3.1) with different values of primary productivity, K. Black vertical lines are the herbivore nullclines, and the others are the plant nullclines at different productivity levels: $K = 4$ (green line), $K = 10$ (magenta line) and $K = 17$ (blue line). Equilibrium points are the intersection points of the two nullclines. Parameter values are $r = 1,\ c_{max} = 1,\ a = 10,\ e_{max} = 0.4,\ d = 0.1,\ b = 0.065$ [56].

half of c_{max}. In the absence of plants, herbivores die at a rate of d. The term $c_{max}\frac{P}{a+P}e^{-bP}$ is the per capita reproductive gain of the herbivore, called the numerical response, which, unlike Holling type II response function, is non-monotonic for high values of plant densities. In this numerical response function, $e_{max}e^{-bP}$ is the reduced conversion efficiency of the herbivore, which is an exponentially decreasing function of plant biomass [56], where b is the reduced conversion rate for lower digestion efficiency and $e_{max} \in (0, 1)$. The behaviour of the herbivore's response function for varied plant density for two values of b is shown in Figure 3.1a. A Holling type II curve is similar to the herbivore's numerical response when the b value is very small ($b = 0.001$) for a reasonable range of plant density. For higher values of b, in the same range of plant density, the numerical response curve increases first and then decreases (see the curve for $b = 0.065$). This figure suggests that the herbivores' growth is low at plant scarcity and abundance. It is maximum at an intermediate plant density, reflecting the plant's bottom-up control of herbivores.

The model (3.1) may attain at most four equilibrium points, depending on the parameter values: the trivial equilibrium $E_0(0,0)$, herbivore-free (semi-trivial) equilibrium point $E_1 = (K, 0)$, and two coexisting (non-trivial) equilibrium points $E^*_{1,2} = (P^*_{1,2}, H^*_{1,2})$, where the herbivore equilibrium levels are

$$H^*_{1,2} = \frac{r}{c_{max}} \left(1 - \frac{P^*_{1,2}}{K}\right)(a + P^*_{1,2}),$$

and the plant equilibrium levels $P^*_{1,2}$ are the positive solutions of the transcendental equation

$$e_{max} \left(\frac{P^*_{1,2}}{a + P^*_{1,2}}\right) e^{-bP^*_{1,2}} = d.$$

The equilibrium components of the coexistence equilibrium points are hard to express in a closed form of parameters as the equations are transcendental. Thus, with a variation of primary productivity (K), the distinct scenarios of the existence of equilibrium points are shown using nullcline analysis of the system (3.1) in Fig. 3.1b. This figure shows that the system has one herbivore-free equilibrium (E_1) but no nontrivial equilibrium at low productivity ($K = 4$). One coexistence equilibrium E^*_1 (where the magenta curve cuts the first herbivore nullcline) and one herbivore-free equilibrium E_1 (where the magenta curve meets the horizontal axis) exist at an intermediate level of productivity ($K = 10$). Two nontrivial equilibrium points (where the blue curve cuts both herbivore nullclines) and one herbivore-free equilibrium E_1 (where the blue curve meets the horizontal axis) exist when the productivity is high ($K = 17$). The herbivore nullcline suggests that the plant densities of the coexistence equilibrium point E^*_1 remain unchanged with the variation of the productivity level. Similarly, the plant densities of the equilibrium E^*_2, for higher values of K, remain unchanged when it exists. However, the plant density of the latter equilibria is always greater than that of the former. We call $E^*_1 = (P^*_1,\ H^*_1)$ as the low-vegetated coexistence state and $E^*_2 = (P^*_2,\ H^*_2)$ as the high-vegetated coexistence state (see Fig. 3.1 for $K = 17$).

The community matrix of the non-spatial system (3.1) at an arbitrary equilibrium point $\hat{E} = (\hat{P}, \hat{H})$ reads

$$\hat{J} = \begin{pmatrix} \hat{J}_{11} & \hat{J}_{12} \\ \hat{J}_{21} & \hat{J}_{22} \end{pmatrix}_{(\hat{P},\ \hat{H})},$$

where

$$\begin{aligned} \hat{J}_{11} &= r\left(1 - \frac{\hat{P}}{K}\right) - \frac{r}{K}\hat{P} - \frac{c_{max}\hat{H}}{a + \hat{P}} + \frac{c_{max}\hat{P}\hat{H}}{(a + \hat{P})^2}, \qquad \hat{J}_{12} = -\frac{c_{max}\hat{P}}{a + \hat{P}}, \\ \hat{J}_{21} &= -\frac{e_{max}\hat{H}(b\hat{P}^2 + ab\hat{P} - a)}{(a + \hat{P})^2} e^{-b\hat{P}}, \qquad \hat{J}_{22} = \frac{e_{max}\hat{P}}{a + \hat{P}} e^{-b\hat{P}} - d. \end{aligned} \tag{3.2}$$

The population extinction equilibria E_0 is inevitably unstable as the two eigenvalues r and $-d$ of the above community matrix evaluated at this equilibrium point are of opposite signs. The community matrix at the herbivore-free equilibria (E_1) has the eigenvalues $-r$ and $e_{max}\frac{K}{a+K}e^{-bK}-d$. Thus, E_1 may be a stable (node) or an unstable (saddle) equilibrium point depending on the sign of the latter eigenvalue. Note that when $K \to 0$, then the second eigenvalue becomes negative. The second eigenvalue remains negative giving stable E_1 in the intervals $K < K_{T_1}$ and $K_{T_2} < K$, where K_{T_1} and K_{T_2} are the roots of the transcendental equation $e_{max}\frac{K}{a+K}e^{-bK} = d$. E_1 becomes unstable in the interval $K_{T_1} < K < K_{T_2}$. K_{T_1} and K_{T_2} are the transcritical bifurcation points, where the E_1 equilibrium interchanges its stability with the new born coexistence equilibrium points E_1^* and E_2^*, respectively.

The community matrix at the coexistence state $E_{1,2}^*$ is

$$J^* = \begin{pmatrix} J_{11}^* & J_{12}^* \\ J_{21}^* & J_{22}^* \end{pmatrix}. \tag{3.3}$$

From (3.2), $J_{12}^* < 0$ and $J_{22}^* = 0$. Thus, $\mathrm{Tr}(J^*) = J_{11}^*$ and $\det(J^*) = -J_{12}^* J_{21}^*$. The coexistence equilibrium point will be stable if and only if

$$\mathrm{Tr}(J^*) < 0 \text{ and } \det(J^*) > 0, \tag{3.4}$$

implying $J_{11}^* < 0$ and $J_{21}^* > 0$. A Hopf bifurcation may occur around E_1^* when parametric conditions satisfy $J_{11}^* = 0$.

Figure. 3.2 provides a concise demonstration of the system's behaviour and the bifurcations that occur in the non-spatial system (3.1) in response to the gradual increment of the primary productivity (K) of the system. This one-parameter bifurcation diagram explains the changes from a monostable to a bistable state and the stability of the equilibrium points. The herbivore-free state is stable at low productivity ($K < K_{T_1} = 5.65$). Therefore, herbivores cannot survive in acute plant scarcity. A transcritical bifurcation at $K = K_{T_1}$ yields the coexistence state E_1^*. As the productivity exceeds K_{T_1}, the herbivore survives with plant biomass, stabilizing the coexistence equilibrium E_1^*. A further increase in K results in a new coexistence state E_2^* through another transcritical bifurcation at $K = K_{T_2} = 12.01$. However, the high-vegetated coexistence equilibrium point E_2^* is always unstable (see Fig. 3.2). The plant densities of the two coexistence equilibrium points, i.e., P_1^* and P_2^*, remains equal to the transcritical bifurcation points with respect to the carrying capacities, K_{T_1} and K_{T_2}, respectively.

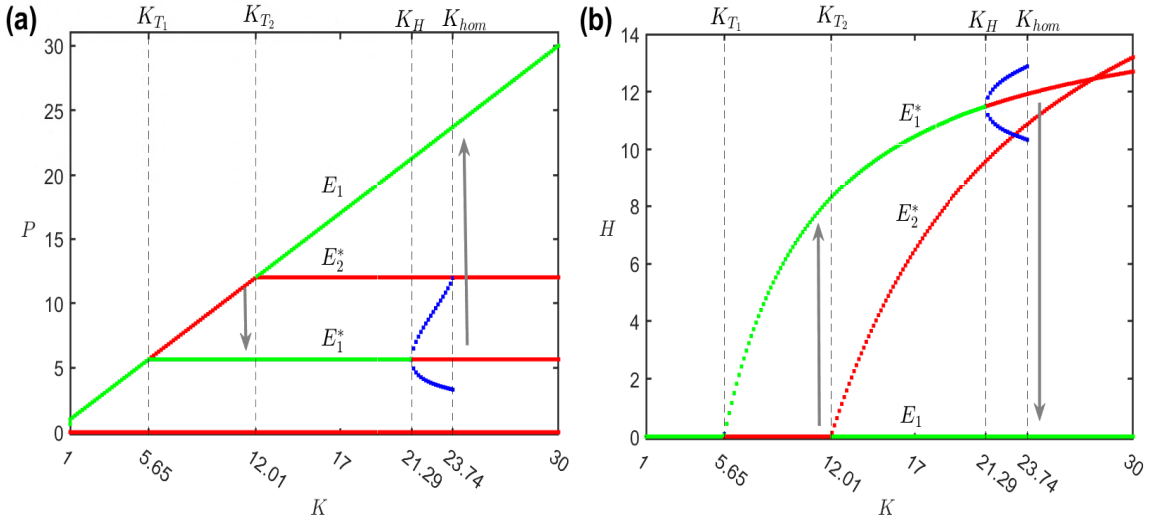

FIGURE 3.2: One-parameter bifurcation diagram with respect to productivity, K: **(a)** Bifurcation of plant-density, and **(b)** Bifurcation of herbivore density. Green and red dots represent the stable and unstable steady states. Blue dots are the amplitude of the stable limit cycle. Vertical dotted lines are the bifurcation points: K_{T_1} & K_{T_2} are the transcritical bifurcation points, K_H is the Hopf bifurcation point, and K_{hom} is the homoclinic bifurcation point. The upward (downward) arrow indicates a transition of species density from lower to higher (higher to lower) state as productivity increases (decreases). Parameter values are as in Fig. 3.1.

A bistability with stable herbivore-free state (E_1) and stable coexistence state (E_1^*) is seen in the interval (K_{T_2}, K_H). For E_1, herbivore goes to extinction and plant density increases with the increase in productivity. However, for E_1^* equilibrium, the herbivore population level increases in the same interval, keeping the vegetation level constant (see Figs. 3.2a, b). The former one is the plant-dominated bottom-up controlled state. The latter is the herbivore-dominated, top-down controlled state. Nevertheless, a Hopf bifurcation at $K = K_H = 21.29$ induces oscillations about the coexistence state E_1^* upon further increase of K. As productivity rises, the amplitude of the limit cycle approaches the unstable equilibrium E_2^* and collides with it. The limit cycle vanishes via a homoclinic bifurcation at $K = K_{hom} = 23.74$, and the system collapses to the only stable herbivore-free state E_1 for $K > K_{hom}$.

3.3 Spatiotemporal model

Allowing the species to diffuse in the space over time, the non-spatial model (3.1) becomes a spatiotemporal model, which reads

$$\begin{aligned}\frac{\partial P}{\partial t} &= rP\left(1-\frac{P}{K}\right)-c_{max}\left(\frac{P}{a+P}\right)H+D_p\nabla^2 P,\\ \frac{\partial H}{\partial t} &= e_{max}\left(\frac{P}{a+P}\right)e^{-bP}H-dH+D_h\nabla^2 H+D_{hp}\nabla^2 P.\end{aligned} \tag{3.5}$$

Here, P and H are functions of both time and space, instead of time only as it was in the non-spatial temporal model (3.1) and $\nabla^2 = \frac{\partial^2}{\partial x^2} + \frac{\partial^2}{\partial y^2}$ is the Laplacian operator. The terms D_p, D_h and D_{hp} are the diffusion coefficients of the species. The self-diffusion coefficient, D_p, describes how plants spread via lateral growth, or how seeds spread, referred to as vegetative propagation [121, 154, 155]. Either way, the spread will happen gradually, moving from densely vegetated to less densely vegetated regions in search of a better scope of proliferation. To prevent overcrowding and competition, herbivore species self-diffuse from high-density to low-density areas [30]. Obviously, D_h is larger than D_p since herbivores have higher spatial mobility than vegetation propagation. The effect of bottom-up control by the plants has its consequence on the spatial movements of the herbivores, where herbivores diffuse towards low-density plants. This relative dispersal of the herbivores with respect to plant density is incorporated using the cross-diffusion term (D_{hp}). This cross-diffusion rate is higher than their self-diffusion rate, giving $D_{hp} > D_h$. We consider D_{hp} positive because herbivores shift from a high to a low vegetated condition to avoid unfavourably high vegetated areas.

3.3.1 Turing instability

One species must diffuse more quickly than the other for self-diffusion to produce Turing patterns. Moreover, generating patterns requires an activator-inhibitor system [136]. Nevertheless, these conditions are not necessary if the cross-diffusion term appears in the system.

It is worth mentioning that the Turing patterns appear when a stable system is destabilized due to diffusion. We, therefore, concentrate on the interval (K_{T_1}, K_H), where the coexistence equilibrium is stable, for Turing instability analysis. The classical Turing instability is a linear analysis. So, we gave a small perturbation in space and time around the arbitrary equilibrium point $\hat{E}$ and linearized the system (3.5). The

perturbation terms, when expanded in spatial wavenumbers using a Fourier series representation, read

$$\Delta P(\vec{x},t) = \sum_{\vec{\omega}} C_\omega exp(\lambda t + i\vec{\omega}\vec{x}),$$
$$\Delta H(\vec{x},t) = \sum_{\vec{\omega}} D_\omega exp(\lambda t + i\vec{\omega}\vec{x}),$$

where C_ω, D_ω are non-zero coefficients of perturbation, λ is the frequency, and $\vec{\omega} = (\omega_1, \omega_2)$ is the wavenumber vector with $\omega = |\vec{\omega}|$. Substituting the above relations in (3.5) and neglecting the higher order terms, one obtains the linear system. Then the characteristic equation is given by

$$|J_\omega - \lambda I| = 0,$$

where $J_\omega = \hat{J} - \omega^2 D$, $\hat{J}$ is the community matrix corresponding to the non-spatial system, and $D = \begin{pmatrix} D_p & 0 \\ D_{hp} & D_h \end{pmatrix}$ is the diffusion matrix. On expansion, the characteristic equation may be expressed as

$$\lambda^2 - \mathrm{Tr}(J_\omega)\lambda + \Delta_\omega = 0,$$

giving the characteristic roots

$$\lambda_{1,2}(\omega) = \frac{1}{2}\left[\mathrm{Tr}(J_\omega) \mp \sqrt{\mathrm{Tr}(J_\omega)^2 - 4\Delta_\omega}\right],$$

where $\mathrm{Tr}(J_\omega) = \mathrm{Tr}(\hat{J}) - \omega^2(D_p + D_h)$ and $\Delta_\omega = \det(J_\omega) = D_p D_h \omega^4 - (D_h \hat{J}_{11} + D_p \hat{J}_{22} - D_{hp}\hat{J}_{12})\omega^2 + \Delta$, $\Delta = \det(\hat{J})$.

Turing bifurcation occurs when the steady state, which is stable in the absence of diffusion, undergoes a transition to instability in the presence of diffusion. In this case, heterogeneous species distribution over the space will occur, forming the Turing patterns. However, if the diffusion does not cause instability, population densities will remain homogeneous, as in the non-spatial system, and no patterns will appear.

The spatiotemporal system will remain stable if $\mathrm{Tr}(J_\omega) < 0$ and $\Delta_\omega > 0$. Since the stability of the non-spatial system guarantees that $\mathrm{Tr}(\hat{J}) < 0$ at the equilibrium $\hat{E}$, so

$$T(J_\omega) = \mathrm{Tr}(\hat{J}) - \omega^2(D_p + D_h) < \mathrm{Tr}(\hat{J}) < 0.$$

Thus, the equilibrium point might be unstable only if $\Delta_\omega < 0$. The determinant Δ_ω is the following quadratic polynomial in ω^2:

$$\mathcal{H}(\omega^2) = \Gamma\omega^4 - \Lambda\omega^2 + \Delta,$$

where $\Gamma = D_h D_p$, $\Lambda = D_h \hat{J}_{11} + D_p \hat{J}_{22} - D_{hp}\hat{J}_{12}$. A straight forward calculation expresses $\mathcal{H}(\omega^2)$ in the form

$$\mathcal{H}(\omega^2) = \left(\omega^2\sqrt{\Gamma} - \frac{\Lambda}{2\sqrt{\Gamma}}\right)^2 + \left(\Delta - \frac{\Lambda^2}{4\Gamma}\right).$$

The minimum value of $\mathcal{H}$ occurs when the first square term vanishes, giving $\omega^2_{min} = \frac{\Lambda}{2\Gamma}$ and the corresponding minimum value of $\mathcal{H}(\omega^2)$ is

$$\mathcal{H}(\omega^2_{min}) = \Delta - \frac{\Lambda^2}{4\Gamma}.$$

Thus, the Turing instability requires the condition $\mathcal{H}(\omega^2_{min}) < 0$. The critical wavenumber of Turing instability is $\omega^2_{cr} = \sqrt{\frac{\Delta}{\Gamma}}$ and the corresponding critical wavelength is $\lambda_T = \frac{2\pi}{\omega_{cr}}$. It can be easily observed that the range of the wavenumber for which the $\mathcal{H}(\omega^2) < 0$ is given by $\omega_1 < \omega < \omega_2$ where

$$\omega^2_{1,2} = \frac{\Lambda}{2\Gamma} \mp \frac{1}{2\Gamma}\sqrt{\Lambda^2 - 4\Gamma\Delta}.$$

Bounds of the wavenumber, ω_1 and ω_2 are real if $\Lambda^2 - 4\Gamma\Delta \geq 0$ which holds consequently with $\mathcal{H}(\omega^2_{min}) \leq 0$. The parametric conditions of Turing instability in terms of the model parameters are satisfied if

$$\mathrm{Tr}(\hat{J}) < 0,\ \Delta > 0 \quad \text{and} \tag{3.6a}$$

$$D_h \hat{J}_{11} + D_p \hat{J}_{22} - D_{hp}\hat{J}_{12} > 2\sqrt{D_h D_p \Delta}. \tag{3.6b}$$

The equilibrium point $\hat{E}$ is stable under the conditions (3.6a) when there is no diffusion, and the condition (3.6b) allows instability to occur in the presence of diffusion. The equality of the last condition gives the Turing bifurcation curve.

3.3.2 Identification of Turing regions in the parameter space

We identify the stability and instability regions in the parameter space, where heterogeneity in the population density prevails, causing the appearance of Turing patterns.

The parameter selection is based on two main factors. The first is the system's primary productivity, which evokes the bottom-up control mechanism at its high value. The second factor is the dispersal rate D_h of the herbivores based on the plant density relative to the cross-diffusion coefficient D_{hp}, which is considered to be the effect of bottom-up control of plants on the herbivores. To elucidate the impact of primary productivity and this relative dispersal rate of herbivores on the species dynamics and pattern formation, we performed the bifurcation analysis by simultaneously varying the parameters K and D_{hp}.

We set the parameter values as $r = 1,\ c_{max} = 1,\ a = 10,\ e_{max} = 0.4,\ d = 0.1,\ b = 0.065$ [56]. The self-diffusion coefficients are considered $D_p = 0.5,\ D_h = 5$. Figure. 3.3 illustrates the two-parameter bifurcation diagram, which provides a detailed picture of the parameter space, including the pattern-forming Turing instability caused by changes in the relative herbivore dispersal and productivity gradient. The range of the productivity parameter was chosen so that the non-spatial system remains stable around the coexistence equilibrium (see Fig. 3.2). The region within the two transcritical bifurcation points K_{T_1} and K_{T_2} is the monostable regime of the equilibrium E_1^*. Whereas the region $K_{T_2} < K < K_H$ is a bistable regime of the underlying non-spatial system, where both E_1^* and E_1 are stable. The parameter space is divided into five regions (R_1-R_5) by the Turing curves TC^* and TC_1 corresponding to the equilibrium points E_1^* and E_1 and the transcritical bifurcation curve $K = K_{T_2}$. In the presence of diffusion, the equilibrium E_1^* is unstable above the curve TC^* but stable below it. Conversely, the equilibrium E_1 is unstable above and stable below the curve TC_1. The curves TC^* and TC_1 are plotted using the equality sign in Eq. (3.6b) for the equilibrium points E_1^* and E_1, respectively. The stability classification of the equilibrium points E_1^* and E_1 in each of the five regions is provided in Table 3.2.

The equilibrium E_1^* is stable in the monostable area R_1, allowing the homogeneous plant and herbivore densities to continue with the population levels of the coexistence state of the non-spatial system even in the presence of diffusion. In the monostable region R_2, the Turing instability triggered by diffusion occurs around the coexistence equilibrium point E_1^*. The non-spatial system's herbivore-free state E_1 is always unstable in these two areas (see Table 3.2), so Turing instability is not an issue for this equilibrium point. But with high productivity ($K > K_{T_2}$), the alternative plant-dominated steady state E_1 is always stable in the absence of diffusion. So, there is a possibility that species diffusion could make it unstable along with the coexistence equilibrium E_1^*.

In the right side of K_{T_2}, three different regions R_3R_5 are observed corresponding to the spatiotemporal system. In R_3, both equilibrium points E_1 and E_1^* are stable in the presence of diffusion (see Table 3.2). Only E_1^* undergoes diffusive instability

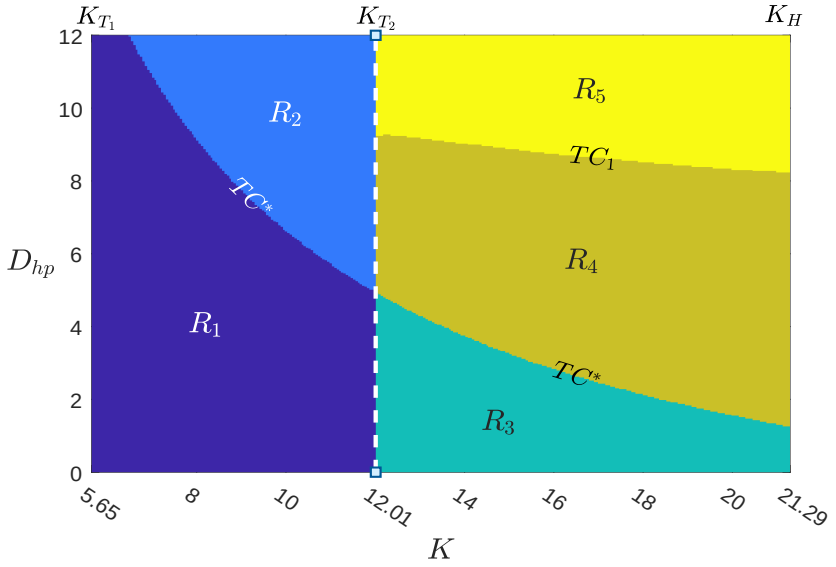

FIGURE 3.3: Two-parameter bifurcation diagram in K-D_{hp} plane. The white vertical dashed line is the transcritical bifurcation point K_{T_2} separating the monostable and bistable regime. The region (K_{T_1}, K_{T_2}) is monostable, where the equilibrium point E_1^* is stable, and the region $K > K_{T_2}$ is the bistable region, where E_1^* and E_1 both are stable. The curves TC^* and TC_1 are the Turing curves corresponding to the equilibrium E_1^* and E_1. Different regions of stability/instability of the spatiotemporal model (3.5) are denoted by R_1 to R_5. See Table 3.2 for the characterization of the regions. Parameter values are same as in Fig. 3.2 with $D_p = 0.5,\ D_h = 5$.

TABLE 3.2: This table describes the stability nature of the equilibrium points in each region $R_1 - R_5$ of Fig. 3.3, in the absence and presence of diffusion.

Region	Equilibrium points	Stability in the absence of diffusion	Stability in the presence of diffusion
R_1	E_1	unstable	unstable
	E_1^*	stable	stable
R_2	E_1	unstable	unstable
	E_1^*	stable	unstable (Turing)
R_3	E_1	stable	stable
	E_1^*	stable	stable
R_4	E_1	stable	stable
	E_1^*	stable	unstable (Turing)
R_5	E_1	stable	unstable (Turing)
	E_1^*	stable	unstable (Turing)

in the middle region R_4. However, in R_5, Turing instability occurs about both the

equilibrium points.

3.3.3 Patterns for different productivity gradients

Here, we show the patterns that arise from the productivity gradient while relative diffusion is constant. We select K from monostable and bistable regions and compare the generated patterns. It should be noted that Turing patterns are independent of the initial value in the monostable area. Although the spatiotemporal patterns may initially vary, they will display qualitatively similar patterns in the long run [156]. On the other hand, the patterns in the bistable area might be greatly influenced by the initial value. We simulate the spatiotemporal system (3.5) using Euler's method with a time step size of $\Delta t = 0.01$ and space step size $\Delta h = 1$, where five-point central difference discretization of the Laplacian operator is considered. We took non-negative initial value and Neumann boundary conditions with a spatial system size of 128×128 space units.

3.3.4 Patterns in the monostable state

In the monostable regions, we consider two primary productivity values: $K = 7$ and $K = 10$, keeping the dispersal rate constant at $D_{hp} = 8$. For low productivity, the point $(K, D_{hp}) = (7, 8)$ lies in the region R_1. So, the population densities remain homogeneous as in the non-spatial system, and no pattern is generated (see Fig. 3.4, top row). The heterogeneity appears in the population densities due to diffusion-driven (Turing) instability for the higher productivity ($K = 10$), as it belongs to the Turing region R_2 (Fig. 3.4, bottom row). Some spots with low vegetation appear in the dense vegetation (Fig. 3.4c). Since herbivores avoid dense plants, herbivore density will be low where plant density is high, causing opposite patterns in the herbivore density compared to the plant distribution patterns (Fig. 3.4d).

3.3.5 Patterns in the bistable state

The existence of two stable equilibrium points in the same parametric range ($12.01 < K < 21.29$) may impact the spatiotemporal dynamics of the system and related patterns. Consequently, the results of the bistable regime may not agree with the pattern selection and analysis methods for a monostable state [104]. The initial value determines the system dynamics and the associated patterns for a bistable system.

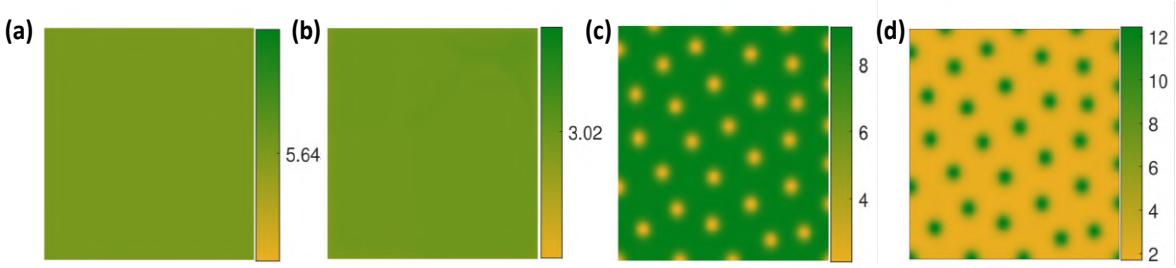

FIGURE 3.4: Snapshots of plant distribution (a, c) and herbivore distribution (b, d) for the productivities $K = 7$ (top row) and $K = 10$ (bottom row) at time $T = 10000$. The colour bars indicate the population density. The parameter values are as in Fig. 3.3 with $D_{hp} = 8$. A random initial value around the coexistence equilibrium point E_1^* are used.

As the equilibrium point E_1 is stable along with E_1^* in the bistable region, a diffusion-driven instability can also occur in the herbivore-free equilibrium point E_1.

We examined two qualitatively distinct sets of initial values: S_1 and S_2. The initial value S_1 is considered around the stable coexistence equilibrium E_1^* so that all random initial values remain inside the domain of attraction of E_1^*. The other initial value S_2 is selected around the unstable equilibrium E_2^* on the domain boundary of E_1^* to ensure that some of the randomly chosen initial values remain in the E_1^* domain of attraction and some lie outside, which is the domain of attraction of the other stable equilibrium point E_1 (See Fig. 3.5). Thus, the initial points considered are

$$(S_1): \quad P(\vec{x}, t=0) = P_1^* + \psi, \; H(\vec{x}, t=0) = H_1^* + \psi, \tag{3.7a}$$
$$(S_2): \quad P(\vec{x}, t=0) = P_2^* + \psi, \; H(\vec{x}, t=0) = H_2^* + \psi, \tag{3.7b}$$

where ψ is a random number chosen uniformly from the interval $(-0.5, 0.5)$.

Under initial conditions (S_1), patterns undergo a transition from a blend of stripes and spots of low vegetation to predominantly low-density vegetation with smaller patches of densely vegetated hot spots with increasing productivity (see Fig. 3.6, Top row). On the contrary, Fig. 3.6, bottom row, illustrates a noticeable change in vegetation patterns from cold spots in the dense vegetation to labyrinth patterns in the primarily low vegetated area with increasing productivity if the initial population levels are chosen as (S_2). Thus, the system may show different patterns due to distinct initial values even when the parameters remain identical. For example, when $K = 18$, the vegetation pattern for initial values S_1 shows hot spots and stripes amid low-density vegetated states, while hot labyrinth patterns are generated for the second set (S_2) of initial values.

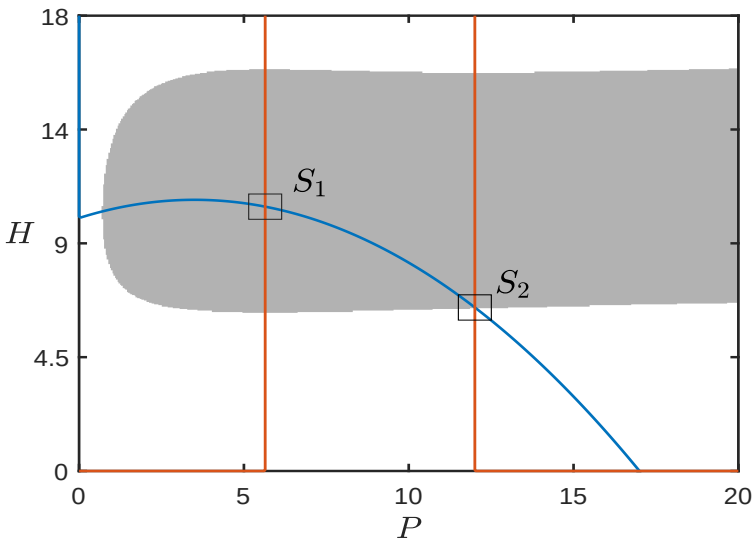

FIGURE 3.5: The phase plane shows the basins of attractions of the equilibrium points E_1^* (dark shaded) and E_1 (white region), respectively. Two sets of initial conditions are shown by two black-coloured rectangular areas, where S_1 corresponds to initial condition (3.7a) and S_2 corresponds to initial condition (3.7b). Red and blue curves are the predator and prey nullclines for $K = 17$. The rest of the parameters are in Fig. 3.3.

For each of the two sets of initial values, we plotted the population distributions at each spatial grid at various time steps (Fig. 3.7) for two different relative dispersal rates of herbivores, D_{hp}= 6 and 8, with fixed productivity level $K = 18$. When $D_{hp} = 8$, the blue dots in the phase space at time $T = 10$ units for the initial condition S_1 indicate that the population densities are slightly dispersed from the equilibrium value E_1^*. Still, all lie in the domain of attraction of E_1^* (see Fig. 3.7a). This implies that the population densities in all the 128×128 spatial grids vary slightly from their initial values when the system's evolution time is short. At the same time, the initial set S_2 exhibits concentrated populations around the equilibrium point E_2^* in the phase plane, suggesting that the population concentrations are nearly uniform to the initial densities across all grids and fall into the domains of attraction of E_1^* and E_1 (see Fig. 3.7c). After a long time ($T = 10000$ units), population densities in the grids are heterogeneous with a steady state, and the population distribution in both situations appears comparable in the phase plane and spread in both basins of attraction (Figs. 3.7b,d). However, the corresponding spatial patterns that evolved from the two distinct initial conditions are very different, as shown in Fig. 3.6 for $K = 18$. In contrast, when the cross-diffusion value is low ($D_{hp} = 6$), the blue dots in the phase plane at time $T = 10$ units for both the initial conditions are concentrated around the respective coexistence equilibrium values (Figs. 3.7e,g), but eventually, both shift to the equilibrium state E_1 (Figs. 3.7f,h). This shows that there will be

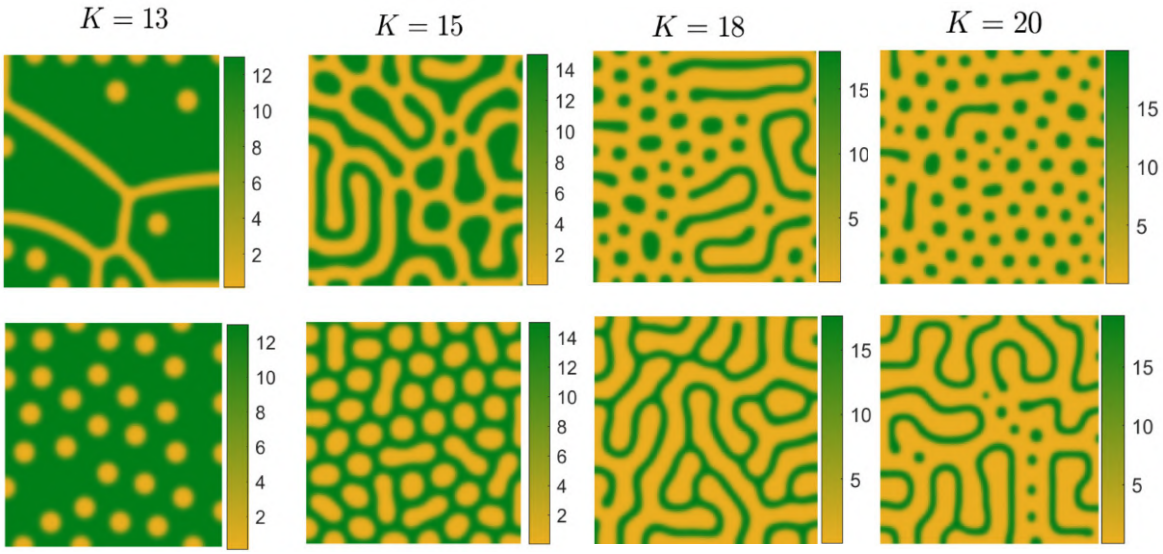

FIGURE 3.6: Snapshots of plant distribution ($P(\vec{x}, t)$) of simulation of the spatiotemporal system (3.5) for productivity level $K = 13$ to 20 and initial conditions (3.7a), (3.7b). The density level of vegetation is shown using the colour bars. **Top row**: Patterns generated from initial conditions S_1 of Fig. 3.5. **Bottom row**: Patterns generated from initial conditions S_2 of Fig. 3.5. These figures demonstrate that the system shows distinct patterns for two initial values but the same productivity. The snapshots are taken at $T = 10000$. Parameter values are as in Fig. 3.3 with $D_{hp} = 8$.

no herbivores in the domain, and the biomass of plants will be distributed uniformly at the equilibrium density of $E_1(K, 0)$.

In addition to the spatial distribution of species, the spatiotemporal scenario allows the observation of each species' population level in terms of its spatial means. A greater or lesser mean population density accordingly signifies a better or worse situation for the particular species. Since a transition from monostable to bistable regime occurs at the bifurcation point K_{T_2} for the non-spatial system (3.1), it is important to observe the transition at the same point in the corresponding spatial system. To observe the nature of transition in mean values of the population levels, we continue the simulation of the system (3.5) with initial value S_1 by varying the parameter K in the range $[6, 21.25]$ for three D_{hp} values: $7, 8, 10$ (see Fig. 3.8).

For each value of D_{hp}, the population densities of both species remain the same for the non-spatial and spatiotemporal systems till the productivity crosses the Turing bifurcation value. The mean population densities of the plant of the spatial model

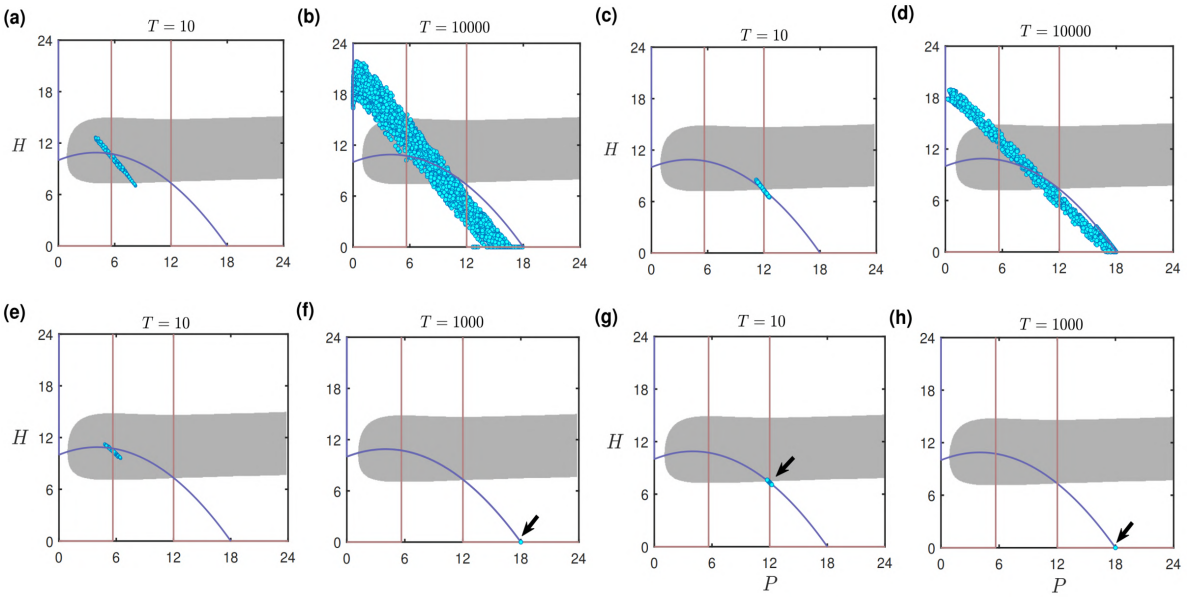

FIGURE 3.7: Population distributions at different time steps for herbivores' high relative dispersal $D_{hp} = 8$ (a, b, c, d) and low relative dispersal $D_{hp} = 6$ (e, f, g, h) for the two initial conditions. Initial condition considered for Figs. (a,b,e,f) is S_1 and for Figs. (c,d,g,h) is S_2 of Fig. 3.5. The rest of the parameter values are in Fig. 3.6. See the text for explanations of these figures.

then increase with increasing K and then decrease when $D_{hp} = 8$ (Fig. 3.8, top). The mean plant biomass is much lower at $K = 21.29$ than that of the homogeneous steady state of the non-spatial system. However, the spatial model's mean population densities of herbivores decrease after crossing the Turing bifurcation point and then increase with increasing K (Fig. 3.8, bottom). The mean herbivore density is much higher than that of the homogeneous steady state of the non-spatial system for $K = 21.29$. A similar behaviour is observed in the plant and herbivore densities for $D_{hp} = 10$. The spatial system's mean population densities drastically change for the low cross-diffusion rate, $D_{hp} = 7$. Even though the system starts with the initial values around the coexistence stable state, E_1^*, the herbivore population declines after crossing the Turing critical value and eventually becomes extinct after crossing the bifurcation point K_{T_2} (Fig. 3.8, bottom). The plant density eventually reaches its maximum level, K (Fig. 3.8, top).

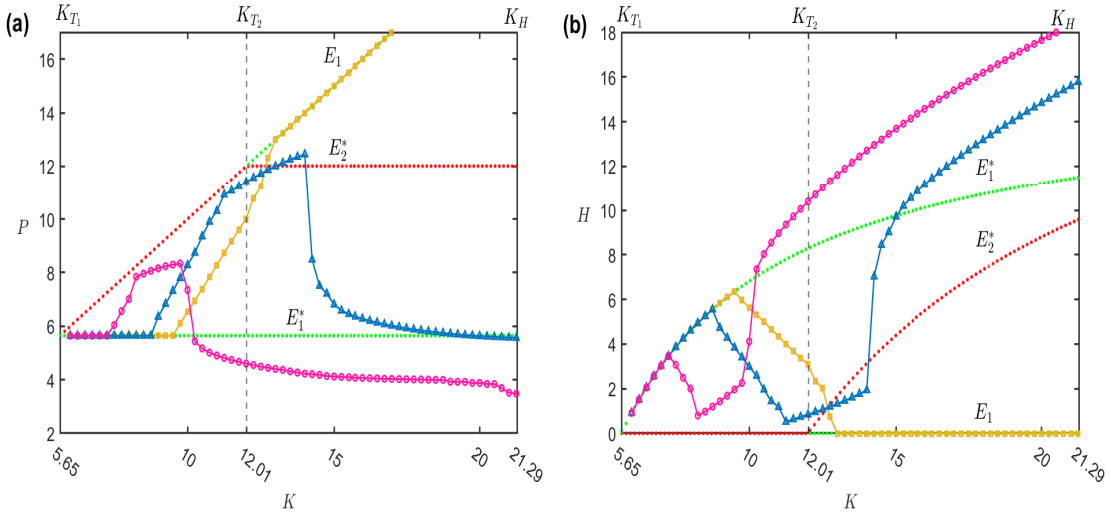

FIGURE 3.8: These figures show the mean population densities of vegetation (a) and herbivores (b) of the spatiotemporal model (3.5) at $T = 10000$ with increasing productivity for three values of D_{hp}: 7 (yellow line), 8 (blue line), and 10 (magenta line). Green and red dots represent the non-spatial system's stable and unstable steady states, as in Fig. 3.2. The parameter values are the same as in Fig. 3.6, and the initial value is S_1.

3.3.6 Patterns for relative dispersal of herbivores

The transition of vegetation pattern is observed here with a change of herbivores' relative dispersal rate or the cross-diffusion coefficient D_{hp}. The herbivores tend to avoid densely vegetated regions to avoid competition and increased probability of predation. Due to the herbivores' avoidance, vegetation grows in this area, and tiny spots of dense vegetation eventually appear. Patterns in the Turing region are observed with increasing values of the cross-diffusion coefficient when primary productivity remains fixed at $K = 10$ (Fig. 3.9). A cold-spotted vegetation pattern, where plant density is low, is shown for $D_{hp} = 8$ (see Fig. 3.9a). In the case of $D_{hp} = 10.5$, a labyrinth pattern of low-density vegetation emerges (see Fig. 3.9b), which becomes high-density labyrinth with increased cross-diffusion value $D_{hp} = 11.5$ (Fig. 3.9c) with comparatively scant vegetated areas, which is conducive for herbivore grazing. Smaller patches of isolated dense vegetated spot patterns, along with some stripes, emerge when $D_{hp} = 13.5$ (Fig. 3.9d).

We compared the mean plant and herbivore densities with the homogeneous steady-state population densities for the spatiotemporal system for the change of the herbivores' cross-diffusion (see Fig. 3.10). With an increase in D_{hp}, the mean plant density

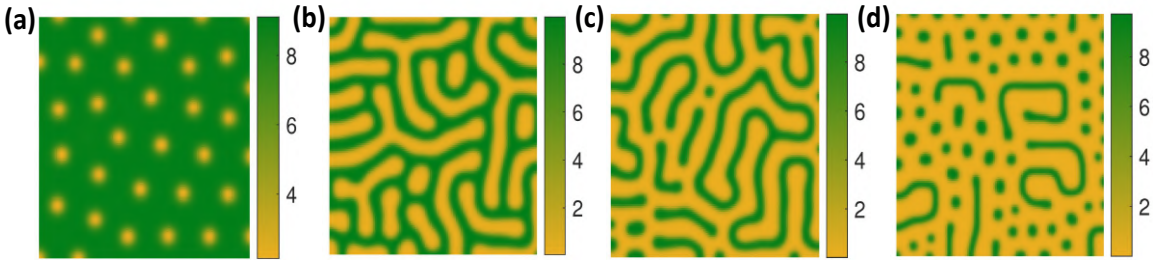

FIGURE 3.9: Snapshots of plant distribution ($P(\vec{x}, t)$) of the spatiotemporal system (3.5) taken at $T = 10000$ for different values of D_{hp} with initial conditions (S_1). (a) $D_{hp} = 8$, (b) $D_{hp} = 10.5$, (c) $D_{hp} = 11.5$, (d) $D_{hp} = 13.5$. The density level of vegetation is shown by the colour bars. Parameter values are $K = 10$, and the rest are the same as Fig. 3.3.

first rises and then falls. For herbivores, the situation is the opposite. Thus, the cross-diffusion coefficient of herbivores can be seen as herbivores' avoidance towards highly vegetated states. When the cross-diffusion increases further, the mean herbivore density rises above the homogeneous steady-state density of the non-diffusive system. In contrast, the mean plant density is much lower than in a similar non-spatial system.

3.4 Discussion

This work intends to assess a spatiotemporal plant-herbivore interaction model and self-organized pattern formations due to their non-spatial interaction and dispersal. The non-spatial interaction is based on the model of Koppel et al. [56], demonstrating a bottom-up control mechanism at higher productivity and generating bistability with a coexistence state and herbivore-free equilibrium state. The empirical and theoretical investigation on a local scale showed a high herbivore population at the intermediate vegetated states rather than the high vegetated state [56]. There was, however, no extensive observation regarding the spread of the species. We extended the non-spatial model presented in [56] and made it a spatiotemporal model by incorporating a diffusion process of both species. A self-diffusion is considered for both species, where the species moves from higher to lower densities. According to the bottom-up control in plant-herbivore interaction, herbivore's fitness optimizes at an intermediate plant density [56]. So, herbivores move from higher to lower plant-density areas, permitting us to consider a cross-diffusion term in the herbivore rate equation. This extension of the non-spatial system to the spatiotemporal system allows us to depict the species' large-scale spatial distribution and explain the heterogeneity and pattern formation over time and space as observed in many natural systems [30].

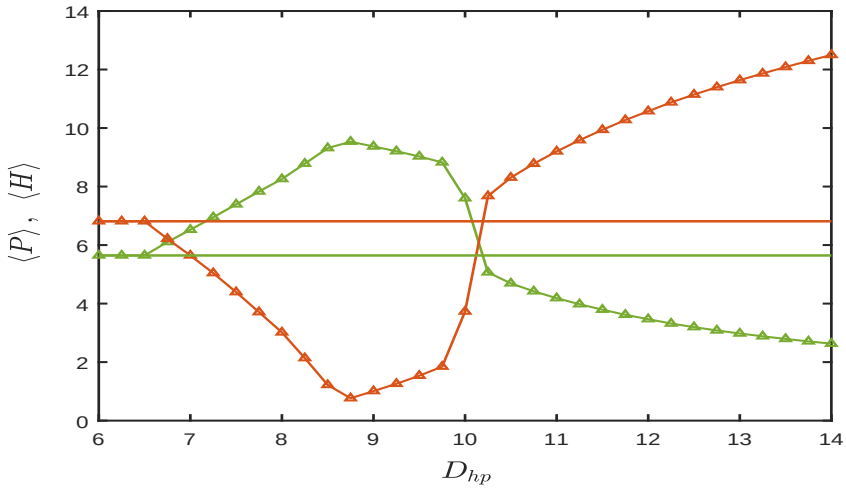

FIGURE 3.10: Mean population densities of plants (green curves) and herbivores (red curves) of the spatiotemporal system (3.5) at $T = 10000$ for the variation of the cross-diffusion, D_{hp}. The curves with markers denote the mean population densities in presence of diffusion. The curves without markers denote mean population densities in absence of diffusion which is, as expected, equal to the respective homogeneous steady state values. Parameter values are the same as in Fig. 3.9.

A predator-prey system usually shows a paradox of enrichment, which states that the predator population increases due to the enrichment of the system, keeping the prey population constant [107, 157]. The coexistence equilibrium becomes unstable, and both populations oscillate as the system enriches. The amplitude of oscillations grows with the increasing enrichment and becomes extinct due to environmental noise when the oscillatory population is close to zero. These are the typical behaviours of a predator-prey model that follows the paradox of enrichment phenomenon [158, 159]. The considered plant-herbivore (prey-predator) non-spatial model exhibits similar behaviours with increasing productivity. The plant density remains too low at the low productivity. The herbivore population cannot sustain itself when productivity is low, causing the herbivore-free equilibrium E_1 to be stable. As the productivity crosses the lower threshold value K_{T_1}, the plant biomass can support the herbivores and their population grows with the increasing productivity, keeping the plant density constant (see Fig. 3.2), referred to as the herbivore-dominated top-down controlled state. The low-vegetated coexistence equilibrium remains stable till a Hopf bifurcation occurs at $K = K_H$. Noticeably, the herbivore density increases with the productivity in the range $K_{T_1} < K < K_H$ but not the plant density, which is similar to the paradox of enrichment phenomenon. Both plants and herbivores begin to oscillate with increasing amplitude when productivity exceeds K_H.

A further increase in productivity sends oscillatory populations to extinction. This extinction, however, does not follow the paradox of enrichment theory. Here, the amplitude of oscillations remains far away from the horizontal axis, so environmental noise cannot be the reason for the population extinction. From a dynamical viewpoint, it happens due to the occurrence of a homoclinic bifurcation at $K = K_{hom}$, where a stable limit cycle colloids with an unstable equilibrium point (E_2^* here), causing sudden disappearance of both the species. In a bistable system, some alternate state exists where the system may shift after a homoclinic bifurcation. In our case, the system experiences a critical transition from an oscillatory coexistence of plants and herbivores to the alternate stable herbivore-free state (E_1) after the collision. In this situation, the entire domain is covered with dense plants of homogeneous density.

We prescribed the analytical conditions for diffusion-driven (Turing) instability and used them to plot the stability and instability regimes of the spatiotemporal system in the parametric plane of primary productivity and relative diffusion rate of herbivores. Since the non-spatial system needs to be stable for the existence of the Turing instability in the spatial system, we considered the productivity range in $K_{T_1} < K < K_H$, where the non-spatial system attains at least one stable coexistence equilibrium E_1^*. The Turing curve separates the $K - D_{hp}$ parametric plane into Turing and homogeneous steady state regimes, and the bifurcation curve K_{T_2} separates the entire plane into monostable and bistable regimes (Fig. 3.3). For a Turing pattern to exist, the relative herbivore diffusion rate decreases with increasing productivity. Also, the relative herbivore diffusion rate in the monostable range should be much higher than that for the bistable range. In the monostable regime, some (cold) spots with low vegetation are observed in predominantly dense vegetation. Since the herbivores avoid the highly vegetated locations, their density remains sparse in most areas except at some points where vegetation is relatively low, resulting in hot spots of high herbivore density (see Fig. 3.4d). It is to be mentioned that the distribution of plants and herbivores has a negative correlation with their population densities, so their densities will be opposite. This finding to some extent agrees with the conclusions of [56], which show that higher herbivore is found in intermediate vegetation stages rather than in regions with higher plant density.

In the non-spatial system's bistable regime, diffusion-driven Turing instability analysis is inconclusive since this analysis is merely a local stability analysis around a monostable equilibrium point. Our simulation results revealed that the bistable regime's dynamics and corresponding patterns are initial value dependent (see Fig. 3.6). The system shows contrasting patterns for the same set of parameter values but different initial values due to bistability. Such initial value-dependent patterns do not occur in the monostable state. The long-term patterns in the monostable Turing state will be similar, although short-term patterns may differ.

For higher relative diffusivity, both species may coexist heterogeneously over the entire domain when the initial species distribution is considered within or outside of the basin of the coexistence state (Fig. 3.7). In contrast, Rodrigues et al. [152] found that two coexistence equilibriums are stable without diffusion in a generalist predator-prey model. The self-diffusion of species causes one of the bistable equilibrium points to become unstable but does not cause any instability in the other. It was demonstrated that the system jumps to the stable equilibria and produces a homogeneous distribution when the initial values are taken from the basin of the diffusion-induced unstable equilibria. However, this is different in our system if the relative dispersal rate is high. In this case, both species coexist heterogeneously over space instead of converging to the alternate stable equilibrium state E_1. On the contrary, if the relative dispersal rate is low, the system converges to the alternate steady state E_1. Here, the dense plant biomass is uniformly distributed throughout the domain, and the herbivores are extinct due to fitness reduction at high plant density. In this sense, that switching occurs between two stable equilibrium points, the observation is similar to that of [152].

The patterns cannot provide information about the species' overall population levels within the considered domain. Estimating the spatial mean population densities with the change in productivity and relative herbivore spread is therefore crucial. It is revealed that if productivity is low and stays below the Turing critical value, the mean population density will remain unchanged with the non-spatial system's equilibrium value (see Fig. 8). The occurrence of increased plant density and the related suppression of herbivore density, following the bottom-up control by plants, is observed for all values of relative herbivore dispersal as the productivity crosses the Turing critical value. However, bottom-up control is replaced by top-down control, where a higher herbivore population dominates over the plant density, with increasing productivity provided the relative dispersal rate of herbivores is high. This observation contradicts the result of the non-spatial system, which states that herbivore density is low when productivity is high [56]. Thus, non-spatial system dynamics, which show local interaction behaviour, may differ from their spatial counterpart, which describes system behaviour on a larger spatial scale, allowing species to disperse and interact simultaneously. Experimental observations of Jia et al. [116] reported such top-down control in terrestrial plant-herbivore interactions. On the other hand, when the relative dispersal rate is low, plant density rises with productivity. As fitness declines at high plant density, the population of herbivores steadily declines, leading to the eventual extinction of herbivores, supporting the bottom-up control as observed in [56].

Our study replicates different vegetation patterns observed empirically. The work also demonstrates the impact of bistability on spatiotemporal system dynamics and pattern formation. The non-spatial results might not be valid when species dispersal

is considered. The non-spatial study suggests that the herbivore's density may not decrease at higher productivity but reduces following the bottom-up control mechanism. Our spatial analysis reveals that this observation is also valid in the spatial system if the relative dispersal of the herbivores is low. But, if the relative dispersal of the herbivores is high, then the observation of the spatial system is invalid. Instead, top-down control is established with increasing productivity, and the herbivore population dominates the plant density. Our research provides a theoretical framework for the spatiotemporal distribution of plants and herbivores and clarifies the circumstances in which a different control mechanism in plant-herbivore interaction may be observed.

There are scopes for further modifications in the model system. For example, herbivore populations vary seasonally, affecting the plant-herbivore interaction. The availability of plant foliage depends on the season. During the wet season, green foliage becomes more abundant compared to dry time, when defoliation is more intense, affecting the community composition [160]. It is, therefore, essential to consider the seasonal effect in the model and unveil the non-spatial and spatial dynamics. Field and experimental observations suggest that herbivores select their food based on the nutritional value and body size for optimal foraging [161]. Classifying the herbivore population depending on the body size and modifying their predation function by explicitly incorporating their food preferences is necessary. This will increase the system dimension to three or higher but make the model more realistic. In arid and semi-arid ecosystems, soil-water infiltration and vegetation growth create a positive feedback loop of mutual facilitation through diffusion. So, another potential modification to the model system could be done by incorporating the density of soil water and monitoring the effects of rainfall and infiltration feedback [162] on the transitions between vegetation and herbivore densities, as well as the patterns that result from these changes.

Chapter 4

Multiscale vegetation patterns in drylands: A two-layer reaction-diffusion model with phenotypic plasticity

4.1 Introduction

In arid and semi-arid regions, where water is limited and rainfall is scarce, vegetation patterns emerge as a result of self-organizing ecological processes driven by complex feedbacks between plants and soil moisture. These landscapes serve as natural laboratories for exploring how vegetation adapts to harsh environmental conditions through ecohydrological interactions that optimize biomass production [163]. Field studies have uncovered remarkable spatial vegetation patterns, from isolated plant clusters [164] and continuous vegetation bands [165] to the striking "fairy circles" found in the Namib and Australian deserts [57, 73]. Once considered anomalies, these formations are now recognized as emergent outcomes of plant-soil water feedbacks shaped by stress, competition, and adaptation [166]. They promote spatial heterogeneity, resource sharing, and ecological resilience, highlighting the remarkable adaptability of life under extreme climatic stress.

A key driver of this adaptability is phenotypic plasticity, the ability of plants to alter their form and function in response to environmental cues [66, 67, 68]. Among its manifestations, root system plasticity is particularly vital in water-limited environments. By changing root length, density, and branching, plants expand their access

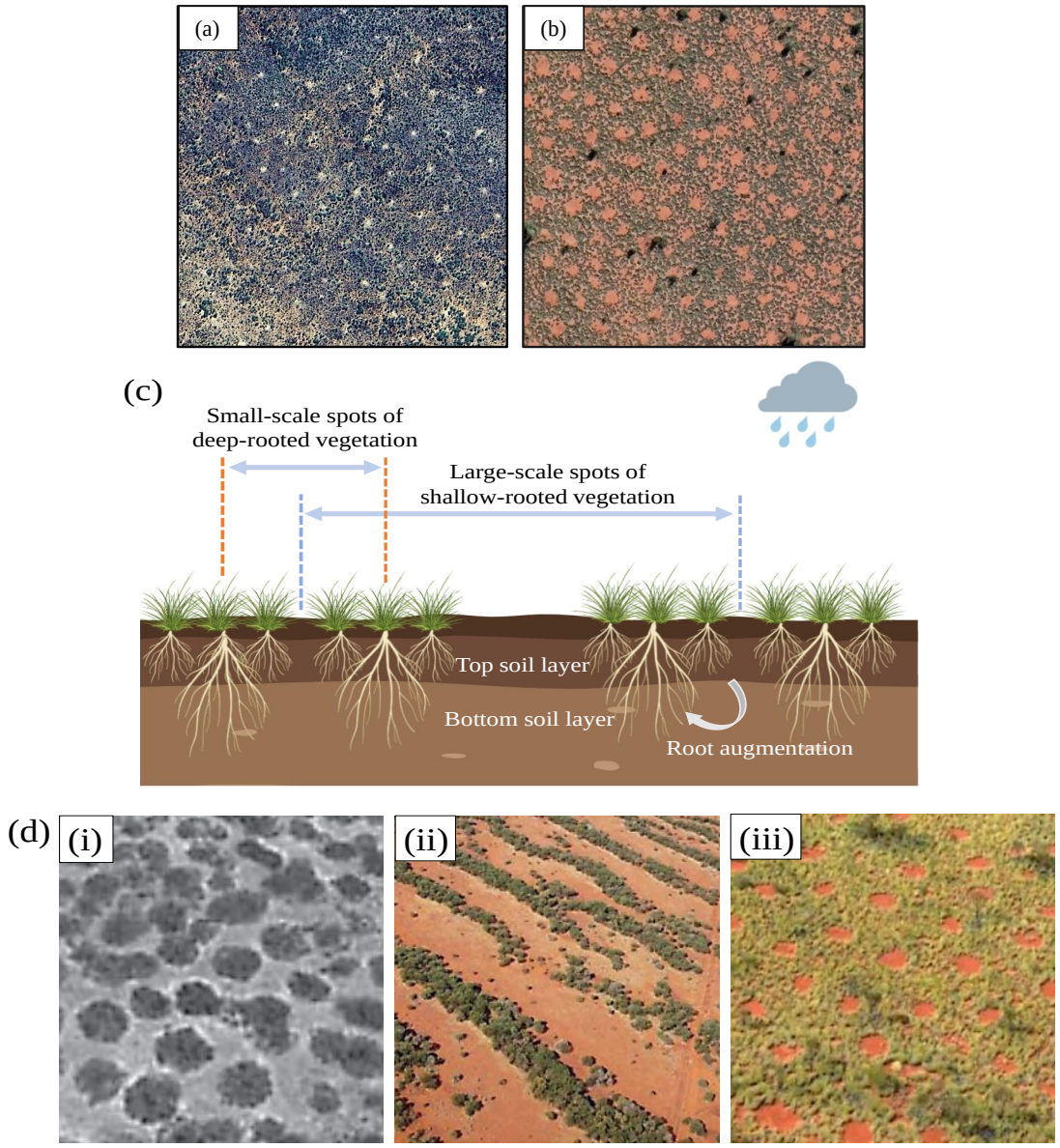

FIGURE 4.1: Examples of some regular vegetation patterns across different regions of the world. Snapshots are taken from Google Earth Web. The regions and coordinates are: (a) Namibia, 23°25'11"S 119°50'20"E, (b) Australia, 20°07'13"S 16°15'11"E. **(c)** Schematic diagram of multi-scale arrangement, where shallow rooted plants create large scale self-organization and deep-rooted plants create small-scale self-organization. **(d)** Combination of large-scale cold-spot and small-scale hot-spot (i), large-scale stripe, small-scale hot-spot (ii), large-scale hot-spot and small-scale hot-spot (iii), taken from [167].

to water and nutrients, improving competitiveness under hydric stress [168]. One essential form of this response is hydrotropism, the directional growth of roots toward

moisture-rich zones—a phenomenon widely observed across plant species [69]. This behavior is especially important in vertically layered soils, where moisture tends to accumulate at depth. Walter's two-layer hypothesis [70, 71] offers a valuable framework that proposes coexistence of different plant species arise from vertical soil moisture partitioning: shallow- and deep-rooted species access different water niches, thereby reducing direct competition and enhancing community stability.

Mathematical modeling of vegetation patterns has traditionally employed reaction-diffusion or integro-differential systems to describe the interplay between local plant growth and spatial dispersal [57, 58, 59, 26]. These models, often based on Turing's instability framework [41], explain how spatial structures like spots and stripes can emerge spontaneously from uniform conditions. However, many ecosystems exhibit multiscale patterns—nested or overlapping structures at different spatial resolutions [169, 64]. Recent studies emphasize that such complexity can be overlooked without explicit multiscale analysis [170, 171, 62]. For example, Bennett et al. [62] observed in Namibia that large barren zones coexist with smaller vegetated patches, forming hierarchical structures suggestive of nested self-organization [61, 60, 171].

Interestingly, multiscale pattern formation is not unique to ecological systems. Analogous behavior has been observed in layered chemical systems, where differences in diffusion rates across stacked layers lead to complex structures like superlattices and "white-eye" patterns via interactions between Turing and wave instabilities [64, 172, 173]. Similarly, Huang et al. [65] reported nested plankton distributions in thermally stratified aquatic systems using models with gradient-dependent interlayer coupling. In the limit of weak coupling, they identified a coexistence of distinct spatial patterns, including hexagons and stripes, through weakly nonlinear analysis. These findings highlight the universal role of multiscale interactions across natural systems.

Building on this work, Bennett et al. [62] developed a sophisticated integro-differential model incorporating phenotypic plasticity and stratified soil moisture to explain multiscale patterns in the dominant grass Stipagrostis in the Namib Desert. Extending this perspective, our study demonstrates that individual-level plant adaptations, when coupled with environmental stratification, can also generate multiscale vegetation patterns. Unlike prior chemical models that rely on simplified interlayer gradients [64, 172, 65], our model incorporates empirically grounded biophysical processes observed in arid ecosystems [163, 167, 62, 171]. We use a more tractable modeling approach based on coupled reaction-diffusion equations inspired by Hardenberg et al. [57], offering a mechanistically clear yet ecologically rich framework for understanding multiscale vegetation dynamics.

The remainder of this chapter is as follows: Section 4.2 and 4.3 deals with dynamics of single layer model with monoscale vegetation pattern formation dynamics with linear

and weakly nonlinear analysis. Section 4.4 proposes idealized theoretical framework of two-layer vegetation model and this model is improved into a more realistic model and analyzed in section 4.5.

4.2 Analysis of single-layer vegetation model

Let P and W denote the plant biomass and soil water concentration, respectively, at a spatiotemporal point $(\vec{x}, t)$. The following non-dimensionalized coupled reaction-diffusion equations, proposed by Hardenberg et al. [57], describe the single-layer vegetation model with uniform root structures:

$$\frac{\partial P}{\partial t} = \frac{\gamma W}{1+\sigma W} P - P^2 - \mu P + D_1 \nabla^2 P, \tag{4.1a}$$

$$\frac{\partial W}{\partial t} = r - (1-\rho P)W - W^2 P + D_2 \nabla^2 (W - \beta P). \tag{4.1b}$$

Plant water uptake is modeled using a saturating function characterized by a half-saturation constant of $\frac{1}{\sigma}$, and a maximum uptake rate of $\frac{\gamma}{\sigma}$. Plant mortality consists of two components: a natural death rate proportional to the biomass, represented by $-\mu P$, and an intraspecific competition term, represented by $-P^2$. Water enters the system at a constant precipitation rate r, and is lost through two main pathways: plant uptake at a rate of $W^2 P$, and evaporation at a rate of $(1-\rho P)W$, where the parameter ρ accounts for the reduction in evaporation due to plant shading. Plant biomass spreads spatially via vegetative propagation, moving toward regions of lower biomass. This diffusion process is governed by the coefficient D_1. Soil water also diffuses, driven by both self-diffusion (with coefficient D_2) and cross-diffusion (represented by $-\beta D_2$), the latter modeling root-induced suction that draws water toward regions with higher plant density. For further details on the structure of the model, readers are referred to [57]. In this formulation, a flat terrain is assumed, and topographic effects such as slope-induced water runoff are excluded.

4.3 Monoscale pattern formation mechanism: Linear and weakly nonlinear analysis

The system (4.1) can be expressed in the vectorized form as:

$$\frac{\partial \vec{X}}{\partial t} = \vec{F}(\vec{X}) + D\nabla^2 \vec{X}, \tag{4.2}$$

where $\vec{X} = (P, W) \in \mathbb{R}^2_+$ is the vector of densities of two interacting agents $P(\vec{x}, t)$ and $W(\vec{x}, t)$ at the position vector $\vec{x} = (x, y)$ at time t. The local rate of change of the interacting species is defined by the rate function vector $\vec{F} = (f, g)^T$, where $f, g : \mathbb{R}^2 \to \mathbb{R}$ and $f, g \in \mathcal{C}^1(\mathbb{R})$. The spatial mechanism follows the diffusion process represented by the diffusion coefficient matrix

$$D = \begin{pmatrix} D_1 & 0 \\ -\beta D_2 & D_2 \end{pmatrix}.$$

4.3.1 Linear stability analysis

Turing instability and the resulting spatially periodic heterogeneity arise in system (4.2) when a spatially non-uniform perturbation, corresponding to a specific wave mode, grows over time due to the presence of a positive eigenvalue of the variational matrix of the system (4.2) evaluated at the uniform steady state. To identify these unstable modes, we linearize the system around its spatially uniform steady state, denoted by $\vec{X}^* = (P^*, W^*)$, which corresponds to the equilibrium of the non-diffusive system (i.e., when $D_1 = D_2 = 0$). Small spatiotemporal perturbations around this equilibrium are then expressed in the form of a generalized Fourier series as:

$$P(\vec{x}, t) = P^* + \sum_k P_k e^{\lambda(k)t + j\vec{k}\vec{x}}, \quad \text{and} \quad W(\vec{x}, t) = W^* + \sum_k W_k e^{\lambda(k)t + j\vec{k}\vec{x}}, \tag{4.3}$$

where P_k and W_k's are constant coefficients corresponding to the spatial wavemode $e^{j\vec{k}\vec{x}}$ ($j = \sqrt{-1}$) with wavenumber $k = |\vec{k}| = \sqrt{k_x^2 + k_y^2}$. Plugging perturbation terms (4.3) into (4.2), the following eigenvalue problem of different spatial wavemodes k is obtained:

$$\begin{aligned} & |J - \lambda(k) I_{2\times 2} - k^2 D| = 0 \\ \text{or,} \quad & \prod_{j=1,2} \left(J_{jj} - D_j k^2 - \lambda\right) - J_{12}\left(J_{21} + \beta D_2 k^2\right) = 0 \\ \text{or,} \quad & \mathcal{P}(\lambda) = \lambda^2 - \sum_{i,j=1,2} (J_{jj} - D_j k^2)\lambda + \prod_{j=1,2} \left(J_{jj} - D_j k^2\right) - J_{12}\left(J_{21} + \beta D_2 k^2\right) = 0, \end{aligned} \tag{4.4}$$

where $J = (J_{ij})_{2\times 2}$ is the Jacobian matrix at the uniform steady state (P^*, W^*) and $\lambda(k)$ is the eigenvalue or linear growth factor corresponding to the spatial wavemode with wavenumber k. If, for some non-zero spatial wavenumber, the eigenvalue $\lambda(k)$ becomes positive, then that particular spatial wavemode increases in time and contributes to the spatially heterogeneous distribution of species. Diffusion-driven Turing

instability appears when the non-diffusive system remains stable around the uniform steady state but becomes unstable in its presence. The stability of a two-dimensional non-diffusive system about the uniform steady state is obtained if the trace is negative and the determinant is positive at $k = 0$, giving

$$\mathcal{T} = J_{11} + J_{22} < 0, \quad \text{and} \quad \mathcal{D} = J_{11}J_{22} - J_{12}J_{21} > 0. \tag{4.5}$$

The coefficient of λ in equation (4.4) is

$$\sum_{j=1,2} (J_{jj} - D_j k^2) = \tau - k^2(D_1 + D_2) < 0, \quad \forall k.$$

The constant term in the characteristic equation (4.4) may be expressed as

$$\begin{aligned} \mathcal{M}(k^2) &= \prod_{j=1,2} \left(J_{jj} - D_j k^2\right) - J_{12}\left(J_{21} + \beta D_2 k^2\right) \\ &= \left(J_{11} - D_1 k^2\right)\left(J_{22} - D_2 k^2\right) - J_{12}\left(J_{21} + \beta D_2 k^2\right) \\ &= D_1 D_2 k^4 - \left(D_1 J_{22} + D_2 J_{11} + \beta D_2 J_{12}\right) k^2 + \left(J_{11}J_{22} - J_{12}J_{21}\right). \end{aligned} \tag{4.6}$$

Positivity of $\mathcal{M}(k^2)$ at $k = 0$ is satisfied as $J_{11}J_{22} - J_{12}J_{21} > 0$. The following lemma provides the necessary and sufficient conditions for stationary bifurcations.

Lemma 4.1. *[29] The eigenroots of a n-degree characteristic equation*

$$\mathcal{P}(\lambda) = A_0\lambda^n + A_1\lambda^{n-1} + A_2\lambda^{n-2} + ... + A_{n-1}\lambda + A_n = 0,$$

corresponding to a n-dimensional dynamical system have negative real parts if and only if $det(\mathcal{H}_i) > 0$ *for all* $i = 1, 2, ..., n-1$ *(where* $\mathcal{H}_i$ *are the Hurwitz matrices) and* $A_n > 0$*. The dynamical system shows a stationary bifurcation if a real root becomes negative to positive. This occurs if and only if* A_n *changes its sign from* $A_n > 0$ *to* $A_n < 0$*, keeping* $det(\mathcal{H}_i) > 0$ *for all* $i = 1, 2, ..., n-1$*.* □

Therefore, according to Lemma 4.1, Turing instability appears only when $\mathcal{M}(k^2) < 0$ holds for some $k \neq 0$. Some straightforward simplification [141] provides the Turing instability conditions as follows.

Proposition 4.2. *Diffusion-driven Turing instability occurs in system (4.2) if*

$$\begin{aligned} &(1) \quad \mathcal{T} = J_{11} + J_{22} < 0, \quad \mathcal{D} = J_{11}J_{12} - J_{21}J_{22} > 0, \\ &(2) \quad \Lambda = D_1 J_{22} + D_2 J_{11} + \beta D_2 J_{12} > 2\sqrt{D_1 D_2 \mathcal{D}} > 0. \end{aligned}$$

At the Turing bifurcation point, the critical wavenumber is $k_T = \sqrt[4]{\frac{\mathcal{D}}{D_1 D_2}}$, *and the interval of wavenumbers for which Turing instability appears is* (k_1, k_2), *where*

$$k_{1,2} = \frac{1}{(2D_1D_2)^{\frac{1}{2}}}\left[\Lambda \mp \sqrt{\Lambda^2 - 4D_1D_2\mathcal{D}}\right]^{\frac{1}{2}}.$$

□

Condition (2) in the above proposition specifies the critical values of control parameters that lead to Turing instability. The associated unstable wavenumbers correspond to spatial modes that grow over time, giving rise to pattern formation. The wavenumber k is inversely related to the pattern's wavelength λ via the relation $\lambda = \frac{2\pi}{k}$. Hence, higher wavenumbers result in finer, small-scale patterns, while lower wavenumbers yield broader, large-scale structures. The range of wavenumbers that trigger Turing instability lies within the interval $k \in (k_1, k_2)$, which depends explicitly on the diffusion coefficients. Consequently, variations in diffusion coefficients directly influence the scale (or wavelength) of the emergent spatial patterns, as further elaborated in the following theorem.

Theorem 4.3. *If the diffusion coefficient matrix* (D) *of the reaction-diffusion system* (4.2) *are scaled into proportion of* s, *i.e.,* $s \times D$, *then the wavelength of the corresponding patterns will change in a proportion of* $s^{\frac{1}{2}}$. □

Proof. Let the diffusion coefficient matrix $D = \begin{pmatrix} D_1 & 0 \\ -\beta D_2 & D_2 \end{pmatrix}$ is scaled by a scaling factor s to the new diffusion coefficient matrix sD. Therefore, following Proposition (4.2), critical wavenumber of Turing instability becomes

$$k_T^{(s)} = \sqrt[4]{\frac{\mathcal{D}}{sD_1sD_2}} = \frac{1}{s^{\frac{1}{2}}}\sqrt[4]{\frac{\mathcal{D}}{D_1D_2}} = \frac{1}{s^{\frac{1}{2}}}k_T. \tag{4.7}$$

Similarly, the interval of unstable wavenumbers reduces to

$$\begin{aligned} k_{1,2}^{(s)} &= \frac{1}{(2s^2D_1D_2)^{\frac{1}{2}}}\left[s\Lambda \mp \sqrt{s^2\Lambda^2 - 4s^2D_1D_2\mathcal{D}}\right]^{\frac{1}{2}} \\ &= \frac{1}{s^{\frac{1}{2}}}\left(\frac{1}{(2D_1D_2)^{\frac{1}{2}}}\left[\Lambda \mp \sqrt{\Lambda^2 - 4D_1D_2\mathcal{D}}\right]^{\frac{1}{2}}\right) \\ &= \frac{1}{s^{\frac{1}{2}}}k_{1,2}. \end{aligned} \tag{4.8}$$

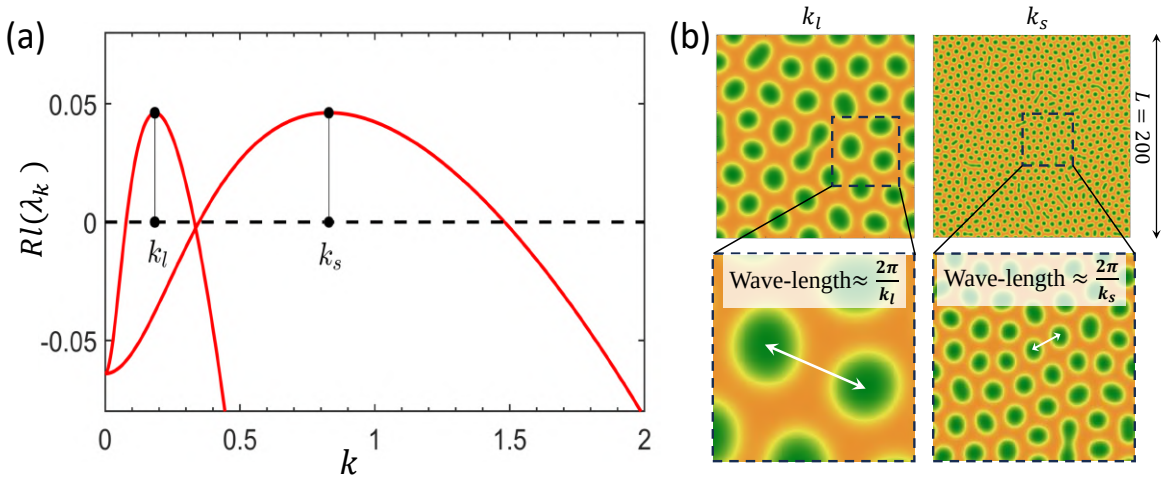

FIGURE 4.2: **(a)** Dispersion relations of the single-layer system (4.1) are shown for two contrasting diffusion scales: a large diffusion case with $(D_1, D_2) = (1, 100)$, and a small diffusion case with $(D_1, D_2) = (0.05, 5)$. The dominant wavenumbers for these cases are denoted by k_l and k_s, respectively. **(b)** The corresponding spatial patterns (upper row) for k_l and k_s.The highlighted regions shown at an enlarged scale in the lower row. The white arrow indicates the wavelength, measured as the distance between two consecutive peaks. Parameter values are $\gamma = 1.6,\ \sigma = 1.6,\ \mu = 0.2,\ \rho = 1.5,\ \beta = 3$.

The wavelength of the unstable modes that drive pattern formation is inversely related to the wavenumber, given by $\lambda = \frac{2\pi}{k}$. Under spatial rescaling by a factor s, the wavenumber transforms as $k \mapsto \frac{k}{\sqrt{s}}$, implying that the characteristic wavelength scales as $\lambda \propto \sqrt{s}$. Notably, the parametric conditions for the onset of Turing instability remain unchanged under this spatial scaling, indicating that the instability criteria are scale-invariant.

□

The result above can be validated through the dispersion relation, which describes the behavior of the unstable eigenvalues $\lambda(k)$ corresponding to each spatial wavenumber k. The dispersion relation (Fig. 4.2a) reveals the range of unstable wavenumbers (k_1, k_2) (as stated in Proposition 4.2), where $\mathrm{Re}(\lambda(k)) > 0$. To illustrate the influence of diffusion coefficients, we compare the dispersion relations for two different diffusion scales while keeping all other parameters fixed. For the case with higher diffusion coefficients, $(D_1, D_2) = (1, 100)$, the dominant eigenvalue corresponds to a wavenumber $k_l \approx 0.18$. When the diffusion coefficients are reduced by a factor of 20 to $(D_1, D_2) = (0.05, 5)$, the dominant wavenumber shifts to $k_s \approx 0.83$. The dominant unstable mode, i.e., the mode corresponding to the wavenumber $k_{\max}$ that maximizes

$\mathrm{Re}(\lambda(k))$, ultimately determines the characteristic wavelength of the emerging spatial pattern. While there is no exact closed-form expression for $k_{\max}$, it can be closely approximated by the critical wavenumber at the Turing bifurcation point, k_T, where $k_{\max} = k_T$. Even away from the bifurcation point, $k_{\max} \approx k_T$ remains a good approximation. Therefore, the expression for k_T (as discussed in Theorem 4.3) provides insight into how diffusion coefficients influence the pattern scale. Since the wavelength is inversely related to the wavenumber ($\lambda = \frac{2\pi}{k}$), a higher dominant wavenumber k_s leads to finer, smaller-scale patterns. In contrast, a lower wavenumber k_l corresponds to broader, larger-scale patterns. This is evident in the vegetation hotspot patterns shown in Fig. 4.2b, generated under the two diffusion regimes. Simulated over the same domain size $L = 200$, the patterns associated with k_l are approximately $\sqrt{20} \approx 4.6$ times larger in scale than those corresponding to k_s, since $k_s \approx 4.6\, k_l$. The wavelength, estimated as the distance between two adjacent high-density peaks, is roughly given by $\frac{2\pi}{k_{l,s}}$. Due to system nonlinearities, especially when far from the Turing bifurcation, the observed patterns may deviate from ideal symmetric hexagonal (H_+) structures. However, this approximation still provides a useful scale estimate.

4.3.2 Weakly nonlinear analysis and monoscale pattern selection

The transitions between different spatial patterns in a two-dimensional domain, as well as pattern selection driven by variations in model parameters, can be systematically analyzed using well-established amplitude equations derived through standard weakly nonlinear (WNL) multiscale analysis. Without going into the detailed derivation, we present the general form of the amplitude equation in the following theorem. For a comprehensive treatment, readers are referred to [105, 141]. In two-dimensional space, Turing patterns typically arise from the superposition of three resonant mode pairs $(\vec{k}_j, -\vec{k}_j)$ for $j = 1, 2, 3$, where each wavevector $\vec{k}_j$ forms an angle of $\frac{2\pi}{3}$ with the others, satisfying the resonance condition $\sum_j \vec{k}_j = \vec{0}$. This triad of active wave modes effectively captures the structure of hexagonal Turing patterns [106]. Using the results of the WNL analysis, one can derive explicit expressions for the coefficients of the amplitude equations. These coefficients govern the bifurcation behavior and stability of the resulting patterns, and they play a central role in determining pattern transitions. A summary of these results is given in the following theorem.

Theorem 4.4. *For the two-species reaction-diffusion system (4.2), the amplitude equations up to the second-ordered perturbations, sufficiently close to the critical Turing bifurcation point (say $r = r_T$), can be expressed as*

$$\tau_0 \frac{\partial A_1}{\partial t} = \eta A_1 + h\bar{A}_2\bar{A}_3 - \left[g_1|A_1^2| + g_2(|A_2|^2 + |A_3|^2)\right] A_1, \tag{4.9}$$

$$\tau_0 \frac{\partial A_2}{\partial t} = \eta A_2 + h\bar{A}_3\bar{A}_1 - \left[g_1|A_2^2| + g_2(|A_3|^2 + |A_1|^2)\right] A_2, \tag{4.10}$$

$$\tau_0 \frac{\partial A_3}{\partial t} = \eta A_3 + h\bar{A}_1\bar{A}_2 - \left[g_1|A_3^2| + g_2(|A_1|^2 + |A_2|^2)\right] A_3, \tag{4.11}$$

where A_j, $j = 1, 2, 3$, are the amplitudes of the perturbation and $\eta = \frac{r - r_T}{r_T}$ is the relative parameter deviation from the critical Turing bifurcation point. The amplitudes can be decomposed into modes (ρ_j) and phase-angles (ξ_j) as $A_i = \rho_i e^{j\xi_i}$, $i = 1, 2, 3$, where $j = \sqrt{-1}$. Then, the following equations determine the stability of the steady state patterns close to the Turing bifurcation point:

$$\tau_0 \frac{d\xi}{dt} = -h\frac{\rho_1^2\rho_2^2 + \rho_2^2\rho_3^2 + \rho_3^2\rho_1^2}{\rho_1\rho_2\rho_3} sin(\xi), \tag{4.12}$$

$$\tau_0 \frac{d\rho_1}{dt} = \eta\rho_1 + h\rho_2\rho_3 cos(\xi) - g_1\rho_1^3 - g_2(\rho_1^2 + \rho_3^2)\rho_1, \tag{4.13}$$

$$\tau_0 \frac{d\rho_2}{dt} = \eta\rho_2 + h\rho_3\rho_1 cos(\xi) - g_1\rho_2^3 - g_2(\rho_3^2 + \rho_1^2)\rho_2, \tag{4.14}$$

$$\tau_0 \frac{d\rho_3}{dt} = \eta\rho_3 + h\rho_1\rho_2 cos(\xi) - g_1\rho_3^3 - g_2(\rho_1^2 + \rho_2^2)\rho_3, \tag{4.15}$$

where $\xi = \xi_1 + \xi_2 + \xi_3$. With respect to the relative deviation term η, from the critical Turing bifurcation point (at $\eta = 0$), stability and existence of patterned states are defined in the vicinity of the critical Turing bifurcation point.

1. *Homogeneous steady state: Modes are $(\rho_1, \rho_2, \rho_3) = (0, 0, 0)$ with stability condition $\eta < \eta_2$, where $\eta_2 = 0$.*

2. *Stripes (S): Modes are $(\rho_1, \rho_2, \rho_3) = (\sqrt{\frac{\eta}{g_1}}, 0, 0)$ with existence condition $\eta > \eta_2$ and stability condition $\eta > \eta_3$, where $\eta_2 = 0$ and $\eta_3 = \frac{h^2 g_1}{(g_2 - g_1)^2}$.*

3. *Hexagonal patterns (H_+) and (H_-): Modes of H_+ and H_- are $(\rho_1, \rho_2, \rho_3) = (\rho_\pm, \rho_\pm, \rho_\pm)$, where $\rho_\pm = \frac{|h| \pm \sqrt{h^2 + 4(g_1 + 2g_2)\eta}}{2(g_1 + 2g_2)}$ with existence condition $\eta > \eta_1$. H_+ is stable if $\eta < \eta_4$ but H_- is unstable conditionally, where $\eta_1 = -\frac{h^2}{4(g_1 + 2g_2)}$ and $\eta_4 = -\frac{h^2(2g_1 + g_2)}{(g_1 - g_2)^2}$.*

4. *Mixed mode pattern: Modes are* $(\rho_1, \rho_2, \rho_3) = (\rho_1^*, \rho_2^*, \rho_2^*)$, *where* $\rho_1^* = \frac{|h|}{g_2 - g_1}$, *and* $\rho_2^* = \sqrt{\frac{\eta - g_1\rho_1^2}{g_1+g_2}}$ *with existence condition* $g_2 > g_1$, $\eta_1 > g_1\rho_1^2$ *and it is always unstable.*

The evolution of patterns can be tracked with respect to the control parameter r as it deviates from the critical Turing bifurcation point $r = r_T$. Detailed derivation of above theorem is as in Chapter 2, Subsection 2.3.3. □

4.3.3 Numerical simulation of single layer system

Figure 4.3 presents a bifurcation overview of the single-layer model (4.1) under varying water input rate r. In the absence of spatial diffusion, a transcritical bifurcation occurs at the critical threshold $r = r_{\mathrm{Tr}} = 0.155$, marked by the black vertical dashed line in the figure. Below this threshold, the vegetated state ceases to exist, and only the bare-soil state remains stable. As r increases beyond r_{Tr}, a uniform vegetated equilibrium becomes stable (solid green line), with vegetation density increasing with the water input. When spatial diffusion is introduced, the system undergoes a Turing instability about the uniform vegetation state within a specific range of water input values, (r_{T_1}, r_{T_2}), shown by the two blue vertical dashed lines in Fig. 4.3. For the chosen parameter set, these critical values are $r_{T_1} = 0.169$ and $r_{T_2} = 0.413$. These Turing bifurcation points are determined from the critical condition given in Theorem 4.2. Within this intermediate range of water input, the spatial system supports self-organized vegetation patterns. Under water-limited conditions, vegetation reconfigures into spatial patches that enhance water capture and retention, promoting survival and productivity. Outside this Turing-unstable interval, specifically in the ranges $(r_{\mathrm{Tr}}, r_{T_1}) \cup (r_{T_2}, \infty)$, the system maintains a spatially uniform vegetated state. Numerical simulations of the one-layer reaction-diffusion model (4.1) were carried out on a square domain of side length $L = 200$, subject to Neumann (no-flux) boundary conditions.

The weakly nonlinear analysis (WNA) predicts the type of spatial pattern that emerges, like hot-spot, labyrinth, or cold-spot, as the control parameter r varies. As detailed in Theorem 4.4, Fig. 4.4 illustrates the amplitudes and stabilities of different patterned states near the two Turing bifurcation points of the system (4.1). Near the first Turing bifurcation point r_{T_1}, the amplitude of the H_+ hexagonal pattern (commonly referred to as the hot-spot pattern) is stable within the range $\eta \in (\eta_2, \eta_3)$ (see Fig. 4.4a). Ecologically, this corresponds to a predominantly bare landscape interspersed with small, concentrated clusters of vegetation. As r (or equivalently η) increases further into the range (η_3, ∞), the system transitions to stripe (labyrinthine)

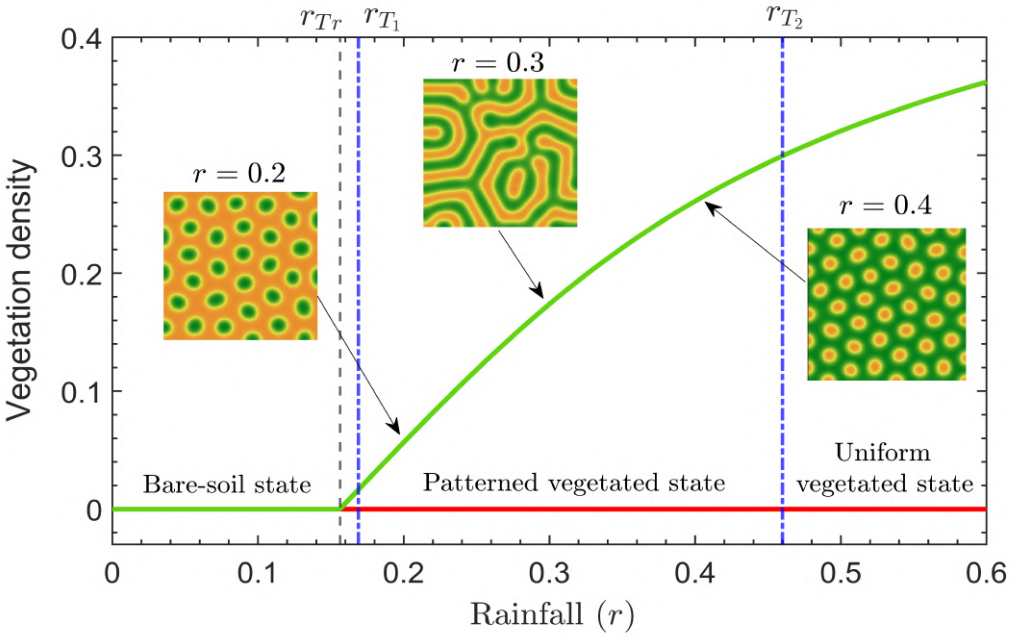

FIGURE 4.3: The bifurcation of equilibrium vegetation densities obtained from the local (non-spatial) system. The solid curves represent the uniform steady states (USS) of the local system, with green segments indicating stable equilibria and red segments indicating unstable ones. The black dashed vertical line marks the transcritical bifurcation point at $r = r_{\mathrm{Tr}} = 0.155$, above which the uniform vegetated state is stable, while below it, only the bare-soil state is stable. The blue dashed vertical lines indicate the Turing bifurcation thresholds at $r_{T_1} = 0.169$ and $r_{T_2} = 0.413$, which define the parameter range over which spatial patterns emerge due to diffusion-driven instability. Representative patterns of the spatiotemporal system (4.1) simulated on a domain of size $L = 200$ are displayed for three different precipitation values: $r = 0.2$ (hot-spot pattern), $r = 0.3$ (labyrinth pattern) and $r = 0.4$ (cold-spot pattern). Parameter values are $\gamma = 1.6,\ \sigma = 1.6,\ \mu = 0.2,\ \rho = 1.5,\ \beta = 3, D_1 = 1, D_2 = 100$.

patterns. However, it is important to note that the WNA becomes less accurate farther from the bifurcation point ($\eta = 0$), and predictions based solely on amplitude equations may not fully capture the system's behavior in these regions. On the other side, near the second Turing point r_{T_2}, the H_- hexagonal pattern (cold-spot pattern) is stable in the range $\eta \in (\eta_3, \eta_2)$ (see Fig. 4.4b). Here, the negative values of η indicate that the Turing instability arises as r decreases from r_{T_2}. Ecologically, this corresponds to a predominantly vegetated landscape interrupted by small barren patches. As r continues to decrease into the range $(-\infty, \eta_3)$, the system undergoes a transition from cold-spot patterns to stripes. Thus, within the Turing-unstable

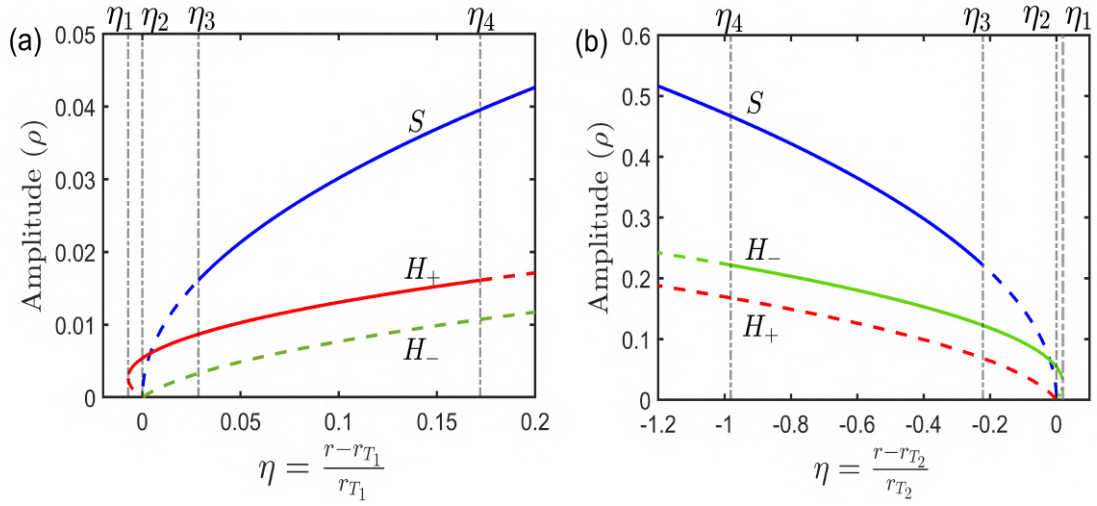

FIGURE 4.4: Amplitude equations are shown with respect to the relative parameter deviation η from the critical Turing bifurcation points r_{T_1} (Fig. (a)) and r_{T_2} (Fig. (b)). The blue curves represent the amplitude of the stripe pattern (S), the red curves correspond to the hot-spot pattern (H_+), and the green curves indicate the cold-spot pattern (H_-). Vertical dashed lines mark the bifurcation points of the respective patterned states. In Fig. (a), the vertical dashed lines from left to right denote the critical values η_1 to η_4 with $(\eta_1, \eta_2, \eta_3, \eta_4) = (-0.007, 0, 0.029, 0.1721)$. Near the Turing bifurcation point $r = r_{T_1}$, the small-amplitude hot-spot pattern (H_+) is stable. In Fig. (b), the vertical dashed lines from right to left denote η_1 to η_4, where $(\eta_1, \eta_2, \eta_3, \eta_4) = (0.0193, 0, -0.2216, -0.9813)$. Near the Turing bifurcation point $r = r_{T_2}$, the small-amplitude cold-spot pattern (H_-) is stable. Further away from both bifurcation points, the stripe pattern (S) with larger amplitude becomes the stable solution.

interval (r_{T_1}, r_{T_2}), the system exhibits a progression of pattern transitions:

$$H_+ \text{ (hot spots)} \rightarrow S \text{ (stripes)} \rightarrow H_- \text{ (cold spots)}$$

as the mean water input rate r increases. According to the WNA, near r_{T_1}, at $r = 0.2$, the system favors hot-spot patterns. Near r_{T_2}, at $r = 0.4$, cold-spot patterns are observed. For intermediate values, such as $r = 0.3$, the system tends to produce stripe or labyrinthine patterns, as illustrated in Fig. 4.3. The total vegetation cover decreases as the water input rate r is reduced.

4.4 Multi-layer vegetation model

In classical single-layer reaction-diffusion systems, the dispersion relation typically displays a single peak, corresponding to a unique most-unstable wavenumber. This leads to the selection of a characteristic wavelength and the formation of spatial patterns with a monoscale structure. However, when the system consists of two coupled layers with markedly different diffusion coefficients, as in our model, the dispersion relation may exhibit multiple peaks at distinct wavenumbers [64]. The presence of multiple unstable modes allows for the coexistence of different spatial scales, resulting in the emergence of multiscale patterns. In this study, we explore this phenomenon in the context of vegetation pattern formation in arid ecosystems. Specifically, we extend the single-layer model proposed by Hardenberg et al. [57] to a two-layer framework that includes both two soil layers and two plant phenotypes. This extended model follows the multiscale pattern formation mechanism originally proposed by Yang et al. [64] in the context of layered chemical systems. Based on these considerations, we modify the original system (4.1) into a two-plant phenotype, two-soil-layer interaction model, as follows:

$$\frac{\partial P_1}{\partial t} = \frac{\gamma W_1}{1+\sigma W_1} P_1 - P_1^2 - \mu P_1 + D_1^{(1)} \nabla^2 P_1 + \mathcal{C}_1(P_1, W_1, P_2, W_2), \tag{4.16a}$$

$$\frac{\partial W_1}{\partial t} = r_1 - (1-\rho P_1) W_1 - R W_1^2 P_1 + D_2^{(1)} \nabla^2 (W_1 - \beta P_1) + \mathcal{C}_2(P_1, W_1, P_2, W_2), \tag{4.16b}$$

$$\frac{\partial P_2}{\partial t} = \frac{\gamma W_2}{1+\sigma W_2} P_2 - P_2^2 - \mu P_2 + D_1^{(2)} \nabla^2 P_2 + \mathcal{C}_3(P_1, W_1, P_2, W_2), \tag{4.16c}$$

$$\frac{\partial W_2}{\partial t} = r_2 - (1-\rho P_2) W_2 - R W_2^2 P_2 + D_2^{(2)} \nabla^2 (W_2 - \beta P_2) + \mathcal{C}_4(P_1, W_1, P_2, W_2). \tag{4.16d}$$

Here, P_1 and P_2 represent the densities of shallow-rooted and deep-rooted plant phenotypes, respectively, while W_1 and W_2 denote the soil water content in the top and bottom soil layers. The major assumptions underlying this two-layer model extension are outlined below:

- **Plant-soil water feedback mechanism:** The feedback between plants and soil water in each layer follows mechanisms similar to those in the original system (4.1), governed by root structure and water availability. Shallow-rooted plants (P_1) extract water (W_1) from the topsoil, with feedback interactions occurring between these two variables. Similarly, deep-rooted plants (P_2) primarily extract water (W_2) from the deeper soil layer. Although both phenotypes belong to the same species and appear identical above ground, they exhibit different spatial distributions due to varying responses to water stress.
- **Difference in diffusion scales:** The vegetative propagation of deep-rooted plants is assumed to be minimal compared to shallow-rooted plants, as deep

rooting is an adaptive response rather than a fixed trait. Therefore, spatial propagation is attributed primarily to shallow-rooted plants. Additionally, due to greater soil compaction at depth, the water diffusion rate in the bottom layer is lower than in the top layer. Consequently, we assume $D_1^{(1)} \gg D_1^{(2)}$ for plant diffusion and $D_2^{(1)} \gg D_2^{(2)}$ for soil water diffusion across layers.

- **Inter-layer interactions:** In addition to intra-layer feedback mechanisms, inter-layer interactions are incorporated through coupling terms that modify the local reaction dynamics. These include interactions between the two plant phenotypes and between the two soil water layers at each spatial location. The coupling terms are represented by general functions $\mathcal{C}_i(P_1, W_1, P_2, W_2)$ for $i = 1, 2, 3, 4$.

4.4.1 Gradient-dependent coupling

Analytical investigation of the complete four-dimensional system, comprising two plant phenotypes and two soil water layers, is mathematically challenging. To better understand the mechanism behind multiscale pattern formation, we analyze a simplified model that incorporates gradient-dependent coupling between layers. This coupling framework reflects the idea of density-driven transitions. Specifically, in regions where shallow-rooted plants experience high local density, competition for topsoil water increases, potentially triggering a shift to a deep-rooted phenotype. This transition aligns with root augmentation as an adaptive strategy to water stress, a phenomenon well-documented in experimental studies [69]. For analytical convenience, we permit bidirectional transitions between phenotypes based on local density gradients, even though the reverse transition (from deep-rooted to shallow-rooted) is biologically less plausible. This simplification is addressed and corrected in the more realistic two-layer model presented later. Similarly, soil water is assumed to move vertically between layers in response to concentration gradients, with water naturally diffusing from regions of higher to lower moisture content [174]. To maintain analytical tractability, we use linear coupling terms to model these interactions, although more complex, nonlinear formulations could better capture the underlying biophysical processes.

The bidirectional, gradient-dependent coupling terms employed in this simplified framework are given by:

$$\begin{aligned} &\mathcal{C}_1(P_1, W_1, P_2, W_2) = c_1(P_2 - P_1), \quad \mathcal{C}_2(P_1, W_1, P_2, W_2) = c_2(W_2 - W_1), \\ &\mathcal{C}_3(P_1, W_1, P_2, W_2) = c_1(P_1 - P_2), \quad \mathcal{C}_4(P_1, W_1, P_2, W_2) = c_2(W_1 - W_2). \end{aligned} \tag{4.17}$$

4.4.2 Analysis of the multi-layer vegetation model

Assume that the multi-layer model (4.16) with the coupling (4.17) has a uniform steady state of the form $(P_1, W_1, P_2, W_2) = (P_1^*, W_1^*, P_2^*, W_2^*)$. The equilibrium densities of vegetation for the two plant phenotypes (P_1^*, P_2^*) and the equilibrium soil water contents in the two layers (W_1^*, W_2^*) will be identical only under conditions of parametric homogeneity, i.e., when all parameters, except the diffusion coefficients, are equal across the two layers. In the absence of such homogeneity, the equilibrium values of the state variables may differ, leading to $P_1^* \neq P_2^*$ and $W_1^* \neq W_2^*$. Linearization of the system (4.16) with the coupling term (4.17) around the uniform steady state $(P_1^*, W_1^*, P_2^*, W_2^*)$ provides the eigenvalue problem

$$|J - \lambda(k) I_{4\times 4} - k^2 D| = 0,$$

where

$$J = \begin{pmatrix} J_{11}^{(1)} - c_1 & J_{12}^{(1)} & c_1 & 0 \\ J_{21}^{(1)} & J_{22}^{(1)} - c_2 & 0 & c_2 \\ c_1 & 0 & J_{11}^{(2)} - c_1 & J_{12}^{(2)} \\ 0 & c_2 & J_{21}^{(2)} & J_{22}^{(2)} - c_2 \end{pmatrix} \text{ and } D = \begin{pmatrix} D_1^{(1)} & 0 & 0 & 0 \\ -\beta D_2^{(1)} & D_2^{(1)} & 0 & 0 \\ 0 & 0 & D_1^{(2)} & 0 \\ 0 & 0 & -\beta D_2^{(2)} & D_2^{(2)} \end{pmatrix}.$$

Then, the characteristic equation reads

$$\begin{aligned} &\textstyle\prod_{i,j=1,2} \left(J_{jj}^{(i)} - c_j - D_j^{(i)} k^2 - \lambda \right) - \sum_{s=1,2} c_s^2 \prod_{\substack{i,j=1,2 \\ j\neq s}} \left(J_{jj}^{(i)} - c_j - D_j^{(i)} k^2 - \lambda \right) \\ &- \textstyle\sum_{s=1,2} J_{12}^{(s)} J_{21}^{(s)} \prod_{\substack{i,j=1,2 \\ j\neq s}} \left(J_{jj}^{(i)} - c_j - D_j^{(i)} k^2 - \lambda \right) + \prod_{\substack{i,j=1,2 \\ j\neq i}} \left(c_1 c_2 - J_{12}^{(i)} J_{12}^{(j)} \right) \\ &- \beta k^2 \textstyle\sum_{\substack{i,j=1,2 \\ i\neq j}} D_2^{(j)} \left(J_{12}^{(j)} \prod_{s=1,2} \left(J_{ss}^{(j)} - c_s - \lambda - D_s^{(i)} k^2 \right) + J_{12}^{(i)} \left(c_1 c_2 - J_{12}^{(j)} J_{21}^{(i)} \right) \right) \\ &+ 2\beta^2 k^4 J_{12}^{(1)} J_{12}^{(2)} D_2^{(1)} D_2^{(2)} = 0. \end{aligned} \tag{4.18}$$

The expressions $J_{ij}^{(l)} = J_{ij}$, $l = 1, 2$, denotes component of the Jacobian matrix for two layers at the equilibrium concentration $(P_1^*, W_1^*, P_2^*, W_2^*)$. The quartic equation in λ can be solved analytically to find the solutions of λ. With respect to a chosen bifurcation parameter, Turing bifurcation point of the spatiotemporal system is obtained at $Re(\lambda_i(k)) = 0$, $Im(\lambda_i(k)) = 0$ for some $i = 1, 2, 3, 4$, at a critical wavenumber $k = k_T \neq 0$. According to the Lemma (4.1), the spatiotemporal system of two-phenotype, two-soil layer vegetation model (4.16) with gradient-dependent coupling (4.17) undergoes Turing bifurcation if the constant term of the characteristic equation changes its sign from positive to negative at some non-zero spatial wavenumber k.

Setting, $\lambda = 0$ in equation (4.18), the constant term is obtained as

$$\begin{aligned}\mathcal{M}(k^2) = & \prod_{i,j=1,2}\left(J_{jj}^{(i)} - c_j - D_j^{(i)}k^2\right) - \sum_{s=1,2} c_s^2 \prod_{\substack{i,j=1,2\\ j\neq s}}\left(J_{jj}^{(i)} - c_j - D_j^{(i)}k^2\right) \\ & - \sum_{s=1,2} J_{12}^{(s)} J_{21}^{(s)} \prod_{\substack{i,j=1,2\\ j\neq s}}\left(J_{jj}^{(i)} - c_j - D_j^{(i)}k^2\right) + \prod_{\substack{i,j=1,2\\ j\neq i}}\left(c_1c_2 - J_{12}^{(i)}J_{12}^{(j)}\right) \\ & - \beta k^2 \sum_{\substack{i,j=1,2\\ i\neq j}} D_2^{(j)}\left(J_{12}^{(j)}\prod_{s=1,2}\left(J_{ss}^{(j)} - c_s - D_s^{(i)}k^2\right) + J_{12}^{(i)}\left(c_1c_2 - J_{12}^{(j)}J_{21}^{(i)}\right)\right) \\ & + 2\beta^2 k^4 J_{12}^{(1)} J_{12}^{(2)} D_2^{(1)} D_2^{(2)}. \end{aligned} \tag{4.19}$$

Then the following theorem is true:

Theorem 4.5. *Assume that the corresponding non-diffusive system of the two-layer system (4.16) with coupling (4.17) is stable about the uniform steady state* $(P_1^*, W_1^*, P_2^*, W_2^*)$. *Diffusion-driven Turing instability appears in the system if the following conditions hold:*

$$\begin{aligned} &(1) \quad \mathcal{M}(k^2) = 0 \text{ for } k = 0, \quad \text{and} \\ &(2) \quad \mathcal{M}(k^2) > 0 \text{ for some } k \neq 0, \end{aligned}$$

where $\mathcal{M}(k^2)$ *is given by (4.19).*

The conditions for Turing instability and the existence of unstable spatial modes of two different scales are difficult to simplify analytically from the above theorem. However, from the limiting case of weak coupling, an intuitive idea can be drawn about the multiscale pattern formation. For limiting case $c_1 \to 0$, $c_2 \to 0$, the dispersion relation reads

$$\begin{aligned}\lim_{\substack{c_1\to 0\\ c_2\to 0}} \mathcal{M}(k^2) = & \prod_{i,j=1,2}\left(J_{jj}^{(i)} - D_j^{(i)}k^2\right) - \sum_{s=1,2} J_{12}^{(s)} J_{21}^{(s)} \prod_{\substack{i,j=1,2\\ j\neq s}}\left(J_{jj}^{(i)} - D_j^{(i)}k^2\right) \\ & + \prod_{\substack{i,j=1,2\\ j\neq i}} J_{12}^{(i)} J_{12}^{(j)} - \beta k^2 \sum_{\substack{i,j=1,2\\ i\neq j}} D_2^{(j)}\left(J_{12}^{(j)}\prod_{s=1,2}\left(J_{ss}^{(j)} - D_s^{(i)}k^2\right)\right. \\ & \left. - J_{12}^{(i)}J_{12}^{(j)}J_{21}^{(i)}\right) + 2\beta^2 k^4 J_{12}^{(1)} J_{12}^{(2)} D_2^{(1)} D_2^{(2)}. \end{aligned} \tag{4.20}$$

Simplifying the above expression, and using (4.6), we obtain the decoupled expression as follows:

$$\begin{aligned}\lim_{\substack{c_1\to 0\\ c_2\to 0}} \mathcal{M}(k^2) = & \prod_{i=1,2}\left[D_1^{(i)}D_2^{(i)}k^4 - \left(D_1^{(i)}J_{22}^{(i)} + D_2^{(i)}J_{11}^{(i)} + \beta D_2^{(i)}J_{12}^{(i)}\right)k^2\right. \\ & \left. + \left(J_{11}^{(i)}J_{22}^{(i)} - J_{12}^{(i)}J_{21}^{(i)}\right)\right] \\ = & \ \mathcal{M}^{(1)}(k^2)\mathcal{M}^{(2)}(k^2). \end{aligned} \tag{4.21}$$

Therefore, in the case of weak coupling strength (where $c_1, c_2 \to 0$), one gets an almost decoupled form of two dispersion relations in one. Thus, if the scale of the diffusive feedback mechanism is different in individual layers, one gets two distinct peaks for the two-layer coupled system. In such a case, Theorem (4.5) reduces to the simplified theorem as follows:

Theorem 4.6. *Diffusion-driven Turing instability in the two-layer system* (4.16) *with coupling* (4.17) *occurs under in the limiting case of weak coupling, where* $(c_1, c_2) \to (0, 0)$*, if*

$$\begin{aligned} &(1) \quad \mathcal{T}^{(i)} = J_{11}^{(i)} + J_{22}^{(i)} < 0, \quad \mathcal{D}^{(i)} = J_{11}^{(i)} J_{12}^{(i)} - J_{21}^{(i)} J_{22}^{(i)} > 0, \quad \forall\ i = 1, 2, \\ &(2) \quad \mathcal{M}(k^2) > 0 \text{ for some } k \neq 0, \end{aligned}$$

where $\mathcal{M}(k^2)$ *is given by* (4.21).

4.4.3 Multiscale pattern formation in two layer model

To explore the influence of coupling strength on pattern selection, we compare the dispersion relations of two-layer systems under weak and strong coupling scenarios. The diffusion coefficients for the topsoil layer and the shallow-rooted plant phenotype are set as $(D_1^{(1)}, D_2^{(1)}) = (0.5, 50)$. For the bottom soil layer and deep-rooted phenotype, a scaling factor of 1/30 is applied, resulting in $(D_1^{(2)}, D_2^{(2)}) < (D_1^{(1)}, D_2^{(1)})$, ensuring smaller diffusion scales in the lower layer. In the uncoupled case ($c_1 = c_2 = 0$), the dispersion relations of the two independent subsystems display separate peaks corresponding to their respective dominant unstable modes (shown by dashed and dash-dotted black curves in Fig. 4.5a). When weak coupling is introduced ($c_1 = c_2 = 0.003$), the interaction between the two layers begins, producing a combined dispersion relation with two distinct unstable peaks, indicative of multiscale pattern formation (solid orange curve in Fig. 4.5a). As coupling strength increases ($c_1 = c_2 = 0.03$), the peaks become more deformed due to stronger inter-layer interactions (solid blue curve). However, under strong coupling ($c_1 = c_2 = 0.1$), the two initially separate peaks merge into a single dominant unstable mode, suggesting synchronization between the layers and a transition toward a unified spatial structure. Figure 4.5b illustrates the corresponding spatial wavelengths of the unstable modes for weak coupling ($c_1 = c_2 = 0.003$) in a one-dimensional domain. The topsoil layer, with higher diffusion coefficients, supports large-scale patterns characterized by longer wavelengths (solid green and blue curves). In contrast, the bottom layer, with much smaller diffusion rates, exhibits fine-scale patterns with shorter wavelengths and higher spatial frequency (dashed green and blue curves). In both layers, vegetation density and soil water content show strong spatial coherence, peaks in plant biomass align with

regions of high soil moisture. This spatial alignment highlights the tight coupling between ecological (plant growth) and hydrological (water availability) processes in driving pattern formation across scales.

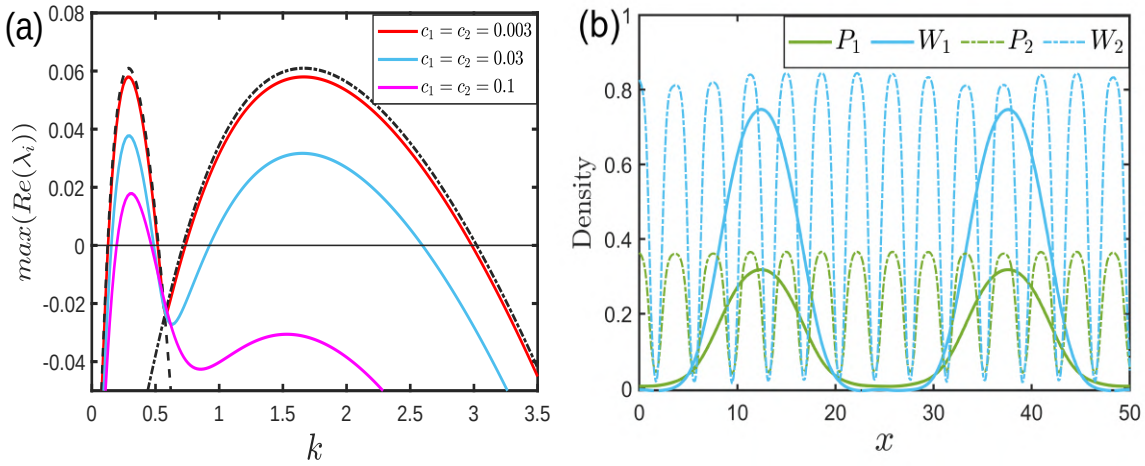

FIGURE 4.5: **(a)** Dispersion relations of the single-layer system (4.1) and the uncoupled two-layer system (4.16) (i.e., when $c_1 = c_2 = 0$). The black dashed and dash-dotted curves represent the dispersion relations of two single-layer subsystems with distinct diffusion scales: $(D_p^{(1)}, D_w^{(1)}) = (0.5, 50)$ for the dashed curve, and $(D_p^{(2)}, D_w^{(2)}) = (0.015, 1.5)$ for the dash-dotted curve. All other parameter values are as in Fig. 4.2. The colored curves illustrate the dispersion relations of the coupled two-layer system under varying coupling strengths: red for weak coupling ($c_1 = c_2 = 0.003$), blue for intermediate coupling ($c_1 = c_2 = 0.03$), and magenta for strong coupling ($c_1 = c_2 = 0.1$). In the weak coupling regime, the composite dispersion relation (red curve) retains two distinct peaks at different wavenumber scales, corresponding to multiscale instability. As coupling strength increases, the interaction between layers causes these peaks to merge. In the strong coupling regime (magenta curve), the system exhibits a single dominant unstable mode, indicating convergence to a unified pattern scale. **(b)** Spatial profiles of the state variables in a one-dimensional domain under weak coupling ($c_1 = c_2 = 0.003$). Solid curves represent the concentrations in the top layer, while dashed curves correspond to the bottom layer. It is evident that the wavelengths of P_1 and W_1 (top layer) are larger than those of P_2 and W_2 (bottom layer), reflecting the difference in diffusion rates between the layers.

Since one-dimensional spatial domains are insufficient to capture complex spatial configurations, such as hexagonal spots and labyrinthine patterns, we extend our analysis to a two-dimensional square domain, which better represents the spatial structures observed in real-world dryland ecosystems. Specifically, we consider the spatial domain $\Omega = [0, L] \times [0, L]$, where L denotes the side length of the square domain. To introduce a clear separation of spatial scales between the two soil layers, we assign diffusion coefficients with a scale disparity of $33\frac{1}{3}$ between the top and bottom layers.

For the topsoil layer and the shallow-rooted plant phenotype, the diffusion coefficients are set as $(D_1^{(1)}, D_2^{(1)}) = (0.5, 50)$, while the bottom soil layer and the deep-rooted phenotype are assigned $(D_1^{(2)}, D_2^{(2)}) = (0.015, 1.5)$. These values satisfy $D_1^{(1)} \gg D_1^{(2)}$ and $D_2^{(1)} \gg D_2^{(2)}$, enabling the emergence of multiscale spatial patterns across the vertically stratified soil profile. The system is initialized by perturbing the uniform steady state $(P_1^*, W_1^*, P_2^*, W_2^*)$ with small-amplitude random fluctuations. Specifically, the initial densities are defined as

$$P_i(x, y, 0) = P_i^* + \epsilon\psi_i, \quad W_i(x, y, 0) = W_i^* + \epsilon\phi_i, \quad i = 1, 2,$$

where $(x, y) \in \Omega$, ψ_i and ϕ_i are random variables drawn from a uniform distribution $\mathcal{U}(-0.5, 0.5)$, and $\epsilon = 10^{-3}$ denotes the perturbation strength. The following zero-flux (Neumann) boundary conditions are applied to prevent mass loss across the domain boundaries:

$$\left.\frac{\partial P_i}{\partial \nu}\right|_{\partial\Omega} = 0, \quad \left.\frac{\partial W_i}{\partial \nu}\right|_{\partial\Omega} = 0, \quad i = 1, 2,$$

where ν denotes the outward normal vector to the boundary $\partial\Omega$. To numerically integrate the coupled reaction-diffusion system, we discretize both space and time using the Forward-Time Central-Space (FTCS) scheme.

To investigate the emergence of multiscale vegetation patterns within a shared spatial domain, we vary the water input rates in the two stratified soil layers: r_1 for the top layer and r_2 for the bottom layer. The analysis is conducted under a weak coupling regime, wherein inter-layer interactions are minimal, allowing each layer to exhibit its intrinsic pattern-forming dynamics independently. We examine the resulting spatial configurations in terms of total vegetation biomass, quantified as the sum of the densities of the shallow-rooted and deep-rooted plant phenotypes, i.e., $P_1(\vec{x}, t) + P_2(\vec{x}, t)$, over a two-dimensional domain of size 200×200 units. The parameters r_1 and r_2 are varied continuously within the range $0.169 \leq r_1, r_2 \leq 0.413$, where r_1 is varied along the vertical axis and r_2 along the horizontal axis of the parameter plane. Figure 4.6 illustrates the spectrum of spatial patterns that emerge across this parameter space. These patterns demonstrate how differences in water availability across soil layers shape the morphology and spatial scale of vegetation structures. At low values of both r_1 and r_2, the model produces hot-spot patterns in both layers, resulting in a composite multiscale structure of overlapping hot spots at different spatial resolutions (bottom-left corner of Fig. 4.6). Conversely, at high values of both r_1 and r_2, the system exhibits overlapping cold-spot patterns at large and small scales (top-right corner). A similar transition is observed when varying r_1 while keeping r_2 fixed at a low value. Moving vertically along the leftmost column of Fig. 4.6, the shallow-rooted phenotype progresses through a sequence of hot-spot,

labyrinth, and cold-spot patterns, superimposed on the relatively persistent small-scale hot-spot patterns of the deep-rooted phenotype. This systematic exploration reveals a total of $3 \times 3 = 9$ distinct multiscale vegetation configurations, resulting from the combination of three large-scale (top layer) and three small-scale (bottom layer) pattern types. These findings highlight the rich diversity of spatial structures that can emerge through coupled plant-water feedbacks under differential water input in vertically stratified soils.

4.5 Realistic inter-layer coupling

Building on the theoretical foundation of two-layer gradient-dependent coupling in multiscale pattern formation in the previous section, we extend the model by introducing modified reaction terms that capture more realistic biophysical processes, namely, soil water infiltration and phenotype-driven root transitions. While these biologically grounded modifications reduce analytical tractability and complicate linear stability and weakly nonlinear analyses, they significantly enhance the model's ecological realism. This extension enables a more accurate and representative depiction of vegetation dynamics in natural dryland ecosystems.

Building on the previously described plant–soil water interaction framework, we now incorporate additional mechanisms that implicitly couple the dynamics of the two soil layers. Unlike the explicit gradient-dependent coupling defined in Eq. (4.17), the coupling here is embedded within the core feedback processes of the system. The revised modeling approach refines and extends the equations in (4.16), removing biologically unrealistic assumptions associated with gradient-based coupling. The key considerations underlying this improved formulation are as follows:

- **Phenotypic transitions and growth:**
  Local dynamics, particularly intraspecific competition and subsoil water availability, drive the transition from shallow- to deep-rooted plant phenotypes. This adaptive shift is modeled through the interaction term $\Psi P_1 W_2$, where Ψ denotes the transition rate. Biologically, this represents a strategic response: when topsoil resources become limiting and deeper water is available, plants invest in deeper rooting to enhance water acquisition. This transition is modeled as unidirectional, unlike the bidirectional structure assumed in the gradient-dependent coupling. Once a plant shifts to the deep-rooted phenotype, it remains in that state. This irreversibility is ecologically justified, as the structural and energetic

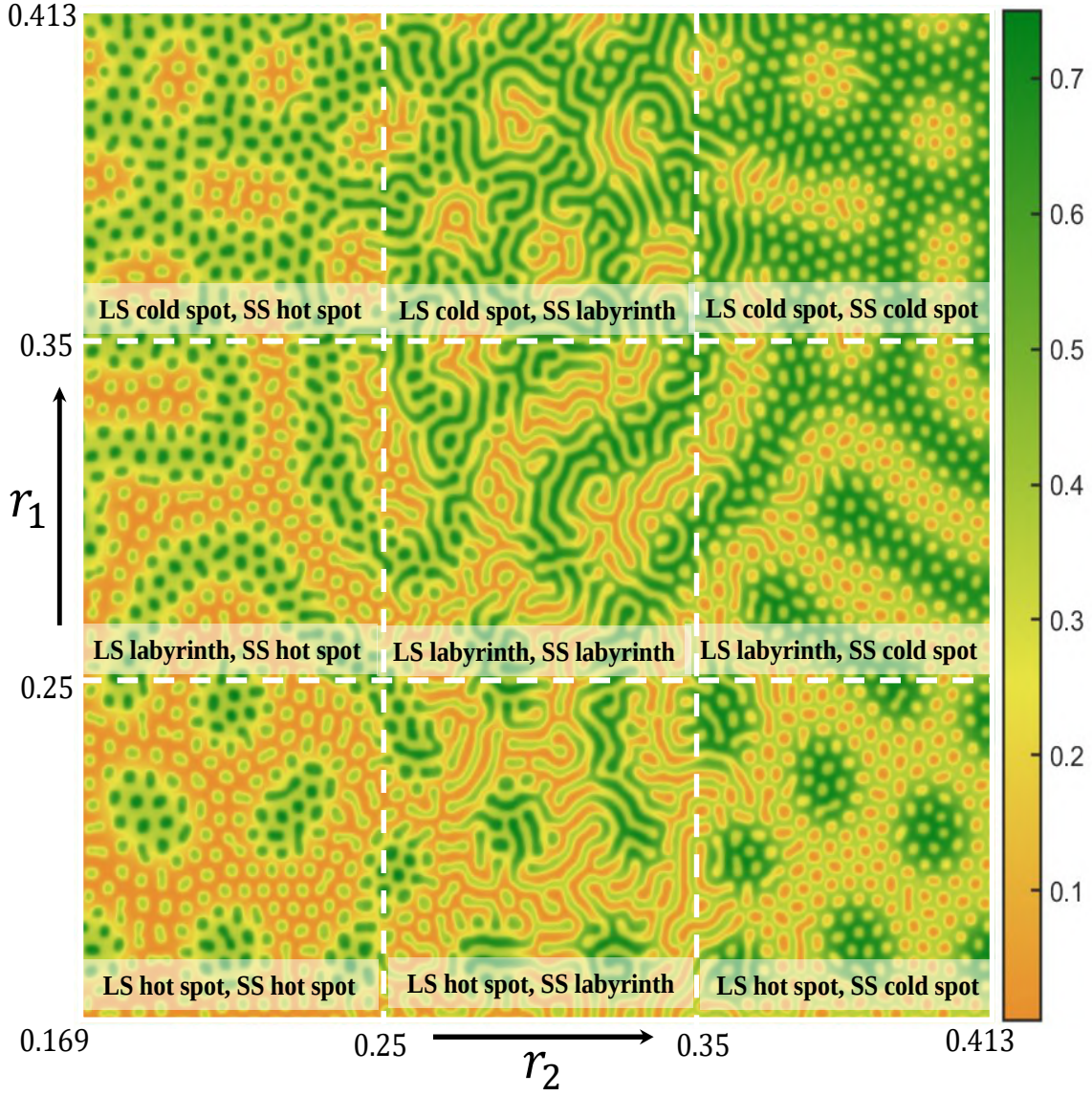

FIGURE 4.6: Spatial distribution of total vegetation density $(P_1 + P_2)$ at heterogeneous steady states. Multiscale patterns from the two-layer model (4.16) with coupling (4.17) are shown for varying r_1 (vertical) and r_2 (horizontal). The system yields 3×3 distinct large-scale (LS) and small-scale (SS) pattern combinations. Simulations use a 200×200 unit domain with horizontal and vertical white lines marking low, intermediate, and high r_1 and r_2. The parameter values are the same as before, with diffusion rates of the two-layer are $(D_1^{(1)}, D_1^{(2)}) = (0.5, 50)$ and $(D_2^{(1)}, D_2^{(2)}) = (0.015, 1.5)$.

investment required for deeper rooting makes reversal impractical or evolutionarily unfavorable [175].

Growth of the deep-rooted phenotype is modeled via a saturating functional response $\frac{\gamma(W_2+\theta_2 W_1)P_2}{1+\sigma(W_2+\theta_2 W_1)}$, reflecting the plant's capacity to utilize water from both layers. It quantifies the principle of partial resource overlap [176], wherein deep-rooted plants primarily exploit subsoil moisture (W_2) but also partially benefit from topsoil water (W_1). This formulation acknowledges the physiological plasticity of deep-rooted plants and their enhanced resilience under fluctuating resource conditions.

- **Water uptake dynamics:**
  The topsoil water (W_1) is primarily absorbed by shallow-rooted plants, which are morphologically optimized to access near-surface moisture. However, deep-rooted plants also extract a limited amount of water from this layer. This asymmetric interaction is captured via the parameter θ_2, which quantifies the fractional uptake by deep-rooted plants. The total water uptake from the topsoil is thus modeled by the term $W_1^2(P_1 + \theta_2 P_2)$. Deep-rooted plants draw water from the bottom soil layer (W_2) through the term $-W_2^2 P_2$, as considered earlier.

- **Topsoil layer evaporation:**
  Evaporation predominantly occurs from the topsoil, which is directly exposed to the atmosphere. In contrast, the subsoil is largely insulated from such loss. Both plant phenotypes contribute to reducing topsoil evaporation through shading. Additionally, root structures improve soil water retention by increasing porosity and limiting hydraulic conductivity [177]. Though deep-rooted plants extract water from the subsoil, their fine roots in the topsoil also help retain moisture. To represent this, we introduce the parameter θ_1, which denotes the fractional influence of deep-rooted plants on topsoil evaporation. Therefore, the net evaporation term is modeled as $-(1-\rho(P_1+\theta_1 P_2))$, where ρ quantifies the strength of the shading effect.

- **Inter-soil layer water movement:**
  Soil water distribution varies vertically due to texture, porosity, and exposure. Topsoil is prone to rapid evaporation and drainage, whereas subsoil retains moisture longer [178]. Vertical water flow is also affected by soil compactness, with compact layers slowing down percolation [179, 180]. We consider that the rainfall (r) enters through the topsoil. A portion percolates into the subsoil at a rate $\tau_1 W_1$, while subsoil water is lost through gravitational drainage at rate $\tau_2 W_2$, representing downward movement beyond the root zone.

- **Differential diffusion:**
  Differential diffusion arises from both ecological strategies and physical constraints. Shallow-rooted plants, representing the default phenotype, spread rapidly through clonal growth and seed dispersal, whereas deep-rooted plants, representing induced phenotypes, spread more slowly. Accordingly, we assume $D_1^{(1)} \gg D_1^{(2)}$. Similarly, subsoil layers possess lower permeability due to compaction and reduced porosity [181, 182], leading to slower water diffusion compared to the topsoil. Hence, $D_2^{(1)} \gg D_2^{(2)}$.

Guided by these assumptions, we reformulate the Hardenberg et al. model (4.1) into a model describing the interaction between two plant phenotypes and two soil layers, as follows:

$$\frac{\partial P_1}{\partial t} = \frac{\gamma W_1 P_1}{1+\sigma W_1} - P_1^2 - \mu P_1 - \Psi P_1 W_2 + D_1^{(1)} \nabla^2 P_1, \tag{4.22a}$$

$$\frac{\partial W_1}{\partial t} = r - (1 - \rho(P_1 + \theta_1 P_2))\, W_1 - R W_1^2 (P_1 + \theta_2 P_2) - \tau W_1 + D_1^{(1)} \nabla^2 (W_1 - \beta P_1), \tag{4.22b}$$

$$\frac{\partial P_2}{\partial t} = \frac{\gamma (W_2 + \theta_2 W_1) P_2}{1+\sigma (W_2 + \theta_2 W_1)} - P_2^2 - \mu P_2 + \Psi P_1 W_2 + D_1^{(2)} \nabla^2 P_2, \tag{4.22c}$$

$$\frac{\partial W_2}{\partial t} = \tau_1 W_1 - \tau_2 W_2 - R W_2^2 P_2 + D_2^{(2)} \nabla^2 (W_2 - \beta P_2). \tag{4.22d}$$

4.5.1 Computational results

The diffusion coefficients are chosen as $(D_1^{(1)}, D_2^{(1)}, D_1^{(2)}, D_2^{(2)}) = (0.5, 50, 0.0035, 0.35)$, reflecting the sharp contrast in lateral dispersal between the two plant phenotypes and the water content in the two soil layers. The corresponding diffusion scale factors, $s = D_1^{(1)}/D_1^{(2)} = 142.86$ for the plant phenotypes and the soil water layers, quantify these disparities. This mobility scale s, whether arising from species traits or environmental properties, plays a critical role in determining the spatial scale of self-organized patterns. Since the pattern wavelength is inversely proportional to the wavenumber, the characteristic wavelength, given by $\frac{2\pi}{k}$, of the unstable pattern-forming modes scales as $s^{1/2}$, where s is the diffusion scaling factor. Interestingly, the onset conditions for Turing instability are unaffected by the value of s. In this setup, the diffusion scale ratio between the two soil layers is approximately $s \approx 142.85$, implying a theoretical wavelength ratio of $s^{1/2} \approx 12.52$. The corresponding dispersion relation (Fig. 4.7a) exhibits two distinct peaks: a low-wavenumber peak at $k_l = 0.29$ associated with shallow-rooted plants and topsoil interactions, and a high-wavenumber peak at $k_s = 3.63$ arising from deep-rooted plants and subsoil processes. This results in a wavenumber ratio of $k_s/k_l = 12.51$, indicating a strong separation

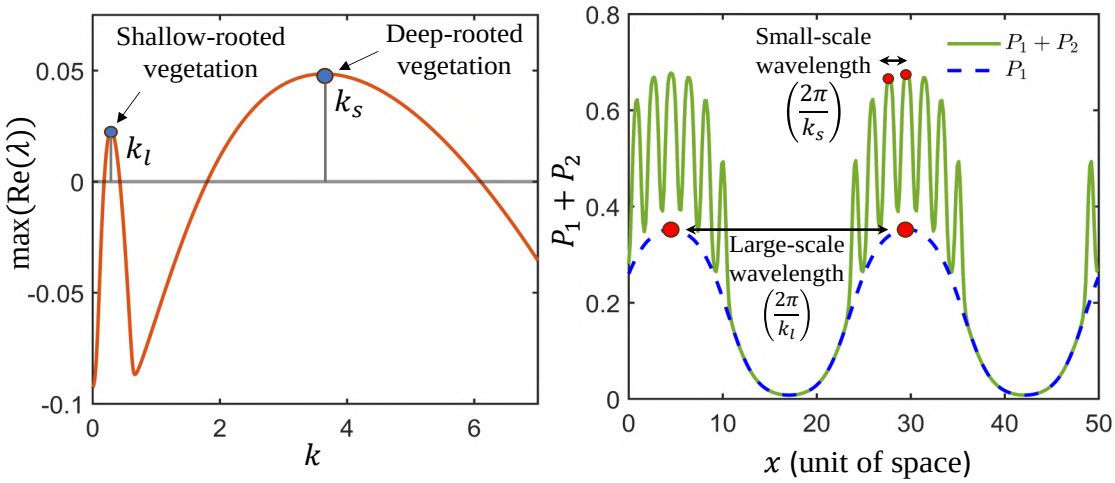

FIGURE 4.7: **(a)** Dispersion relation for the modified two-layer reaction–diffusion system (4.22) showing two dominant peaks. Blue dots mark the unstable wavenumbers k_l (large-scale patterns from shallow-rooted plants) and k_s (small-scale patterns from deep-rooted plants). **(b)** One-dimensional total population patterns illustrate multiscale vegetation structures with distinct wavelengths, with red dots marking vegetation density peaks at both scales. Model parameters are as in Fig. 4.3, with additional inter-layer coupling values $\Psi = 0.01$, $\theta_1 = 0.5$, $\theta_2 = 0.5$, $\tau_1 = 0.1$, and $\tau_2 = 1.2$.

of spatial scales. The simulated one-dimensional patterns (Fig. 4.7b) clearly reflect this separation. Deep-rooted plants generate fine-scale patterns with a characteristic wavelength of approximately $2\pi/k_s = 1.73$, while shallow-rooted plants form coarser patterns with a wavelength of approximately $2\pi/k_l \approx 21.66$. However, the actual pattern wavelengths observed in simulations deviate slightly from those predicted by linear theory. Averaging results from multiple runs yields a large-scale wavelength of $\lambda_l = 24.55$ and a small-scale wavelength of $\lambda_s = 1.85$, resulting in a scale separation ratio of $\lambda_l/\lambda_s \approx 13.27$. This minor discrepancy from the theoretical prediction ($\sqrt{s} \approx 12.52$) is likely due to nonlinear effects inherent in the reaction terms of the system.

We simulated the modified two-layer vegetation model (4.22) over a two-dimensional spatial domain to examine the emergence of multiscale vegetation patterns under three different mean precipitation rates: $r = 0.4$, 0.35, and 0.2 (see Figs. 4.8a–c). As precipitation decreases, the spatial configuration of the shallow-rooted plant population (P_1) undergoes a distinct sequence of pattern transitions from cold-spot patterns (Fig. 4.8a) to stripe-like structures (Fig. 4.8b), and ultimately to hot-spot patterns (Fig. 4.8c). This sequence corresponds well with empirical observations of vegetation pattern transitions in dryland ecosystems under increasing water stress, as illustrated in Fig. 1d(i–iii). Notably, the deep-rooted plant phenotype (P_2) consistently forms

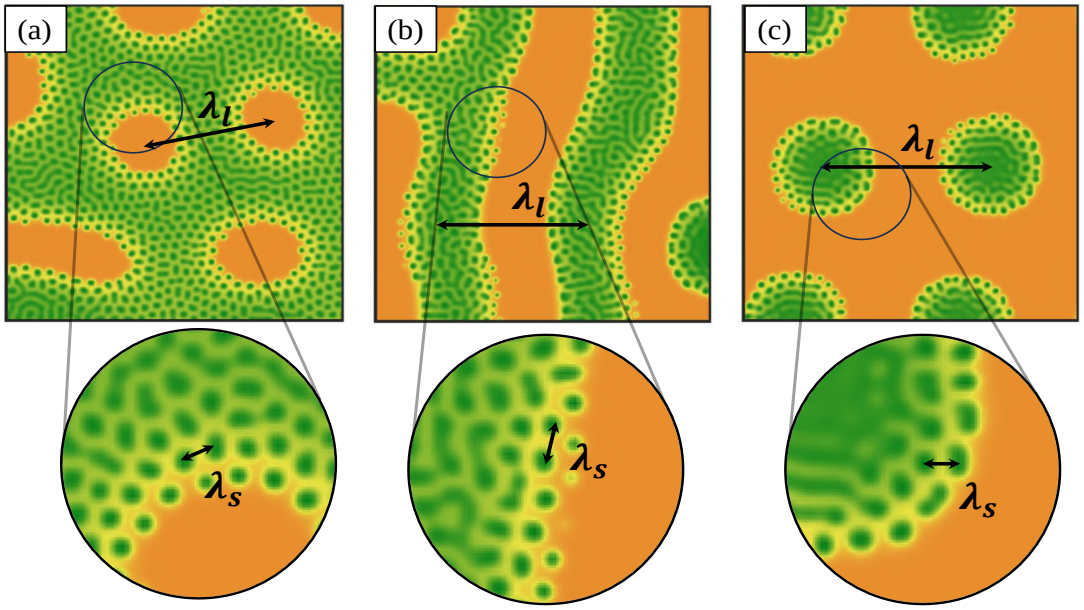

FIGURE 4.8: Vegetation patterns on a two-dimensional domain of size 50×50 units for three precipitation values: $r = 0.4$, 0.35, and 0.2. Plots show the spatial distribution of total vegetation density $P_1 + P_2$. As precipitation decreases, large-scale structures transition from hot-spot to stripe, and finally to cold-spot patterns. In all cases, small-scale hot-spot patterns from deep-rooted vegetation (P_2) persist, superimposed on the large-scale structures formed by shallow-rooted plants (P_1). Zoomed-in panels highlight these fine-scale features, revealing the shorter wavelengths of the deep-rooted phenotype.

fine-scale hot-spot patterns across all precipitation levels. These patterns are spatially clustered around the larger-scale structures formed by the shallow-rooted plants. The persistence of these small-scale distributions is attributed to the deep-rooted plants' ability to access water from the subsoil, allowing them to avoid direct competition for limited moisture in the topsoil.

4.6 Discussion

This study introduces a biologically informed, two-layer reaction-diffusion model incorporating phenotypic plasticity to investigate the emergence of multiscale vegetation patterns in arid and semi-arid ecosystems. Building upon the foundational single-layer models of vegetation pattern formation [58, 167, 57], we extend the framework by integrating a second soil layer and a corresponding deep-rooted plant phenotype.

This extension is inspired by Walter's two-layer hypothesis [70, 71], which emphasizes differential resource uptake from topsoil and subsoil layers by plants with varied rooting depths.

Our model shows that the combination of contrasting diffusion rates between layers and unidirectional phenotypic transitions yields spatial patterns spanning multiple scales. Specifically, shallow-rooted plants, with higher spatial mobility, generate large-scale patterns such as stripes and cold spots, while deep-rooted phenotypes form tightly clustered, small-scale hot-spot patterns. This scale separation mirrors real-world vegetation structures, such as the Namibian "fairy circles" and Australian desert mosaics, where nested or superimposed patterns are observed in satellite imagery and field surveys [163, 164, 166].

Initially, we investigated a simplified framework incorporating gradient-dependent coupling between layers. Linear stability and weakly nonlinear analyses under this setting reveal a dispersion relation with two distinct peaks, each corresponding to a dominant unstable wave mode at a specific spatial scale. This theoretical prediction is validated by numerical simulations, where multiscale vegetation patterns, comprising nested hot-spots, labyrinths, and cold-spots, emerge across a range of precipitation conditions. As expected from classical Turing theory [41], the wavelength of emerging patterns is inversely related to the square root of the diffusion scale. Our findings extend this principle to multilayered systems with anisotropic feedbacks and asymmetric biological transitions.

Notably, the more ecologically realistic model, incorporating gravitational infiltration, soil moisture retention, and unidirectional phenotype switching, exhibits even richer spatial dynamics. While analytical tractability is reduced due to nonlinear interactions, numerical simulations confirm the persistence of multiscale patterns. Importantly, these patterns remain robust under moderate variations in precipitation, indicating the stabilizing role of phenotypic plasticity and vertical resource partitioning. The deep-rooted phenotype, by accessing subsoil moisture unavailable to shallow-rooted plants, mitigates competition and facilitates coexistence, thereby enhancing vegetation cover and pattern resilience under water-limited conditions.

Theoretical insights from our study echo earlier work in layered chemical reaction-diffusion systems [64, 172] and ecological contexts such as plankton blooms [65], where multiscale instabilities give rise to superlattice or nested patterns. In our case, the coupling strength between soil layers plays a crucial role: under weak coupling, distinct spatial modes dominate independently in each layer, resulting in superimposed patterns of different scales. As coupling strength increases, these modes begin to interact, leading to synchronization and eventual convergence toward a single-scale pattern, consistent with previous findings on multiscale instability collapse [173].

This work opens several promising avenues for future research. First, empirical validation through high-resolution remote sensing, combined with field-based measurements of root profiles and soil moisture across depths, would help ground-truth the theoretical predictions and assess the model's applicability to real dryland ecosystems. Second, incorporating environmental variability, such as seasonal rainfall cycles or stochastic precipitation events, could provide insights into the dynamical stability and resilience of multiscale patterns under climate fluctuations. Third, extending spatial realism by exploring vegetation pattern formation in three-dimensional domains or in landscapes with heterogeneity, such as sloped terrains or variable soil textures, could substantially improve the ecological realism of the model. Finally, biodiversity and community interactions could be addressed by integrating additional plant species with diverse competitive strategies, root morphologies, or facilitative interactions [183], enabling investigation of how species diversity both shapes and is shaped by multiscale spatial organization.

In conclusion, our findings highlight the crucial role of vertical soil structure, phenotypic plasticity, and layered feedback mechanisms in shaping vegetation self-organization. By incorporating biologically realistic processes, such as unidirectional phenotypic transitions and vertical water flux, the model reproduces a broader range of spatial configurations consistent with those observed in nature. Through linking theoretical modeling with ecological processes, this work deepens our understanding of dryland vegetation resilience and provides a framework for exploring multiscale pattern formation in complex ecological systems.

4.7 Expressions of variables in amplitude equation

For the two-species reaction-diffusion system in the general form as (4.2), the evolution equation of perturbations containing some order of nonlinear terms, close to the Turing bifurcation point of the control parameter (say r), is given by

$$\frac{\partial \vec{X}}{\partial t} = F(\vec{X}) = L\vec{X} + NL(\vec{X}), \quad \text{where} \quad \vec{X} = \begin{pmatrix} u \\ v \end{pmatrix}, \quad F(\vec{X}) = \begin{pmatrix} f(u,v) \\ g(u,v) \end{pmatrix},$$

where u, v are the perturbation terms about the uniform steady state.

The linear term is

$$\begin{aligned} L &= L_T + (r_T - r)N \\ &= \begin{pmatrix} J_{11}^T + D_{11}\nabla^2 & J_{12}^T + D_{12}\nabla^2 \\ J_{21}^T + D_{21}\nabla^2 & J_{22}^T + D_{22}\nabla^2 \end{pmatrix} + (r_T - r)\begin{pmatrix} n_{11} & n_{12} \\ n_{21} & n_{22} \end{pmatrix}, \end{aligned}$$

with

$$\begin{pmatrix} J_{11}^T & J_{12}^T \\ J_{21}^T & J_{22}^T \end{pmatrix} = \begin{pmatrix} \frac{\partial f}{\partial u} & \frac{\partial f}{\partial v} \\ \frac{\partial g}{\partial u} & \frac{\partial g}{\partial v} \end{pmatrix}_{E^*}, \quad J_{ij}^T = J_{ij}|_{p=p_T}, \quad n_{ij} = -\frac{dJ_{ij}}{dp}\bigg|_{p=p_T} \quad \text{for} \quad i,j = 1,2.$$

The critical value of the control parameter r is r_T. Note that all the J_{ij} in this proposition are at $r = r_T$. Thus, r in the model is a variable parameter, and J_{ij} is dependent on r. The nonlinear terms of perturbations close to the Turing bifurcation points are

$$\begin{aligned} NL(\vec{X}) &= \begin{pmatrix} f_{11}u^2 + f_{12}uv + f_{22}v^2 \\ g_{11}u^2 + g_{12}uv + g_{22}v^2 \end{pmatrix} \\ &+ \begin{pmatrix} f_{111}u^3 + f_{112}u^2v + f_{122}uv^2 + f_{222}v^3 \\ g_{111}u^3 + g_{112}u^2v + g_{122}uv^2 + g_{222}v^3 \end{pmatrix} + o(|\vec{X}|^4), \end{aligned}$$

where

$$\begin{aligned} \begin{pmatrix} f_{11} & f_{12} & f_{22} \\ g_{11} & g_{12} & g_{22} \end{pmatrix} &= \frac{1}{2} \begin{pmatrix} \frac{\partial^2 f}{\partial u^2} & \frac{\partial^2 f}{\partial u \partial v} & \frac{\partial^2 f}{\partial v^2} \\ \frac{\partial^2 g}{\partial u^2} & \frac{\partial^2 g}{\partial u \partial v} & \frac{\partial^2 g}{\partial v^2} \end{pmatrix} \Bigg|_{E^*}, \\ \begin{pmatrix} f_{111} & f_{112} & f_{122} & f_{222} \\ g_{111} & g_{112} & g_{122} & g_{222} \end{pmatrix} &= \frac{1}{6} \begin{pmatrix} \frac{\partial^3 f}{\partial u^3} & \frac{\partial^3 f}{\partial u^2 \partial v} & \frac{\partial^3 f}{\partial u \partial v^2} & \frac{\partial^3 f}{\partial v^3} \\ \frac{\partial^3 g}{\partial u^3} & \frac{\partial^3 g}{\partial u^2 \partial v} & \frac{\partial^3 g}{\partial u \partial v^2} & \frac{\partial^3 g}{\partial v^3} \end{pmatrix} \Bigg|_{E^*}. \end{aligned}$$

At the critical Turing bifurcation point $r = r_T$ and the critical wavenumber is $k_T = \sqrt[4]{\frac{\mathcal{D}}{det(D)}}$ (following proposition (4.2)). Define $\phi = -\frac{J_{12}^T - D_{12}k_T^2}{J_{11}^T - D_{11}k_T^2}$, $\psi = -\frac{J_{12}^T - D_{12}k_T^2}{J_{22}^T - D_{22}k_T^2}$. Then amplitude equations of first-order amplitudes (W_i, $i = 1,2,3$) of perturbations are

$$\begin{aligned} (\phi+\psi)\frac{\partial W_1}{\partial T_1} &= p_1\left[(n_{11}\phi + n_{12}) + \psi(n_{21}\phi + n_{22})\right]W_1 + (I_1 + \psi I_2)2\bar{W}_2\bar{W}_3, \\ (\phi+\psi)\frac{\partial W_2}{\partial T_1} &= p_1\left[(n_{11}\phi + n_{12}) + \psi(n_{21}\phi + n_{22})\right]W_2 + (I_1 + \psi I_2)2\bar{W}_3\bar{W}_1, \\ (\phi+\psi)\frac{\partial W_3}{\partial T_1} &= p_1\left[(n_{11}\phi + n_{12}) + \psi(n_{21}\phi + n_{22})\right]W_3 + (I_1 + \psi I_2)2\bar{W}_1\bar{W}_2, \end{aligned}$$

The amplitude equations upto second-order amplitudes (A_i, $i = 1,2,3$) of perturbations then read

$$\tau_0 \frac{\partial A_1}{\partial t} = \eta A_1 + h\bar{A}_2\bar{A}_3 - \left[g_1|A_1^2| + g_2(|A_2|^2 + |A_3|^2)\right] A_1, \tag{4.23a}$$

$$\tau_0 \frac{\partial A_2}{\partial t} = \eta A_2 + h\bar{A}_3\bar{A}_1 - \left[g_1|A_2^2| + g_2(|A_3|^2 + |A_1|^2)\right] A_2, \tag{4.23b}$$

$$\tau_0 \frac{\partial A_3}{\partial t} = \eta A_3 + h\bar{A}_1\bar{A}_2 - \left[g_1|A_3^2| + g_2(|A_1|^2 + |A_2|^2)\right] A_3, \tag{4.23c}$$

where $\tau_0 = \frac{\phi+\psi}{r_T Q}$, $\eta = \frac{|r_T - r|}{r_T}$, $h = \frac{2(I_1+\psi I_2)}{r_T Q}$, $g_1 = -\frac{G_1}{r_T Q}$, $g_2 = -\frac{G_2}{r_T Q}$ with

$$\begin{aligned}
&I_1 = f_{11}\phi^2 + f_{12}\phi + f_{22},\\
&I_2 = g_{11}\phi^2 + g_{12}\phi + g_{22}\\
&Q = (\phi n_{11} + n_{12}) + \psi(\phi n_{21} + n_{22}),\\
&G_1 = (u_{00} + u_{11})(H_1 + \psi H_2) + (v_{00} + v_{11})(H_3 + \psi H_4) + 3(R_1 + \psi R_2),\\
&G_2 = (u_{00} + u_{22})(H_1 + \psi H_2) + (v_{00} + v_{22})(H_3 + \psi H_4) + 6(R_1 + \psi R_2),\\
&H_1 = 2f_{11}\phi + f_{12}, \quad H_2 = 2g_{11} + g_{12},\\
&H_3 = 2f_{22} + f_{12}\phi, \quad H_4 = 2g_{22} + g_{12}\phi,\\
&R_1 = f_{111}\phi^3 + f_{112}\phi^2 + f_{122}\phi + f_{222},\\
&R_2 = g_{111}\phi^3 + g_{112}\phi^2 + g_{122}\phi + g_{222},
\end{aligned}$$

and

$$\begin{aligned}
\begin{pmatrix} u_{00} \\ v_{00} \end{pmatrix} &= -2L_T^{-1} \begin{pmatrix} I_1 \\ I_2, \end{pmatrix},\\
\begin{pmatrix} u_{11} \\ v_{11} \end{pmatrix} &= -(L_T^{-1} - 4K_T^2 D) \begin{pmatrix} I_1 \\ I_2, \end{pmatrix},\\
\begin{pmatrix} u_{22} \\ v_{22} \end{pmatrix} &= -2(L_T^{-1} - 3K_T^2 D) \begin{pmatrix} I_1 \\ I_2, \end{pmatrix}.
\end{aligned}$$

Chapter 5

Spatiotemporal instabilities and climate-driven extinction in predator-prey systems

5.1 Introduction

Predator-prey systems have become a central focus in the study of Turing patterns. Early ecological applications of Turing's theory include the pioneering work of Segel and Jackson [42], who showed that predator-prey interactions with contrasting diffusion rates of species could spontaneously generate patchiness in ecological systems. Since then, a wide variety of predator-prey models have been shown to admit Turing instabilities, producing spatial patterns ranging from spots and stripes to more intricate labyrinthine structures [184, 185, 186, 48, 187, 141]. Apart from classical Turing patterns, spatiotemporally oscillatory or non-Turing patterns are also observed [188, 189, 190, 191]. The non-Turing patterns encompass spiral patterns [63, 192], traveling waves [193], spatiotemporal chaos [194, 195, 196, 197], etc. Non-Turing instabilities are classified into various categories depending on the nature of unstable spatial modes, such as pure-Hopf, pure-wave, and mixed types, like Hopf-Turing, Hopf-wave, and Hopf-wave-Turing [63, 198, 199]. Particularly, Hopf-Turing instability is interesting as it contains two frequently observed contrasting instabilities, Turing and Hopf [190, 191, 141]. Both are responsible for heterogeneous patterns. Although the former gives nonuniform steady state patterns, the latter gives spatiotemporal oscillations, including spatiotemporal chaos. The dominance of two competing instabilities in the Hopf-Turing state determines the eventual patterns of the system [141, 200].

Spatiotemporal oscillations in predator-prey systems have emerged as a foundational theme in understanding population dynamics across large ecological landscapes. In spatially extended ecosystems, species disperse in search of favourable conditions, seeking to mitigate local resource depletion [201], avoid intraspecific competition [202], and escape predation pressure [203], a process that adds complexity to local and regional population abundance [53]. However, paradoxically, these same dispersal-driven dynamics can give rise to catastrophic outcomes. Among the most dramatic of these is the landscape-scale collapse of both predator and prey populations, due to a synchronized extinction event in which population oscillations across space align in phase and amplitude, culminating in simultaneous global extinction [10, 11]. In a synchronized state, population minima co-occur across the landscape, eliminating high-density refugia and thereby disabling the "rescue effect", the process through which declining populations are replenished by immigrants from highly abundant regions [204, 205]. Thus, the system loses its ability to buffer against localized extinctions, increasing the likelihood of landscape-scale collapse. In contrast, asynchronous population dynamics prevent extinction as troughs in some regions occur concurrently with peaks in others. This asynchrony acts as a safeguard, creating a dynamic mosaic where declines in one location are offset by growth in another. Asynchronous fluctuations thus facilitate recolonization and recovery following local perturbations, reinforcing overall species persistence [206, 207]. Moreover, systems characterized by heterogeneous steady states, where populations reach different stable levels instead of oscillations, are even more resilient [208, 74]. Such heterogeneous configurations sometimes withstand substantial environmental or demographic shocks, preserving population continuity under stress [208, 74, 209, 57].

In metapopulation systems, synchrony is widely studied both theoretically and empirically [10, 210, 211, 212, 213, 214]. However, little attention is given to the spatiotemporal synchrony of reaction-diffusion systems showing different spatiotemporal or non-Turing instabilities. Sherrat et al. [49] reviewed synchrony in oscillatory travelling wave solutions in predator-prey reaction-diffusion system. Chakraborty et al. [198] observed the trend of oscillations under different non-Turing instability regimes in the three-species food web model. They showed synchronous oscillations in the case of Hopf-dominated instabilities (Hopf, Hopf-Turing and Hopf-wave) using population fluctuations in individual spatial locations and spatial mean. Whereas wave instability shows asynchronous spatiotemporal oscillations. However, a compelling and relatively unexplored question in reaction-diffusion systems is how these distinct spatiotemporal dynamics respond to fluctuating environmental conditions?

Recent studies on ecological systems have investigated the effects of climatic fluctuations and tipping phenomena, primarily using non-spatial ODE-based models. Alkhayuon et al. [215] demonstrated phase tipping (P-tipping) in a single-patch predator-prey model, showing that abrupt environmental changes may cause species

extinction from a specific phase of population cycles. This idea is extended to discrete-time host-parasitoid models by Dyck and Tyson [216]. In a different direction, Hasan et al. [217] explored rate tipping (R-tipping) and bifurcation tipping (B-tipping) in spatially extended reaction-diffusion systems, where tipping occurred between homogeneous steady states. However, the impact of competing spatiotemporal instabilities, such as Turing and Hopf modes, on tipping dynamics and species persistence remains largely unexplored.

To address this gap, we spatially extend the predator-prey model used by Alkhayuon et al. [215] to a continuous domain and investigate its spatiotemporal dynamics. Specifically, we focus on the emergence of oscillations under the Hopf-Turing instability regime and examine how dominant instability modes shape species persistence under climatic fluctuations.

Our results demonstrate that the nature of the dominant instability, Turing or Hopf, in the Hopf-Turing instability regime significantly influences system dynamics. When Turing modes dominate, the system transitions from irregular transients to a spatially heterogeneous steady state, enhancing resilience. In contrast, Hopf-dominated dynamics produce near-synchronous oscillations across space, making the system susceptible to abrupt environmental perturbations and synchronized collapses.

We quantify temporal variability and spatial synchrony to distinguish these behaviors, revealing stark differences in system responses. These findings extend the concept of P-tipping from non-spatial to spatial systems, highlighting the crucial roles of spatial heterogeneity and synchrony in determining extinction risk. Our numerical results suggest that Turing-dominated regimes can buffer against environmental variability, while Hopf-dominated patterns, with their high synchrony, amplify the risk of large-scale extinction.

The remainder of the chapter is organized as follows. In Section 5.2, we provide a concise overview of the two-species predator-prey reaction-diffusion model under consideration. Section 5.3 presents a local stability analysis of the equilibrium points without spatial diffusion. In Section 5.4, we derive and analyze the conditions under which spatiotemporal instabilities (pure and mixed) emerge, supported by corresponding numerical simulations. Dynamics at different regimes are verified by temporal fluctuation and synchrony measures. Finally, Section 5.5 explores the influence of environmental fluctuations on the system's dynamical behaviour. The chapter ends with a discussions in Section 5.6.

TABLE 5.1: Parameter descriptions and their default values with reference.

Parameters with definition	Value	Reference
r – Intrinsic prey growth rate	Variable /year	[215]
c – Intraspecies competition coefficient	0.22	[215]
μ – Allee threshold	0.03 (prey/ha)	[215]
ν – positive constant	0.003 (prey/ha)	[215]
α – Maximum predation rate	505 (prey/(predator . yr))	[215]
β – Half-saturation constant	0.3 (prey/ha)	[215]
s – Intrinsic growth rate of predator	0.85 (/year)	[215]
q – Positive parameter	205 (prey/predator)	[215]
ϵ – Positive parameter	0.031 (prey/ha)	–
δ – Diffusion coefficient	Variable	
ξ – Scaling factor	1-10	–

5.2 Model description

We consider the following system of coupled partial differential equations to describe the spatiotemporal interaction of prey and predators over a continuous spatial domain:

$$\frac{\partial X}{\partial t} = r(t)X\left(1-\frac{cX}{r(t)}\right)\left(\frac{X-\mu}{\nu+X}\right) - \frac{\alpha XY}{\beta+X} + \delta\nabla^2 X, \tag{5.1a}$$

$$\frac{\partial Y}{\partial t} = sY\left(1-\frac{qY}{X+\epsilon}\right) + \xi\delta\nabla^2 Y, \tag{5.1b}$$

with non-negative initial values $X(\vec{x}, t=0)$, $Y(\vec{x}, t=0) \geq 0$, where $X(\vec{x}, t)$ and $Y(\vec{x}, t)$ are the prey and predator population abundances at the spatial position $\vec{x} = (x, y) \in \mathbb{R}^2$ at time t. The local or non-spatial dynamics of this spatiotemporal system were studied by Alkhayuon et al. [215]. The local model describes a Leslie-Gower (L-G) predator-prey interaction incorporating a strong Allee effect in the prey population. The predator species exploits its focal prey through a Holling type II functional response. The intrinsic growth rate $r(t)$ varies over time due to climate variation. The system has an environment-dependent carrying capacity. Table 5.1 presents parameter descriptions and their default values.

Spatial dynamics are introduced via diffusion terms, with the two-dimensional Laplacian operator $\nabla^2 = \frac{\partial^2}{\partial x^2} + \frac{\partial^2}{\partial y^2}$. The prey and predator species diffuse through space with diffusion coefficients δ and $\xi\delta$, respectively, where ξ is the scaling factor of diffusion rates between the two species. The spatial domain is bounded within a well-defined region $\Omega \subset \mathbb{R}^2$, subject to Neumann (no-flux) boundary conditions, i.e.,

$\frac{\partial X}{\partial \nu} = \frac{\partial Y}{\partial \nu} = 0$ for all $(x, y) \in \partial\Omega$, where ν denotes the outward normal vector to the boundary. These conditions ensure that species remain confined within the domain and that no net movement occurs across its boundaries, an ecologically realistic assumption for bounded habitat domains or closed systems.

5.3 Dynamics of local system

An understanding of the local system dynamics in the absence of parameter drift is necessary to understand the spatial dynamics. The autonomous local system (obtained by setting $\delta = 0$ and $r(t) = r$, a constant) has four ecologically distinct equilibrium points: trivial equilibrium $E_0 = (0, 0)$, predator-free equilibrium points $E_1(\mu, 0)$ and $E_2(\frac{r}{c}, 0)$, a prey-free equilibrium $E_3 = (0, \frac{\epsilon}{q})$ and interior equilibrium point $E^* = (X^*, Y^*)$. Expression of interior equilibrium components are $Y^* = \frac{X^*+\epsilon}{q}$, where X^* is the positive root of the third degree polynomial

$$\mathcal{H}(X) = X^3 - \left(\mu - \beta + \frac{r}{c} - \frac{\alpha}{cq}\right) X^2 - \left(\beta\mu + \frac{r(\beta-\mu)}{c} - \frac{\alpha(\nu+\epsilon)}{cq}\right) X + \left(\frac{r\beta\mu}{c} + \frac{\alpha\nu\epsilon}{cq}\right).$$

Since the constant coefficient of the above cubic polynomial is always positive, the system may attain either no positive root or exactly two positive roots. When two interior equilibrium points exist, they are denoted by $E^*_{1,2} = (X^*_{1,2}, Y^*_{1,2})$.

The variational matrix of the local autonomous system at an arbitrary equilibrium point $(\tilde{X}, \tilde{Y})$ reads

$$J(\tilde{X}, \tilde{Y}) = \begin{pmatrix} J_{11} & J_{12} \\ J_{21} & J_{22} \end{pmatrix},$$

where
$J_{11} = r\left(1 - \frac{2c\tilde{X}}{r}\right)\left(\frac{\tilde{X}-\mu}{\nu+\tilde{X}}\right) + r\tilde{X}\left(1 - \frac{c\tilde{X}}{r}\right)\frac{\nu+\mu}{(\nu+\tilde{X})^2} - \frac{\alpha\beta\tilde{Y}}{(\beta+\tilde{X})^2}$, $J_{12} = -\frac{\alpha\tilde{X}}{\beta+\tilde{X}}$, $J_{21} = \frac{sq\tilde{Y}^2}{(\tilde{X}+\epsilon)^2}$, $J_{22} = s - \frac{2qs}{\tilde{X}+\epsilon}$.

The eigenvalues at the trivial equilibrium point E_0 are $\frac{\mu r}{\nu}$ and $s(1 - \frac{2q}{\epsilon})$. Thus, E_0 is always unstable. The predator-free equilibrium points E_1 and E_2 have eigenvalue pairs

$$\left(\frac{r(c\mu - r)}{c\nu + r}, s(1 - \frac{2cq}{r + c\epsilon})\right) \text{ and } \left(\frac{\mu(r - c\mu)}{\mu + \nu}, \ s(1 - \frac{2q}{\mu + \epsilon})\right).$$

As μ is the Allee threshold and $\frac{r}{c}$ being the carrying capacity, one must have $\mu < \frac{r}{c}$, making $c\mu - r < 0$. Thus, E_2 is always unstable. Further, E_1 is unstable if $\frac{r}{c} > 2q - \epsilon$.

The predator-free equilibrium E_3 attains eigenvalues

$$\left(-\frac{r\mu}{\nu}-\frac{\alpha\epsilon}{\beta q},\ s(1-\frac{2q}{\epsilon})\right).$$

Whenever $2q-\epsilon>0$ holds, the equilibrium point E_3 is locally asymptotically stable.

Two interior equilibrium points appear when $\mathcal{H}(X)=0$ attains a double root. We consider r as our parameter of interest. Presume that the equilibrium point $E^*_{SN}=(X^*_{SN},Y^*_{SN})$ corresponds to the double root of the equation $\mathcal{H}(X)=0$ at $r=r_{SN}$, giving $\mathcal{H}(X^*_{SN},r_{SN})=\mathcal{H}'(X^*_{SN},r_{SN})=0$. Thus, the non-trivial nullclines

$$\mathcal{F}(X,Y) \;=\; r\left(1-\frac{cX}{r}\right)\left(\frac{X-\mu}{\nu+X}\right)-\frac{\alpha Y}{\beta+X}=0, \tag{5.2}$$

and

$$\mathcal{G}(X,Y) \;=\; s\left(1-\frac{qY}{X+\epsilon}\right)=0 \tag{5.3}$$

become tangent to each other at $r=r_{SN}$, implying that the slope of the two nullclines are identical, giving

$$\frac{\partial Y^{(\mathcal{F})}}{\partial X}=\frac{\partial Y^{(\mathcal{G})}}{\partial X}, \tag{5.4}$$

where $\frac{\partial Y^{(\mathcal{F})}}{\partial X}$ and $\frac{\partial Y^{(\mathcal{G})}}{\partial X}$ are slopes of the tangent lines corresponding to the two non-trivial nullclines $\mathcal{F}$ and $\mathcal{G}$. One can then write the variational matrix at E^*_{SN} and its determinant as

$$J(E^*_{SN}) \;=\; \begin{pmatrix} X\frac{\partial\mathcal{F}}{\partial X} & X\frac{\partial\mathcal{F}}{\partial Y} \\ Y\frac{\partial\mathcal{G}}{\partial X} & Y\frac{\partial\mathcal{G}}{\partial Y}\end{pmatrix}_{(X^*_{SN},Y^*_{SN})} = \begin{pmatrix} -X\frac{\partial\mathcal{F}}{\partial Y}\frac{\partial Y^{(\mathcal{F})}}{\partial X} & X\frac{\partial\mathcal{F}}{\partial Y} \\ -Y\frac{\partial\mathcal{G}}{\partial Y}\frac{\partial Y^{(\mathcal{G})}}{\partial X} & Y\frac{\partial\mathcal{G}}{\partial Y}\end{pmatrix}_{(X^*_{SN},X^*_{SN})}, \tag{5.5}$$

and

$$\mathrm{Det}(J(E^*_{SN}))=\left\{XY\frac{\partial\mathcal{F}}{\partial Y}\frac{\partial\mathcal{G}}{\partial Y}\left(\frac{\partial Y^{(\mathcal{G})}}{\partial X}-\frac{\partial Y^{(\mathcal{F})}}{\partial X}\right)\right\}_{(X^*_{SN},Y^*_{SN})}. \tag{5.6}$$

Following (5.4), one gets $\mathrm{Det}(J(\Xi^*_{SN}))=0$, giving a zero eigenvalue of the variational matrix (5.5). Let, $\zeta=[1,u]^T$ and $\eta=[v,1]^T$ are the eigenvectors of $J(E^*_{SN})$ and $J(E^*_{SN})^T$ corresponding to the zero eigenvalue, where

$$u=\frac{1}{q},\ v=-\frac{s(\beta+X^*_{SN})}{\alpha X^*_{SN}}.$$

The system then experiences a saddle-node bifurcation at $r = r_{SN}$ if the following transversality and non-degeneracy conditions hold at $r = r_{SN}$ [33]:

$$\eta^T R_K(E^*_{SN}; r = r_{SN}) = -\frac{s(\beta + X^*_{SN})(X^*_{SN} - \mu)}{\alpha(\nu + X^*_{SN})}\left(1 - \frac{2cX^*_{SN}}{r_{SN}}\right) \neq 0,$$

$$\eta^T D^2 R(E^*_{SN}; r = r_{SN})(\zeta, \zeta) = \left[\frac{\partial^2 F}{\partial X^2}v^2 + 2\frac{\partial^2 F}{\partial X \partial Y}v + \frac{\partial^2 F}{\partial Y^2} + u\left(\frac{\partial^2 G}{\partial X^2}v^2 + 2\frac{\partial^2 G}{\partial X \partial Y}v + \frac{\partial^2 G}{\partial Y^2}\right)\right]_{(X^*_{SN}, Y^*_{SN})} \neq 0.$$

Stability of an interior equilibrium point $E^* = (X^*, Y^*)$ is verified by the signs of eigenvalues of the variational matrix. By the Routh-Hurwitz criteria, the system undergoes a Hopf bifurcation about E^* at $r = r_H$ if $Trace(J(X^*(r = r_H), Y^*(r = r_H))) = 0$ and $Det(J(X^*(r = r_H), Y^*(r = r_H))) > 0$. The Hopf-bifurcation point (r_H) is computed in terms of r from the following expression (where trace is zero):

$$r\left(1 - \frac{2cX^*}{r}\right)\left(\frac{X^* - \mu}{\nu + X^*}\right) + rX^*\left(1 - \frac{cX^*}{r}\right)\frac{\nu + \mu}{(\nu + X^*)^2} - \frac{\alpha\beta Y^*}{(\beta + X^*)^2} + s - \frac{2qs}{X^* + \epsilon} = 0. \tag{5.7}$$

A limit-cycle appears through a forward Hopf-bifurcation at the point $r = r_H$ if

$$\frac{d}{dr}\left(\mathrm{Tr}(J(E^*; r = r_H))\right) > 0,$$

and a limit-cycle vanishes through a backward Hopf-bifurcation at $r = r_H$ if

$$\frac{d}{dr}\left(\mathrm{Tr}(J(E^*; r = r_H))\right) < 0.$$

The dynamic behaviour of the autonomous local system due to a variation in r is described by the bifurcation diagram in Fig. 5.1a. Three bifurcations occur in the autonomous local system for a range of $r \in [1, 4]$. For the considered parameter values, the predator extinction equilibrium points E_1 and E_2 are always unstable in this range of r (not shown in Fig. 5.1a). The prey extinction equilibrium E_3 is always stable. In the dynamic regime R_1, where $r < r_{SN}$ (see Fig. 5.1a), E_3 is the only stable state. A saddle-node bifurcation of interior equilibrium points occurs at $r = r_{SN} = 1.2044$. It satisfies the transversality condition $\eta^T R_K(E^*_{SN}; r = r_{SN}) = 0.0004 \neq 0$ and non-degeneracy condition $\eta^T D^2 R(E^*_{SN}; r = r_{SN})(\zeta, \zeta) = -10.6974 \neq 0$. Two

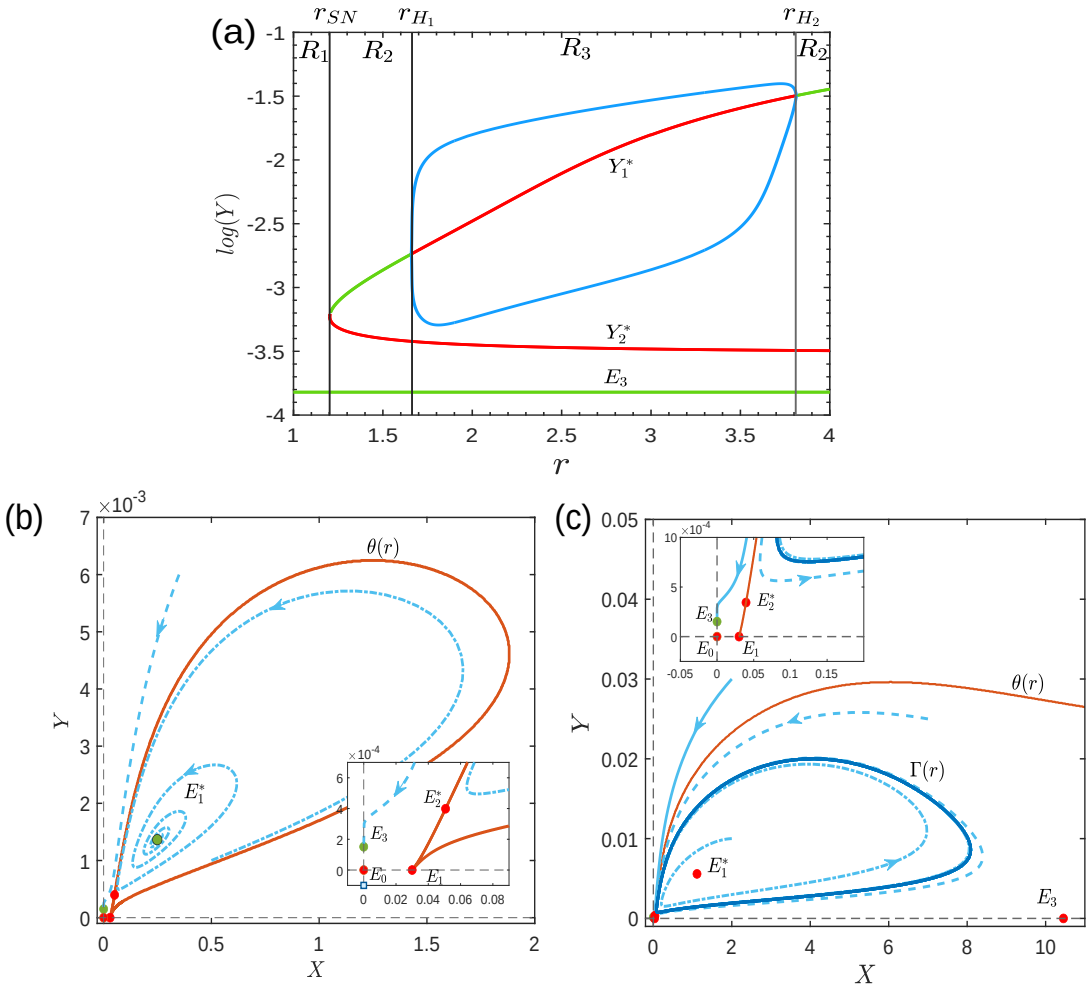

FIGURE 5.1: (a) Bifurcation diagram of the predator population of the autonomous local system. Species density is plotted in a semi-log scale against varying r. Solid vertical lines mark bifurcation points. A saddle node bifurcation occurs at r_{SN}=1.2044; a forward and a backward Hopf bifurcation occurs at r_{H_1}=1.6640 and r_{H_2}=3.8091. Red and green colours denote unstable and stable branches of equilibrium points. The limit cycle is shown in blue curves. Here, R_i $(i = 1, 2, 3, 4)$ are four dynamic regimes divided by the three bifurcation points $(r_{SN}, r_{H_1}, r_{H_2})$. (b) Phase portrait of the local autonomous system at $r = 1.5 \in R_2$. The red trajectory $(\theta(r))$ is the saddle separatrix, which divides the domain of two attractors: the interior equilibrium E_1^* and prey-free equilibrium E_3 (green dot, see the inset figure). (c) Phase portrait of the local autonomous system at $r = 2.3 \in R_3$. The red trajectory $(\theta(r))$ is the saddle separatrix, which divides the domain of two attractors: the stable limit-cycle (dark blue closed loop) and the prey-free equilibrium E_3 (green dot, see the inset figure).

interior equilibrium points appear for $r > r_{SN}$: one stable focus and one unstable saddle. The equilibrium point E_2^*, having predator abundance Y_2^*, is unstable in the entire range (see Fig. 5.1a). The other interior equilibrium point E_1^*, having counterpart Y_1^*, is stable in $r_{SN} < r < r_{H_1}$, marked by regime R_2 (see Fig. 5.1a). The interior equilibrium E_1^* undergoes a forward supercritical Hopf bifurcation at $r = r_{H_1} = 1.6640$, where $\frac{d}{dr}\left(\mathrm{Tr}(J(E_1^*; r = r_{H_1}))\right) = 0.9083$, and generates a stable-limit cycle around E_1^*. The limit cycle disappears via a backward supercritical Hopf bifurcation at $r = r_{H_2} = 3.8095$, where $\frac{d}{dr}\left(\mathrm{Tr}(J(E_1^*; r = r_{H_2}))\right) = -0.8291$, making E_1^* stable again. Here, the Hopf bifurcation points (r_{H_1} and r_{H_2}) are the solutions of the Eq. (5.7) in r. The local system creates a Hopf-bubble in the interval (r_{H_1}, r_{H_2}), which is denoted by the dynamic regime R_3, showing the coexistence of both species in a limit-cycle oscillation. For $r > r_{H_2}$, the interior equilibrium E_1^* again becomes stable.

The dynamic regimes R_2 and R_3 exhibit bistability. In R_2, the system shows bistability between the prey extinction equilibrium E_3 and the coexistence equilibrium E_1^*, while in R_3, bistability occurs between E_3 and a stable limit-cycle representing population persistence in the oscillatory state. In the subsequent analysis, the equilibrium point E_3 is referred to as the population extinction equilibrium [215], since in the absence of the focal prey, the predator persists at a negligible density of $\frac{\epsilon}{q}$. Phase portraits corresponding to two representative values of r from the regimes R_2 and R_3 are shown in Fig. 5.1b and Fig. 5.1c. For $r = 1.5 \in R_2$, the basins of attraction of the two stable equilibria are separated by the saddle separatrix $\theta(r)$, which passes through the saddle point E_2^* (Fig. 5.1b). For $r = 2.3 \in R_3$, the coexisting stable state is a limit cycle, denoted by $\Gamma(r)$ (Fig. 5.1c). Thus, depending on the initial conditions, the system in regimes R_2 and R_3 may evolve toward one of two alternative stable states.

5.4 Spatiotemporal instability

This section discusses the dynamics of the spatiotemporal autonomous system (5.1) and reveals the diffusion-driven instabilities under constant environmental conditions. For such analysis with $r(t) = r =$ constant, we consider that the parameters of the non-diffusive system are in the regimes of R_2 and R_3 (see Fig. 5.1a).

Turing instability

Turing instability occurs when the corresponding non-diffusive system is stable, and destabilization occurs by some non-zero unstable spatial mode of perturbations caused by species diffusion. Turing instability studied here is about the stable coexistence equilibrium point $E_1^*(X_1^*, Y_1^*)$. Linearization of the spatial system is performed about E_1^* with small spatiotemporal perturbations of the form $\Delta X = \sum_{\vec{k}} C_{\vec{k}} e^{\lambda(k)t \pm i\vec{k}\vec{x}}$ and $\Delta Y = \sum_{\vec{k}} D_{\vec{k}} e^{\lambda(k)t \pm i\vec{k}\vec{x}}$, where $\vec{k} = (k_x, k_y)$ is the wavenumber vector of the spatial perturbation and $C_{\vec{k}}$, $D_{\vec{k}}$ are constant coefficients of perturbation. The corresponding characteristic equation reads

$$\lambda^2(k) + B_1(k)\lambda + B_2(k) = 0, \tag{5.8}$$

where $k = |\vec{k}|$ and

$$\begin{aligned} B_1(k) &= Tr(J^*) - \delta k^2(1+\xi), & (5.9)\\ B_2(k) &= \delta^2 \xi k^4 - \delta(\xi J_{11}^* + J_{22}^*)k^2 + Det(J^*), & (5.10) \end{aligned}$$

where J^* is the variational matrix evaluated at E_1^*. The equation (5.8) gives the dispersion relation of the eigenvalues ($\lambda(k)$) with respect to spatial wave numbers k.

Suppose the system is stable around E_1^* in the absence of diffusion, i.e., all λ have negative real parts when $k = 0$. If for some non-zero wavenumber k, λ attains a positive real value, then the Turing instability occurs. However, if $\lambda(k)$ has negative real parts for all k, then no instability occurs, and the spatiotemporal system remains stable in uniform steady state.

Since the local system is stable about the interior equilibrium E_1^*, one have $Tr(J^*) = J_{11}^* + J_{22}^* < 0$ and $Det(J^*) = (J_{11}^* J_{22}^* - J_{12}^* J_{21}^*) > 0$. As the diffusion coefficients are positive, $B_1(k) < 0\ \forall k$. Therefore, $\lambda(k)$ may attain positive eigenvalues only when $B_2(k) < 0$ for some non-zero wavenumber k. Since $\delta^2\xi > 0$, so $B_2(k) < 0$ holds only when $\xi J_{11}^* + J_{22}^* > 0$. Now,

$$\begin{aligned} B_2(k) &= \delta^2 \epsilon k^4 - \delta(\xi J_{11}^* + J_{22}^*)k^2 + Det(J^*) \\ &= \left(\delta\sqrt{\xi}k^2 - \frac{(\xi J_{11}^* + J_{22}^*)}{2\sqrt{\xi}}\right)^2 + \left(Det(J^*) - \frac{(\xi J_{11}^* + J_{22}^*)^2}{4\xi}\right). \end{aligned} \tag{5.11}$$

At the critical point of Turing instability, $\min_{k>0} B_2(k)$ must be equal to zero, leading to $\min_{k>0} B_2(k) = B_2(k_{min})$, where $k_{min} = \sqrt{\frac{J_{11}^* + \xi J_{22}^*}{2\delta\epsilon}}$. With some further reductions, the critical wavenumber for Turing instability k_{T_c} reads $k_{T_c} = \sqrt[4]{\frac{Det(J^*)}{\delta^2\xi}}$. The condition

$B_2(k) < 0$ provides an interval of unstable wavenumbers $k_{T_1} < k < k_{T_2}$ responsible for the Turing instability, where $k_{T_{1,2}}$ are the real roots of $B_2(k) = 0$, given by

$$k_{T_1,T_2} = \frac{1}{2\delta\xi}\left[(J^*_{22} + \xi J^*_{11}) \mp \sqrt{(J^*_{22} + \xi J^*_{11})^2 - 4\xi Det(J^*)}\right]^{\frac{1}{2}}$$

which attains positive real values if

$$J^*_{22} + \xi J^*_{11} > 2\sqrt{\xi Det(J^*)}. \tag{5.12}$$

The conditions of Turing instability can be summarized as follows.

Theorem 5.1. *The system (5.1) with $r(t) = r$ shows Turing instability about the interior equilibrium point E^*_1 if the following conditions hold:*
(i) $Tr(J^*) < 0$ *and* $Det(J^*) > 0$,
(ii) $J^*_{22} + \xi J^*_{11} > 2\sqrt{\xi Det(J^*)} > 0$, *and*
(iii) the spatial wavemodes (k) *lie in* $k_{T_1} < k < k_{T_2}$.

Pure Hopf instability

The pure Hopf instability in the spatial system arises when the stable non-diffusive system undergoes a Hopf bifurcation due to a pair of complex conjugate roots with positive real parts, leading to sustained temporal oscillations, and the spatial system does not show Turing instability. Therefore, the following theorem can characterise pure Hopf instability around the stable coexistence equilibrium E^*_1.

Theorem 5.2. *The system (5.1) with $r(t) = r$ shows pure Hopf instability about the interior equilibrium point E^*_1 if the following conditions hold:*
(i) $Tr(J^*) > 0$ *and* $Det(J^*) > 0$,
(ii) $J^*_{22} + \xi J^*_{11} < 2\sqrt{\xi Det(J^*)}$.

The first criterion gives the conditions for a pair of complex conjugate roots with positive real parts, and the second condition restricts the occurrence of Turing instability.

Mixed instability (Hopf-Turing)

Turing-like unstable modes can emerge even when the local system is not in a steady state. Such non-Turing instabilities, or mixed spatiotemporal instabilities, occur when

local oscillations interact with spatial diffusion. A key example is the Hopf-Turing instability, which arises when the local dynamics exhibit a Hopf bifurcation and the spatiotemporal system also satisfies the conditions for a Turing-type instability. The following theorem assures its existence.

Theorem 5.3. *The system (5.1) with $r(t) = r$ shows Hopf-Turing instability about the interior equilibrium point E_1^* if the following conditions hold:*
(i) $Tr(J^*) > 0$ *and* $Det(J^*) > 0$,
(ii) $J_{22}^* + \xi J_{11}^* > 2\sqrt{\xi Det(J^*)} > 0$,
(iii) the spatial wavemodes lie in $k_{T_1} < k < k_{T_2}$.

Here, the first condition represents Hopf instability, the second condition allows Turing instability and the third condition describes the spatial wavemodes for Turing instability.

Critical scaling factor of diffusion coefficients for Turing instability

We provide a relationship between the diffusion ratio of predator to prey and the occurrence of Turing instability.

Theorem 5.4. *Suppose that the interior equilibrium E_1^* is stable in the absence of diffusion. Then the spatiotemporal model (5.1) with $r(t) = r$ undergoes a Turing instability if the scaling factor of diffusion coefficients exceeds some threshold value ξ_c, i.e., $\xi > \xi_c$, where*

$$\xi_c = \xi_+ = \frac{1}{J_{11}^{*2}}[-(2J_{12}^*J_{21}^* - J_{11}^*J_{22}^*) + \sqrt{(2J_{12}^*J_{21}^* - J_{11}^*J_{22}^*)^2 - J_{11}^{*2}J_{22}^{*2}}].$$

Define the expressions of Turing instability criteria of Theorem 5.1 as follows:

$$\begin{aligned} \mathcal{C}_1(\xi) &= (J_{22}^* + \xi J_{11}^*)^2 - 4\xi det(J^*) \\ &= \xi^2 J_{11}^{*2} + 2\xi(2J_{12}^*J_{21}^* - J_{11}^*J_{22}^*) + J_{22}^{*2}, \\ \mathcal{C}_2(\xi) &= J_{22}^* + \xi J_{11}^*. \end{aligned} \tag{5.13}$$

Setting

$$\begin{aligned} &\mathcal{C}_1(\xi) = 0 \iff \xi^2 J_{11}^{*2} + 2\xi(2J_{12}^*J_{21}^* - J_{11}^*J_{22}^*) + J_{22}^{*2} = 0, \\ &\mathcal{C}_2(\xi) = 0 \iff \xi = -\frac{J_{22}^*}{J_{11}^*} := \xi^*. \end{aligned} \tag{5.14}$$

The two solutions of (5.14) are

$$\xi_{\pm} = \frac{1}{J_{11}^{*2}} \left[-(2J_{12}^{*}J_{21}^{*} - J_{11}^{*}J_{22}^{*}) + \sqrt{(2J_{12}^{*}J_{21}^{*} - J_{11}^{*}J_{22}^{*})^2 - J_{11}^{*2}J_{22}^{*2}} \right]. \tag{5.15}$$

Stability of E_1^* gives $Det(J^*) = (J_{11}^{*}J_{22}^{*} - J_{12}^{*}J_{21}^{*}) > 0$, along with $J_{12}^{*} < 0$, $J_{21}^{*} > 0$, following the expressions of the components of the variational matrix. Therefore, $(2J_{12}^{*}J_{21}^{*} - J_{11}^{*}J_{22}^{*})^2 - J_{11}^{*2}J_{22}^{*2} = 4J_{12}^{*}J_{21}^{*}(J_{12}^{*}J_{21}^{*} - J_{11}^{*}J_{22}^{*}) > 0$, implying that both roots $\xi_{\pm}$ are real. Since $(2J_{12}^{*}J_{21}^{*} - J_{11}^{*}J_{22}^{*}) = J_{12}^{*}J_{21}^{*} - (J_{11}^{*}J_{22}^{*} - J_{12}^{*}J_{21}^{*}) < 0$, so $\xi_{\pm}$ are also positive and

$$0 < \xi_{-} < \xi_{+}.$$

From conditions of activator-inhibitor kinetics, J_{11}^{*} and J_{22}^{*} must attain opposite signs in the presence of Turing instability [30]. Thus, one must get $\xi^{*} > 0$. Now, $\mathcal{C}_1$ is a quadratic polynomial in ξ with constant coefficient and coefficient of ξ^2 is positive. Then, by the mean value theorem, the polynomial must have a negative value in the interval (ξ_{-}, ξ_{+}). Putting $\xi = \xi^{*}$ in $\mathcal{C}_1(\xi)$, we attain a negative value, which implies

$$0 < \xi_{-} < \xi^{*} < \xi_{+}.$$

Conditions of Turing instability are satisfied if $\mathcal{C}_1(\xi) > 0$ and $\mathcal{C}_2(\xi) > 0$ hold simultaneously for the choices of the scaling factor ξ. This is achievable if $\xi \notin (\xi_{-}, \xi_{+})$ and $\xi > \xi_{+}$. Therefore, the critical diffusion ratio for the onset of Turing instability is $\xi_c = \xi_{+}$.

Parametric regimes of different instabilities

Based on the stability and instability conditions established in the earlier section, we investigate the regimes of Turing, pure Hopf, and mixed Hopf-Turing instabilities in a two-parameter bifurcation diagram (Fig. 5.2), where we vary the intrinsic growth rate r and scaling parameter ξ. The diagram reveals four distinct dynamical regions, stable (I), pure Hopf (II), pure Turing (III) and Hopf-Turing (IV), each of which corresponds to a qualitatively different instability. Equation (5.7) provides two Hopf bifurcation curves $r = r_{H_1}$ and $r = r_{H_2}$ (white dashed lines). The Turing bifurcation curve is plotted using the condition $J_{22}^{*} + \xi J_{11}^{*} = 2\sqrt{\xi Det(J^{*})}$, where Turing instability is observed above the curve either in the form of pure Turing instability or Hopf-Turing instability. For a fixed value of r, Turing instability is observed only if the scaling factor ξ is greater than a threshold value $\xi_c(r)$.

Figures 5.2b-e describe each region's dispersion relations for representative parameter pairs (marked as red dots). These figures in each region highlight how the eigenvalues

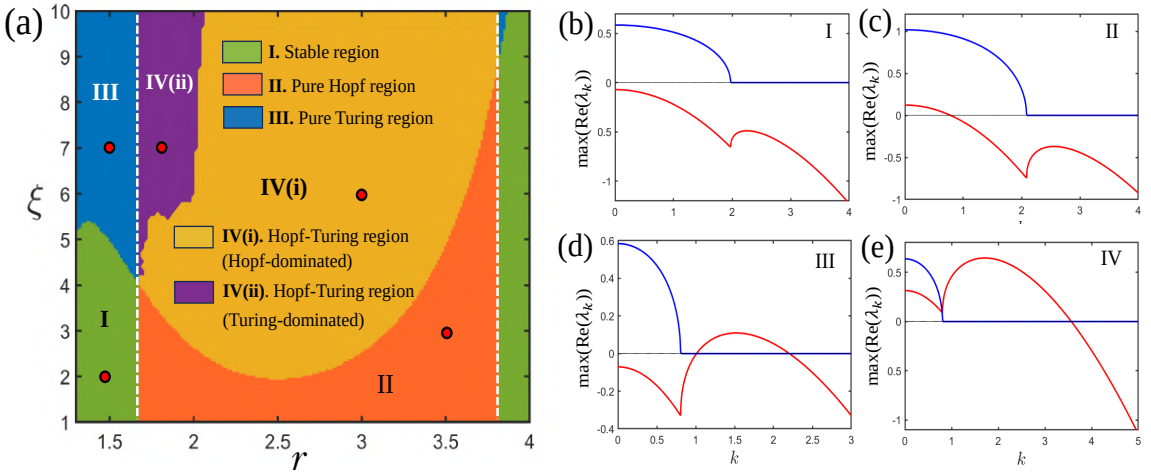

FIGURE 5.2: (a) Two parameter region plots with respect to the parameters r and ξ reveal four dynamic regimes: (I) stable steady state (green), (II) pure Hopf instability (red), (III) pure Turing instability (blue), (IV(i)) Hopf-dominated Hopf-Turing instability (yellow) and (IV(ii)) Turing-dominated Hopf-Turing instability (purple). The corresponding dispersion relations for four observation points are shown in figures (b-e): (I) $(r, \xi) = (1.5, 2)$, (II) $(r, \xi) = (3.5, 3)$, (III) $(r, \xi) = (1.5, 7)$ and (IV) $(r, \xi) = (3, 6)$. The red curves denote the maximum real part of the eigenvalues, and the blue curves are the corresponding imaginary part. The rest of the parameters are the same as in Fig. 5.1 with $\delta = 0.01$.

vary with the variation of wavenumber k, shedding light on the nature and onset of different instabilities. In the stable regime, (Fig. 5.2b for I: $(r, \xi) = (1.5, 2)$), eigenvalues remain negative for all k, confirming stability. The Turing regime (Fig. 5.2d for III: $(r, \xi) = (1.5, 7)$) shows a transition from negative to positive real eigenvalues at finite k, signifying the growth of spatial perturbations. The Hopf regime (Fig. 5.2c for II: $(r, \xi) = (3.5, 3)$) features a pair of complex-conjugate eigenvalues crossing into the right half-plane at $k = 0$, marking the onset of temporal oscillations. In the mixed Hopf-Turing regime (Fig. 5.2e for IV: $(r, \xi) = (3, 6)$), both a complex-conjugate pair crosses the imaginary axis at $k = 0$, and a real eigenvalue becomes positive at $k \neq 0$, indicating the coexistence of oscillatory and heterogeneous steady state instabilities.

We compute the average temporal deviation ($\mathcal{A}$) of prey and predator population levels over the Hopf-Turing domain to differentiate parameter space based on sustained spatiotemporal oscillations and transient chaos resulting in eventual steady states. The average temporal deviation in a specific time interval $[T, T + \Delta T]$ is defined by

$$\mathcal{A} = \frac{1}{2N} \sum_i \left(\mathrm{Var}_{[T,T+\Delta T]}(X_i) + \mathrm{Var}_{[T,T+\Delta T]}(Y_i) \right). \tag{5.16}$$

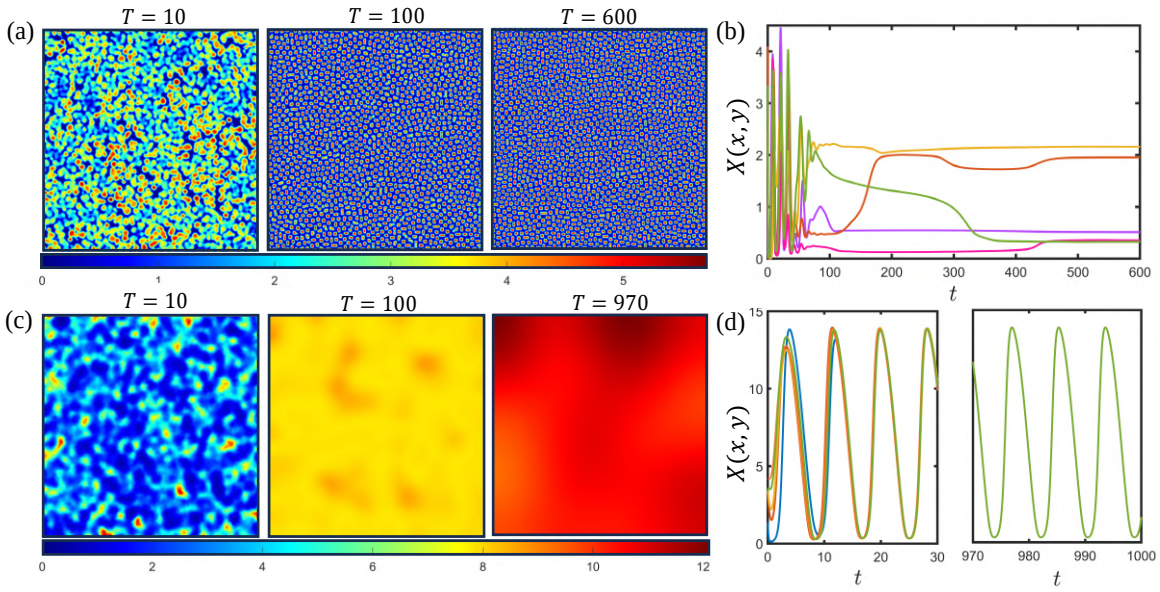

FIGURE 5.3: (a, c) The top row and bottom row are snapshots of spatiotemporal patterns of Turing and Hopf instabilities at different times for the parameter pairs $(r, \xi) = (1.5, 7)$ and $(r, \xi) = (3.5, 3)$. (b,d) The corresponding prey population concentration at five spatial locations $(x, y) = (10, 10)$, $(40, 10)$, $(20, 20)$, $(10, 40)$ and $(40, 40)$. Parameter values are as in Fig. 5.2

In the above expression, $\text{Var}_{[T,T+\Delta T]}(.)$ is the temporal variance of the population density within the time interval $[T, T + \Delta T]$ at a particular spatial location i. Therefore, excluding the initial transient dynamics, if for a sufficiently long time interval of ΔT, the population densities at a grid i converge to constant population abundances, then $\text{Var}_{[T,T+\Delta T]}(X_i/Y_i) = 0$. For a dynamics similar to Turing instability, where temporal steady state is achieved $\mathcal{A} = 0$. Otherwise, $\mathcal{A} > 0$. We compute $\mathcal{A}$ for different parameter pairs (r, ξ) of the Hopf-Turing regime to observe the dominance of Turing and Hopf instability. In Fig. 5.2a, the purple region marks the numerically identified Turing-dominated Hopf-Turing region, and the rest of the yellow region is the Hopf-dominated Hopf-Turing region.

The system settles into a steady state in the Turing instability region (III) with spatially heterogeneous patterns. These patterns manifest as localized regions of high and low prey density, indicative of diffusion-driven instabilities that give rise to non-uniform yet temporally stable structures (Fig. 5.3a) for the parameter pair $(r, \xi) = (1.5, 7)$. The corresponding time series (Fig. 5.7b) of prey density at five selected spatial locations $(x, y) = (10, 10)$, $(40, 10)$, $(20, 20)$, $(10, 40)$ and $(40, 40)$ further confirm this behaviour (see Fig. 5.3b). In contrast, when the parameter pair $(r, \xi) = (3.5, 3)$ is selected from the pure Hopf instability region (II), the snapshots

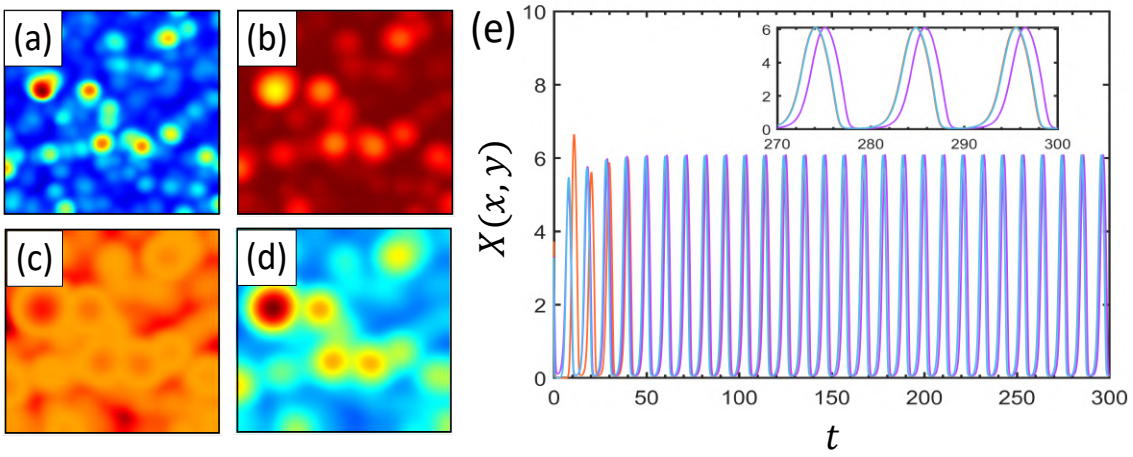

FIGURE 5.4: Spatiotemporal patterns of prey population under Hopf-dominated Hopf–Turing instability region IV(i) for $(r, \xi) = (3, 6)$. The snapshots at four different time points display persistent spatiotemporal fluctuations indicative of sustained oscillatory dynamics with weak spatial heterogeneity characteristic of Hopf-driven behaviour. (a) $t = 100$, (b) $t = 200$, (c) $t = 400$, (d) $t = 500$. (e) The corresponding prey population concentrations at five spatial locations $(x, y) = (10, 10)$, $(40, 10)$, $(20, 20)$, $(10, 40)$ and $(40, 40)$. It shows sustained and near-synchronous oscillations across space with a slight phase difference. Parameter values are as in Fig. 5.2.

(Fig. 5.3c) at different time points reveal that the prey density fluctuates with minimal spatial variation. The corresponding time series of the prey population at five spatial locations exhibit sustained spatiotemporal oscillations (Fig. 5.3d). Here, the dynamics display almost homogeneous temporal oscillations after some initial transient, where the phase and amplitude of oscillating prey population abundance remain largely uniform.

The dynamics and patterns observed in the mixed (Hopf-Turing) instability regime IV are particularly intriguing. In this regime, the dispersion relation reveals the presence of both Hopf and Turing unstable modes (Fig. 5.2e). The system dynamics within this regime are highly sensitive to the parameter pairs. When the parameter set lies far from the Hopf bifurcation boundary, the domination of Hopf instability is found in the dynamics. For example, at $(r, \xi) = (3, 6)$ from region IV(i) in Fig. 5.2a, the system exhibits spatially homogeneous oscillations (see Figs. 5.4a-d) similar to those observed in the pure Hopf regime, with near-synchronous temporal fluctuations across the domain. The time series at the five spatial points show identical amplitudes with minor phase differences (Fig. 5.4e). Conversely, as the parameter pair is shifted closer to the Turing instability region $(r, \xi) = (1.8, 7)$ from region IV(ii), the influence of Hopf mode diminishes, and the spatially heterogeneous steady states, like Turing instability, become more pronounced. The system initially exhibits a complex,

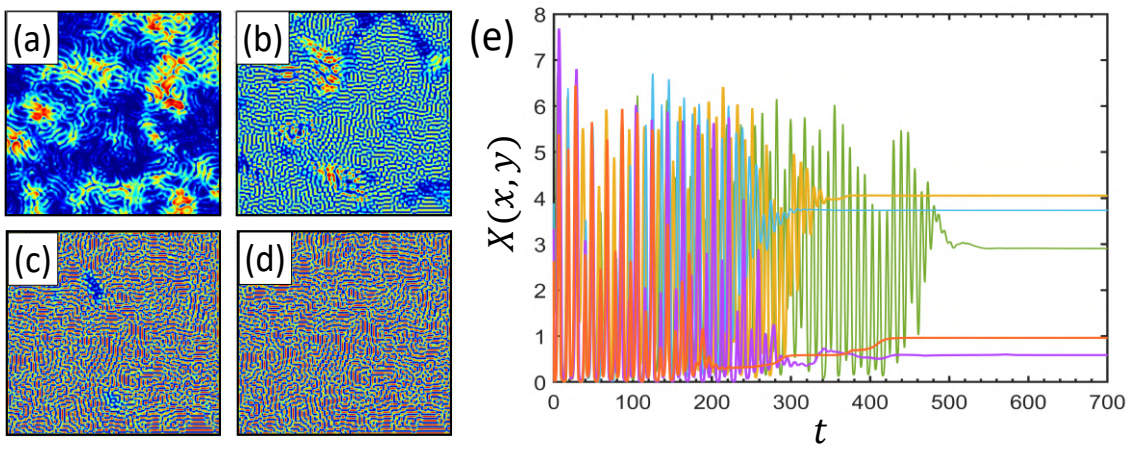

FIGURE 5.5: Spatiotemporal prey patterns under Turing-dominated Hopf–Turing instability region IV(ii) for $(r, \xi) = (1.8, 7)$. The snapshots illustrate the evolution of spatial patterns at (a) $t = 60$, (b) $t = 180$, (c) $t = 400$, (d) $t = 500$. The system initially exhibits dynamic fluctuations, which gradually stabilize into a temporally steady, spatially heterogeneous distribution characteristic of Turing-type pattern formation. (e) The corresponding time series of prey populations at five selected spatial locations. It shows that initial oscillations decay into a spatially heterogeneous steady state. Parameter values are as in Fig. 5.2.

seemingly chaotic spatiotemporal dynamics (Figs. 5.5a, b). However, this transient chaos eventually decays, and the system settles into a stable, spatially heterogeneous steady state by $t = 500$ (Fig. 5.5d). The steady-state nature of the final pattern is further validated by time series data, showing time-invariant densities following a chaotic transient phase (see Fig. 5.5e).

5.5 Climate variations and its effect

The climate fluctuation is modeled as in Hassan et al. [215]. The random variation in the climate causes the intrinsic growth rate and the system's carrying capacity to alter over time. Here, the time-dependent variation in $r(t)$ is represented as a piecewise constant function, where

$$r(t) = r_i \quad \forall t \in [t_i, t_{i+1}), i = 0, 1, 2, ..., \tag{5.17}$$

where t_i and t_{i+1} are the initial and terminal times during which the intrinsic growth remains unchanged. There are two main sources of stochasticity in $r(t)$: (i) switching frequency which determines how often the environment changes from one state to

another and causes a variation in $r(t)$, and (ii) amplitude of fluctuations, which measures the magnitude of changes in $r(t)$.

If $\mathcal{L}_i$ is the variable length of time interval of unchanged climate state, and hence no variation in $r(t)$, then $\mathcal{L}_i = t_{i+1} - t_i$. We consider here a minimum period of 3 years between two successive switches so that $t_{i+1} - t_i \geq 3$. Then, $\mathcal{L}_i$ follows the geometric distribution

$$G(\mathcal{L}_k) = (1-\psi)^{\mathcal{L}_k - 3}\psi, \tag{5.18}$$

where $\mathcal{L}_k = 3, 4, 5... \in \mathbb{N}$ and $\psi \in (0, 1)$ is the switching probability of climatic condition. A higher value of ψ corresponds to increased environmental variation. The amplitude of fluctuations in $r(t)$ is independently sampled from the uniform distribution $\mathcal{U}(r_{min}, r_{max})$, where $(r_{min}, r_{max}) = (1.7, 3.8) \subset [r_{H_1}, r_{H_2}]$. This stochastic formulation enables us to simulate more realistic population dynamics under temporally fluctuating environmental conditions, paving the way for deeper insights into the interplay between ecological parameters and climate-driven disturbances.

Extinction and recovery pattern

Figure 5.6a presents a sample realization of the time-varying growth rate $r(t)$ under stochastic climatic fluctuations, generated using equations (5.17) and (5.18). The profile of $r(t)$ changes randomly in a piecewise manner. Red intervals indicate favorable conditions where $r(t) > \frac{1}{2}(r_{\min} + r_{\max})$, while blue intervals represent unfavorable conditions with $r(t) < \frac{1}{2}(r_{\min} + r_{\max})$ [215]. Abrupt transitions from favorable to unfavorable phases can lead to temporary local extinctions, marked by prey densities falling below the Allee threshold μ.

Figure 5.6b shows the corresponding temporal dynamics of spatial extinction, captured as the proportion of locations where the prey population falls below the extinction threshold. These results demonstrate how sudden climatic deteriorations can lead to immediate ecological consequences, such as local prey extinctions, followed by gradual recolonization via diffusion. A sharp drop in the growth rate at $t = 48$ results in widespread extinction, evidenced by the peak in extinction percentage in Fig. 5.6b. However, this percentage declines over time as the prey population survives in some spatial patches and recolonizes empty regions through dispersal. To further investigate these dynamics, spatial snapshots of prey density at selected time points are shown in Fig. 5.7. White regions denote local extinction, where prey density falls below the Allee threshold. The patterns reveal how spatial dynamics differ under varying climatic conditions. During high climatic variability, the system often exhibits strong spatial synchrony (e.g., Fig. 5.7i,l,n,o), driven by Hopf instability.

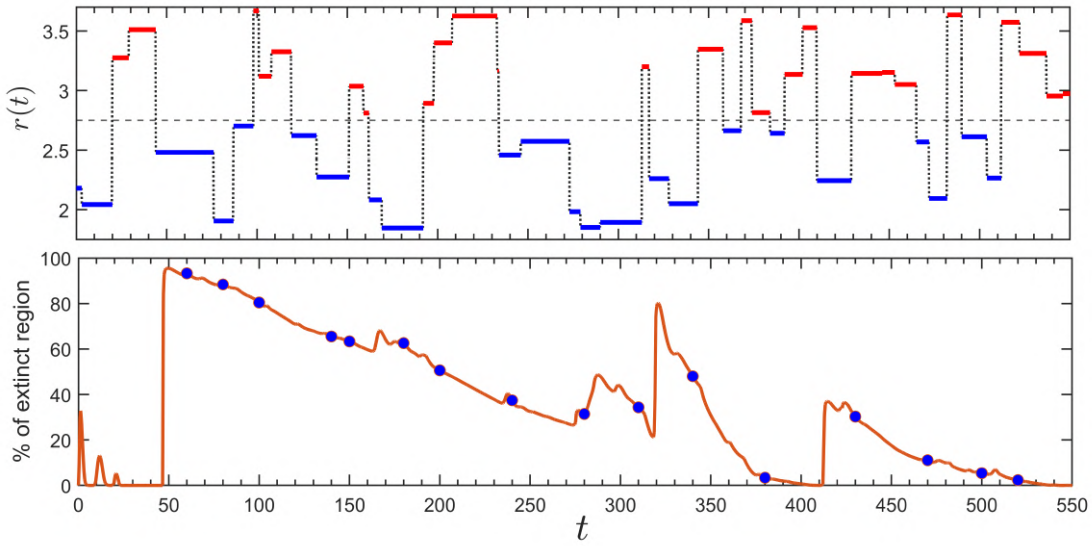

FIGURE 5.6: Top row: A representative realization of climatic fluctuations over time, where the intrinsic growth rate $r(t)$ varies in a piecewise constant manner. Red segments indicate favourable prey survival and growth conditions, while blue segments represent unfavourable climatic phases. The dashed line $r(t) = \frac{1}{2}(r_{\min} + r_{\max})$ separates the red and blue segments. Bottom row: Corresponding temporal evolution of the percentage of spatial grid points ($200 \times 200 = 40000$) where local prey extinction occurs, illustrating the spatial impact of environmental variability on population persistence. Parameter values are as in Fig. 5.2 with $\psi = 0.3$. The time points marked by blue circles will be used subsequently.

Conversely, during periods of low $r(t)$, the system develops steady-state Turing-like spatial heterogeneity, resulting in patchy prey distributions (e.g., Fig. 5.7f,g,j,k). These spatial imperfections help some regions avoid extinction and serve as refugia for recolonization. Following the major collapse around $t = 50$ (see Fig. 5.6a), prey dispersal from a few surviving patches initiates a recovery process. This is illustrated in Figs. 5.7a-h, where wavefronts of prey population gradually repopulate previously extinct areas.

Turing-like steady states, due to their temporal stability, offer greater resilience to sudden environmental disturbances, underscoring their ecological importance. To explore the interplay between spatial and temporal dynamics, we examined the system on a one-dimensional spatial domain (Fig. 5.8) under two temporal profiles of the climatic parameter $r(t)$. The resulting prey population dynamics (Fig. 5.8b), corresponding to the $r(t)$ profiles in Fig. 5.8a, display a coexistence of Turing-like steady states and Hopf-like temporal oscillations. In the spatiotemporal pattern, horizontal stripes indicate regions where prey density remains constant over time, characteristic of Turing-like spatial heterogeneity. In contrast, vertical stripes reflect spatially

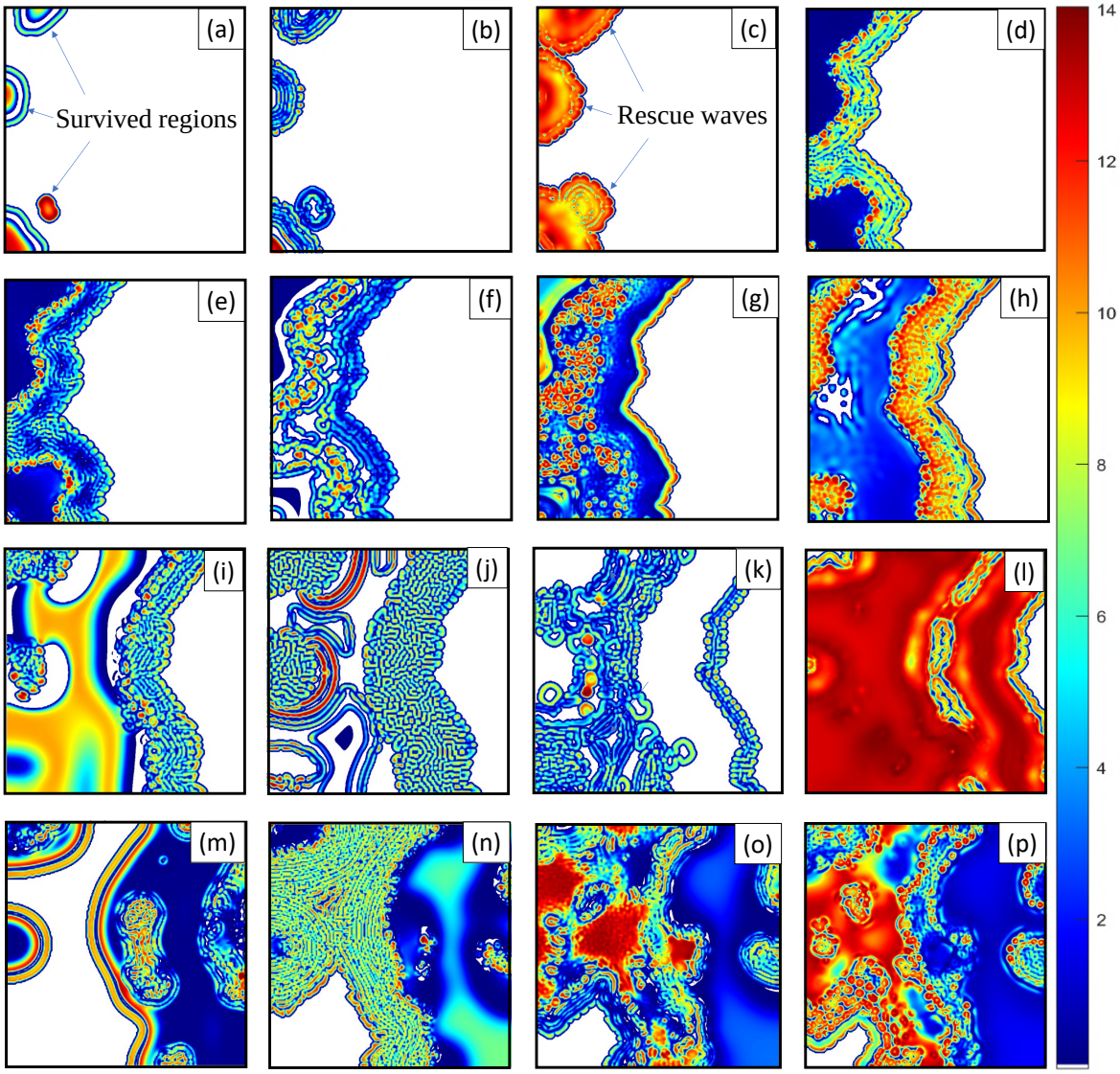

FIGURE 5.7: Spatiotemporal snapshots of prey densities in two-space dimensions under climatic variations as in Fig. 5.6a at selected time points marked at Fig. 5.6b: (a) $t = 60$, (b) $t = 80$, (c) $t = 100$, (d) $t = 140$, (e) $t = 150$, (f) $t = 180$, (g) $t = 200$, (h) $t = 240$, (i) $t = 280$, (j) $t = 310$, (k) $t = 340$, (l) $t = 380$, (m) $t = 430$, (n) $t = 470$, (o) $t = 500$, (p) $t = 520$. White regions indicate areas where prey populations temporarily go extinct (below the Allee threshold level, μ). Parameter values are as in Fig. 5.2.

synchronized oscillations, typical of Hopf-like dynamics. Figure 5.8c shows four major extinction events at $t = 71, 237, 349, 455$, each aligned with abrupt drops in $r(t)$

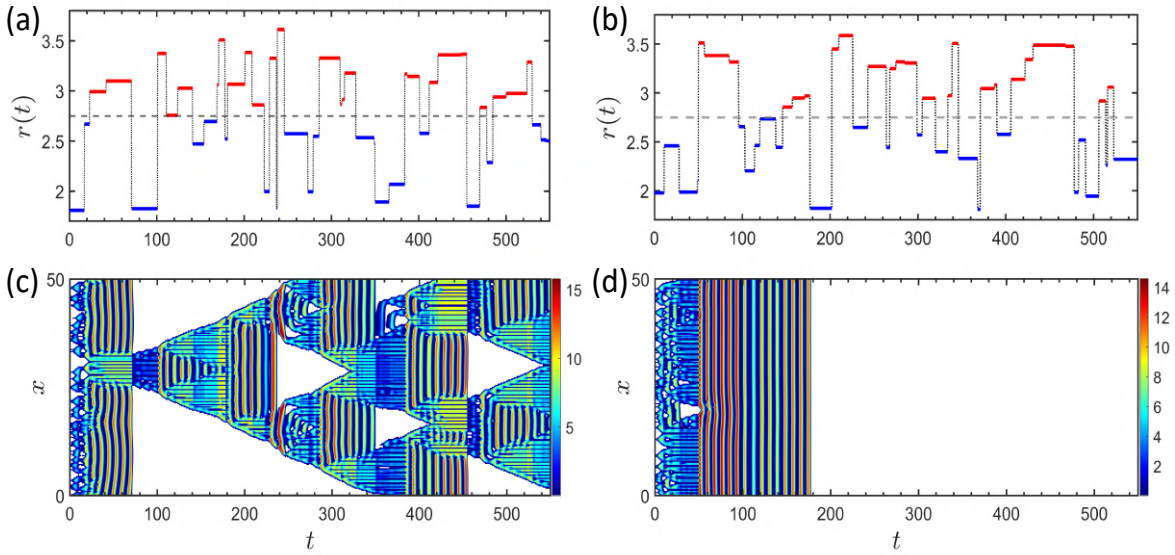

FIGURE 5.8: (a, b) Two realizations of environmental variations. (c, d) Corresponding spatiotemporal snapshots of prey distributions in one space dimension, x. White regions indicate areas where prey populations temporarily go extinct (below the Allee threshold). Parameter values are as in Fig. 5.2.

(see Fig. 5.8a). Notably, during the first climatic downturn at $t = 71$, both steady-state and oscillatory regions coexist, as evidenced by the presence of both horizontal and vertical stripes before $t = 71$. Following this environmental shock, the oscillatory regions collapse rapidly (white area, post $t = 71$), whereas the steady-state regions survive (horizontal stripes). This trend repeats across subsequent declines in $r(t)$: Turing-like regions consistently endure, buffering against environmental shocks, while Hopf-like regions are vulnerable to synchronized extinction (Fig. 5.8c). These results underscore the critical role of steady state spatial heterogeneity in promoting ecological resilience under abrupt climatic stress.

Figures 5.8b and d illustrate a striking case of landscape-scale extinction driven by high spatial synchrony. Before the abrupt climatic decline at $t = 177$ (Fig. 5.8b), the prey population displays globally synchronized oscillations across the entire spatial domain (vertical stripes in Fig. 5.8d). This global synchrony, while initially stable, proves detrimental when the environmental parameter $r(t)$ sharply declines at $t = 177$. With no spatial heterogeneity to buffer the impact, the entire prey population collapses simultaneously, falling below the Allee threshold throughout the domain. The lack of locally stable regions prevents recovery, resulting in an irreversible, system-wide extinction. This example highlights the ecological risk of strong spatial synchrony under abrupt environmental stress.

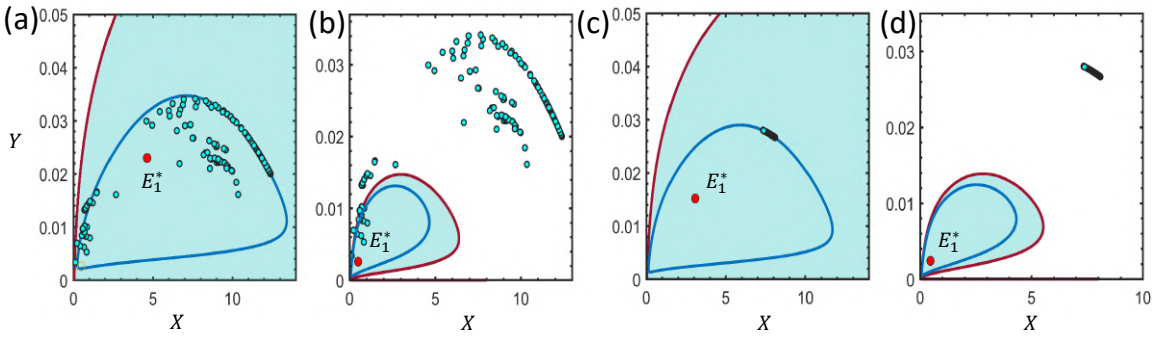

FIGURE 5.9: Phase plots before and after abrupt climatic declines at two key time points. Blue dots represent population levels at different spatial grid points. The red curve denotes the saddle separatrix, the blue curve is the limit cycle, and the red dot marks the unstable equilibrium point E_1^*. (a, b) Phase plots corresponding to Fig. 5.8c, just before and after the climatic drop at $t = 455$. (c, d) Phase plots corresponding to Fig. 5.8d, just before and after the climatic drop at $t = 177$.

Phase plane analyses before and after abrupt climatic shifts highlight how spatial synchrony and asynchrony influence population extinction and persistence. Prior to the climatic decline at $t = 455$, the species distribution (Fig. 5.8c) exhibits a mixture of Turing-like steady states and Hopf-like oscillations. The corresponding phase plot (Fig. 5.9a) shows population densities at each spatial grid just before $t = 455$, overlaid with the limit cycle (blue curve) and saddle-separatrix (red curve) of the local system for $r = 3.3651$ (see Fig. 5.8a). These densities are mostly scattered within the attraction basin of the limit cycle around the coexistence equilibrium E_1^*. Grids undergoing synchronized oscillations lie on the limit cycle, while those with Turing-like dynamics are distributed more broadly within the stable region. When the climatic parameter $r(t)$ abruptly declines to 1.851 at $t = 455$, the separatrix shifts inward, shrinking the attraction domain of the limit cycle (see Fig. 5.8b). As a result, synchronized grids and some asynchronous ones fall into the extinction basin, which momentarily goes to extinction (Fig. 5.8c), while a few remain within the reduced stable domain. Due to spatial heterogeneity, some regions survive and eventually repopulate the extinct zones through rescue waves (Fig. 5.8c). In contrast, when spatial synchrony is high, all population levels across grids oscillate simultaneously along the limit cycle, as shown in the phase plot before $t = 177$ for $r = 2.970$ (Fig. 5.9c). Following the decline to $r = 1.8203$, the entire phase space shifts (Fig. 5.9d), placing all population states into the extinction basin. Without spatially asynchronous or buffered grids, the system undergoes complete and irreversible extinction.

This extinction phenomenon resembles phase-tipping (P-tipping), as described by Alkhayuon et al. [215], where abrupt environmental changes during sensitive phases of population oscillations lead to collapse. Both the abrupt climatic decline and

high synchrony appear to play significant roles in triggering complete population extinction, as seen in previous simulations (Figs. 5.9c, d).

To verify this, we analyzed 500 realizations of complete extinction events occurring within a time interval of 500 units. Climatic fluctuations were considered in the range $(r_{min}, r_{max}) = (1.7, 3.8)$, consistent with earlier simulations. For each extinction event, we recorded the values of the drifting parameter $r(t)$ just before (r_{pre}) and after (r_{post}) the abrupt climatic decline that ultimately led to extinction. These are shown in Fig. 5.10a. The mean values were $r_{pre} = 3.2465$ and $r_{post} = 1.9052$, indicating that extinction is more likely when the climate parameter drops from around 3.25 to below 1.9 or further.

However, not all climatic declines lead to extinction, synchrony plays a crucial role. For the same 500 extinction events, we computed the time-averaged synchrony level using the instantaneous Kuramoto order parameter $\mathcal{R}(t)$ [218, 214] over the spatial grids, defined as

$$\mathcal{R}(t)e^{i\Phi(t)} = \frac{1}{n}\sum_{k=1}^{n} e^{i\theta_k(t)}, \tag{5.19}$$

where $i = \sqrt{-1}$ and n is the total number of spatial grids. $\theta_k(t)$ is the instantaneous phase angle of population abundance about the interior equilibrium point E_1^* defined as $\theta_k(t) = \tan^{-1}\left(\frac{Y_k(t)-Y_1^*}{X_k(t)-X_1^*}\right)$. The overall synchrony of population abundance is averaged over considered time interval. Here, $\mathcal{R}(t) \to 1$ indicates high synchrony, characteristic of Hopf-like oscillations, while lower values reflect asynchronous behavior or mixed dynamics, such as in the Turing-Hopf regime.

Figure 5.10b presents a scatter plot of the time-averaged synchrony levels against the magnitude of climatic decline for these extinction events (green dots). The data suggest that complete extinction predominantly occurs at higher levels of both synchrony and climatic decline. However, extinction can also result when either factor is sufficiently high, even if the other is moderate. This observation is further supported by the histograms in Fig. 5.10b. Thus, in the spatially extended system studied here, the interdependence among spatial grids is critical. High spatial synchrony, though appearing orderly, poses a significant risk: it enables the simultaneous collapse of all regions when exposed to sudden environmental degradation.

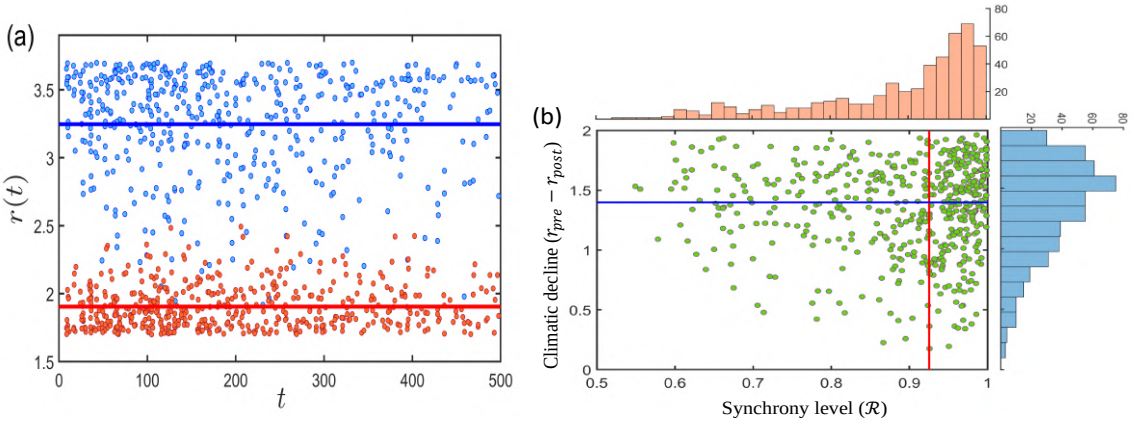

FIGURE 5.10: Analysis of 500 realizations of complete extinction events over a time interval of 500 Units. (a) Blue and red dots represent the r values before (r_{pre}) and after (r_{post}) an abrupt climate decline that led to complete population extinction. The blue and red lines indicate the mean values of r_{pre} and r_{post}, respectively. (b) Scatter plot showing the relationship between synchrony levels and the magnitude of abrupt climatic decline ($r_{pre} - r_{post}$) for the 500 extinction events. The right-side bar plot illustrates the frequency distribution of climatic declines, while the top-side bar plot displays the frequency distribution of synchrony levels associated with extinction. Red and blue lines represent the mean synchrony level and mean climatic decline responsible for complete species extinction.

5.6 Discussion

This study investigates how different spatiotemporal instabilities, namely Turing, Hopf, and mixed Hopf-Turing, influence population persistence and extinction in a predator-prey system subjected to climatic fluctuations. Using a reaction-diffusion framework, it reveals that the interaction between internal ecological dynamics and external environmental variability plays a central role in determining the resilience of ecosystems.

Turing-dominated regimes give rise to temporally steady but spatially heterogeneous population patterns. These patterns introduce spatial asynchrony, which dampens the effects of temporal variability and enhances the system's ability to withstand environmental shocks. In contrast, Hopf-dominated regimes promote spatial synchrony, leading to coordinated oscillations across the entire spatial domain. This synchrony increases vulnerability, as it enables system-wide collapses when environmental parameters change abruptly. In mixed Hopf-Turing regimes, the system may exhibit transient spatiotemporal chaos before stabilizing into either a heterogeneous steady state or sustained oscillations. These transitions depend on the system's proximity to the Hopf or Turing bifurcation boundaries, supporting previous observations that

competing instabilities can generate rich transient dynamics before convergence to long-term states [141, 200]. This work highlights how the dominant instability mode fundamentally shapes ecological outcomes under environmental forcing.

These findings are consistent with ecological theory, which suggests that spatial asynchrony promotes persistence by enabling localized recovery following disturbance [10, 11, 206, 207]. In Turing-like regimes, this manifests through the rescue effect, whereby high-density patches repopulate adjacent low-density ones. Conversely, Hopf dynamics induce strong spatial synchrony, resulting in synchronized tipping: abrupt climatic declines cause the entire spatial domain to collapse simultaneously, as seen in simulations (e.g., Fig. 5.8b,d). While metapopulation theory has recognized the dangers of synchrony [10, 210, 211, 212, 213, 214], this study incorporates dynamic parameter drift and demonstrates the possibility of irreversible extinction in such settings.

A major contribution of this work is the extension of phase-induced tipping (P-tipping) theory to spatially extended systems. Prior studies on non-spatial models showed that populations may collapse if climatic shocks occur during vulnerable phases of oscillatory cycles [215]. Here, this mechanism is shown to be spatially structured: the synchrony of oscillations across the spatial domain becomes a critical determinant of tipping risk. Under Hopf-dominated dynamics, abrupt declines in the prey growth rate $r(t)$ lead to synchronized collapse because all spatial locations share the same oscillatory phase. In contrast, Turing-like patterns support asynchronous dynamics, which localize and buffer the effects of environmental shocks. Rescue waves, mediated by diffusion, can repopulate extinct patches and prevent global extinction. This illustrates that extinction risk cannot be predicted by local dynamics or environmental thresholds alone; rather, it is the interaction between internal instability modes and spatial synchrony that determines system-level resilience or collapse.

Another important finding is the emergence of Turing-like spatial structures under non-autonomous conditions, where climatic parameters vary in a piecewise constant manner. Even under fluctuating environmental conditions, the system forms quasi-stationary spatial patterns that persist and buffer against extinction. These structures are ecologically significant because they resist collapse during sudden climatic downturns, in contrast to the fragility of synchronized oscillations [208, 74].

This study bridges important conceptual gaps by connecting spatiotemporal pattern formation theory with climate-driven extinction dynamics, offering a more comprehensive understanding of ecosystem stability. From an applied perspective, these findings suggest that promoting spatial heterogeneity, through habitat mosaics or disturbances that break synchrony, can increase resilience under climate variability. The results also motivate further development of tipping theory in spatially extended

systems, including the role of non-Turing instabilities (e.g., wave or mixed modes), multi-trophic interactions, adaptive movement strategies, and dispersal heterogeneity. Studying the effects of anisotropic diffusion and noise-induced transitions may yield deeper insights into the mechanisms that govern persistence and collapse. These insights hold practical implications for biodiversity conservation and ecosystem management, particularly in the face of climate change. Understanding how internal dynamics interact with environmental variability to drive tipping events can support the design of robust landscapes and early warning indicators that reduce the risk of synchronized extinction.

Chapter 6

Dynamic characteristics of an hyperbolic reaction-diffusion predator-prey system with self-diffusion and non-identical inertia [3]

.

6.1 Introduction

All the earlier models are formulated using parabolic-type reaction-diffusion (PRD) partial differential equations. Although the PRD system has been extensively used, it fails to describe spatial dispersal appropriately due to its unrealistic characteristics [219]. From the fundamental solution of a parabolic type partial differential equation, it is known that the initially localized disturbance propagates infinitely fast through the space [29]. However, species often exhibit inertia which results in a persistence effect in their spatial movement, i.e., the species does not change their direction frequently while moving at least at short timescales, dissimilar to the Brownian motion.

[3] Published article by Marick, S., Ghorai, S., & Bairagi, N. (2023). Dynamic characteristics of a hyperbolic reaction–diffusion predator–prey system with self-diffusion and nonidentical inertia. Mathematical Methods in the Applied Sciences, 46(13), 14407-14421. *https://doi.org/10.1002/mma.9326*

In microscopic models, the optimal foraging strategy of animals is better characterized by Levy walks and correlated random walks than the Brownian motion [220], having empirical evidence of persisting movement. As a result, the effect of sudden perturbation in a population density at some spatial point should not instantly affect the entire space. Macroscopic description of diffusive behaviour in population dynamics is considered to follow Fick's law which is analogous to Fourier's law in the context of heat flow. In the context of heat flow in the rigid body, it is noted that the undesirability of the parabolic type diffusion originates from neglecting the principle of microscopic reversibility [221]. This deficiency can be removed if we recognize that Fourier's law of flux equation is merely an approximate description of the diffusion process that neglects the time needed for acceleration of the heat flow [221]. A damped version of Fourier's law, which considers a heat–flux relaxation term, may overcome such anomalies. The relaxation or inertial delay time $\tau(> 0)$ is the response time for the onset of substance flow when a concentration gradient is suddenly imposed. Eventually, it gave rise to the well-known telegraph equation. In recent years, the hyperbolic reaction-diffusion (HRD) system has been used to extend the PRD systems. Different forms of the HRD systems, developed on the basis of different phenomenological constructions, have been used to study the spread of forest-fire [31], chemical reaction systems [222, 223], spread of infectious diseases [224, 225], predator-prey models [226, 227, 228] and network models [229, 230].

Predator-prey models are considered the building blocks of more complex ecosystems of food chains and food webs. Their extension to spatial predator-prey systems has further ecological significance in understanding species' spatial dispersal and distribution. It helps study the species distribution in a geographical region and the spread of diseases in spatially distributed animal groups. The PRD systems usually represent macroscopic models of such phenomena. This paper has studied the simplest HRD system of predator-prey interaction with self-diffusion and non-identical inertia. A general study of this type of HRD system, deriving the algebraic conditions of different instabilities, is done by Zemskov and Horsthemke [32] on two different prototypical chemical reactions with identical inertial times. Díaz et al.[226] performed a numerical study of an HRD predator-prey model with a ratio-dependent functional response. Adopting a finite difference scheme, they showed the existence and uniqueness of the solutions, which shows second-order consistency. Very recently, the work in [32] was extended by Ghorai et al. [231] by considering the non-identical inertia.

A predator-prey non-spatial model with Holling type III functional response and prey refuge was studied by Huang et al. [232]. The extension of this model to a PRD system was done by Chakraborty and Bairagi [138]. We extend the model further to an HRD system with different inertia and discuss the effects of the species-dependent inertial delay on the spatiotemporal distribution of species and its pattern formation. We derived the analytical conditions for wave instability and the corresponding wave

numbers. Our simulation results revealed complex spatiotemporal oscillatory patterns under the wave instability regime. In contrast to Turing instability, these patterns give descriptions of natural temporally oscillatory patterns, which have been less explored, especially in two-species systems. The rest of the paper is organized as follows. In the immediate next Section 6.2, we have described the mean-field predator-prey model and its extension to the HRD system. Section 6.3 includes the linear stability analysis of the system around the coexistence equilibrium state and provides the necessary and sufficient conditions for different diffusion-driven instabilities (Turing and wave). In Section 6.4, we have provided the computational scheme and validated the analytical results numerically. The effect of inertial time in the stability and pattern formation are demonstrated. The paper ends with a summary of our findings in Section 6.5.

6.2 Main Model

Consider the following system of hyperbolic reaction-diffusion equation representing the interaction of n species:

$$\vec{\tau}\frac{\partial^2\vec{X}}{\partial t^2} + \frac{\partial\vec{X}}{\partial t} = \vec{F}(\vec{X}) + D\nabla^2\vec{X}. \tag{6.1}$$

Here $\vec{X} = (X_1, X_2, ..., X_n) \in \mathbb{R}^n_+$ is the vector of densities of n species. $X_i = X_i(\vec{x}, t)$ is the density of i-th species at the position $\vec{x} = (x, y)$ at time t. $F_i : \mathbb{R}^n \to \mathbb{R}$, $i = 1, 2, ..., n$, represents the i-th component of the local interaction function $\vec{F}$ and $\vec{\tau} = (\tau_1, \tau_2, ..., \tau_i) \in \mathbb{R}^n_+$ is the inertial time vector of the n-species. The diagonal matrix $D = diag(D_1, D_2, ..., D_n) \in \mathbb{R}^{n\times n}$ is the diffusion coefficient matrix, whose elements are called the self-diffusion coefficients, and $\nabla^2 = \frac{\partial^2}{\partial x^2} + \frac{\partial^2}{\partial y^2}$ is the Laplacian operator for two-dimensional space. The self-diffusion coefficients are positive, implying the population dispersal from higher to lower concentrations at the local level.

For our case, the mean-field system of predator-prey interaction is represented as [232]

$$\begin{aligned}\frac{dX}{dt} &= aX - bX^2 - \frac{\alpha(1-m)^2X^2Y}{\beta^2 + (1-m)^2X^2},\\ \frac{dY}{dt} &= -cY + \frac{k\alpha(1-m)^2X^2Y}{\beta^2 + (1-m)^2X^2},\end{aligned} \tag{6.2}$$

where X and Y are, respectively, the concentrations of prey and predator populations at time t. The model illustrates that the prey population X grows logistically in the absence of its predator Y with the intrinsic growth rate a and carrying capacity $\frac{a}{b}$.

The growth rate of predators in the absence of their prey decays exponentially at a rate of c. The parameter k is the conversion efficiency of the predator, measuring its reproductive gain for each captured prey. The death of prey due to predation follows Holling type III functional response, having a maximum predation rate α and half-saturation constant β. The refuge parameter m $(0 \leq m < 1)$ describes the fraction of the prey population which is completely protected from the predation, leaving the $(1-m)$ fraction exposed to predation.

Using the transformations [232]

$$X = \beta\sqrt{\frac{c}{k\alpha - c}}\bar{X}, \quad Y = \frac{\beta}{\alpha}\sqrt{c(k\alpha - c)}\bar{Y}, \quad dt = \frac{c(1-m)^2\bar{X} + (k\alpha - c)}{c(k\alpha - c)}d\bar{t}, \tag{6.3}$$

and then dropping the bars, we get the simplified form of the kinetic system (6.2) as

$$\begin{aligned} \frac{dX}{dt} &= X(A_0 + A_1X + A_2X^2 + A_3X^3) - (1-m)^2X^2Y = F_1(X,Y), \\ \frac{dY}{dt} &= (1-m)^2X^2Y - Y = F_2(X,Y), \end{aligned} \tag{6.4}$$

where $A_0 = \frac{a}{c}(> 0)$, $A_1 = -\frac{b\beta}{c}\sqrt{\frac{c}{k\alpha - c}}(< 0)$, $A_2 = \frac{a(1-m)^2}{k\alpha - c}(> 0)$ and $A_3 = -\frac{b\beta(1-m)^2}{k\alpha - c}\sqrt{\frac{c}{k\alpha - c}}(< 0)$. The transformations will not change the qualitative behaviour of the system but will change the scale of the species concentrations. An inverse transformation will bring the required values of the system with reaction terms as in (6.2). Chakraborty and Bairagi [138] considered self-diffusion in (6.4) and studied the PRD system

$$\begin{aligned} \frac{\partial X}{\partial t} &= F_1(X,Y) + D_1\nabla^2 X, \\ \frac{\partial Y}{\partial t} &= F_2(X,Y) + D_2\nabla^2 Y. \end{aligned} \tag{6.5}$$

It was proved that the model does not show Turing instability but exhibits non-Turing instabilities and the corresponding patterns due to the variation of refuge parameter m and self-diffusion coefficients D_1, D_2. We have extended the PRD system (6.5) to the HRD system of the form (6.1) as

$$\begin{aligned} \tau_1\frac{\partial^2 X}{\partial t^2} + \frac{\partial X}{\partial t} &= F_1(X,Y) + D_1\nabla^2 X, \\ \tau_2\frac{\partial^2 Y}{\partial t^2} + \frac{\partial Y}{\partial t} &= F_2(X,Y) + D_2\nabla^2 Y. \end{aligned} \tag{6.6}$$

Here $\tau_1(> 0)$ and $\tau_2(> 0)$ are the inertial times of the prey and predator species,

respectively, which signifies inertial delay in concentration flow of that species when perturbed from the uniform steady state. Thus, the PRD system (6.5) becomes a limiting case of the HRD system (6.6) for $\tau_1, \tau_2 \to 0$. The diffusion effect acting here is local, i.e., dispersion of species is dependent only on the local gradient of the population density. To study the diffusion-driven instabilities for the system (6.6), we need to study the corresponding non-diffusive system

$$\begin{aligned} \tau_1 \frac{d^2X}{dt^2} + \frac{dX}{dt} &= F_1(X, Y), \\ \tau_2 \frac{d^2Y}{dt^2} + \frac{dY}{dt} &= F_2(X, Y). \end{aligned} \tag{6.7}$$

6.3 Equilibria and linear stability analysis

We are interested in the coexistence of uniform steady-state (USS), $E^* = (X^*, Y^*)$, of the system (6.7), where both the prey and predator species have non-zero population densities. The equilibrium population densities are given by

$$X^* = \frac{1}{1-m} \qquad \text{and} \qquad Y^* = \frac{k\alpha}{c(1-m)(k\alpha - c)} \left(a - \frac{b\beta}{1-m} \sqrt{\frac{c}{k\alpha - c}} \right).$$

To ensure biologically meaningful equilibrium values, one needs $0 \leq m < m_1$, where $m_1 = 1 - \frac{b\beta}{a}\sqrt{\frac{c}{k\alpha - c}}$ and $k\alpha > c$. It is to be noted that the spatial model (6.6) has the same USS of population densities as that of the kinetic systems (6.4) and (6.7). To perform the linear stability analysis of the spatial model (6.6), we impose small heterogeneous perturbations

$$\begin{aligned} \delta X(\vec{x}, t) &= X(\vec{x}, t) - X^*, \\ \delta Y(\vec{x}, t) &= Y(\vec{x}, t) - Y^*. \end{aligned} \tag{6.8}$$

Here $\delta X(\vec{x}, t)$ and $\delta Y(\vec{x}, t)$ have the form

$$\begin{aligned} \delta X(\vec{x}, t) &= C_X \, exp(\lambda t + i\vec{k}\vec{x}), \\ \delta Y(\vec{x}, t) &= C_Y \, exp(\lambda t + i\vec{k}\vec{x}), \end{aligned} \tag{6.9}$$

where $\vec{k} = (k_1, k_2)$ is the wavenumber vector ($k^2 = |\vec{k}^2| = k_1^2 + k_2^2$), λ is the eigenvalue and C_X, C_Y are constants. Substituting (6.8) in (6.6) and linearizing about E^*, one

obtains

$$\begin{aligned}\tau_1\frac{\partial^2\delta X}{\partial t^2}+\frac{\partial\delta X}{\partial t}&=J_{11}\delta X+J_{12}\delta Y+D_1\nabla^2\delta X,\\ \tau_2\frac{\partial^2\delta Y}{\partial t^2}+\frac{\partial\delta Y}{\partial t}&=J_{21}\delta X+J_{22}\delta Y+D_2\nabla^2\delta Y.\end{aligned}\tag{6.10}$$

Plugging the expressions of the perturbations from (6.9), we get the matrix form

$$\begin{pmatrix}J_{11}-k^2D_1-\tau_1\lambda^2-\lambda & J_{12}\\ J_{21} & J_{22}-k^2D_2-\tau_2\lambda^2-\lambda\end{pmatrix}\begin{pmatrix}C_X\\ C_Y\end{pmatrix}=0.$$

For the existence of nontrivial perturbations, the determinant value of the above matrix must be zero, giving the characteristic equation

$$P(\lambda)=\sum_{i=0}^{4}\mu_i(k)\lambda^{4-i}=0,\tag{6.11}$$

where

$$\begin{aligned}&\mu_0(k)=\tau_1\tau_2,\quad \mu_1(k)=\tau_1+\tau_2,\quad \mu_2(k)=k^2(D_1\tau_2+D_2\tau_1)-J_{11}\tau_2-J_{22}\tau_1+1,\\ &\mu_3(k)=k^2(D_1+D_2)-T,\quad \mu_4(k)=D_1D_2k^4-k^2(D_1J_2+D_2J_1)+\Gamma.\end{aligned}\tag{6.12}$$

Here T and Γ are, respectively, the trace and determinant of the Jacobian matrix $J=(J_{ij})_{2\times2}$ of the non-inertial kinetic system (6.4) evaluated at E^*, the components of which read

$$\begin{aligned}J_{11}&=\left(\frac{a}{c}\right)\left(\frac{2c-k\alpha}{k\alpha-c}\right)-\left(\frac{2b\beta}{1-m}\right)\left(\frac{1}{k\alpha-c}\right)\left(\sqrt{\frac{c}{k\alpha-c}}\right),\\ J_{12}&=-1,\\ J_{21}&=\frac{2k\alpha}{c(k\alpha-c)}\left(a-\frac{b\beta}{1-m}\sqrt{\frac{c}{k\alpha-c}}\right),\\ J_{22}&=0.\end{aligned}\tag{6.13}$$

The stability criteria of the coexistence equilibrium E^* for the non-inertial kinetic system (6.4) can be summarized in the following theorem.

Theorem 6.1. *[138] The interior equilibrium E^* of the kinetic system (6.4) is locally asymptotically stable if $m^*<m<m_1$ and unstable if $0\le m<m^*$. Stability switch occurs through a Hopf bifurcation at $m=m^*$, where $m^*=1-\frac{2bc\beta}{a(2c-k\alpha)}\sqrt{\frac{c}{k\alpha-c}}$ and $m_1=1-\frac{b\beta}{a}\sqrt{\frac{c}{k\alpha-c}}$.*

6.3.1 Bifurcation analysis

Spatially homogeneous perturbation for the system (6.7) is obtained by setting $k^2 = 0$ in (6.9). The corresponding characteristic equation reads

$$P(\lambda) = \sum_{i=0}^{4} \mu_i(0)\lambda^{4-i} = 0, \tag{6.14}$$

where

$$\mu_0(0) = \tau_1\tau_2, \quad \mu_1(0) = \tau_1 + \tau_2, \quad \mu_2(0) = -J_{11}\tau_2 - J_{22}\tau_1 + 1, \quad \mu_3(0) = -T, \quad \mu_4(0) = \Gamma. \tag{6.15}$$

The USS of the kinetic system (6.7) will be stable if all roots of (6.14) have negative real parts. Routh-Hurwitz determinants [29] $\Delta_i(0)$ (0 stands for $k^2 = 0$) for $i = 1, 2, 3, 4$, of different orders are given by

$$\begin{aligned}
\Delta_1(0) &= \mu_1(0) = \tau_1 + \tau_2,\\
\Delta_2(0) &= \mu_1(0)\mu_2(0) - \mu_0(0)\mu_3(0) = -J_{11}\tau_2^2 - J_{22}\tau_1^2 + \tau_1 + \tau_2,\\
\Delta_3(0) &= \mu_1(0)\mu_2(0)\mu_3(0) - \mu_1(0)^2\mu_4(0) - \mu_0(0)\mu_3(0)^2\\
&= J_{11}^2\tau_2^2 + J_{22}^2\tau_1^2 + J_{12}J_{21}(\tau_1^2 + \tau_2^2) - 2\tau_1\tau_2\Gamma - (\tau_1 + \tau_2)T,\\
\Delta_4(0) &= \mu_4(0)\Delta_3(0).
\end{aligned} \tag{6.16}$$

The linear stability and Hopf instability conditions of the kinetic system (6.7) can be summarized as follows.

Theorem 6.2. *The USS E^* of the kinetic system (6.7) is locally asymptotically stable if and only if*

$$\Delta_i(0) > 0, \ \forall i = 2, 3 \quad \& \quad \mu_4(0) > 0.$$

The critical condition of the Hopf bifurcation, following Orlando's formula [29], is $\Delta_3(0) = 0$.

We now consider the spatially nonhomogeneous perturbations (6.9) on E^*, which may create the spatiotemporal patterns in the system (6.6). The stability analysis will be similar to the study of Theorem 6.2 but with non-zero wavenumbers. In this case,

the Routh-Hurwitz determinants for the spatially nonhomogeneous system reads

$$\begin{aligned}
\Delta_1(k) &= \mu_1(k) = \tau_1 + \tau_2, \\
\Delta_2(k) &= \mu_1(k)\mu_2(k) - \mu_0(k)\mu_3(k) = k^2\left(D_1\tau_2^2 + D_2\tau_1^2\right) + \Delta_2(0), \\
\Delta_3(k) &= \mu_1(k)\mu_2(k)\mu_3(k) - \mu_1(k)^2\mu_4(k) - \mu_0(k)\mu_3(k)^2 \\
&= k^4(D_1\tau_2 - D_2\tau_1)^2 + k^2(2(J_{11}\tau_2 - J_{22}\tau_1)(D_2\tau_1 - D_1\tau_2) \\
&\quad + (D_1 + D_2)(\tau_1 + \tau_2)) + \Delta_3(0), \\
\Delta_4(k) &= \mu_4(k)\Delta_3(k).
\end{aligned} \tag{6.17}$$

Diffusion-driven instabilities occur in the system (6.6) if the USS is stable in the absence of diffusion but unstable in its presence. It occurs when nonhomogeneous perturbation imposed on the USS grows over time. This is possible if the real part of at least one eigenvalue of (6.11) becomes positive from its negative value for some nonzero wavenumbers. Notice that $\Delta_1(k) > 0$ always holds, and $\Delta_2(k) > 0$ also holds, provided the non-diffusive system is stable. Therefore, diffusion-driven instability occurs if the conditions of the following theorem hold.

Theorem 6.3. *Assume that stability conditions of USS E^* of Theorem 6.2 hold. A set of necessary and sufficient conditions for the diffusion-driven instability to occur in the HRD system (6.6) is either $\Delta_3(k) < 0$ or $\mu_4(k) < 0$ for some nonzero wavenumbers.*

It is to be mentioned that the condition $\Delta_3(k) < 0$ gives the wave instability and the condition $\mu_4(k) < 0$ (provided $\Delta_3(k) > 0$) gives the Turing instability [29]. The following subsections describe the critical conditions for arising different instabilities.

6.3.2 Turing instability

Turing instability occurs if the stable USS E^* becomes unstable due to diffusion when a real eigenvalue changes from negative to positive for some positive k. Therefore, to occur the Turing instability for the system (6.6), stability conditions given in the Theorem 6.2 have to hold along with $\Delta_3(k) > 0$ but $\mu_4(k) < 0$. At the onset of Turing instability, we must have

$$\mu_4(k) = \phi_0 k^4 - \phi_1 k^2 + \phi_2 = 0, \tag{6.18}$$

where $\phi_0 = D_1D_2,\ \phi_1 = D_1J_{22} + D_2J_{11},\ \phi_2 = \Gamma$.

Since $\Gamma > 0$ for the stability of the corresponding non-diffusive system, and D_1, D_2 are both positive, so $\mu_4(k) < 0$ is possible only if

$$\phi_1 = D_1 J_{22} + D_2 J_{11} > 0. \tag{6.19}$$

Solving (6.18) for k^2, one gets the interval of wavenumbers $k_{T_1}^2 < k_T^2 < k_{T_2}^2$ for which the Turing instability is possible, where

$$k_{T_1}^2, k_{T_2}^2 = \frac{\phi_1 \mp \sqrt{\phi_1^2 - 4\phi_0\phi_2}}{2\phi_0}. \tag{6.20}$$

For the feasible range of wavenumbers, one needs $\phi_1^2 - 4\phi_0\phi_2 = (\phi_1 + 2\sqrt{\phi_0\phi_2})(\phi_1 - 2\sqrt{\phi_0\phi_2}) > 0$. Stability conditions of the non-diffusive system, and the condition (6.19) ensure $\phi_1 + 2\sqrt{\phi_0\phi_2} > 0$. Therefore, positivity of $\phi_1^2 - 4\phi_0\phi_2$ is ensured if $\phi_1 - 2\sqrt{\phi_0\phi_2}$ becomes positive. Therefore, the critical condition for Turing instability to occur, where the discriminant is zero, is $\phi_1 = 2\sqrt{\phi_0\phi_2}$, and the critical wavenumber is $k_T = \sqrt[4]{\frac{\Gamma}{D_1 D_2}}$. Thus, we state the following theorem.

Theorem 6.4. *Assume that the stability criteria of the USS E^* of Theorem (6.2) hold. A necessary and sufficient condition for the Turing instability to occur in the HRD system (6.6) is $\phi_1 - 2\sqrt{\phi_0\phi_2} > 0$, and the corresponding range of the wavenumber is $k_{T_1}^2 < k^2 < k_{T_2}^2$, where $k_{T_1}^2$ and $k_{T_2}^2$ are given in (6.20).*

Note that the stability conditions of the USS for the two kinetic systems (6.4) and (6.7) are different due to the presence of the inertial time in the latter system. However, the additional condition required for the existence of the diffusion-driven instability (Turing) of the USS for their corresponding reaction-diffusion systems (Eqs. (6.5) and (6.6)) is the same, $\phi_1 > 2\sqrt{\phi_0\phi_2} > 0$. It is also independent of the inertial time. For the occurrence of Turing instability, the underlying noninertial kinetic system (6.4) should be of activator-inhibitor type, which comes from the signs of J_{11} and J_{22} at E^*. Since J_{22} is always zero (see (6.13)) for both the kinetic systems, Turing instability is absent in both the PRD system (6.5) and HRD system (6.6).

6.3.3 Wave instability

The wave instability occurs if the stable USS E^* loses its stability due to diffusion when the real parts of a pair of complex eigenvalue change from a negative real part to a positive real part for some positive k. Therefore, to occur the wave instability for the system (6.6), stability conditions of Theorem 6.2 must hold along with $\mu_4(k) > 0$,

but $\Delta_3(k) < 0$. Thus, at the onset of wave instability,

$$\Delta_3(k) = a_0 k^4 + a_1 k^2 + a_2 = 0, \tag{6.21}$$

where $a_0 = (D_1\tau_2 - D_2\tau_1)^2$, $a_1 = 2(J_{11}\tau_2 - J_{22}\tau_1)(D_2\tau_1 - D_1\tau_2) + (D_1 + D_2)(\tau_1 + \tau_2)$, $a_2 = \Delta_3(0)$.
Observe that a_0 is always non-negative, and the stability of the non-diffusive system implies positivity of a_2. Therefore, wave instability is possible only if $a_1 < 0$. The roots of (6.21) give the interval of nonzero wavenumbers, $k_{W_1}^2 < k^2 < k_{W_2}^2$, where $k_{W_1}^2$ and $k_{W_2}^2$ are

$$k_{W_1}^2, k_{W_2}^2 = \frac{-a_1 \mp \sqrt{a_1^2 - 4a_0a_2}}{2a_0}. \tag{6.22}$$

For the feasibility of wavenumbers, the discriminant in (6.22) should be positive, giving $a_1^2 - 4a_0a_2 = (a_1 + 2\sqrt{a_0a_2})(a_1 - 2\sqrt{a_0a_2}) > 0$. Noting the stability criteria of the non-diffusive system, one can see that $a_1 - 2\sqrt{a_0a_2} < 0$. So, $a_1^2 - 4a_0a_2 > 0$ holds if $a_1 + 2\sqrt{a_0a_2} < 0$. At the critical point of wave instability, one have $k_W = \sqrt[4]{-\frac{a_1}{2a_0}}$. Thus, the conditions for wave instability can be summed up in the following theorem.

Theorem 6.5. *Assume that the stability conditions of the USS E^* stated in Theorem (6.2) hold. A set of necessary and sufficient conditions for the wave instability to occur in the HRD system (6.6) is $a_1 + 2\sqrt{a_0a_2} < 0$. The wave instability occurs in the range $k_{W_1}^2 < k^2 < k_{W_2}^2$, where $k_{W_1}^2$ and $k_{W_2}^2$ are given in (6.22).*

The critical condition of wave instability depends on the sign of the coefficient a_1, which is further dependent on the parameters m, τ_1 and τ_2. Therefore, for our model, prey refuge and inertial time play a vital role in the occurrence of wave instability. It is interesting to note a contrasting behaviour between PRD and HRD systems. A quintessential characteristic of a two-species HRD system with self-diffusion only is that it can exhibit wave instability. However, the corresponding PRD system is unable to produce it. Since two species spatiotemporal predator-prey interaction models with diagonal diffusion matrices are mostly based on PRD systems, diffusion-driven wave instability is not studied much.

6.4 Numerical simulations

Comparison of kinetic systems

To study the diffusive instability of the system (6.6) numerically, we first need to study the stability of the corresponding kinetic system (6.7). The underlying kinetic

system for the HRD system (6.6) is different to that of its parabolic counterpart (6.5) due to the presence of second-order time-derivatives. For the initial values of kinetic system (6.7), one needs the initial rate of change of the species concentrations. Since we are considering that the initial response of the system subjected to a perturbation is not likely to propagate instantly through the space, the rate of change of initial concentrations $\frac{dX}{dt}$, $\frac{dY}{dt}$ are considered zero, and the initial values of concentrations $(X(t=0), Y(t=0))$ are taken close to the equilibrium value (X^*, Y^*). For the simulations of the second-order ODE system (6.7), we first transform it into a system of four first-order ODEs by considering $\frac{dX}{dt}$, $\frac{dY}{dt}$ as the new state variables, and then solve it numerically using MATLAB, version R2019b.

We now compare the stability natures of the kinetic system (6.4) with no inertia with that of the system (6.7) with inertia. For this, the parameter values are taken from Chakraborty and Bairagi [138], except the refuge parameter m. The stability range of the coexistence equilibrium E^* under non-inertial situation is $m \in (m^*, m_1)$ (see Theorem 6.1), where $m^* = 0.5859$ and $m_1 = 0.9408$. We observe the effects of the inertial times τ_1, τ_2 on the stability and instability of the coexistence equilibrium for some fixed values of m taken from the stability range (Fig. 6.1). The unstable region II is separated by the Hopf bifurcation curve from the stable region I. As m is the refuge parameter, a greater value of m means more fraction of the prey population is abundant from predation. The inertial time can be considered a delay in the specie's response to a perturbation. The coexistence equilibrium is likely to be stable under spatial dispersal if the delay time of the prey is less than the delay time of the predator. If the refuge population increases, it will be easier for the prey population to survive, as more prey population becomes protected from predation. So, prey can afford more delayed responses. Therefore, the stable region grows with the increasing value of the refuge parameter. It is to be mentioned that the equilibrium E^* is stable for the considered parameter values if there is no inertial time (i.e., $\tau_1 = 0 = \tau_2$). Thus, inertia causes instability by reducing the stable region of the USS E^*.

For further comparison, we have represented time series solutions (see Fig. 6.2) of the systems (6.4) and (6.7) for different pairs of (τ_1, τ_2) when $m = 0.85$. The time series solutions decipher that the asymptotic behaviour of the two systems is similar when inertial times are small (see Fig. 6.2a). However, the solutions are different if τ_1 and τ_2 are significantly large. In fact, the solution of (6.7) shows limit cycle behaviour for $(\tau_1, \tau_2) = (0.7, 1)$ (Fig. 6.2b) or even chaotic behavior for $(\tau_1, \tau_2) = (1.3, 1.3)$ (Fig. 6.2c). However, the solution of the non-inertial (i.e., PRD) system (6.4) (represented by red line) is always stable. Figures 6.2(d-f) are the corresponding phase-portraits of the kinetic system (6.7).

A two-parameter bifurcation diagram on $\tau_2 - \tau_1$ parametric space, representing the existence of different periodic oscillations, is provided in Fig. 6.3a. For the fixed value

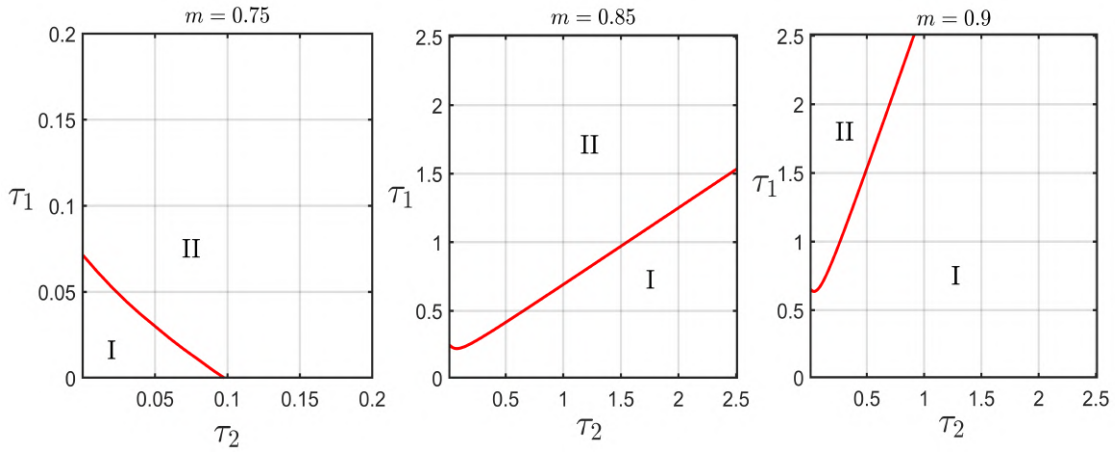

FIGURE 6.1: Stable region (I) and unstable region (II) of E^* in $\tau_1 - \tau_2$ plane for some fixed values of m. The Hopf bifurcation curve $\Delta_3(0) = 0$ separates the stable region from the unstable region. Parameter values are $a = 1$, $b = 0.1$, $c = 0.07$, $k = 0.4$, $\alpha = 0.3$, $\beta = 0.5$ [138].

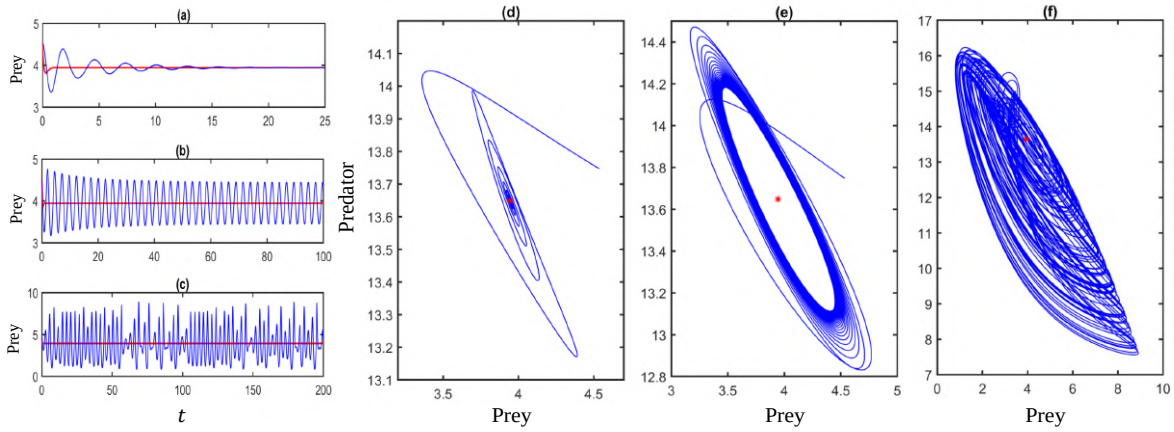

FIGURE 6.2: **(a)-(c)**: Time series solutions of prey population of the kinetic system (6.7) for various inertial times: (a) $(\tau_1, \tau_2) = (0.5, 1)$, (b) $(\tau_1, \tau_2) = (0.7, 1)$, (c) $(\tau_1, \tau_2) = (1.3, 1.3)$. Red coloured time series is for the system (6.4). **(d)-(f)**: The corresponding phase portraits. A red star is the equilibrium point E^* of the kinetic system. Here $m = 0.85$ and the other parameters are as in Fig. 6.1.

of $\tau_2 = 1$, the prey bifurcation diagram (Fig. 6.3b) with respect to the prey inertial time τ_1 shows a period doubling route to chaos. It specifies that the first stability switch occurs through a Hopf bifurcation at $\tau_1 = 0.6873$. The stable population begins to oscillate periodically as the prey inertial time increases. The oscillations, however, become aperiodic through multiple bifurcations, and the system enters into a chaotic

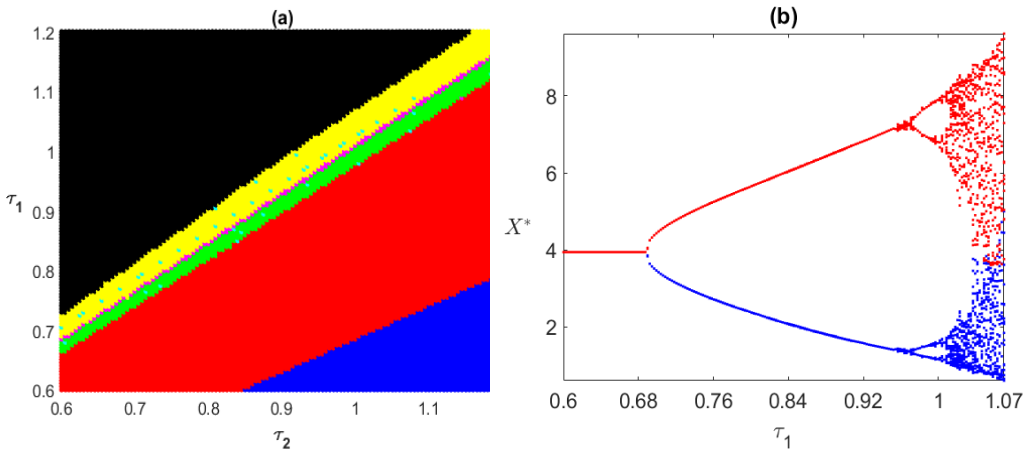

FIGURE 6.3: **(a)** The two-parameter bifurcation plot with respect to τ_1 and τ_2. **Blue region**: E^* is stable, **Red region**: One period oscillations, **Green region**: two period oscillations, **Cyan region**: three period oscillations, **Magenta region**: four period oscillations and **Yellow region**: five and higher period of oscillations including chaos. **Black region**: The region where the solution blows up. **(b)** Bifurcation of the prey density with respect to the prey inertial time τ_1 when $\tau_2 = 1$. Other parameter values are same as Fig. 6.1 with $m = 0.85$.

regime as τ_1 is gradually increased. It encapsulates that when the prey response time τ_1 is faster, then the prey population sustains strongly at its asymptotic value, assuring the sustainability of the predator population as well. But instability sets in as the prey response time is delayed due to higher inertial time.

Spatially extended system

An analytical solution of the spatiotemporal interaction model (6.6) with high nonlinearity is difficult to obtain. Especially, the hyperbolic reaction-diffusion system in two species does not generally possess analytical solutions. In such a case, a numerical solution is a good option to understand the behaviour of the solutions and visualize the patterns effectively. We, therefore, simulate our HRD predator-prey model (6.6) in the certain bounded spatial domain $\Omega = [0, L_x] \times [0, L_y]$ with time $t \in [0, \infty)$ with zero flux boundary conditions

$$\frac{\partial X}{\partial \nu} = \frac{\partial Y}{\partial \nu} = 0, \quad \forall (x, y) \in \partial\Omega, \qquad \forall t > 0,$$

where $\partial\Omega$ is the boundary of the domain Ω and ν is the outward normal vector on the boundary $\partial\Omega$. The two-dimensional space with $L = L_x = L_y$ is discretized into

smaller grids of length $\delta x = \delta y$ unit and time-step δt unit. The grid lengths of space and time are chosen suitably so that the stability of the numerical scheme satisfies the Courant-Friedrichs-Lewy (CFL) stability criterion [40]. The Laplacian is approximated using the standard five-point discretization formula. For the discretization scheme of second and first-order derivatives, the central difference formula and the forward difference formula were considered, respectively, with the step-size δt as

$$\tau_1 \frac{X_{i,j}^{n+1} - 2X_{i,j}^{n} + X_{i,j}^{n-1}}{\delta t^2} + \frac{X_{i,j}^{n+1} - X_{i,j}^{n}}{\delta t} = F_1(X_{i,j}^{n}, Y_{i,j}^{n}) + D_1 \mathcal{L} X^n,$$
$$\tau_2 \frac{Y_{i,j}^{n+1} - 2Y_{i,j}^{n} + Y_{i,j}^{n-1}}{\delta t^2} + \frac{Y_{i,j}^{n+1} - Y_{i,j}^{n}}{\delta t} = F_2(X_{i,j}^{n}, Y_{i,j}^{n}) + D_2 \mathcal{L} Y^n,$$

where $\mathcal{L}$ is the five-point discretized Laplacian operator for the two-dimensional spatial grid. In the notation $X_{i,j}^{n}$, n stands for the n-th time-step and i, j stands for (i, j)-th spatial grid. Since an HRD system (6.6) has second-order derivatives in time, we need values of the population concentrations at two-time steps to describe the future time steps uniquely. Small uniformly distributed random perturbations $(\Theta X_{i,j}, \Theta Y_{i,j})$ distributed within the range $[-10^{-4}, 10^{-4}]$ about the equilibrium point E^* are taken as

$$X_{i,j}^{0} = X_{i,j}^{1} = X^* + \Theta X_{i,j} > 0, \quad Y_{i,j}^{0} = Y_{i,j}^{1} = Y^* + \Theta Y_{i,j} > 0.$$

In these expressions, the equal values in the first two time steps imply that the rate of change of perturbations is zero initially, as we have discussed it earlier for the kinetic system (6.7).

6.4.1 Pure wave and Hopf-wave patterns

Here we study the pattern formation phenomenon of the system (6.6) by varying the prey inertial time and the prey diffusion coefficient, while fixing the same for the predator population. The pure wave, Hopf-wave and the stability regions are demonstrated in $D_1 - \tau_1$ parametric plane (see Fig. 6.4a). The Hopf wave region is separated by the curve $\Delta_3(0) = 0$ (red dashed line), following Theorem 6.2. The region below this curve is the stable zone of E^* in the absence of diffusion. Following Theorem 6.5, diffusion separates this zone into a stable and a wave region by the curve $a_1 + 2\sqrt{a_0 a_2} = 0$ (blue dashed line). The dispersion relations for the wave instability (Fig. 6.4b) and Hopf-wave instability (Fig. 6.4c) are presented for two sample points $(D_1, \tau_1) = (0.3, 0.5)$ and $(D_1, \tau_1) = (0.55, 0.7)$, respectively. In pure wave instability, the dispersion curve starts with a negative value for $k = 0$ and becomes positive for non-zero k. The existence of an imaginary part (see inset) for the entire range of k

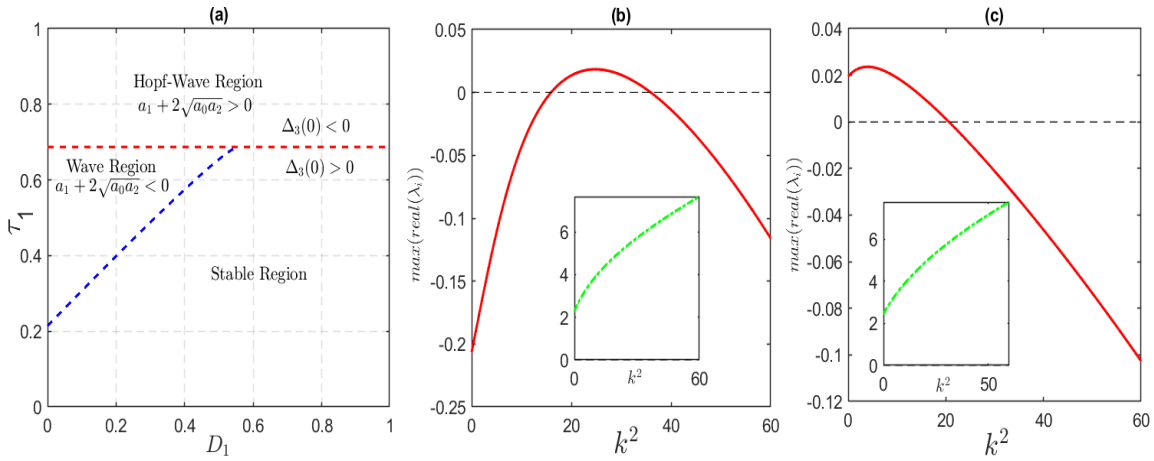

FIGURE 6.4: **(a)** Stability and instability in (D_1, τ_1) parametric plane with $\tau_2 = 1$ and $D_2 = 1$. Red dashed line is the Hopf bifurcation curve and the blue dashed line represents the curve $a_1 + 2\sqrt{a_0 a_2} = 0$. **(b)-(c)** Dispersion relations corresponding to the point $(D_1, \tau_1) = (0.3, 0.5)$, taken from the wave region of Fig. 6.4a. The same is drawn for the point $(D_1, \tau_1) = (0.55, 0.7)$, taken from the Hopf-wave region. The corresponding imaginary parts are shown in the inset. Here $m = 0.85$ and the other parameters are as in Fig. 6.1.

indicates that the eigenvalue is complex. In the case of Hopf-wave instability (Fig. 6.4c), the real part of the complex eigenvalue starts with a positive value for $k = 0$. The range of wave numbers, causing the wave instability, is obtained from (6.22) as 3.9895 to 5.9947 (see Fig. 6.4b).

To visualize the patterns in the pure wave region, we have provided some snapshots in the plane of $x - y$ space variables (see Fig. 6.5). These snapshots, after long transient time, depict the spatial distribution of the prey population. It shows that the species density oscillates in a particular repetitive sequence of patterns. It is to be mentioned that the patterns under pure wave instability are dependent on the initial values. As we have considered the initial spatial distribution as random, so they are different for each run, and consequently, the patterns are different as well. It is to be noted that the transient dynamics of the HRD system (6.6) is affected by all possible unstable eigenmodes corresponding to unstable wavenumbers within (k_{W_1}, k_{W_2}). But, after sufficiently long time, the eigenmode corresponding to the dominant eigenvalue and the nonlinearities in the reaction terms emerge as the determining factors of the pattern dynamics, resulting the repetitive sequence of patterns. The dominant eigenmode is obtained for the wavenumber k for which the real part of the eigenvalues becomes maximum (as shown in Fig. 6.4b). Although these patterns are different, they are qualitatively similar, as all are oscillatory. The time series at a randomly chosen spatial grid (x_i, y_j), and the corresponding phase portraits show pure oscillations (Fig. 6.6). The time series for Hopf-wave instability is qualitatively similar to

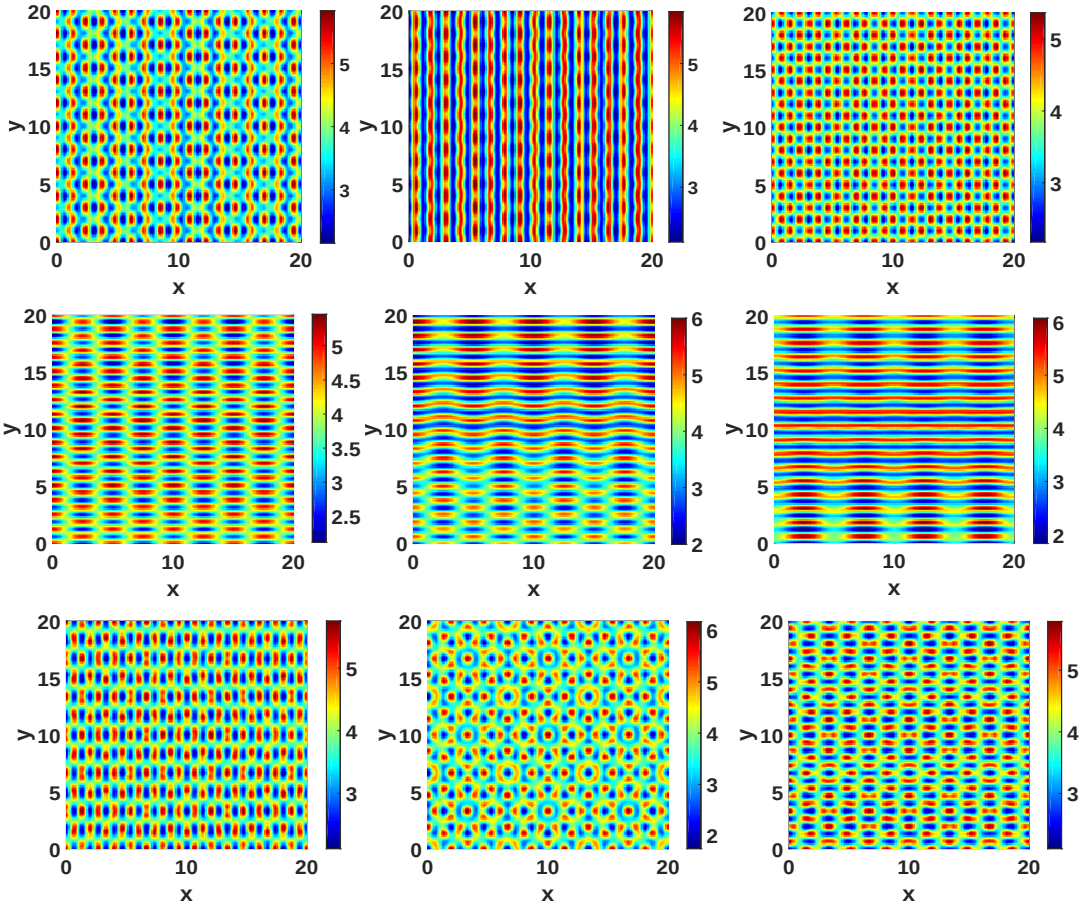

FIGURE 6.5: Patterns generated by prey species in pure-wave parameter regime with $(D_1, \tau_1) = (0.3, 0.5)$. Each row of snapshots is generated in a single simulation at different times (within $t = 4000$ to 5000). Random initial values around E^* is chosen for each row. Here $L = 20$, $\delta x = 0.1$, $\delta t = 0.01$ and the other parameters are same as in Fig. 6.1 with $m = 0.85, D_2 = 1$ and $\tau_2 = 1$.

the wave instability, but the patterns here are not dependent on the initial species distribution. After a sufficiently long time in every run with different initial conditions, the patterns oscillate identically as in Fig. 6.7. Therefore, the Hopf-wave patterns are not sensitive to initial concentrations. The two-parameter bifurcation (Fig. 6.4a) shows that if τ_1 is gradually increased, keeping D_1 fixed, it generates spatiotemporal instabilities, as mentioned in the previous section. Here change may occur in the sequence: stable→pure wave→Hopf-wave or stable→Hopf-wave (see Fig. 6.4a). On the other hand, the variation of prey diffusion coefficient from lower to higher value for some fixed τ_1 shifts the system from a pure wave instability region to a stable homogeneous state. Theoretically and empirically, predators disperse in habitat

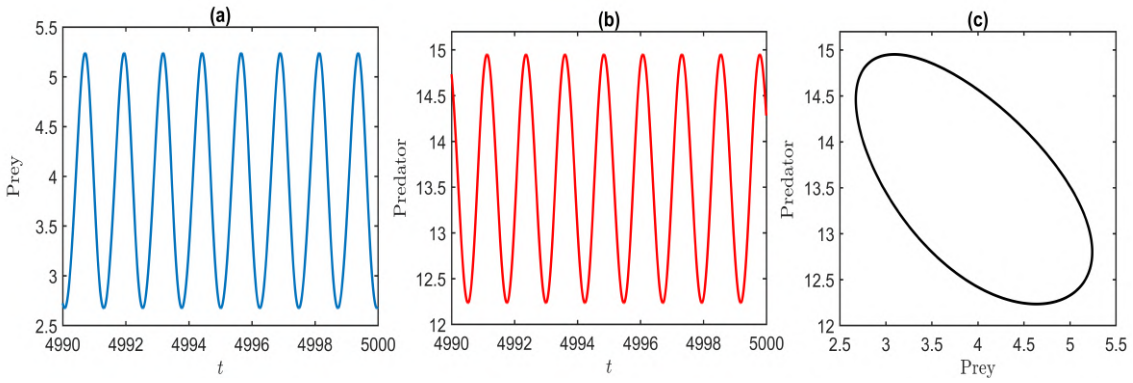

FIGURE 6.6: **(a-b)** The time series of prey and predator species at an arbitrary spatial grid for pure wave instability. **(c)** The corresponding phase portrait. Parameters are as in Fig. 6.5

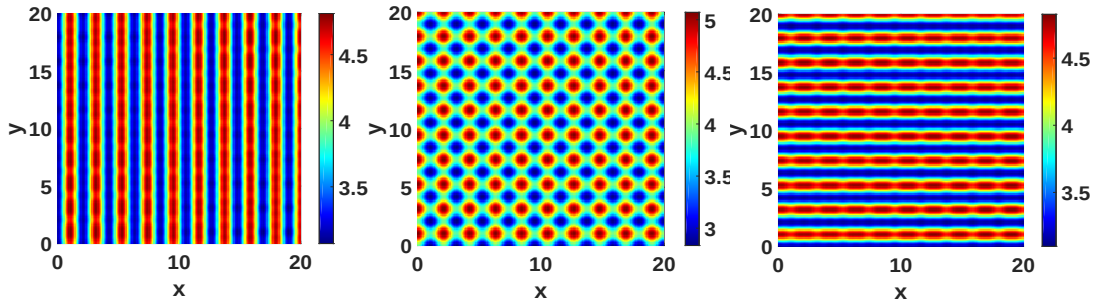

FIGURE 6.7: Snapshots of patterns generated by the prey population in Hopf-wave parameter regime with $(\tau_1, D_1) = (0.7, 0.55)$. Parameters are as in Fig. 6.5.

comparatively more than prey. A necessary condition for generating patterns in the predator-prey system also needs $D_2 >> D_1$ [102, 233, 234]. Our model analysis found that spatiotemporal instability is triggered by a higher value of prey inertial time, corroborating the natural observations.

6.4.2 Hopf-Turing pattern

As described earlier, inertial time has no effect on generating pure Turing instability and this instability is not possible in our system (See Section 6.3.2) but Hopf-Turing instability is possible. Hopf-Turing instability appears when the conditions of Hopf and Turing instability are satisfied simultaneously. The condition (6.19) for Turing instability involving the diffusion coefficients is not satisfied when $m^* < m < m_1$, because $J_{22} = 0$ (cf. (6.13)) and $J_{11} < 0$ in this stable range of m. But, when m lies in $0 < m < m^*$, then J_{11} becomes positive and the Turing condition (6.19)

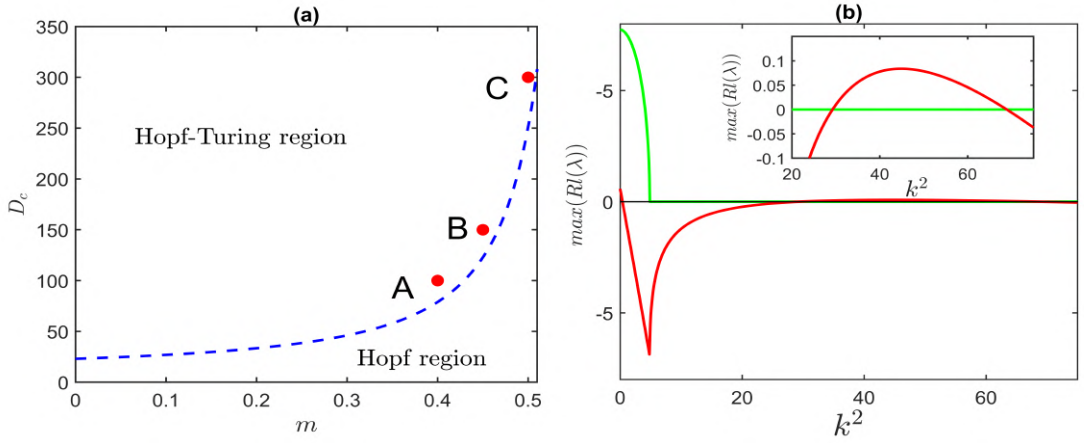

FIGURE 6.8: **(a)** Hopf-Turing and Hopf instability regions in $m - D_c$ plane for $\tau_1 = 0.001$, $\tau_1 = 0.002$. The blue dashed line is the Hopf-Turing curve that separates the Hopf-Turing region from the Hopf region. Here A, B and C are three observational points, having positions $(m = 0.4, D_c = 80)$ (for $(D_1, D_2) = (0.01, 0.8)$), $(m = 0.45, D_c = 150)$ (for $(D_1, D_2) = (0.01, 1.5)$), and $(m = 0.5, D_c = 300)$ (for $(D_1, D_2) = (0.01, 3)$), to be used in the next figure. **(b)** Dispersion relation corresponding to the point $(m, D_c) = (0.5, 300)$ (with $D_1 = 0.01$, $D_2 = 3$), taken from the Hopf-Turing region. Red curve: Maximum real part of the eigenvalues, Green curve: corresponding imaginary part. Other parameters are as in Fig. 6.1.

may be satisfied. Only remaining condition to be hold for the Turing instability is $\phi_1 - 2\sqrt{\phi_0\phi_2} > 0$ (See Theorem 6.4), giving a critical diffusion ratio for Hopf-Turing instability,

$$D_c = \frac{D_2}{D_1} = \frac{4\Gamma}{J_{11}^2}. \tag{6.23}$$

The Hopf-Turing curve $D_c = 0$ delineates the Hopf-Turing region from the Hopf region.

The change of D_c with refuge parameter m in Fig. 6.8 clearly shows that D_c increases with increasing m. Ecologically it means, as more and more fraction of prey becomes abundant from predation, then the Hopf-Turing instability may occur only if the predator disperses in space significantly faster compared to prey. Dispersion relation (Fig. 6.8b) for the point taken from the Hopf-Turing instability region (marked by C in Fig. 6.8a) shows the occurrence of Hopf and Turing instabilities. Observe that the maximum real part of the eigenvalues (red line) is positive for $k = 0$ and the corresponding imaginary part (green curve) is non-zero, implying that the system experiences Hopf bifurcation for $k = 0$. Then imaginary part becomes zero at $k = 2.2090$ and the root becomes real. This real root changes its sign (becomes positive) for the non-zero wavenumbers $(5.4087 < k < 8.2999)$ (see Eq. (6.20)), showing the

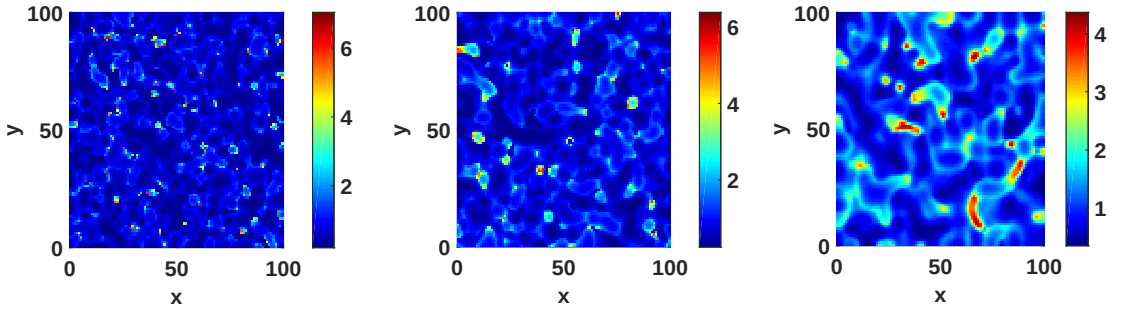

FIGURE 6.9: Hopf-Turing patterns for different pairs of (m, D_c). The snapshots presented from left to right corresponds, respectively, to the observation points A, B and C of Fig. 6.8. Snapshots are taken at time $T = 1000$ with $L = 100$, $\delta x = 1$ and $\delta t = 0.005$. Other parameters are as in Fig. 6.8a.

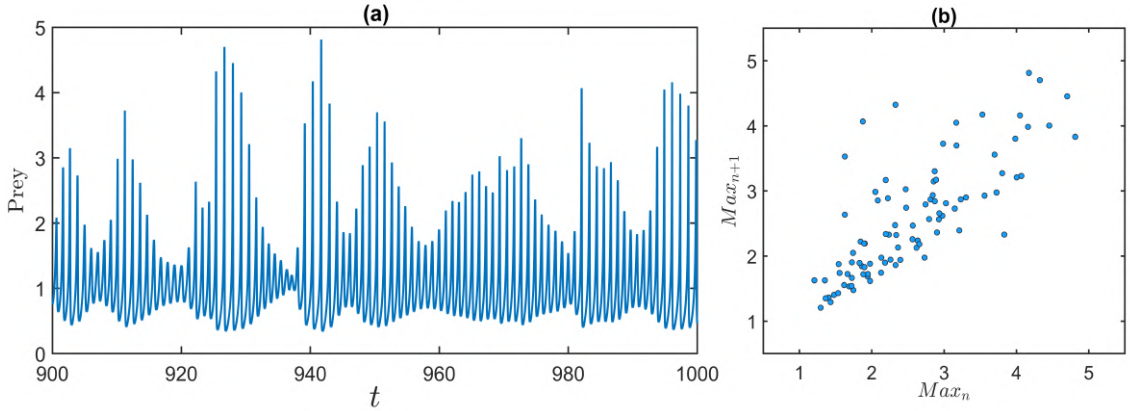

FIGURE 6.10: **(a)** The time series of prey density for a randomly chosen spatial grid of Hopf-Turing region shows spatiotemporal chaos. Parameters are as in Fig. 6.8a with $D_1 = 0.01$, $D_2 = 3$ and $m = 0.5$. **(b)** Corresponding scatter diagram of Poincaré maximum return map. Other parameters are as in Fig. 6.1.

existence of Turing instability. Figure. 6.9 shows the existence of spatiotemporal chaos in the prey population corresponding to the points A, B and C, respectively, taken from the Hopf-Turing region (see Fig. 6.8a). Time series for the observation point C, at a randomly chosen spatial grid in space, shows chaotic time series (see Fig. 6.10a). The Poincaré maximum return map (Fig. 6.10b) of the corresponding time series confirms the existence of spatiotemporal chaos.

6.5 Discussion

This paper illustrates the spatiotemporal dynamics of the predator-prey model with Holling type III functional response and prey refuge using a hyperbolic reaction-diffusion system with non-identical inertia. HRD system eliminates the unrealistic features of the infinite speed of the perturbation in the parabolic system, usually used to study spatiotemporal dynamics. The HRD equation considers an inertial time, contrary to the PRD equation, which facilitates a delayed dispersal of perturbation applied at a certain point in space. A well-studied predator-prey model with type III response function and prey refuge is considered here to represent the local interaction terms of the HRD system. The aim was to study the effects of species-dependent inertial times and prey refuge on the pattern forming instabilities. To the best of our knowledge, such a study for predator-prey HRD systems is rare in the literature.

Here, two types of diffusion-driven instabilities exist for the considered system: pure wave instability and mixed instability (Hopf-Turing and Hopf-wave). We have obtained the analytical conditions for the existence of such instabilities. Since the conditions for Turing instability do not depend on the inertial times, the Turing instability is absent here, as in the case of its parabolic counterpart [138]. The role of refuge parameter and inertial time in causing different instabilities are evident from our analysis. For fixed refuge value, we noticed that greater prey inertia initiates to create instability. Similar to the PRD system, the diffusive instabilities are created for higher values of predator diffusion rate.

The patterns generated in the pure-wave instability regime are fascinating. It creates a complex heterogeneous oscillating sequence of spatially symmetric patterns. These patterns are highly dependent on the initial conditions, and the sequence of patterns in different simulation runs are strikingly distinct. Although, the qualitative behaviours at a randomly chosen spatial grid are similar and give pure oscillations. Such wave instability is never possible in the corresponding PRD system. Wave instability or heterogeneous oscillatory distribution is worth exploring to describe the oscillatory sequence of patterns observed in nature. A possible explanation for such patterns observed through wave instability in a two-species HRD system is the consequence of considering the microscopic reversibility. For a Turing-type diffusion-driven instability, when a heterogeneous perturbation is imposed, Fickian diffusion becomes more dominant, which forces the species to diffuse from higher to lower concentrations, creating a heterogeneous steady state. In contrast, for wave instability, the reversibility of substance flow becomes more dominant, which does not allow the heterogeneous pattern to settle down. Therefore, a heterogeneous steady state (Turing) is not achievable in this case; instead, the patterns are repeated periodically.

Chapter 7

Conclusion

7.1 Key findings

This thesis investigates how spatial heterogeneity, local nonlinear interactions, and dispersal processes shape ecological outcomes in predator–prey and vegetation systems. Using a combination of analytical methods and numerical simulations, the work highlights the critical role of bistability, pattern formation due to diffusion-driven instabilities, and environmental fluctuations in determining species persistence, coexistence, and extinction. The main contributions of Chapters 2 to 6 are as follows:

- Bistability as a fundamental ecological mechanism: Several models (Chapters 2, 3, and 5) exhibit bistability between predator–prey coexistence and extinction states or between vegetated and barren regimes. This bistability implies that ecosystems may respond differently to identical external conditions depending on their initial states, making them highly sensitive to perturbations. Such dynamics underscore the importance of understanding basins of attraction in predicting long-term outcomes.
- Diffusion acts both as a stabilizer and a destabilizer: Diffusion-driven processes play a dual role. On one hand, dispersal can rescue populations from local extinctions by recolonizing empty patches (Chapter 3). On the other hand, differential diffusion rates can trigger Turing instabilities that destabilize uniform equilibria and lead to heterogeneous spatial patterns (Chapters 2, 3, 4, 6). This reveals the complexity of dispersal, which cannot be simplistically classified as beneficial or harmful.

- Patters generation: Emergence of spatial self-organization across vegetation and predator–prey models, spatial self-organization emerges as a recurrent phenomenon. Turing instabilities produce spot, stripe, labyrinth, and wave-like patterns (Chapters 2, 4, 6). These self-organized patterns are not externally imposed but arise from internal feedbacks between local interactions and movement. This finding aligns with empirical observations of banded vegetation in drylands and cyclic predator-prey distributions.

- Effects of climate variation: Climate variability drives extinction risk. Chapter 5 demonstrates that climate fluctuations can synchronize local dynamics across patches, leading to large-scale coordinated collapses. This mechanism explains how otherwise resilient systems can undergo sudden regional extinctions when exposed to climate forcing. The results resonate with real-world cases such as forest insect outbreaks and drought-induced vegetation collapse.

- Hyperbolic diffusion enriches ecological dynamics: The extension to hyperbolic diffusion in Chapter 6 reveals new classes of spatiotemporal patterns, including traveling waves and Hopf–Turing interactions, which parabolic diffusion models do not capture. This highlights the importance of considering dispersal delays and finite propagation speeds, particularly in systems where organisms exhibit inertia in movement.

7.2 Limitations and future perspectives

Despite offering substantial insights into spatiotemporal dynamics and species persistence, the present work is not without limitations, which simultaneously point toward promising directions for future research. The models developed here are primarily restricted to two-species interactions within simplified spatial settings, whereas natural ecosystems often involve multiple trophic levels, interspecific competition, and mutualistic interactions, all of which could reshape bistability, extinction thresholds, and pattern formation in unforeseen ways. The spatial domains considered are mostly homogeneous and idealized, overlooking the influence of environmental heterogeneity, patch connectivity, and higher-dimensional terrain structures that play a decisive role in real landscapes. The assumption of random, diffusion-like dispersal provides a useful first approximation but fails to capture adaptive strategies such as predator pursuit, prey refuge seeking, or movement guided by resource gradients, which could fundamentally alter ecological outcomes. Climate forcing has been addressed in a stylized manner, yet long-term ecological shifts are often governed by intricate feedbacks between climate variability and ecosystem processes, including resource redistribution and extreme events, which warrant deeper integration of ecological and

climate models. Similarly, stochastic perturbations were shown to modify persistence and extinction risks, but their potential to induce novel transitions, stabilize coexistence through stochastic resonance, or generate noise-driven spatial patterns remains to be fully explored. Another limitation lies in the theoretical emphasis of the thesis, as empirical calibration and validation against field data, long-term monitoring records, or remotely sensed vegetation patterns would enhance ecological realism and provide a stronger bridge between mathematics and applied ecology. Addressing these gaps in future work by extending the framework to multi-species networks, higher-dimensional and fragmented landscapes, adaptive movement ecology, and stochastic climate–ecosystem couplings will not only refine the theoretical understanding of ecological complexity but also yield practical implications for conservation policy and ecosystem management. By identifying parameter regimes that favor coexistence, recognizing early-warning signals of tipping points, and predicting spatial signatures of ecological collapse, such extensions would contribute to designing targeted interventions that enhance resilience and ensure species persistence under accelerating global change.

This thesis has highlighted that the persistence of ecological systems is not dictated solely by local interactions but is deeply conditioned by the spatial and temporal contexts in which they operate. By revealing how nonlinear feedbacks, dispersal, and environmental variability combine to generate bistability, extinction, and complex spatial structures, the study contributes to a growing body of knowledge that situates ecology firmly within the realm of dynamical systems theory. The results not only enrich theoretical ecology but also resonate with pressing global challenges, such as biodiversity loss, desertification, and climate-induced collapse of species. In bringing together mathematics, ecological insight, and spatiotemporal complexity, this work aspires to serve as a foundation for future research that advances both theory and practice, while also emphasizing the urgency of preserving the resilience of ecosystems in a rapidly changing world.

Bibliography

[1] S. A. Levin, "The problem of pattern and scale in ecology: the robert h. macarthur award lecture," *Ecology*, vol. 73, no. 6, pp. 1943–1967, 1992.

[2] I. Hanski, "Metapopulation dynamics," *Nature*, vol. 396, no. 6706, pp. 41–49, 1998.

[3] K. S. McCann, J. Rasmussen, and J. Umbanhowar, "The dynamics of spatially coupled food webs," *Ecology Letters*, vol. 8, no. 5, pp. 513–523, 2005.

[4] P. Amarasekare, "Spatial dynamics of foodwebs," *Annual Review of Ecology, Evolution, and Systematics*, vol. 39, no. 1, pp. 479–500, 2008.

[5] R. D. Holt, "Food webs in space: on the interplay of dynamic instability and spatial processes," *Ecological Research*, vol. 17, no. 2, pp. 261–273, 2002.

[6] P. A. Moran, "The statistical analysis of the canadian lynx cycle.," *Australian Journal of Zoology*, vol. 1, no. 3, pp. 291–298, 1953.

[7] F. Borgogno, P. D'odorico, F. Laio, and L. Ridolfi, "Mathematical models of vegetation pattern formation in ecohydrology," *Reviews of Geophysics*, vol. 47, no. 1, 2009.

[8] S. A. Levin, "Dispersion and population interactions," *The American Naturalist*, vol. 108, no. 960, pp. 207–228, 1974.

[9] I. Hanski, *Metapopulation ecology*. Oxford University Press, 1999.

[10] A. Liebhold, W. D. Koenig, and O. N. Bjørnstad, "Spatial synchrony in population dynamics," *Annu. Rev. Ecol. Evol. Syst.*, vol. 35, no. 1, pp. 467–490, 2004.

[11] B. Blasius, A. Huppert, and L. Stone, "Complex dynamics and phase synchronization in spatially extended ecological systems," *Nature*, vol. 399, no. 6734, pp. 354–359, 1999.

[12] C. Elton and M. Nicholson, "The ten-year cycle in numbers of the lynx in canada," *The Journal of Animal Ecology*, pp. 215–244, 1942.

[13] E. Ranta, V. Kaitala, and J. Lindström, "Dynamics of canadian lynx populations in space and time 1," *Ecography*, vol. 20, no. 5, pp. 454–460, 1997.

[14] R. T. Paine, "Food web complexity and species diversity," *The American Naturalist*, vol. 100, no. 910, pp. 65–75, 1966.

[15] T. Royama, "Population dynamics of the spruce budworm choristoneura fumiferana," *Ecological Monographs*, vol. 54, no. 4, pp. 429–462, 1984.

[16] A. R. Sinclair, C. Packer, S. A. Mduma, and J. M. Fryxell, *Serengeti III: human impacts on ecosystem dynamics*. University of Chicago Press, 2009.

[17] C. Skov, M. C. Lucas, and L. Jacobsen, "Spatial ecology," in *Biology and Ecology of Pike*, pp. 83–120, CRC Press, 2018.

[18] S. P. Ojanen, M. Nieminen, E. Meyke, J. Pöyry, and I. Hanski, "Long-term metapopulation study of the glanville fritillary butterfly (melitaea cinxia): survey methods, data management, and long-term population trends," *Ecology and Evolution*, vol. 3, no. 11, pp. 3713–3737, 2013.

[19] R. M. Penczykowski, E. Walker, S. Soubeyrand, and A.-L. Laine, "Linking winter conditions to regional disease dynamics in a wild plant–pathogen metapopulation," *New Phytologist*, vol. 205, no. 3, pp. 1142–1152, 2015.

[20] J. A. Sherratt, "An analysis of vegetation stripe formation in semi-arid landscapes," *Journal of Mathematical Biology*, vol. 51, no. 2, pp. 183–197, 2005.

[21] V. Deblauwe, P. Couteron, O. Lejeune, J. Bogaert, and N. Barbier, "Environmental modulation of self-organized periodic vegetation patterns in sudan," *Ecography*, vol. 34, no. 6, pp. 990–1001, 2011.

[22] J. A. Ludwig, B. P. Wilcox, D. D. Breshears, D. J. Tongway, and A. C. Imeson, "Vegetation patches and runoff–erosion as interacting ecohydrological processes in semiarid landscapes," *Ecology*, vol. 86, no. 2, pp. 288–297, 2005.

[23] E. Meron, E. Gilad, J. Von Hardenberg, M. Shachak, and Y. Zarmi, "Vegetation patterns along a rainfall gradient," *Chaos, Solitons & Fractals*, vol. 19, no. 2, pp. 367–376, 2004.

[24] E. Gilad, J. Von Hardenberg, A. Provenzale, M. Shachak, and E. Meron, "Ecosystem engineers: from pattern formation to habitat creation," *Physical Review Letters*, vol. 93, no. 9, p. 098105, 2004.

[25] T. M. Scanlon, K. K. Caylor, S. A. Levin, and I. Rodriguez-Iturbe, "Positive feedbacks promote power-law clustering of kalahari vegetation," *Nature*, vol. 449, no. 7159, pp. 209–212, 2007.

[26] C. A. Klausmeier, "Regular and irregular patterns in semiarid vegetation," *Science*, vol. 284, no. 5421, pp. 1826–1828, 1999.

[27] S. Kéfi, M. Rietkerk, C. L. Alados, Y. Pueyo, V. P. Papanastasis, A. ElAich, and P. C. De Ruiter, "Spatial vegetation patterns and imminent desertification in mediterranean arid ecosystems," *Nature*, vol. 449, no. 7159, pp. 213–217, 2007.

[28] M. Berdugo, M. Delgado-Baquerizo, S. Soliveres, R. Hernández-Clemente, Y. Zhao, J. J. Gaitán, N. Gross, H. Saiz, V. Maire, A. Lehmann, *et al.*, "Global ecosystem thresholds driven by aridity," *Science*, vol. 367, no. 6479, pp. 787–790, 2020.

[29] V. Mendez, S. Fedotov, and W. Horsthemke, *Reaction-transport systems: mesoscopic foundations, fronts, and spatial instabilities*. Springer Science & Business Media, 2010.

[30] J. D. Murray and J. D. Murray, *Mathematical Biology: II: Spatial Models and Biomedical Applications*, vol. 3. Springer, 2003.

[31] V. Méndez and J. E. Llebot, "Hyperbolic reaction-diffusion equations for a forest fire model," *Physical Review E*, vol. 56, no. 6, p. 6557, 1997.

[32] E. P. Zemskov and W. Horsthemke, "Diffusive instabilities in hyperbolic reaction-diffusion equations," *Physical Review E*, vol. 93, no. 3, p. 032211, 2016.

[33] L. Perko, *Differential equations and dynamical systems*, vol. 7. Springer Science & Business Media, 2013.

[34] N. D. Alikakos, "Lp bounds of solutions of reaction-diffusion equations," *Communications in Partial Differential Equations*, vol. 4, no. 8, pp. 827–868, 1979.

[35] W. Hahn *et al.*, *Stability of motion*, vol. 138. Springer, 1967.

[36] M. Rietkerk and J. van de Koppel, "Alternate stable states and threshold effects in semi-arid grazing systems," *Oikos*, pp. 69–76, 1997.

[37] B. E. Beisner, D. T. Haydon, and K. Cuddington, "Alternative stable states in ecology," *Frontiers in Ecology and the Environment*, vol. 1, no. 7, pp. 376–382, 2003.

[38] S. Kéfi, M. B. Eppinga, P. C. de Ruiter, and M. Rietkerk, "Bistability and regular spatial patterns in arid ecosystems," *Theoretical Ecology*, vol. 3, no. 4, pp. 257–269, 2010.

[39] T. M. Lenton, "Environmental tipping points," *Annual Review of Environment and Resources*, vol. 38, no. 1, pp. 1–29, 2013.

[40] C. A. De Moura and C. S. Kubrusly, "The Courant–Friedrichs–Lewy (CFL) condition," *AMC*, vol. 10, no. 12, pp. 45–90, 2013.

[41] A. M. Turing, "The chemical basis of morphogenesis," *Bulletin of Mathematical Biology*, vol. 52, pp. 153–197, 1990.

[42] L. A. Segel and J. L. Jackson, "Dissipative structure: an explanation and an ecological example," *Journal of Theoretical Biology*, vol. 37, no. 3, pp. 545–559, 1972.

[43] B. Dubey and J. Hussain, "Spatiotemporal dynamics of a prey–predator system with harvesting," *Ecological Complexity*, vol. 41, p. 100816, 2020.

[44] M. Sen, M. Banerjee, *et al.*, "Spatiotemporal patterns in a prey–predator model with harvesting," *Mathematical Biosciences*, vol. 236, no. 1, pp. 64–73, 2012.

[45] T. K. Kar and H. Matsuda, "Controllability of a harvested prey-predator system with time delay," *Journal of Biological Systems*, vol. 14, no. 02, pp. 243–254, 2006.

[46] R. Gupta, M. Banerjee, *et al.*, "Michaelis–menten type harvesting in prey–predator models: dynamics and bifurcations," *Mathematical Biosciences and Engineering*, vol. 15, no. 6, pp. 1405–1426, 2018.

[47] K. Das, S. Samanta, *et al.*, "Impact of michaelis–menten type harvesting in prey–predator system with prey refuge," *Applied Mathematics and Computation*, vol. 403, p. 126188, 2021.

[48] H. Malchow, S. V. Petrovskii, and E. Venturino, *Spatiotemporal patterns in ecology and epidemiology: theory, models, and simulation*. Chapman and Hall/CRC, 2007.

[49] J. A. Sherratt and M. J. Smith, "Periodic travelling waves in cyclic populations: field studies and reaction–diffusion models," *Journal of the Royal Society Interface*, vol. 5, no. 22, pp. 483–505, 2008.

[50] S. V. Petrovskii and H. Malchow, "A minimal model of pattern formation in a prey-predator system," *Mathematical and Computer Modelling*, vol. 29, no. 8, pp. 49–63, 1999.

[51] N. Shigesada, K. Kawasaki, and E. Teramoto, "Spatial segregation of interacting species," *Journal of Theoretical Biology*, vol. 79, no. 1, pp. 83–99, 1979.

[52] A. Okubo and S. A. Levin, *Diffusion and ecological problems: modern perspectives*, vol. 14. Springer Science & Business Media, 2002.

[53] R. S. Cantrell and C. Cosner, *Spatial ecology via reaction-diffusion equations*. John Wiley & Sons, 2004.

[54] M. D. Hunter and P. W. Price, "Playing chutes and ladders: heterogeneity and the relative roles of bottom-up and top-down forces in natural communities," *Ecology*, pp. 724–732, 1992.

[55] G. A. Polis, "Why are parts of the world green? multiple factors control productivity and the distribution of biomass," *Oikos*, pp. 3–15, 1999.

[56] J. van de Koppel, J. Huisman, R. van der Wal, and H. Olff, "Patterns of herbivory along a prouductivity gradient: An empirical and theoretical investigation," *Ecology*, vol. 77, no. 3, pp. 736–745, 1996.

[57] J. von Hardenberg, E. Meron, M. Shachak, and Y. Zarmi, "Diversity of vegetation patterns and desertification," *Physical Review Letters*, vol. 87, no. 19, p. 198101, 2001.

[58] O. Lejeune, M. Tlidi, and P. Couteron, "Localized vegetation patches: a self-organized response to resource scarcity," *Physical Review E*, vol. 66, no. 1, p. 010901, 2002.

[59] M. Rietkerk, M. C. Boerlijst, F. Van Langevelde, R. HilleRisLambers, J. v. de Koppel, L. Kumar, H. H. Prins, and A. M. de Roos, "Self-organization of vegetation in arid ecosystems," *The American Naturalist*, vol. 160, no. 4, pp. 524–530, 2002.

[60] N. Juergens, "Exploring common ground for different hypotheses on namib fairy circles," *Ecography*, vol. 38, no. 1, pp. 12–14, 2015.

[61] C. E. Tarnita, J. A. Bonachela, E. Sheffer, J. A. Guyton, T. C. Coverdale, R. A. Long, and R. M. Pringle, "A theoretical foundation for multi-scale regular vegetation patterns," *Nature*, vol. 541, no. 7637, pp. 398–401, 2017.

[62] J. J. Bennett, B. K. Bera, M. Ferré, H. Yizhaq, S. Getzin, and E. Meron, "Phenotypic plasticity: A missing element in the theory of vegetation pattern formation," *Proceedings of the National Academy of Sciences*, vol. 120, no. 50, p. e2311528120, 2023.

[63] L. Yang, M. Dolnik, A. M. Zhabotinsky, and I. R. Epstein, "Pattern formation arising from interactions between turing and wave instabilities," *The Journal of Chemical Physics*, vol. 117, no. 15, pp. 7259–7265, 2002.

[64] L. Yang, M. Dolnik, A. M. Zhabotinsky, and I. R. Epstein, "Spatial resonances and superposition patterns in a reaction-diffusion model with interacting turing modes," *Physical Review Letters*, vol. 88, no. 20, p. 208303, 2002.

[65] T. Huang, C. Yu, Z. Lin, H. Zhang, R. Liu, R. Li, Y. Yang, and Y. Tian, "Self-organization of nested patterns in a coupled spatiotemporal phytoplankton-zooplankton system," *Communications in Nonlinear Science and Numerical Simulation*, vol. 130, p. 107804, 2024.

[66] R. Fischer and N. C. Turner, "Plant productivity in the arid and semiarid zones," *Annual Review of Plant Physiology*, vol. 29, no. 1, pp. 277–317, 1978.

[67] C. D. Schlichting, "The evolution of phenotypic plasticity in plants," *Annual Review of Ecology and Systematics*, pp. 667–693, 1986.

[68] R. M. Callaway, S. C. Pennings, and C. L. Richards, "Phenotypic plasticity and interactions among plants," *Ecology*, vol. 84, no. 5, pp. 1115–1128, 2003.

[69] D. Eapen, M. L. Barroso, G. Ponce, M. E. Campos, and G. I. Cassab, "Hydrotropism: root growth responses to water," *Trends in Plant Science*, vol. 10, no. 1, pp. 44–50, 2005.

[70] D. Ward, K. Wiegand, and S. Getzin, "Walter's two-layer hypothesis revisited: back to the roots!," *Oecologia*, vol. 172, pp. 617–630, 2013.

[71] A. Kulmatiski and K. H. Beard, "A modern two-layer hypothesis helps resolve the 'savanna problem'," *Ecology Letters*, vol. 25, no. 9, pp. 1952–1960, 2022.

[72] E. Meron, "Pattern formation–a missing link in the study of ecosystem response to environmental changes," *Mathematical Biosciences*, vol. 271, pp. 1–18, 2016.

[73] S. Getzin, H. Yizhaq, B. Bell, T. E. Erickson, A. C. Postle, I. Katra, O. Tzuk, Y. R. Zelnik, K. Wiegand, T. Wiegand, *et al.*, "Discovery of fairy circles in australia supports self-organization theory," *Proceedings of the National Academy of Sciences*, vol. 113, no. 13, pp. 3551–3556, 2016.

[74] Z. Ge, "The hidden order of turing patterns in arid and semi-arid vegetation ecosystems," *Proceedings of the National Academy of Sciences*, vol. 120, no. 42, p. e2306514120, 2023.

[75] J. A. Hutchings, "Collapse and recovery of marine fishes," *Nature*, vol. 406, no. 6798, pp. 882–885, 2000.

[76] J.-G. Winther, M. Dai, T. Rist, A. H. Hoel, Y. Li, A. Trice, K. Morrissey, M. A. Juinio-Meñez, L. Fernandes, S. Unger, *et al.*, "Integrated ocean management for a sustainable ocean economy," *Nature Ecology & Evolution*, vol. 4, no. 11, pp. 1451–1458, 2020.

[77] S. Hossain, M. M. Haque, M. H. Kabir, M. O. Gani, and S. Sarwardi, "Complex spatiotemporal dynamics of a harvested prey–predator model with crowley–martin response function," *Results in Control and Optimization*, vol. 5, p. 100059, 2021.

[78] L. N. Guin, S. Pal, S. Chakravarty, and S. Djilali, "Pattern dynamics of a reaction-diffusion predator-prey system with both refuge and harvesting," *International Journal of Biomathematics*, vol. 14, no. 01, p. 2050084, 2021.

[79] R. K. Upadhyay, P. Roy, and J. Datta, "Complex dynamics of ecological systems under nonlinear harvesting: Hopf bifurcation and turing instability," *Nonlinear Dynamics*, vol. 79, pp. 2251–2270, 2015.

[80] N. Iqbal, R. Wu, and W. W. M., "Pattern formation induced by fractional cross-diffusion in a 3-species food chain model with harvesting," *Mathematics and Computers in Simulation*, vol. 188, pp. 102–119, 2021.

[81] H. Baek, "Spatiotemporal dynamics of a predator-prey system with linear harvesting rate," *Mathematical Problems in Engineering*, vol. 2014, 2014.

[82] C. W. Clark, "Mathematical models in the economics of renewable resources," *SIAM Review*, vol. 21, no. 1, pp. 81–99, 1979.

[83] M. L. Rosenzweig and R. H. MacArthur, "Graphical representation and stability conditions of predator-prey interactions," *The American Naturalist*, vol. 97, no. 895, pp. 209–223, 1963.

[84] A. D. Bazykin, *Nonlinear dynamics of interacting populations*. World Scientific, 1998.

[85] P. Turchin, "Complex population dynamics," in *Complex Population Dynamics*, Princeton University Press, 2013.

[86] J. K. Craig, J. A. Rice, L. B. Crowder, and D. A. Nadeau, "Density-dependent growth and mortality in an estuary-dependent fish: an experimental approach with juvenile spot leiostomus xanthurus," *Marine Ecology Progress Series*, vol. 343, pp. 251–262, 2007.

[87] E. A. McGehee, N. Schutt, D. A. Vasquez, and E. Peacock-Lopez, "Bifurcations, and temporal and spatial patterns of a modified lotka–volterra model," *International Journal of Bifurcation and Chaos*, vol. 18, no. 08, pp. 2223–2248, 2008.

[88] A. Moussaoui and P. Auger, "A bioeconomic model of a fishery with saturated catch and variable price: Stabilizing effect of marine reserves on fishery dynamics," *Ecological Complexity*, vol. 45, p. 100906, 2021.

[89] Y. Lv, Y. Pei, and Y. Wang, "Bifurcations and simulations of two predator–prey models with nonlinear harvesting," *Chaos, Solitons & Fractals*, vol. 120, pp. 158–170, 2019.

[90] V. Tiwari, J. P. Tripathi, S. Abbas, J.-S. Wang, G.-Q. Sun, and Z. Jin, "Qualitative analysis of a diffusive crowley–martin predator–prey model: the role of nonlinear predator harvesting," *Nonlinear Dynamics*, vol. 98, pp. 1169–1189, 2019.

[91] X. Gao, S. Ishag, S. Fu, W. Li, and W. Wang, "Bifurcation and turing pattern formation in a diffusive ratio-dependent predator–prey model with predator harvesting," *Nonlinear Analysis: Real World Applications*, vol. 51, p. 102962, 2020.

[92] L. N. Guin, R. Murmu, H. Baek, and K.-H. Kim, "Dynamical analysis of a beddington–deangelis interacting species system with prey harvesting," *Mathematical Problems in Engineering*, vol. 2020, pp. 1–22, 2020.

[93] M. Chen, R. Wu, B. Liu, and L. Chen, "Pattern selection in a predator-prey model with michaelis–menten type nonlinear predator harvesting," *Ecological Complexity*, vol. 36, pp. 239–249, 2018.

[94] E. McCauley and W. W. Murdoch, "Predator–prey dynamics in environments rich and poor in nutrients," *Nature*, vol. 343, no. 6257, pp. 455–457, 1990.

[95] N. Bairagi, S. Saha, S. Chaudhuri, and S. K. Dana, "Zooplankton selectivity and nutritional value of phytoplankton influences a rich variety of dynamics in a plankton population model," *Physical Review E*, vol. 99, no. 1, p. 012406, 2019.

[96] J. M. Tubay, H. Ito, T. Uehara, S. Kakishima, S. Morita, T. Togashi, K. Tainaka, M. P. Niraula, B. E. Casareto, Y. Suzuki, *et al.*, "The paradox of enrichment in phytoplankton by induced competitive interactions," *Scientific Reports*, vol. 3, no. 1, p. 2835, 2013.

[97] D. Adak, N. Bairagi, and R. Hakl, "Chaos in delay-induced Leslie–Gower prey–predator–parasite model and its control through prey harvesting," *Nonlinear Analysis: Real World Applications*, vol. 51, p. 102998, 2020.

[98] S. Chakraborty, S. Pal, and N. Bairagi, "Predator–prey interaction with harvesting: mathematical study with biological ramifications," *Applied Mathematical Modelling*, vol. 36, no. 9, pp. 4044–4059, 2012.

[99] J. K. Hale and J. K. Hale, "Retarded functional differential equations: basic theory," *Theory of Functional Differential Equations*, pp. 36–56, 1977.

[100] G. Birkhoff and G. C. Rota, *Ordinary differential equations*. John Wiley & Sons, 1978.

[101] E. Zemskov, K. Kassner, M. Hauser, and W. Horsthemke, "Turing space in reaction-diffusion systems with density-dependent cross diffusion," *Physical Review E*, vol. 87, no. 3, p. 032906, 2013.

[102] J. D. Murray, *Mathematical biology II: Spatial models and biomedical applications*, vol. 3. Springer New York, 2001.

[103] A. C. Newell and J. A. Whitehead, "Finite bandwidth, finite amplitude convection," *Journal of Fluid Mechanics*, vol. 38, no. 2, pp. 279–303, 1969.

[104] X.-C. Zhang, G.-Q. Sun, and Z. Jin, "Spatial dynamics in a predator-prey model with beddington-deangelis functional response," *Physical Review E*, vol. 85, no. 2, p. 021924, 2012.

[105] G. H. Gunaratne, Q. Ouyang, and H. L. Swinney, "Pattern formation in the presence of symmetries," *Physical Review E*, vol. 50, no. 4, p. 2802, 1994.

[106] N. Wu, L. F. Pease, and W. B. Russel, "Electric-field-induced patterns in thin polymer films: weakly nonlinear and fully nonlinear evolution," *Langmuir*, vol. 21, no. 26, pp. 12290–12302, 2005.

[107] M. Rosenzweig, "Paradox of enrichment: destabilization of exploitation ecosystems in ecological time," *Science*, vol. 171, no. 3969, pp. 385–387, 1971.

[108] B. Bolker and S. W. Pacala, "Using moment equations to understand stochastically driven spatial pattern formation in ecological systems," *Theoretical Population Biology*, vol. 52, no. 3, pp. 179–197, 1997.

[109] J. A. Hutchings, "Renaissance of a caveat: Allee effects in marine fish," *ICES Journal of Marine Science*, vol. 71, no. 8, pp. 2152–2157, 2014.

[110] W. K. Dodds and J. J. Cole, "Expanding the concept of trophic state in aquatic ecosystems: it's not just the autotrophs," *Aquatic Sciences*, vol. 69, pp. 427–439, 2007.

[111] A. C. Staver, J. O. Abraham, G. P. Hempson, A. T. Karp, and J. T. Faith, "The past, present, and future of herbivore impacts on savanna vegetation," *Journal of Ecology*, vol. 109, no. 8, pp. 2804–2822, 2021.

[112] M. C. Vidal and S. M. Murphy, "Bottom-up vs. top-down effects on terrestrial insect herbivores: A meta-analysis," *Ecology Letters*, vol. 21, no. 1, pp. 138–150, 2018.

[113] R. Bagchi, L. M. Brown, C. S. Elphick, D. L. Wagner, and M. S. Singer, "Anthropogenic fragmentation of landscapes: mechanisms for eroding the specificity of plant–herbivore interactions," *Oecologia*, vol. 187, pp. 521–533, 2018.

[114] Z. Feng and D. DeAngelis, *Mathematical Models of Plant-Herbivore Interactions*. CRC Press, 2017.

[115] M. Schädler, T. Rottstock, and R. Brandl, "Do nutrients and invertebrate herbivory interact in an artificial plant community?," *Basic and Applied Ecology*, vol. 9, no. 5, pp. 550–559, 2008.

[116] S. Jia, X. Wang, Z. Yuan, F. Lin, J. Ye, Z. Hao, and M. S. Luskin, "Global signal of top-down control of terrestrial plant communities by herbivores," *Proceedings of the National Academy of Sciences*, vol. 115, no. 24, pp. 6237–6242, 2018.

[117] J. Nauta, P. Simoens, Y. Khaluf, and R. Martinez-Garcia, "Foraging behaviour and patch size distribution jointly determine population dynamics in fragmented landscapes," *Journal of the Royal Society Interface*, vol. 19, no. 191, p. 20220103, 2022.

[118] D. E. Burkepile and J. D. Parker, "Recent advances in plant-herbivore interactions," *F1000Research*, vol. 6, 2017.

[119] W. Macfadyen, "Vegetation patterns in the semi-desert plains of british somaliland," *The Geographical Journal*, vol. 116, no. 4/6, pp. 199–211, 1950.

[120] M. Tlidi, M. Clerc, D. Escaff, P. Couteron, M. Messaoudi, M. Khaffou, and A. Makhoute, "Observation and modelling of vegetation spirals and arcs in isotropic environmental conditions: dissipative structures in arid landscapes," *Philosophical Transactions of the Royal Society A: Mathematical, Physical and Engineering Sciences*, vol. 376, no. 2135, p. 20180026, 2018.

[121] R. HilleRisLambers, M. Rietkerk, F. van den Bosch, H. H. Prins, and H. de Kroon, "Vegetation pattern formation in semi-arid grazing systems," *Ecology*, vol. 82, no. 1, pp. 50–61, 2001.

[122] M. Rietkerk, P. Ketner, J. Burger, B. Hoorens, and H. Olff, "Multiscale soil and vegetation patchiness along a gradient of herbivore impact in a semi-arid grazing system in west africa," *Plant Ecology*, vol. 148, pp. 207–224, 2000.

[123] E. Sheffer, H. Yizhaq, E. Gilad, M. Shachak, and E. Meron, "Why do plants in resource-deprived environments form rings?," *Ecological Complexity*, vol. 4, no. 4, pp. 192–200, 2007.

[124] E. Sheffer, H. Yizhaq, M. Shachak, and E. Meron, "Mechanisms of vegetation-ring formation in water-limited systems," *Journal of Theoretical Biology*, vol. 273, no. 1, pp. 138–146, 2011.

[125] M. D. Cramer and N. N. Barger, "Are namibian "fairy circles" the consequence of self-organizing spatial vegetation patterning?," *PloS One*, vol. 8, no. 8, p. e70876, 2013.

[126] C. Fernandez-Oto, M. Tlidi, D. Escaff, and M. Clerc, "Strong interaction between plants induces circular barren patches: fairy circles," *Philosophical Transactions of the Royal Society A: Mathematical, Physical and Engineering Sciences*, vol. 372, no. 2027, p. 20140009, 2014.

[127] C. Fernandez-Oto, D. Escaff, and J. Cisternas, "Spiral vegetation patterns in high-altitude wetlands," *Ecological Complexity*, vol. 37, pp. 38–46, 2019.

[128] M. K. Pal and S. Poria, "Role of herbivory in shaping the dryland vegetation ecosystem: Linking spiral vegetation patterns and nonlinear, nonlocal grazing," *Physical Review E*, vol. 107, no. 6, p. 064403, 2023.

[129] A. J. Hester, M. Bergman, G. R. Iason, and J. Moen, "Impacts of large herbivores on plant community structure and dynamics," *Conservation Biology Series, Cambridge* -, vol. 11, p. 97, 2006.

[130] N. Owen-Smith, J. M. Fryxell, and E. H. Merrill, "Foraging theory upscaled: the behavioural ecology of herbivore movement," *Philosophical Transactions of the Royal Society B: Biological Sciences*, vol. 365, no. 1550, pp. 2267–2278, 2010.

[131] L. Edelstein-Keshet and M. D. Rausher, "The effects of inducible plant defenses on herbivore populations. 1. mobile herbivores in continuous time," *The American Naturalist*, vol. 133, no. 6, pp. 787–810, 1989.

[132] H. Pavia and G. B. Toth, "Inducible chemical resistance to herbivory in the brown seaweed ascophyllum nodosum," *Ecology*, vol. 81, no. 11, pp. 3212–3225, 2000.

[133] M. Vos, B. W. Kooi, D. L. DeAngelis, and W. M. Mooij, "Inducible defences and the paradox of enrichment," *Oikos*, vol. 105, no. 3, pp. 471–480, 2004.

[134] G.-Q. Sun, S.-L. Wang, Q. Ren, Z. Jin, and Y.-P. Wu, "Effects of time delay and space on herbivore dynamics: linking inducible defenses of plants to herbivore outbreak," *Scientific Reports*, vol. 5, no. 1, p. 11246, 2015.

[135] B. Dubey, B. Das, and J. Hussain, "A predator–prey interaction model with self and cross-diffusion," *Ecological Modelling*, vol. 141, no. 1-3, pp. 67–76, 2001.

[136] V. K. Vanag and I. R. Epstein, "Cross-diffusion and pattern formation in reaction–diffusion systems," *Physical Chemistry Chemical Physics*, vol. 11, no. 6, pp. 897–912, 2009.

[137] W. Wang, Q.-X. Liu, and Z. Jin, "Spatiotemporal complexity of a ratio-dependent predator-prey system," *Physical Review E*, vol. 75, no. 5, p. 051913, 2007.

[138] B. Chakraborty and N. Bairagi, "Complexity in a prey-predator model with prey refuge and diffusion," *Ecological Complexity*, vol. 37, pp. 11–23, 2019.

[139] R. K. Upadhyay and P. Roy, "Disease spread and its effect on population dynamics in heterogeneous environment," *International Journal of Bifurcation and Chaos*, vol. 26, no. 01, p. 1650004, 2016.

[140] B. Chakraborty, S. Ghorai, and N. Bairagi, "Reaction-diffusion predator-prey-parasite system and spatiotemporal complexity," *Applied Mathematics and Computation*, vol. 386, p. 125518, 2020.

[141] S. Marick, S. Bhattacharya, and N. Bairagi, "Dynamic properties of a reaction–diffusion predator–prey model with nonlinear harvesting: A linear and weakly nonlinear analysis," *Chaos, Solitons & Fractals*, vol. 175, p. 113996, 2023.

[142] L. N. Guin and S. Acharya, "Dynamic behaviour of a reaction–diffusion predator–prey model with both refuge and harvesting," *Nonlinear Dynamics*, vol. 88, pp. 1501–1533, 2017.

[143] L. Chang, S. Gao, and Z. Wang, "Optimal control of pattern formations for an sir reaction–diffusion epidemic model," *Journal of Theoretical Biology*, vol. 536, p. 111003, 2022.

[144] C. Liu and R. Cui, "Qualitative analysis on an sirs reaction–diffusion epidemic model with saturation infection mechanism," *Nonlinear Analysis: Real World Applications*, vol. 62, p. 103364, 2021.

[145] G.-Q. Sun, A. Chakraborty, Q.-X. Liu, Z. Jin, K. E. Anderson, and B.-L. Li, "Influence of time delay and nonlinear diffusion on herbivore outbreak," *Communications in Nonlinear Science and Numerical Simulation*, vol. 19, no. 5, pp. 1507–1518, 2014.

[146] F. Yu, L. Wang, and J. Watmough, "Transient spatio-temporal dynamics of a diffusive plant–herbivore system with neumann boundary conditions," *Journal of Biological Dynamics*, vol. 10, no. 1, pp. 477–500, 2016.

[147] F. Sánchez-Garduño and V. F. Breña-Medina, "Searching for spatial patterns in a pollinator–plant–herbivore mathematical model," *Bulletin of Mathematical Biology*, vol. 73, pp. 1118–1153, 2011.

[148] C.-H. Zhang and Z.-Z. Li, "Dynamics in a diffusive plant–herbivore model with toxin-determined functional response," *Computers & Mathematics with Applications*, vol. 67, no. 8, pp. 1439–1449, 2014.

[149] A. Goldbeter, "Dissipative structures in biological systems: bistability, oscillations, spatial patterns and waves," *Philosophical Transactions of the Royal Society A: Mathematical, Physical and Engineering Sciences*, vol. 376, no. 2124, p. 20170376, 2018.

[150] É. Diz-Pita and M. V. Otero-Espinar, "Predator–prey models: A review of some recent advances," *Mathematics*, vol. 9, no. 15, p. 1783, 2021.

[151] A. Schröder, L. Persson, and A. M. De Roos, "Direct experimental evidence for alternative stable states: a review," *Oikos*, vol. 110, no. 1, pp. 3–19, 2005.

[152] V. Weide Rodrigues, D. Cristina Mistro, and L. A. Diaz Rodrigues, "Pattern formation and bistability in a generalist predator-prey model," *Mathematics*, vol. 8, no. 1, p. 20, 2019.

[153] M. Scheffer, E. H. Van Nes, M. Holmgren, and T. Hughes, "Pulse-driven loss of top-down control: the critical-rate hypothesis," *Ecosystems*, vol. 11, pp. 226–237, 2008.

[154] J. H. Priestley and C. F. Swingle, *Vegetative propagation from the standpoint of plant anatomy.* No. 151, US Department of Agriculture, 1929.

[155] A. Okubo, "Diffusion and ecological problems: mathematical models," *Biomath*, vol. 10, 1980.

[156] S. Ghorai, P. Chakraborty, S. Poria, and N. Bairagi, "Dispersal-induced pattern-forming instabilities in host–parasitoid metapopulations," *Nonlinear Dynamics*, vol. 100, pp. 749–762, 2020.

[157] R. Arditi and L. R. Ginzburg, "Coupling in predator-prey dynamics: ratio-dependence," *Journal of Theoretical Biology*, vol. 139, no. 3, pp. 311–326, 1989.

[158] S. Roy and J. Chattopadhyay, "The stability of ecosystems: a brief overview of the paradox of enrichment," *Journal of Biosciences*, vol. 32, pp. 421–428, 2007.

[159] S. Chakraborty, S. Pal, and N. Bairagi, "Dynamics of a ratio-dependent eco-epidemiological system with prey harvesting," *Nonlinear Analysis: Real World Applications*, vol. 11, no. 3, pp. 1862–1877, 2010.

[160] K. E. Veblen, "Season-and herbivore-dependent competition and facilitation in a semi-arid savanna," *Ecology*, vol. 89, no. 6, pp. 1532–1540, 2008.

[161] G. E. Belovsky, "Optimal foraging and community structure: the allometry of herbivore food selection and competition," *Evolutionary Ecology*, vol. 11, pp. 641–672, 1997.

[162] X. Wang, W. Wang, and G. Zhang, "Vegetation pattern formation of a water-biomass model," *Communications in Nonlinear Science and Numerical Simulation*, vol. 42, pp. 571–584, 2017.

[163] S. Getzin, S. Holch, J. M. Ottenbreit, H. Yizhaq, and K. Wiegand, "Spatio-temporal dynamics of fairy circles in Namibia are driven by rainfall and soil infiltrability," *Landscape Ecology*, vol. 39, no. 7, p. 122, 2024.

[164] M. Tlidi, R. Lefever, and A. Vladimirov, "On vegetation clustering, localized bare soil spots and fairy circles," in *Dissipative solitons: from optics to biology and medicine*, pp. 1–22, Springer, 2008.

[165] V. Deblauwe, P. Couteron, J. Bogaert, and N. Barbier, "Determinants and dynamics of banded vegetation pattern migration in arid climates," *Ecological Monographs*, vol. 82, no. 1, pp. 3–21, 2012.

[166] M. D. Cramer and W. R. Tschinkel, "Fairy circle research: Status, controversies and the way forward," *Perspectives in Plant Ecology, Evolution and Systematics*, p. 125851, 2025.

[167] E. Meron, "Vegetation pattern formation: The mechanisms behind the forms," *Physics Today*, vol. 72, no. 11, pp. 30–36, 2019.

[168] S. E. Sultan, "Phenotypic plasticity for plant development, function and life history," *Trends in plant science*, vol. 5, no. 12, pp. 537–542, 2000.

[169] L. Würthner, F. Brauns, G. Pawlik, J. Halatek, J. Kerssemakers, C. Dekker, and E. Frey, "Bridging scales in a multiscale pattern-forming system," *Proceedings of the National Academy of Sciences*, vol. 119, no. 33, p. e2206888119, 2022.

[170] K. Markham, A. E. Frazier, K. K. Singh, and M. Madden, "A review of methods for scaling remotely sensed data for spatial pattern analysis," *Landscape Ecology*, vol. 38, no. 3, pp. 619–635, 2023.

[171] S. Getzin, C. Löns, H. Yizhaq, T. E. Erickson, M. Muñoz-Rojas, A. Huth, and K. Wiegand, "High-resolution images and drone-based lidar reveal striking patterns of vegetation gaps in a wooded spinifex grassland of western australia," *Landscape Ecology*, pp. 1–17, 2022.

[172] L. Yang, M. Dolnik, A. M. Zhabotinsky, and I. R. Epstein, "Turing patterns beyond hexagons and stripes," *Chaos: An Interdisciplinary Journal of Nonlinear Science*, vol. 16, no. 3, 2006.

[173] L. Yang and I. R. Epstein, "Oscillatory turing patterns in reaction-diffusion systems with two coupled layers," *Physical review letters*, vol. 90, no. 17, p. 178303, 2003.

[174] J. H. Richards and M. M. Caldwell, "Hydraulic lift: substantial nocturnal water transport between soil layers by artemisia tridentata roots," *Oecologia*, vol. 73, pp. 486–489, 1987.

[175] T. Colombi, B. K. Pandey, A. Chawade, M. J. Bennett, S. J. Mooney, and T. Keller, "Root plasticity versus elasticity–when are responses acclimative?," *Trends in Plant Science*, vol. 29, no. 8, pp. 856–864, 2024.

[176] H. Li, B. Liu, M. L. McCormack, Z. Ma, and D. Guo, "Diverse belowground resource strategies underlie plant species coexistence and spatial distribution in three grasslands along a precipitation gradient," *New Phytologist*, vol. 216, no. 4, pp. 1140–1150, 2017.

[177] R. B. Neumann and Z. G. Cardon, "The magnitude of hydraulic redistribution by plant roots: a review and synthesis of empirical and modeling studies," *New Phytologist*, vol. 194, no. 2, pp. 337–352, 2012.

[178] W. Korres, T. Reichenau, P. Fiener, C. Koyama, H. R. Bogena, T. Cornelissen, R. Baatz, M. Herbst, B. Diekkrüger, H. Vereecken, *et al.*, "Spatio-temporal soil moisture patterns–a meta-analysis using plot to catchment scale data," *Journal of Hydrology*, vol. 520, pp. 326–341, 2015.

[179] N. Juergens, A. Groengroeft, and F. Gunter, "Evolution at the arid extreme: the influence of climate on sand termite colonies and fairy circles of the Namib desert," *Philosophical Transactions of the Royal Society B*, vol. 378, no. 1884, p. 20220149, 2023.

[180] D. Hillel, *Introduction to environmental soil physics*. Elsevier, 2003.

[181] P. Kuncoro, K. Koga, N. Satta, and Y. Muto, "A study on the effect of compaction on transport properties of soil gas and water i: Relative gas diffusivity, air permeability, and saturated hydraulic conductivity," *Soil and Tillage Research*, vol. 143, pp. 172–179, 2014.

[182] M. F. Nawaz, G. Bourrie, and F. Trolard, "Soil compaction impact and modelling. a review," *Agronomy for Sustainable Development*, vol. 33, pp. 291–309, 2013.

[183] C. Gai and T. Kolokolnikov, "Resource-mediated competition between two plant species with different rates of water intake," *SIAM Journal on Applied Mathematics*, vol. 83, no. 2, pp. 576–602, 2023.

[184] A. B. Medvinsky, S. V. Petrovskii, I. A. Tikhonova, H. Malchow, and B. L. Li, "Spatiotemporal complexity of plankton and fish dynamics," *SIAM review*, vol. 44, no. 3, pp. 311–370, 2002.

[185] S. Petrovskii and H. Malchow, "Wave of chaos: new mechanism of pattern formation in spatiotemporal population dynamics," *Theoretical Population Biology*, vol. 59, no. 2, pp. 157–174, 2001.

[186] S. Petrovskii, B.-L. Li, and H. Malchow, "Transition to spatiotemporal chaos can resolve the paradox of enrichment," *Ecological Complexity*, vol. 1, no. 1, pp. 37–47, 2004.

[187] V. Volpert and S. Petrovskii, "Reaction–diffusion waves in biology," *Physics of life reviews*, vol. 6, no. 4, pp. 267–310, 2009.

[188] F. Sánchez-Garduno, A. L. Krause, J. A. Castillo, and P. Padilla, "Turing–hopf patterns on growing domains: the torus and the sphere," *Journal of Theoretical Biology*, vol. 481, pp. 136–150, 2019.

[189] M. L. Steyn-Ross, D. A. Steyn-Ross, and J. W. Sleigh, "Interacting turing-hopf instabilities drive symmetry-breaking transitions in a mean-field model of the cortex: a mechanism for the slow oscillation," *Physical Review X*, vol. 3, no. 2, p. 021005, 2013.

[190] Y. A. Logvin and T. Ackemann, "Interaction between hopf and static instabilities in a pattern-forming optical system," *Physical Review E*, vol. 58, no. 2, p. 1654, 1998.

[191] A. Rovinsky and M. Menzinger, "Interaction of turing and hopf bifurcations in chemical systems," *Physical Review A*, vol. 46, no. 10, p. 6315, 1992.

[192] M. Le Berre, E. Ressayre, A. Tallet, and M. Tlidi, "Spiral patterns, spiral breakup, and zigzag spirals in an optical device," *Physical Review E*, vol. 71, no. 3, p. 036224, 2005.

[193] H. R. Wilson, R. Blake, and S.-H. Lee, "Dynamics of travelling waves in visual perception," *Nature*, vol. 412, no. 6850, pp. 907–910, 2001.

[194] K. J. Painter and T. Hillen, "Spatio-temporal chaos in a chemotaxis model," *Physica D: Nonlinear Phenomena*, vol. 240, no. 4-5, pp. 363–375, 2011.

[195] R. K. Upadhyay, N. Kumari, and V. Rai, "Wave of chaos in a diffusive system: Generating realistic patterns of patchiness in plankton–fish dynamics," *Chaos, Solitons & Fractals*, vol. 40, no. 1, pp. 262–276, 2009.

[196] S. Ghorai and S. Poria, "Turing patterns induced by cross-diffusion in a predator-prey system in presence of habitat complexity," *Chaos, Solitons & Fractals*, vol. 91, pp. 421–429, 2016.

[197] S. Ghorai, B. Chakraborty, and N. Bairagi, "Preferential selection of zooplankton and emergence of spatiotemporal patterns in plankton population," *Chaos, Solitons & Fractals*, vol. 153, p. 111471, 2021.

[198] B. Chakraborty, S. Marick, and N. Bairagi, "Diffusion-driven instabilities in a tri-trophic food web model: From turing to non-turing patterns and waves," *Chaos, Solitons & Fractals*, vol. 189, p. 115634, 2024.

[199] S. Marick, S. Ghorai, and N. Bairagi, "Dynamic characteristics of a hyperbolic reaction–diffusion predator–prey system with self-diffusion and nonidentical inertia," *Mathematical Methods in the Applied Sciences*, vol. 46, no. 13, pp. 14407–14421, 2023.

[200] G. Hu and Z. Feng, "Turing instability and pattern formation in a strongly coupled diffusive predator–prey system," *International Journal of Bifurcation and Chaos*, vol. 30, no. 08, p. 2030020, 2020.

[201] D. Tilman and P. Kareiva, *Spatial ecology: the role of space in population dynamics and interspecific interactions*, vol. 30. Princeton University Press, 1997.

[202] A. Hastings, "Can spatial variation alone lead to selection for dispersal?," *Theoretical Population Biology*, vol. 24, no. 3, pp. 244–251, 1983.

[203] S. L. Lima and L. M. Dill, "Behavioral decisions made under the risk of predation: a review and prospectus," *Canadian Journal of Zoology*, vol. 68, no. 4, pp. 619–640, 1990.

[204] S. Kundu, S. Majhi, S. K. Sasmal, D. Ghosh, and B. Rakshit, "Survivability of a metapopulation under local extinctions," *Physical Review E*, vol. 96, no. 6, p. 062212, 2017.

[205] I. Hanski and M. Gilpin, "Metapopulation dynamics: brief history and conceptual domain," *Biological journal of the Linnean Society*, vol. 42, no. 1-2, pp. 3–16, 1991.

[206] D. J. Earn, S. A. Levin, and P. Rohani, "Coherence and conservation," *Science*, vol. 290, no. 5495, pp. 1360–1364, 2000.

[207] J. Greenman and T. Benton, "The impact of environmental fluctuations on structured discrete time population models: resonance, synchrony and threshold behaviour," *Theoretical Population Biology*, vol. 68, no. 4, pp. 217–235, 2005.

[208] K. Siteur, E. Siero, M. B. Eppinga, J. D. Rademacher, A. Doelman, and M. Rietkerk, "Beyond turing: The response of patterned ecosystems to environmental change," *Ecological Complexity*, vol. 20, pp. 81–96, 2014.

[209] S. Marick, F. Takasu, and N. Bairagi, "How do productivity gradient and diffusion shape patterns in a plant–herbivore grazing system?," *Journal of Theoretical Biology*, vol. 590, p. 111856, 2024.

[210] O. N. Bjørnstad, R. A. Ims, and X. Lambin, "Spatial population dynamics: analyzing patterns and processes of population synchrony," *Trends in Ecology & Evolution*, vol. 14, no. 11, pp. 427–432, 1999.

[211] J. Bascompte and R. V. Solé, *Modeling spatiotemporal dynamics in ecology*. Springer Berlin, 1998.

[212] S. Kundu, S. Majhi, P. Muruganandam, and D. Ghosh, "Diffusion induced spiral wave chimeras in ecological system," *The European Physical Journal Special Topics*, vol. 227, pp. 983–993, 2018.

[213] S. Marick and N. Bairagi, "Effect of dispersal-induced death in predator–prey metapopulation system with bistable local dynamics," *Physica D: Nonlinear Phenomena*, vol. 476, p. 134597, 2025.

[214] S. Saha, N. Bairagi, and S. K. Dana, "Chimera states in ecological network under weighted mean-field dispersal of species," *Frontiers in Applied Mathematics and Statistics*, vol. 5, p. 15, 2019.

[215] H. Alkhayuon, R. C. Tyson, and S. Wieczorek, "Phase tipping: how cyclic ecosystems respond to contemporary climate," *Proceedings of the Royal Society A*, vol. 477, no. 2254, p. 20210059, 2021.

[216] B. F. Dyck and R. Tyson, "Host-parasitoid systems are vulnerable to extinction via p-tipping: Forest tent caterpillar as an example," *Bulletin of Mathematical Biology*, vol. 86, no. 12, pp. 1–17, 2024.

[217] C. R. Hasan, R. M. Cárthaigh, and S. Wieczorek, "Rate-induced tipping in heterogeneous reaction-diffusion systems: An invariant manifold framework and geographically shifting ecosystems," *SIAM Journal on Applied Dynamical Systems*, vol. 22, no. 4, pp. 2991–3024, 2023.

[218] Y. Kuramoto, "Chemical turbulence," in *Chemical oscillations, waves, and turbulence*, pp. 111–140, Springer, 1984.

[219] E. P. Zemskov, M. A. Tsyganov, and W. Horsthemke, "Wavy fronts in a hyperbolic fitzhugh-nagumo system and the effects of cross diffusion," *Physical Review E*, vol. 91, no. 6, p. 062917, 2015.

[220] A. James, M. J. Plank, and A. M. Edwards, "Assessing lévy walks as models of animal foraging," *Journal of the Royal Society Interface*, vol. 8, no. 62, pp. 1233–1247, 2011.

[221] D. Jou, J. Casas-Vázquez, and G. Lebon, "Extended irreversible thermodynamics revisited (1988-98)," *Reports on Progress in Physics*, vol. 62, no. 7, pp. 1035–1142, 1999.

[222] M. Al-Ghoul and B. C. Eu, "Hyperbolic reaction- diffusion equations, patterns, and phase speeds for the brusselator," *The Journal of Physical Chemistry*, vol. 100, no. 49, pp. 18900–18910, 1996.

[223] M. Al-Ghoul and B. C. Eu, "Hyperbolic reaction-diffusion equations and irreversible thermodynamics: Cubic reversible reaction model," *Physica D: Nonlinear Phenomena*, vol. 90, no. 1-2, pp. 119–153, 1996.

[224] E. Barbera, C. Curro, and G. Valenti, "A hyperbolic reaction–diffusion model for the hantavirus infection," *Mathematical Methods in the Applied Sciences*, vol. 31, no. 4, pp. 481–499, 2008.

[225] E. Barbera, G. Consolo, and G. Valenti, "Spread of infectious diseases in a hyperbolic reaction-diffusion susceptible-infected-removed model," *Physical Review E*, vol. 88, no. 5, p. 052719, 2013.

[226] J. Macías-Díaz and H. Vargas-Rodríguez, "Analysis and simulation of numerical schemes for nonlinear hyperbolic predator–prey models with spatial diffusion," *Journal of Computational and Applied Mathematics*, vol. 404, p. 113636, 2022.

[227] E. Barbera, G. Consolo, and G. Valenti, "A two or three compartments hyperbolic reaction-diffusion model for the aquatic food chain," *Mathematical Biosciences & Engineering*, vol. 12, no. 3, p. 451, 2015.

[228] E. Barbera, C. Currò, and G. Valenti, "Wave features of a hyperbolic prey–predator model," *Mathematical Methods in the Applied Sciences*, vol. 33, no. 12, pp. 1504–1515, 2010.

[229] T. Carletti and R. Muolo, "Finite propagation enhances turing patterns in reaction–diffusion networked systems," *Journal of Physics: Complexity*, vol. 2, no. 4, p. 045004, 2021.

[230] G. Bertaglia and L. Pareschi, "Hyperbolic models for the spread of epidemics on networks: kinetic description and numerical methods," *ESAIM: Mathematical Modelling and Numerical Analysis*, vol. 55, no. 2, pp. 381–407, 2021.

[231] S. Ghorai, S. Poria, and N. Bairagi, "Diffusive instability in hyperbolic reaction–diffusion equation with different inertia," *Chaos: An Interdisciplinary Journal of Nonlinear Science*, vol. 32, no. 1, p. 013101, 2022.

[232] Y. Huang, F. Chen, and L. Zhong, "Stability analysis of a prey–predator model with Holling type III response function incorporating a prey refuge," *Applied Mathematics and Computation*, vol. 182, no. 1, pp. 672–683, 2006.

[233] P. Chow and W. Tam, "Periodic and traveling wave solutions to volterra-lotka equations with diffusion," *Bulletin of Mathematical Biology*, vol. 38, no. 6, pp. 643–658, 1976.

[234] W. Wang, L. Zhang, H. Wang, and Z. Li, "Pattern formation of a predator–prey system with ivlev-type functional response," *Ecological Modelling*, vol. 221, no. 2, pp. 131–140, 2010.

[235] T. K. Kar and H. Matsuda, "Harvesting in a two-prey one-predator fishery: a catch-per-unit-effort approach," *Journal of Theoretical Biology*, vol. 238, no. 1, pp. 117–129, 2006.

[236] D. Pal and J. Chattopadhyay, "Dynamics of prey–predator system with cpue harvesting," *Nonlinear Dynamics*, vol. 82, pp. 1531–1543, 2015.

[237] J. A. Sherratt, "Waves, pattern and predators," *Journal of Mathematical Biology*, vol. 32, pp. 491–527, 1994.

[238] H. Malchow, S. Petrovskii, *et al.*, "Spatiotemporal patterns in ecology and epidemiology: theory, models, and simulation," *Mathematics and Computers in Simulation*, vol. 78, no. 1, pp. 1–16, 2008.

[239] M. Rietkerk and J. van de Koppel, "Regular pattern formation in real ecosystems," *Trends in Ecology & Evolution*, vol. 23, no. 3, pp. 169–175, 2008.

[240] J. J. Bennett, A. S. Gomes, M. A. Ferré, B. K. Bera, F. Borghetti, R. M. Callaway, and E. Meron, "Evidence for scale-dependent root-augmentation feedback and its role in halting the spread of a pantropical shrub into an endemic sedge," *PNAS Nexus*, vol. 2, no. 1, p. pgac294, 2023.

[241] I. Riyaz, S. Shafi, A. Zaffar, M. A. Wani, S. M. Zargar, M. Djanaguiraman, P. V. Prasad, and P. A. Sofi, "Differential spatial plasticity response in common bean (phaseolus vulgaris l.) root architecture under water stress is driven by increased root diameter, surface area and volume at deeper layers," *Discover Plants*, vol. 1, no. 1, p. 6, 2024.

[242] W. R. Gardner, "Dynamic aspects of water availability to plants," *Soil Science*, vol. 89, no. 2, pp. 63–73, 1960.

[243] D. Miller and W. Gardner, "Water infiltration into stratified soil," *Soil Science Society of America Journal*, vol. 26, no. 2, pp. 115–119, 1962.

[244] D. Escaff, C. Fernandez-Oto, M. Clerc, and M. Tlidi, "Localized vegetation patterns, fairy circles, and localized patches in arid landscapes," *Physical Review E*, vol. 91, no. 2, p. 022924, 2015.

[245] L. Eigentler and J. A. Sherratt, "Analysis of a model for banded vegetation patterns in semi-arid environments with nonlocal dispersal," *Journal of mathematical biology*, vol. 77, no. 3, pp. 739–763, 2018.

[246] J. Liang, C. Liu, G.-Q. Sun, L. Li, L. Zhang, M. Hou, H. Wang, and Z. Wang, "Nonlocal interactions between vegetation induce spatial patterning," *Applied Mathematics and Computation*, vol. 428, p. 127061, 2022.

[247] P. J. Kramer and J. S. Boyer, *Water relations of plants and soils*. Academic press, 1995.

[248] F. R. Gantmakher, *The theory of matrices*, vol. 1. American Mathematical Soc., 1959.

[249] S. Focardi, P. Marcellini, and P. Montanaro, "Do ungulates exhibit a food density threshold? a field study of optimal foraging and movement patterns," *Journal of Animal Ecology*, pp. 606–620, 1996.

[250] L. N. Guin, "Existence of spatial patterns in a predator–prey model with self-and cross-diffusion," *Applied Mathematics and Computation*, vol. 226, pp. 320–335, 2014.

[251] L. N. Guin and P. K. Mandal, "Spatiotemporal dynamics of reaction–diffusion models of interacting populations," *Applied Mathematical Modelling*, vol. 38, no. 17-18, pp. 4417–4427, 2014.

[252] M. Banerjee and S. Petrovskii, "Self-organised spatial patterns and chaos in a ratio-dependent predator–prey system," *Theoretical Ecology*, vol. 4, pp. 37–53, 2011.

[253] M. Baurmann, T. Gross, and U. Feudel, "Instabilities in spatially extended predator–prey systems: Spatio-temporal patterns in the neighborhood of turing–hopf bifurcations," *Journal of Theoretical Biology*, vol. 245, no. 2, pp. 220–229, 2007.

[254] K. E. Anderson, B. D. Inouye, and N. Underwood, "Can inducible resistance in plants cause herbivore aggregations? spatial patterns in an inducible plant/herbivore model," *Ecology*, vol. 96, no. 10, pp. 2758–2770, 2015.

[255] G.-Q. Sun, J. Zhang, L.-P. Song, Z. Jin, and B.-L. Li, "Pattern formation of a spatial predator–prey system," *Applied Mathematics and Computation*, vol. 218, no. 22, pp. 11151–11162, 2012.

[256] A. M. Turing, "The chemical basis of morphogenesis," *Philosophical Transactions of the Royal Society of London. Series B, Biological Sciences*, vol. 237, no. 641, pp. 37–72, 1952.

[257] S. Ghorai and S. Poria, "Pattern formation and control of spatiotemporal chaos in a reaction diffusion prey–predator system supplying additional food," *Chaos, Solitons & Fractals*, vol. 85, pp. 57–67, 2016.

[258] B. Chakraborty, H. Baek, and N. Bairagi, "Diffusion-induced regular and chaotic patterns in a ratio-dependent predator–prey model with fear factor and prey refuge," *Chaos: An Interdisciplinary Journal of Nonlinear Science*, vol. 31, no. 3, 2021.

[259] H. T. Dublin, A. R. Sinclair, and J. McGlade, "Elephants and fire as causes of multiple stable states in the serengeti-mara woodlands," *The Journal of Animal Ecology*, pp. 1147–1164, 1990.

[260] A. Dobson and M. Crawley, "Pathogens and the structure of plant communities," *Trends in Ecology & Evolution*, vol. 9, no. 10, pp. 393–398, 1994.

[261] W. F. Morris and G. Dwyer, "Population consequences of constitutive and inducible plant resistance: herbivore spatial spread," *The American Naturalist*, vol. 149, no. 6, pp. 1071–1090, 1997.

[262] L. Li, Z. Jin, and J. Li, "Periodic solutions in a herbivore-plant system with time delay and spatial diffusion," *Applied Mathematical Modelling*, vol. 40, no. 7-8, pp. 4765–4777, 2016.

[263] N. Xiang, Q. Wu, and A. Wan, "Spatiotemporal patterns of a diffusive plant–herbivore model with toxin-determined functional responses: Multiple bifurcations," *Mathematics and Computers in Simulation*, vol. 187, pp. 337–356, 2021.

[264] C.-H. Zhang and X.-P. Yan, "Formation of time patterns in a diffusive plant–herbivore system with toxin-determined functional response," *International Journal of Biomathematics*, vol. 8, no. 04, p. 1550051, 2015.

[265] Z. Feng, W. Huang, and D. L. DeAngelis, "Spatially heterogeneous invasion of toxic plant mediated by herbivory," *Mathematical Biosciences & Engineering*, vol. 10, no. 5&6, pp. 1519–1538, 2013.

[266] D. DeAngelis, P. Mulholland, A. Palumbo, A. Steinman, M. Huston, and J. Elwood, "Nutrient dynamics and food-web stability," *Annual Review of Ecology and Systematics*, vol. 20, no. 1, pp. 71–95, 1989.

[267] R. Kumbhakar, S. Pal, N. Pal, and P. K. Tiwari, "Bistability and tristability in a predator–prey model with strong allee effect in prey," *Journal of Biological Systems*, vol. 31, no. 01, pp. 215–243, 2023.

[268] A. Erbach, F. Lutscher, and G. Seo, "Bistability and limit cycles in generalist predator–prey dynamics," *Ecological Complexity*, vol. 14, pp. 48–55, 2013.

[269] B. Barnes and H. Sidhu, "Plant-herbivore models, where more grass means fewer grazers," *Bulletin of Mathematical Biology*, vol. 67, pp. 33–55, 2005.

[270] J. Eccard, R. Walther, and S. Milton, "How livestock grazing affects vegetation structures and small mammal distribution in the semi-arid karoo," *Journal of Arid Environments*, vol. 46, no. 2, pp. 103–106, 2000.

[271] E. N. Mueller, J. Wainwright, A. J. Parsons, and L. Turnbull, *Patterns of land degradation in drylands*. Springer, 2014.

[272] J. van de Koppel, M. Rietkerk, F. van Langevelde, L. Kumar, C. A. Klausmeier, J. M. Fryxell, J. W. Hearne, J. van Andel, N. de Ridder, A. Skidmore, *et al.*, "Spatial heterogeneity and irreversible vegetation change in semiarid grazing systems," *The American Naturalist*, vol. 159, no. 2, pp. 209–218, 2002.

[273] R. Turkington, "Top-down and bottom-up forces in mammalian herbivore–vegetation systems: an essay review," *Botany*, vol. 87, no. 8, pp. 723–739, 2009.

[274] P. E. O'Keeffe and S. Wieczorek, "Tipping phenomena and points of no return in ecosystems: beyond classical bifurcations," *SIAM Journal on Applied Dynamical Systems*, vol. 19, no. 4, pp. 2371–2402, 2020.

[275] X. Wang and Y. Wang, "Novel dynamics of a predator–prey system with harvesting of the predator guided by its population," *Applied Mathematical Modelling*, vol. 42, pp. 636–654, 2017.

[276] M. Kot, *Elements of mathematical ecology*. Cambridge University Press, 2001.

[277] M. Banerjee, S. Ghorai, and N. Mukherjee, "Study of cross-diffusion induced turing patterns in a ratio-dependent prey-predator model via amplitude equations," *Applied Mathematical Modelling*, vol. 55, pp. 383–399, 2018.

[278] X. Chen, R. Hambrock, and Y. Lou, "Evolution of conditional dispersal: a reaction–diffusion–advection model," *Journal of mathematical biology*, vol. 57, no. 3, pp. 361–386, 2008.

[279] J. B. Jackson, M. X. Kirby, W. H. Berger, K. A. Bjorndal, L. W. Botsford, B. J. Bourque, R. H. Bradbury, R. Cooke, J. Erlandson, J. A. Estes, *et al.*, "Historical overfishing and the recent collapse of coastal ecosystems," *science*, vol. 293, no. 5530, pp. 629–637, 2001.

[280] R. Hilborn, C. J. Walters, and D. Ludwig, "Sustainable exploitation of renewable resources," *Annual Review of Ecology and Systematics*, vol. 26, no. 1, pp. 45–67, 1995.

[281] J. Shi and R. Shivaji, "Persistence in reaction diffusion models with weak allee effect," *Journal of Mathematical Biology*, vol. 52, no. 6, pp. 807–829, 2006.

[282] J. D. Murray, *Mathematical biology: I. An introduction*. Springer, 2002.

[283] N. Bairagi, S. Bhattacharya, P. Auger, and B. Sarkar, "Bioeconomics fishery model in presence of infection: Sustainability and demand-price perspectives," *Applied Mathematics and Computation*, vol. 405, p. 126225, 2021.

[284] D. Hu and H. Cao, "Stability and bifurcation analysis in a predator–prey system with michaelis–menten type predator harvesting," *Nonlinear Analysis: Real World Applications*, vol. 33, pp. 58–82, 2017.

[285] N. Mukherjee, S. Ghorai, and M. Banerjee, "Detection of turing patterns in a three species food chain model via amplitude equation," *Communications in Nonlinear Science and Numerical Simulation*, vol. 69, pp. 219–236, 2019.

[286] H. Matsuda and P. A. Abrams, "Maximal yields from multispecies fisheries systems: rules for systems with multiple trophic levels," *Ecological Applications*, vol. 16, no. 1, pp. 225–237, 2006.

[287] E. Benincà, K. D. Jöhnk, R. Heerkloss, and J. Huisman, "Coupled predator–prey oscillations in a chaotic food web," *Ecology Letters*, vol. 12, no. 12, pp. 1367–1378, 2009.

[288] A. A. Berryman, "The orgins and evolution of predator-prey theory," *Ecology*, vol. 73, no. 5, pp. 1530–1535, 1992.

[289] J. Hu, L. Zhu, and M. Peng, "Analysis of turing patterns and amplitude equations in general forms under a reaction–diffusion rumor propagation system with allee effect and time delay," *Information Sciences*, vol. 596, pp. 501–519, 2022.

[290] Y. Cai, M. Banerjee, Y. Kang, and W. Wang, "Spatiotemporal complexity in a predator–prey model with weak allee effects," *Mathematical Biosciences & Engineering*, vol. 11, no. 6, p. 1247, 2014.

[291] G. Gambino, M. Lombardo, and M. Sammartino, "Cross-diffusion-induced subharmonic spatial resonances in a predator-prey system," *Physical Review E*, vol. 97, no. 1, p. 012220, 2018.

[292] M. Alqhtani, K. M. Owolabi, and K. M. Saad, "Spatiotemporal (target) patterns in sub-diffusive predator-prey system with the caputo operator," *Chaos, Solitons & Fractals*, vol. 160, p. 112267, 2022.

[293] F. Souna, M. Belabbas, and Y. Menacer, "Complex pattern formations induced by the presence of cross-diffusion in a generalized predator–prey model incorporating the holling type functional response and generalization of habitat complexity effect," *Mathematics and Computers in Simulation*, vol. 204, pp. 597–618, 2023.

[294] B. Liu, R. Wu, and L. Chen, "Patterns induced by super cross-diffusion in a predator-prey system with michaelis–menten type harvesting," *Mathematical Biosciences*, vol. 298, pp. 71–79, 2018.

[295] J. F. Riebesell, "Paradox of enrichment in competitive systems," *Ecology*, vol. 55, no. 1, pp. 183–187, 1974.

[296] L. Bunting, P. Leavitt, G. Simpson, B. Wissel, K. Laird, B. Cumming, A. St. Amand, and D. Engstrom, "Increased variability and sudden ecosystem state change in lake winnipeg, canada, caused by 20th century agriculture," *Limnology and Oceanography*, vol. 61, no. 6, pp. 2090–2107, 2016.

[297] B. Xie, Z. Zhang, and N. Zhang, "Influence of the fear effect on a holling type ii prey–predator system with a michaelis–menten type harvesting," *International Journal of Bifurcation and Chaos*, vol. 31, no. 14, p. 2150216, 2021.

[298] S. Saha, A. Maiti, and G. Samanta, "A michaelis–menten predator–prey model with strong allee effect and disease in prey incorporating prey refuge," *International Journal of Bifurcation and Chaos*, vol. 28, no. 06, p. 1850073, 2018.

[299] R. Wu, M. Chen, B. Liu, and L. Chen, "Hopf bifurcation and turing instability in a predator–prey model with michaelis–menten functional response," *Nonlinear Dynamics*, vol. 91, no. 3, pp. 2033–2047, 2018.

[300] R. Gupta and P. Chandra, "Bifurcation analysis of modified Leslie–Gower predator–prey model with Michaelis–Menten type prey harvesting," *Journal of Mathematical Analysis and Applications*, vol. 398, no. 1, pp. 278–295, 2013.

[301] T. Kar and B. Ghosh, "Impacts of maximum sustainable yield policy to prey–predator systems," *Ecological Modelling*, vol. 250, pp. 134–142, 2013.

[302] S. K. Sasmal, "Population dynamics with multiple allee effects induced by fear factors–a mathematical study on prey-predator interactions," *Applied Mathematical Modelling*, vol. 64, pp. 1–14, 2018.

[303] C. Neuhauser, "Mathematical challenges in spatial ecology," *Notices of the AMS*, vol. 48, no. 11, pp. 1304–1314, 2001.

[304] J. P. Stover, B. E. Kendall, and G. A. Fox, "Demographic heterogeneity impacts density-dependent population dynamics," *Theoretical Ecology*, vol. 5, no. 2, pp. 297–309, 2012.

[305] R. Upadhyay, V. Volpert, and N. Thakur, "Propagation of Turing patterns in a plankton model," *Journal of Biological Dynamics*, vol. 6, no. 2, pp. 524–538, 2012.

[306] G. Sun, S. Sarwardi, P. Pal, and M. S. Rahman, "The spatial patterns through diffusion-driven instability in modified leslie-gower and holling-type ii predator-prey model," *Journal of Biological Systems*, vol. 18, no. 03, pp. 593–603, 2010.

[307] D. Alonso, F. Bartumeus, and J. Catalan, "Mutual interference between predators can give rise to turing spatial patterns," *Ecology*, vol. 83, no. 1, pp. 28–34, 2002.

[308] J. D. Murray, "Discussion: Turing's theory of morphogenesis—its influence on modelling biological pattern and form," *Bulletin of Mathematical Biology*, vol. 52, no. 1, pp. 117–152, 1990.

[309] M. Wang, "Stationary patterns for a prey–predator model with prey-dependent and ratio-dependent functional responses and diffusion," *Physica D: Nonlinear Phenomena*, vol. 196, no. 1-2, pp. 172–192, 2004.

[310] M. Wang, "Stationary patterns of strongly coupled prey–predator models," *Journal of Mathematical Analysis and Applications*, vol. 292, no. 2, pp. 484–505, 2004.

[311] M. Wang, "Stationary patterns caused by cross-diffusion for a three-species prey-predator model," *Computers & Mathematics with Applications*, vol. 52, no. 5, pp. 707–720, 2006.

[312] R. Muolo, L. Gallo, V. Latora, M. Frasca, and T. Carletti, "Turing patterns in systems with high-order interactions," *Chaos, Solitons & Fractals*, vol. 166, p. 112912, 2023.

[313] J. Zhao and Y. Shao, "Bifurcations of a prey-predator system with fear, refuge and additional food," *Mathematical Biosciences and Engineering*, vol. 20, no. 2, pp. 3700–3720, 2023.

[314] G. Q. Sun, Z. Jin, Q. X. Liu, and L. Li, "Dynamical complexity of a spatial predator–prey model with migration," *Ecological Modelling*, vol. 219, no. 1-2, pp. 248–255, 2008.

[315] P. P. Liu, "An analysis of a predator–prey model with both diffusion and migration," *Mathematical and Computer Modelling*, vol. 51, no. 9-10, pp. 1064–1070, 2010.

[316] E. Venturino and S. Petrovskii, "Spatiotemporal behavior of a prey–predator system with a group defense for prey," *Ecological Complexity*, vol. 14, pp. 37–47, 2013.

[317] M. C. Köhnke, I. Siekmann, and H. Malchow, "Taxis-driven pattern formation in a predator-prey model with group defense," *Ecological Complexity*, vol. 43, p. 100848, 2020.

[318] S. J. Brentnall, K. J. Richards, J. Brindley, and E. Murphy, "Plankton patchiness and its effect on larger-scale productivity," *Journal of Plankton Research*, vol. 25, no. 2, pp. 121–140, 2003.

[319] J. M. G. Vilar, R. V. Solé, and J. M. Rubı, "On the origin of plankton patchiness," *Physica A: Statistical Mechanics and its Applications*, vol. 317, no. 1-2, pp. 239–246, 2003.

[320] J. Shi, Z. Xie, and K. L., "Cross-diffusion induced instability and stability in reaction-diffusion systems," *Journal of Applied Analysis and Computation*, vol. 1, no. 1, pp. 95–119, 2011.

[321] X. Li, W. Jiang, and J. Shi, "Hopf bifurcation and turing instability in the reaction–diffusion holling–tanner predator–prey model," *IMA Journal of Applied Mathematics*, vol. 78, no. 2, pp. 287–306, 2013.

[322] A. L. Lin, M. Bertram, K. Martinez, H. L. Swinney, A. Ardelea, and G. F. Carey, "Resonant phase patterns in a reaction-diffusion system," *Physical Review Letters*, vol. 84, no. 18, p. 4240, 2000.

[323] Y. Cai, Y. Kang, M. Banerjee, and W. Wang, "Complex dynamics of a host–parasite model with both horizontal and vertical transmissions in a spatial heterogeneous environment," *Nonlinear Analysis: Real World Applications*, vol. 40, pp. 444–465, 2018.

[324] T. Hillen, "A turing model with correlated random walk," *Journal of Mathematical Biology*, vol. 35, no. 1, pp. 49–72, 1996.

[325] T. Hillen, "Invariance principles for hyperbolic random walk systems," *Journal of Mathematical Analysis and Applications*, vol. 210, no. 1, pp. 360–374, 1997.

[326] H. G. Othmer, S. R. Dunbar, and W. Alt, "Models of dispersal in biological systems," *Journal of mathematical biology*, vol. 26, no. 3, pp. 263–298, 1988.

[327] J. Smoller, *Shock waves and reaction—diffusion equations*, vol. 258. Springer Science & Business Media, 2012.

[328] L. Onsager, "Reciprocal relations in irreversible processes. ii.," *Physical Review*, vol. 38, no. 12, p. 2265, 1931.

[329] P. Maini, K. Painter, and H. P. Chau, "Spatial pattern formation in chemical and biological systems," *Journal of the Chemical Society, Faraday Transactions*, vol. 93, no. 20, pp. 3601–3610, 1997.

[330] A. T. Winfree, "Spiral waves of chemical activity," *Science*, vol. 175, no. 4022, pp. 634–636, 1972.

[331] A. Gierer and H. Meinhardt, "A theory of biological pattern formation," *Kybernetik*, vol. 12, no. 1, pp. 30–39, 1972.

[332] K. W. Rogers and A. F. Schier, "Morphogen gradients: from generation to interpretation," *Annual Review of Cell and Developmental Biology*, vol. 27, pp. 377–407, 2011.

[333] J. Ma, Y. Xu, G. Ren, and C. Wang, "Prediction for breakup of spiral wave in a regular neuronal network," *Nonlinear Dynamics*, vol. 84, no. 2, pp. 497–509, 2016.

[334] Y. Xu, W. Jin, and J. Ma, "Emergence and robustness of target waves in a neuronal network," *International Journal of Modern Physics B*, vol. 29, no. 23, p. 1550164, 2015.

[335] Q. Ouyang and H. L. Swinney, "Transition from a uniform state to hexagonal and striped turing patterns," *Nature*, vol. 352, no. 6336, pp. 610–612, 1991.

[336] M. C. Cross and P. C. Hohenberg, "Pattern formation outside of equilibrium," *Reviews of Modern Physics*, vol. 65, no. 3, p. 851, 1993.

[337] J. Sprott, "A simple chaotic delay differential equation," *Physics Letters A*, vol. 366, no. 4-5, pp. 397–402, 2007.

[338] S. R. Dunbar, "Traveling waves in diffusive predator–prey equations: periodic orbits and point-to-periodic heteroclinic orbits," *SIAM Journal on Applied Mathematics*, vol. 46, no. 6, pp. 1057–1078, 1986.

[339] P. C. Fife, *Mathematical aspects of reacting and diffusing systems*, vol. 28. Springer Science & Business Media, 2013.

[340] F. Verhulst, *Nonlinear differential equations and dynamical systems*. Springer Science & Business Media, 2006.

[341] H. Baek, "Bifurcation analysis of a predator-prey system with self-and cross-diffusion and constant harvesting rate," *Electronic Journal of Qualitative Theory of Differential Equations*, vol. 2014, no. 29, pp. 1–14, 2014.

[342] D. Walgraef, *Spatio-temporal pattern formation: with examples from physics, chemistry, and materials science*. Springer Science & Business Media, 2012.

[343] C. Cosner, "Reaction-diffusion-advection models for the effects and evolution of dispersal," *Discrete & Continuous Dynamical Systems*, vol. 34, no. 5, p. 1701, 2014.

[344] M. Lewis, "Spatial coupling of plant and herbivore dynamics: the contribution of herbivore dispersal to transient and persistent" waves" of damage," *Theoretical Population Biology*, vol. 45, no. 3, pp. 277–312, 1994.

[345] C. C. Wilmers, E. Post, and A. Hastings, "A perfect storm: the combined effects on population fluctuations of autocorrelated environmental noise, age structure, and density dependence," *The American Naturalist*, vol. 169, no. 5, pp. 673–683, 2007.

[346] R. M. May, *Stability and complexity in model ecosystems*. Princeton university press, 2019.

[347] B. Anderson, J. Jackson, and M. Sitharam, "Descartes' rule of signs revisited," *The American Mathematical Monthly*, vol. 105, no. 5, pp. 447–451, 1998.

[348] R. Tyson, S. Haines, and K. E. Hodges, "Modelling the Canada lynx and snowshoe hare population cycle: the role of specialist predators," *Theoretical Ecology*, vol. 3, pp. 97–111, 2010.

[349] F. Courchamp, L. Berec, and J. Gascoigne, *Allee effects in ecology and conservation*. OUP Oxford, 2008.

[350] J. D. Murray, "Spatial models and biomedical applications," *Mathematical Biology*, 2003.

[351] S. A. Levin and L. A. Segel, "Hypothesis for origin of planktonic patchiness," *Nature*, vol. 259, no. 5545, pp. 659–659, 1976.

[352] Z. Liang and H. Pan, "Qualitative analysis of a ratio-dependent holling–tanner model," *Journal of Mathematical Analysis and Applications*, vol. 334, no. 2, pp. 954–964, 2007.

[353] J. Horváth, I. Szalai, and P. De Kepper, "An experimental design method leading to chemical turing patterns," *Science*, vol. 324, no. 5928, pp. 772–775, 2009.

[354] S. Kondo and T. Miura, "Reaction-diffusion model as a framework for understanding biological pattern formation," *science*, vol. 329, no. 5999, pp. 1616–1620, 2010.

[355] L. Guo, X. Shi, and J. Cao, "Turing patterns of gierer–meinhardt model on complex networks," *Nonlinear Dynamics*, vol. 105, pp. 899–909, 2021.

[356] H. G. Othmer and L. Scriven, "Non-linear aspects of dynamic pattern in cellular networks," *Journal of Theoretical Biology*, vol. 43, no. 1, pp. 83–112, 1974.

[357] I. Hanski and D. Simberloff, "The metapopulation approach, its history, conceptual domain, and application to conservation," *Metapopulation Biology*, pp. 5–26, 1997.

[358] S. Harrison and A. D. Taylor, "Empirical evidence for metapopulation dynamics," *Metapopulation Biology*, pp. 27–42, 1997.

[359] H. G. Othmer and L. Scriven, "Instability and dynamic pattern in cellular networks," *Journal of Theoretical Biology*, vol. 32, no. 3, pp. 507–537, 1971.

[360] A. S. Mikhailov and K. Showalter, "Control of waves, patterns and turbulence in chemical systems," *Physics Reports*, vol. 425, no. 2-3, pp. 79–194, 2006.